Thermally Stable Moisture Responsive Chitosan based Mixed Matrix Membranes for Selective CO_2 Separation

A report is submitted to the Indian Institute

of Technology Guwahati in partial

fulfillment for the degree of

DOCTOR of PHILOSOPHY

By

AVITI KATARE

Roll No. (196107001)

Department of Chemical Engineering

Indian Institute of Technology Guwahati

Assam, Guwahati, India

June 2024

Department of Chemical Engineering
Indian Institute of Technology Guwahati
Guwahati, Assam 781039

Statement

I certify that the information in the thesis with the title "**Thermally Stable Moisture Responsive Chitosan based Mixed Matrix Membranes for Selective CO_2 Separation**" is the result of research I carried out at the Department of Chemical Engineering at the Indian Institute of Technology Guwahati in Guwahati, India, under the guidance of Prof. Bishnupada Mandal. According to the accepted practise for publishing scientific observations, appropriate acknowledgements have been included in all cases where the study presented is based on the findings of other researchers.

Aviti Katare
Candidate
Department of Chemical Engineering
Indian Institute of Technology Guwahati
Guwahati, Assam 781039
India

June 2024

Department of Chemical Engineering
Indian Institute of Technology Guwahati
Guwahati, Assam 781039

Certificate

It is endorsed that the research described in this thesis, "**Thermally Stable Moisture Responsive Chitosan based Mixed Matrix Membranes for Selective CO_2 Separation**" completed by Miss. Aviti Katare (Roll No. 196107001) for the award of a Doctor of Philosophy degree, is an authentic record of the results obtained from the research work carried out under my supervision in the Department of Chemical Engineering, Indian Institute of Technology Guwahati.

According to the rules of the institute, this thesis has, in my perspective, achieved the level necessary to meet the requirements for the award of the degree of Doctor of Philosophy.

Prof. Bishnupada Mandal
Thesis supervisor
Department of Chemical Engineering
Indian Institute of Technology Guwahati
Guwahati, 781039
Assam, India

June 2024

Acknowledgments

Without the blessings of Baba Mahakaleshwar and the assistance and encouragement of numerous individuals and organizations, this thesis would not have been successfully completed. I take this opportunity to express my profound gratitude to all who contributed to the fulfillment of this thesis.

First and foremost, I express my deepest gratitude to the Almighty, Baba Mahakaleshwar, for the strength, guidance and blessings bestowed upon me throughout the journey of completing this thesis. In moments of challenge and uncertainty, I found solace in faith and I am truly thankful for the divine support that has sustained me.

I sincerely thank my Ph.D. supervisor, Prof. Bishnupada Mandal, for providing invaluable advice that shaped me as a researcher. His guidance and support allowed me the freedom to organize, think through and carry out my research ideas, forming a strong foundation for this thesis. His expertise has not only shaped this work but also profoundly influenced my growth as a researcher. I am truly fortunate to have had the opportunity to work under his mentorship. Thank you for your patience, wisdom and belief in my abilities. I extend my appreciation to the chairperson of my doctoral committee, Prof. G. Pugazenthi from the Department of Chemical Engineering and the members of my doctoral committee, Prof. M.K. Purkait from the Department of Chemical Engineering and Prof. Debasis Manna from the Department of Chemistry, for their insightful comments, thoughtful assessments and considerate guidance during my progress review seminars.

I am grateful to the Indian Institute of Technology Guwahati and the Ministry of Health and Research Development, India, for providing the necessary resources and funding that enabled me to complete my research. I also express my sincere gratitude to the staff of the Central Instruments Facility (especially Dr Dolly Gogoi, Dr. Sidananda Sarma, Mr. Sujit Kumar Deb, Bhaskar Da and Kishor Da) and Analytical Laboratory (especially Mr. Pankaj Kumar) in the Department of Chemical Engineering and Chemistry for their assistance and guidance in using the instrumental facilities.

Several people deserve praise for going from being amateur to professional. I am deeply grateful to my lab mates, whose unwavering support and collaborative spirit made this research possible. Swapnil, Sikha, Thangsei Baite, Himali, Shashibhushan, Savan, Ahana, Shubham, Pradip, Adarsh, Rajashree, Babul, Arish, Sukanya, Geetanjali, Phani, Harshit, Ida and Shankari thank you for being not just labmates but also advisors and true friends who made my time in the lab and department more comfortable. My special thanks go to Swapnil Sharma, his dedication and willingness to help have been truly remarkable and I am deeply appreciative of his efforts. I am deeply grateful to my MTech supervisor as well, Prof. Prabirkumar Saha, for his encouragement during my research. Under his guidance, I developed a keen interest in pursuing a Ph.D. I thank him for his mentorship and inspiration.

Next, I want to express my wholehearted thanks to my family, who have been my pillar of strength and the primary source of energy throughout my life. Maa, Mrs. Sangeeta Katare and Nani Maa, Mrs. Urmila Tiwari have provided unwavering love and faith in me, giving me the encouragement needed to advance in my life and put considerable effort into this thesis. My Pitaji, Mr. Naresh Katare and MamaJi, Mr. Rabindranath Nagaich (late), have shaped me with their guidance, wisdom and selfless deeds, instilling in me the zeal and confidence that drive me to pursue my objectives. I extend my heartfelt thanks to Aditi Katare and Mantu. Without their unwavering support, this journey would have been so difficult. My beloved other family members, including Bhagwandas Nagaich (Late Nanaji), Mrs. Kalpana Nagaich (Mami), Mrs. Krishna Katare (Late Dadi Maa), Suresh Katare (Late Bade Papa), Annu Nagaich, Sohil Mishra, Aastik Katare, Anuj Nagaich, Anurag Nagaich, Sachin Dixit, Pragati Mishra, Sakshi Mishra, Sunayana Katare, Ranu Tiwari, Jyoti Tiwari, Mayank Sharma, Kapil Sharma, Vinay Tiwari, Lucky Tiwari, Nalin Katare, Sachin Katare, Rachana Katare, Saroj Katare (Mom), R.K. Mishra (Fufaji) and Prabha Mishra, Suman Tiwari, Maya Dixit, Rekha Sharma, Kiran Tiwari (Bua), also share in this achievement.

Although words are inadequate to express my gratitude adequately, I would like to thank a few close ones from my B.E. college (Government Engineering College Ujjain). A special acknowledgment goes to Dr. Sarita Sharma and Dr. Ashok Sharma, esteemed Professors of my B.E. college. Friends have always been my greatest source of strength and morale and I would like to thank my closest friends from Ujjain, including Tushar Rajguru, Mamta Rawat, Ritika Sharma, Surbhi Jain, Komal Wagh, Vishakha Gupta, Hima Harode, Vaishali Kawadker, Pooja Wagadre, Rashmi Sharma, Durgesh Jumde, Abhishek Rathore,

Abhiruchi Bais, Jay Kumar, Bhagyashri Prajapati, Stuti Dubey, Darshana Soni, Tina Dhakiya, Divya Tomar, Yogendra Parmar, Akshay Tiwari, Nikhil Dubey and my Hostel Juniors. Your belief in me, your willingness to lend an ear, your insightful feedback, endless encouragement and occasional pep talks kept me motivated even during the toughest times. Completing a PhD is a monumental achievement and I am proud to have shared this accomplishment with you.

Last but not least, I express my heartfelt gratitude to people from the IITG campus who played a crucial role in my Ph. D. journey. I truly appreciate the unwavering support and encouragement you provided throughout these years. Special thanks to Swapnil, Manish, Shikha, Khushbu, Jhuma, Sushmita, Pratiksha, Sharanya, Kanika, Arhita, Mosam, Diya, Pallavi, Twinkle, Vidhi, Shagun, Nishtha, Bharti, Riya, Tanuja, Radhika, Ishita Mandal and all the B.Tech 2021 & 2022 batch girls of Subansiri Hostel. I extend my gratitude to Bineet, Chandra Bhan, Mangal, Sarthak, Venugopal Kumari, Biba, Ramgopal, Janaki, Imran, Mukesh Sharma Bhaiya, Anweshan Da, Pranjal Da and Niladari Da. Thank you, everyone. I would also like to convey special thanks to Sourav Bhowmick for his invaluable and timely assistance and support. I want to express my deepest gratitude to Asst. Prof. Mahima Arrawatia (ex. warden and vice-chairman), Prof. Gagan Kumar (ex. Chairperson HAB), Prof. P K Iyer (ex. officiating Director of IIT Guwahati), Mrs. Dipti Devi, the caretaker of my hostel, Abhijeet Da, Hireney Da and Safikul Da. Their parental presence and genuine concern for my well-being have been a source of comfort and strength throughout my time at the hostel.

It is challenging to incorporate all the names into a single work of literature. As a result, any omissions from this brief acknowledgement do not reflect a lack of appreciation.

अविति कटारे

DEDICATED TO...

बाबा महाकालेश्वर,
पिताजी, माँ, नानी माँ,
&
MY MENTOR

Table of Contents

List of Figures

Appendix

List of Tables

by all the optimized membranes with ~4 µm selective layer thickness conducted under this research study at 85 °C and absolute feed/sweep pressure = 2.21/1.21 bar having feed/sweep water flow rate of 0.03/0.05 $mL.min^{-1}$

Abstract

CO_2 is the major component of greenhouse gases and is responsible for the surge in global temperature. Therefore, carbon capture, utilization and sequestration (CCS) are the need of the hour to control global warming. Chitosan (CS) polymeric membranes containing amine carriers have received much attention in CO_2 separation because of their easy fabrication, low cost and excellent separation performance. The optimum performance of CO_2/N_2 was observed at 85 °C temperature, 2.21 bar feed pressure, 1.21 bar sweep pressure, with feed and sweep moisture flow of 0.03 mL/min and 0.05 mL/min, respectively. Neat CS membrane with ~0.6 µm active layer thickness showed CO_2 separation results with CO_2 permeance of 60 GPU and CO_2/N_2 selectivity of 21. The membrane performance could not surpass Robeson Upper bound Trade-off. To improve the separation performance many techniques were utilized and presented in this thesis. To increase amine content in the matrix, covalent conjugation of L-tyrosine (Tyr) onto CS was accomplished by using carbodiimide as a coupling agent. The defect-free dense selective layers of tyrosine-conjugated-chitosan with thickness within the range of ~0.6 µm was cast and employed for mixed gas (CO_2/N_2) separation study. It showed reasonably good CO_2 permeance of around 103 GPU, CO_2/N_2 selectivity of 31 and the separation performance was stable upto 150 h. But it did not show promising outcomes and could not surpass Robeson curve. Further modifications in CS matrix was done with phenylalanine (Phe) and we compared the effects of two approaches: amine blending and grafting with polymer matrix and their contribution to gas separation (GS) performance. The results suggest that the grafting and blending of Phe with CS matrix boosted the CO_2 permeance and CO_2/N_2 selectivity of the fabricated membranes, respectively, when compared to the bare CS membrane and Tyr-c-CS membrane. The highest obtained CO_2 permeance was 106 GPU in the Phe-grafted-CS (Phe-*g*-CS) membrane and optimal selectivity was 97 in the 20 wt% Phe-

blended-CS (Phe-*b*-CS) membrane when both the membranes had 4 μm thick selective layer onto polyethersulfone (PES) support. The stability tests were also conducted for both the types of membranes. The results suggested that chemical grafting is more stable than physical blending due to its high durability upon long run of almost 400 h. Advanced membrane materials with higher gas separation capabilities have developed a lot of interest in CO_2 separation. So, we created MMMs of the CS matrix using L-lysine conjugated graphene oxide (Lys-c-GO) nanosheets as nanofillers. The fabricated defect-free dense layer with selective layer thickness of ~4 μm demonstrated CO_2 permeance of 44 GPU and strong CO_2/N_2 selectivity of 88. MOF materials has gained enormous attention as nanofiller in the field of MMMs. Taking this into consideration, MIL-100(Fe) nanoparticles was created using HF-free environment at ambient conditions and utilized as nanofillers in CS matrix to fabricate MMMs with desired thickness of ~1-1.5 μm onto the PES support. The fabricated MMM 15-weight % MIL-100(Fe) loaded membrane showed CO_2/N_2 selectivity and permeance of 59 and 85 GPU, respectively. Further, a CO_2-philic zirconium-based MOF NPs (Zr BDC or UIO-66) was synthesized, decorated with L-lysine amino acids and utilized as nanofiller into a CS matrix to synthesize MMM. The high porosity and surface area of the MOF NPs aided in the CO_2 separation permeance, while the selectivity was addressed by the amine functional groups present in L-lysine. After successful characterization studies, it was discovered that fabricated MMMs with a 7 wt % loading of lysine-conjugated Zr BDC (lys-c-ZrBDC) NPs with ~4 μm selective layer thickness demonstrated better results than the pristine CS and the Zr BDC-embedded CS MMM. The composite Lys-c-ZrBDC incorporated CS MMM showed a CO_2 permeance of 135.2 GPU and a steady CO_2 separation factor of 71.5under humid conditions. Furthermore, extensive studies have demonstrated that, when subjected to optimal conditions, the engineered membranes, namely Phe-g-CS, Phe-b-CS and Lys-c-ZrBDC/CS, have not only shown promising separation performances but also surpassed the Robeson upper

bound curve. This remarkable achievement showcases the exceptional performance and potential of these membranes for practical and commercial applications.

CHAPTER 1

Introduction, Literature Survey, Objectives and Organization of thesis

This chapter of the thesis enlightens the interactions between greenhouse gas emissions (GHG), climate change and its adverse effects on human health and the ecosystem. Further, the emphasis on how CO_2 emission significantly impacts climate change amongst all the greenhouse gases and the importance of CO_2 separation has been briefed. This chapter also discusses the various existing CO_2 separation technologies and the advantages of membrane separation technology over others. After an in-depth study of membrane types, the advantage and importance of facilitated transport mixed matrix membranes over other membranes have been discussed. Finally, after a thorough literature survey, the research objectives have been defined based on the gaps and challenges.

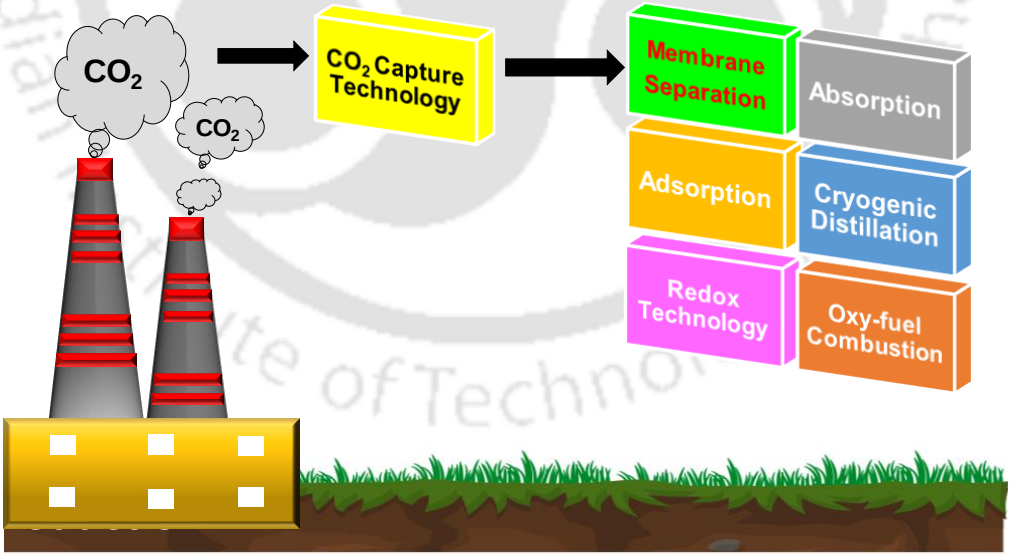

1.1. Overview of CO_2 Emission

The Intergovernmental Panel on Climate Change (IPCC) conducted an extensive analysis of over 100 climate modeling simulations aligned with the goals of the Paris Agreement. Their 2014 report revealed that the anthropogenic increase in greenhouse gas (GHG) concentration is unprecedented in history.[1] While industrialization has undeniably bolstered economies, it also stands as a significant driver of greenhouse gas emissions and thus, a key factor contributing to global climate change.[2] Anthropogenic emissions of greenhouse gases, such as CO_2, CH_4, CO, SOx, NOx, CCl_2F_2, CHF_3, among others, have profoundly disturbed the temperature distribution in the lithosphere, atmosphere and biosphere.[3] Past 135 years have witnessed the most pronounced fluctuations in the climate system, particularly over the last two decades.[4] Of all the sources contributing to CO_2 emissions, industrial activities, including fermentation, calcination and the combustion of fossil fuels, hold the largest share.[5] Notably, human-driven activities, such as land-use changes, fossil fuel burning, agriculture, industrial product release and traffic emissions, have become pivotal forces that reshape numerous environmental characteristics, affecting air quality and biodiversity at local, regional and global scales.[6]

NASA has reported a continuous and escalating increase in atmospheric CO_2 emissions, reaching a record high of 419 ppm in January 2023.[7] The predominant means of meeting the global energy demand involves post-combustion processes, with a primary reliance on the combustion of coal and natural gas.[8] The remarkable surge in energy demand over the preceding years has resulted in approximately 33 Gt of CO_2 emissions in 2019. According to the International Energy Agency (IEA), nearly 30% of these emissions originated from coal-fired energy generation plants.[9]

Continued emissions of CO_2 will cause a further rise in global temperatures, which will

be responsible for severe and irreversible impacts on both humans and the ecosystem. These impacts include the melting of sea ice and glaciers, a rise in sea levels and ecological imbalances. The extremely extended lifespan of CO_2, estimated to be 100-300 years, in the atmosphere would continue to exacerbate the global warming problem for the rest of the century, even if humans were to stop discharging CO_2 into the atmosphere.[10] Thus, we can conclude that CO_2 emissions due to fossil fuel burning may produce an irreversible effect on climate change on human timescales. Hence, there is an urgent need to reduce the CO_2 level using efficient and environmentally friendly techniques.

In the pre-industrial era, plants acted as the natural carbon sink, efficiently utilizing CO_2 through photosynthesis to synthesize their food while releasing oxygen. However, with the societal transition from preindustrial to industrial stages, deforestation and the rapid escalation of CO_2 concentration levels, the photosynthesis process's productivity has been significantly impacted. Consequently, in the contemporary era, relying solely on plants cannot suffice to effectively mitigate atmospheric CO_2 levels.

To address this challenge, reducing energy demand through the adoption of cutting-edge, energy-efficient technologies represents one viable approach. Additionally, curtailing CO_2 emissions can be achieved by transitioning from fossil fuels to non-fossil fuel alternatives. Finally, the development of advanced and highly efficient carbon capture, utilization and sequestration technologies offers another promising avenue to tackle the issue of rising CO_2 concentrations in the atmosphere.[11]

1.2. CO_2 Capture Processes

The release of CO_2 into the atmosphere could result from pre-combustion, post-combustion, oxyfuel combustion, or chemical-looping combustion processes.[12,13] Based on

these, the CO_2 capture processes can be envisaged as follows:

(1) Pre-combustion carbon capture: It involves the separation and capture of CO_2 produced during the synthesis gas (H_2 + CO) production after the conversion of CO into CO_2;

(2) Post-combustion carbon capture: It consists of the separation and capture of CO_2 after the complete combustion of fossil fuels like coal, natural gas and oil, etc. in the presence of air.

(3) Oxyfuel combustion carbon capture: It involves the separation and capture of CO_2 produced from fossil fuel burning in the presence of a nitrogen-free, oxygen-rich atmosphere.

(4) Chemical looping combustion capture: It involves the separation and capture of CO_2 from burning fuels in the presence of metal oxides like CuO, Fe_2O_3, Mn_2O_3, etc. which act as oxygen carriers during the combustion processes.

Flue gas streams produced from post-combustion processes contain a low CO_2 concentration of approximately 10-14%. The remaining flue gas is N_2 (approximately 75%), excess O_2, water and traces of other impurities (SO_x, NO_x, etc.).[14] Since the flue gas is at atmospheric pressure, the partial pressure of CO_2 is very low at approximately 0.15 bar. Low feed gas pressure and low CO_2 concentration in the flue gas makes it difficult to separate and capture CO_2.[15] However, the main advantage of post-combustion carbon capture is that it can be retrofitted in existing industrial plants like power plant, cement, iron, steel, textile production industries and has the liberty of upgradation, connection/disconnection according to the need.[15] Hence, the post-combustion carbon capture process is suitable for CO_2 mitigation from various fossil fuel-burning industries.

1.3. CO_2 Capture Technologies

Various CO_2 capture technologies have been studied, designed and patented over the

past few decades. The existing carbon capture technologies involve absorption, adsorption, cryogenic fractionation, oxyfuel combustion, redox technology and membrane separation.[16] A brief description of these technologies is discussed below:

1.3.1. Absorption

Absorption is a two-stage gas-liquid mass transfer operation in which the bulk liquid solvent selectively absorbs the molecules or ions of the target gaseous component. The choice of solvent plays a critical role in scrubbing CO_2 from the flue gas stream. It should have a high affinity towards CO_2 but not dissolve other gases in the flue gas stream like N_2, O_2, etc. Alkanolamines such as monoethanolamine (MEA),[17] diethanolamine (DEA),[18] and methyldiethanolamine (MDEA)[19] are some of the most commonly used amine-based, post-combustion CO_2 capture absorbents. Amines have a very high rate of reaction towards CO_2 capture and thus show high CO_2 selectivity, but at the same time, they show low CO_2 loading (kg CO_2 absorbed per kg absorbent).[20] Aqueous ammonia has received considerable attention over conventional alkanolamine solvents to capture post-combustion CO_2 due to its low cost, low regeneration energy, no sorbent degradation and the simultaneous capture of multiple pollutants.[21] While absorption is a matured CCS technique and does possess substantial advantages, it has some limitations based on the solution used, such as high solvent regeneration cost, low thermal resistance, poor stability in the presence of oxides such as SO_x, NO_x, etc.[22] These limitations are not ignorable and motivate towards the development of more hybrid systems.

1.3.2. Adsorption

Adsorption is another widely used technique to separate CO_2 from flue gas streams produced by fossil fuel power plants. The use of solid adsorbent to selectively adsorb the target

components is the fundamental theory of the adsorption separation process. This happens because the functional groups on the surface of the adsorbent have different affinities for the diffused guest molecules or ions. The target component or ions are attracted and trapped by the surface groups of the sorbent via chemisorption or physio-sorption process. Like absorption, the adsorptive gas separation process involves two main steps: adsorption and desorption. Solid adsorbent shows similar advantages and disadvantages as wet absorbers.

Good adsorbent should possess a large surface area, fast absorption-desorption kinetics, high mechanical stability, high thermal stability, ease of regeneration ability, etc.[23] The polarity and pore size of the adsorbent plays a vital role in the adsorption process.[24] The most widely used and commercially available adsorbents include activated carbon,[25] silica-gel,[26] zeolites,[27] bauxite,[28,] etc. Metal oxyhydroxide-carbon composites such as Al/Fe oxyhydroxide,[29] carbon, aluminum, magnesium and iron oxyhydroxide composites[30] and metallic organic frameworks (MOFs) such as $Zn_2(cnc)_2(dpt)$,[31] PCN-26,[32] etc. can be considered as new, modified and more efficient adsorbents. Poor selectivity, low CO_2 loading capacity, high time consumption and non-compatibility at high temperatures are some of the major drawbacks of the adsorbents that make them unfit for post-combustion CO_2 capture.[33] Adsorbents can also be chemically modified using amines or other functional groups to create active sites to improve CO_2 uptake capacities.[34] The resulting adsorbents though broadly used, but low capacity, poor thermal stability and high cost add to their utility limitations.[34]

1.3.3. Cryogenic Distillation

Cryogenic distillation is no different than conventional distillation except that the temperatures are considerably lower.[35] Cryogenic distillation is a process in which condensable compounds are separated from non-condensable gases based on their differences in freezing point. The process operates at very low temperatures and high pressure and separates CO_2 from

other compounds at different locations in the column. The main advantage of cryogenic distillation is that it directly produces liquefied CO_2, saving additional compression costs for transportation and storage.[36] The major drawback of this separation process is that solid formation occurs inside the column at higher pressure, which hinders the performance of the process. To overcome these limitations, many researchers have modified the existing conventional process. Holmes et al. (1983) added heavier hydrocarbon in the condenser to avoid CO_2 solidification and the process is called extractive cryogenic distillation.[37] Clodic et al. (2005) have modified the process where CO_2 is desublimated as a solid onto the surfaces of heat exchangers, followed by a regeneration step at elevated pressures.[38] Further, Tuinier et al. (2010, 2011) have developed a process based on the periodic operation of cryogenically cooled packed beds.[39] The process is mainly used for pre-combustion CO_2 capture. However, post-combustion CO_2 capture is also possible via the application of a dynamically moving packed bed cryogenic separation process.[40] Cryogenic distillation being a complex process with high energy penalty due to refrigeration and high capital expenditure than other technologies, limits its usage in industrial purpose.[41]

1.3.4. Oxyfuel Combustion

Oxyfuel combustion is a promising technology that greatly facilitates the capture of CO_2 from flue gases generated by fossil fuel power plants. This process utilizes nitrogen-free oxygen instead of air for fuel-burning purposes. The flue gas produced has a very high concentration of CO_2, along with some amounts of N_2, O_2 and water vapors. The produced flue gas can be stored directly or purified to remove N_2, O_2, H_2O, etc., using dehydration followed by low-temperature purification.[42] The main application of oxyfuel combustion is to provide CO_2-rich flue gas for enhanced oil recovery (EOL) purposes.[43] Hence this process can be termed as near-zero-emission technology. Both processes are energy-intensive and result in a

large efficiency penalty, if employed as part of the oxyfuel combustion process.[44] This drawback limits its utility for industrial purposes.

1.3.5. Redox Technology

Redox technology is another method proposed by National Renewable Energy Laboratory to capture CO_2. To bind CO_2, a redox-active carrier is used at higher pressure and after successful binding, it is released at lower pressure.[45] The technology is called redox technology because reduction allows the carrier to pick up CO_2 while oxidation causes it to release the CO_2. The most commonly used oxidative-reductive agents developed so far are CoO, Fe_2O_3 and NiO, etc., using Al_2O_3, TiO_2, MgO, $NiAl_2O_4$ and YSZ (yttria-stabilized zirconia) by M. Ishida et al.[46]

1.3.6. Membrane Separation

In recent times, traditional separation methodologies, such as absorption, adsorption and cryogenic distillation, have been complemented by a novel approach involving the use of semi-permeable membranes. These membranes act as interfaces between two phases, controlling the selective transport of different components in a specific manner. The efficacy of these membranes relies significantly on the driving forces present across them, such as differences in partial pressure or concentration. Among the various technologies discussed, membrane technology stands out as the preferred choice for CO_2 separation due to its noteworthy advantages: energy efficiency, cost-effectiveness and ease of handling. Furthermore, its modular and compact design enables seamless integration into industrial processes without occupying excessive space.[47] Consequently, membrane technology emerges as the most promising solution for achieving optimal CO_2 reduction.

1.3.6.1. Brief Historical Background

It has been more than a century since the gas separation properties of the membrane have been realized. The first recorded description of semi-permeable membranes was in 1748 when Jean Antoine (Abbe) Nollet reported that a pig bladder (i.e., a natural membrane) was more permeable to water than to ethanol.[48] Later, in 1831, Fick observed gas transport across the nitrocellulose membrane and developed the very famous Adolph Fick's laws of diffusion.[49] At the same time, Mitchell et al. measured the escape rates of ten gases through natural rubber balloons.[50] Later, in 1866, Graham et al. developed the concept of Knudsen diffusion by observing the separation performance of the gases through natural rubber.[51] Then, in 1920, Daynes et al. observed the non-steady transport behavior of gases through a membrane and developed the relationship between the diffusion coefficient and time lag.

Despite many experimental works, it took over a century to scale up the first membrane-based separation plant, which was developed to concentrate the uranium-235. The major drawbacks associated with the early membrane separation technology were their poor selectivity and low fluxes. To overcome these limitations, Loeb et al. successfully prepared an asymmetric "skinned" cellulose acetate membrane with a thin dense layer responsible for the selective separation and porous sublayer that provided the mechanical strength to the selective dense layer with minimum resistance to the permeation of components. Since these membranes lost their separation properties after drying, they were found inappropriate for gas separation. Then Burris et al.[52] added the surfactant to the water and solved the problem as the addition of surfactants reduced the interfacial tension between the water molecule and membrane walls. Ward et al. developed a composite membrane with a higher separation factor and permeance.[53]

1.3.6.2. Gas Transport Mechanisms in Membranes

Membrane gas separation represents a pressure-driven, non-equilibrium process in which the desired separation is facilitated by the partial pressure difference of gases across the

membrane, present in both the feed and permeate sides. The gas molecules targeted for separation initially undergo adsorption on the upstream side of the composite membrane, followed by diffusion through the membrane's thickness and ultimately desorption on the downstream side. Various mechanisms underpinning membrane separation include capillary condensation, Knudson diffusion, molecular sieving, surface diffusion and solution diffusion.[54] Dense polymeric gas separation membranes primarily rely on "solution-diffusion" and "Facilitated transport" as the main transport mechanisms. [55]

Solution-Diffusion Mechanism

Solution diffusion mechanism as shown in Figure 1.1 is the basic mechanism of gas transport through all polymeric membranes. Here selectivity and permeability are used to determine the separation performance of the membrane. For a binary system consisting of two gases, say: CO_2 and N_2, with CO_2 as the target component. Permeability is the product of the solubility coefficient $(S_{CO_2}, cm^3(STP)cm^{-3}cmHg^{-1})$ and diffusion coefficient (D_{CO_2}, cm^2s^{-1}) and is given by equation 1.1.[56]

$$P_{CO_2} = S_{CO_2} \times D_{CO_2} \tag{1.1}$$

For dense membranes, it is most commonly expressed in Barrer units.

In contrast, for thin-film composite membranes, permeance is the more commonly used term defined as the permeability divided by the gas-selective layer thickness. It is most commonly expressed in Gas Permeation Unit (GPU). Gas solubility depends primarily upon the gas condensability and interaction between the gas molecule and membrane matrix. The diffusion coefficient depends upon the void spaces between the polymer chains called free volume.

Selectivity can be viewed as the capability of the membrane to separate one gas from

another. It can be defined as the concentration ratio of CO_2 to N_2 on the permeate side over the concentration ratio of CO_2 to N_2 on the retentate side:

$$\alpha_{CO_2/N_2} = \frac{y_{CO_2} / y_{N_2}}{x_{CO_2} / x_{N_2}} \tag{1.2}$$

Where α is the selectivity coefficient, y_{CO_2} and y_{N_2} are the concentration on the permeate side and x_{CO_2} and x_{N_2} are the concentrations on the retentate side. Whereas ideal selectivity is given by equation (3) and is defined as the ratio of the two pure gas permeabilities:

$$\alpha_{CO_2/N_2} = \frac{P_{CO_2}}{P_{N_2}} = \frac{S_{CO_2} D_{CO_2}}{S_{N_2} D_{N_2}} \tag{1.3}$$

Solubility selectivity depends largely on the differences in the condensability of the penetrant gases. Diffusive selectivity arises from the difference in the size of the penetrant gases and polymer size-sieving capability.[57]

Facilitated Transport Mechanism

The transport mechanism of the gas through the membranes bearing reactive carriers, which can react reversibly with the target molecules or ions, is called facilitated transport membranes. The CO_2 separation performance of the membrane is higher than that discussed earlier because the acidic nature of the CO_2 allows the reaction with amines and alkaline carbonate solution.[8]

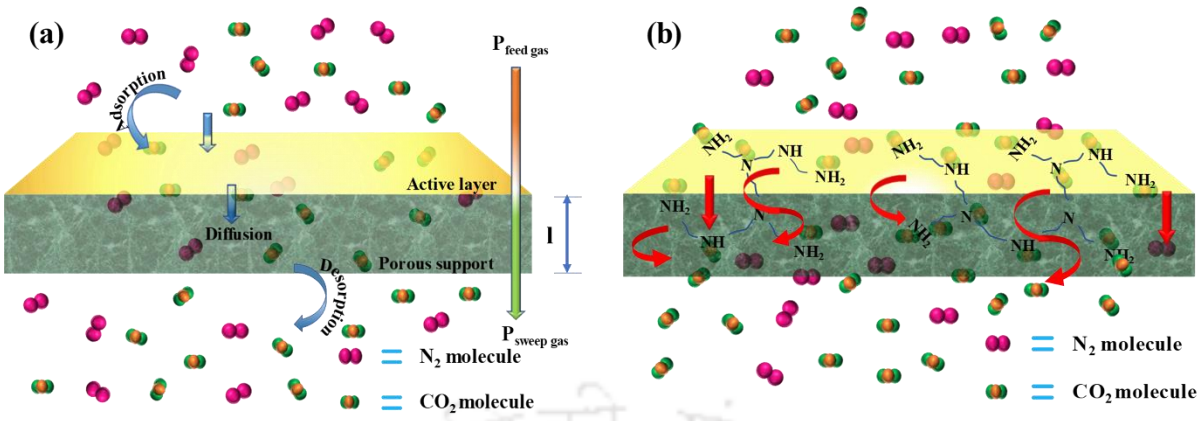

Figure 1.1. Schematic of CO_2 and N_2 transport across the membrane through (a) solution diffusion and (b) facilitated transport mechanism.

The zwitterion mechanism explains the reaction between the CO_2 and carrier amines as:[58]

$$CO_2 + 2RNH_2 \rightleftharpoons RHNCOO^- + RNH_3^+ \quad (1.4)$$

$$CO_2 + 2RR'NH \rightleftharpoons 2RR'NCOO^- + RR'NH_2^+ \quad (1.5)$$

The above reactions show that CO_2 loading is 0.5 mol of CO_2 per mol of amine. The presence of water greatly affects CO_2 loading, which can be understood by the reactions below.

$$2CO_2 + 2RNH_2 + H_2O \rightleftharpoons RHNCOOH + RNH_3^+ + HCO_3^- \quad (1.6)$$

$$2CO_2 + 2RR'NH + H_2O \rightleftharpoons RR'NCOOH + RR'NH_2^+ + HCO_3^- \quad (1.7)$$

The above reactions show that the theoretically maximum CO_2 loading, i.e., 1 mol of CO_2 per mol of amine, can be achieved in the presence of a water molecule.

$$CO_2 + 2RR'R''N + H_2O \rightleftharpoons RR'R''N^+ + HCO_3^- \quad (1.8)$$

The above equation states that, unlike primary and secondary amines, tertiary amines in the polymers cannot facilitate CO_2 permeation under dry conditions.

In facilitated transport membranes, the CO_2 is passed in two forms: CO_2 molecules and CO_2 carrier complexes. The total gas transport flux can be expressed by Fick's law of diffusion as:

$$J_A = \frac{D_A}{l}\Delta C_A + \frac{D_{AX}}{l}\Delta C_{AX} \quad (1.9)$$

Where D_A and D_{AX} are the diffusion coefficients for CO_2 molecule and CO-carrier complexes, respectively, ΔC_A and ΔC_{AX} are the concentration differences for CO_2 molecule and CO-carrier complexes, respectively and l is the thickness of the membrane

1.3.6.3. Classification of Membranes

Based on the usage of base material, membrane technology can be mainly classified as polymeric membranes, inorganic membranes and mixed matrix membranes (MMM) as shown in Figure 1.2. All these membranes have their own set of advantages and disadvantages as discussed below:

Polymeric Membranes

The choice of polymer material to prepare a polymeric membrane plays a crucial role in separation performance. So far, the polymeric membranes have been used to separate different binary systems such as CO_2/N_2, CO_2/CH_4, H_2/O_2, He/N_2, CO_2/H_2, etc.[59,60] Cellulose acetate was the first material used to fabricate asymmetric membrane and also one of the polymers initially used in commercial gas separations.[61] Houde et al. reported the separation performance of Cellulose Acetate for CO_2/CH_4 gas mixtures and found the CO_2 permeability of 3.23 Barrer and CO_2/CH_4 selectivity of 33.8 at a temperature of 35 °C and feed pressure of 10.1 bar.[62] Apart from cellulose acetate, other materials such as polysulfones (PS),[63] chitosan,[64] polyimides, PEBAX,[65] matrimid,[66] polyvinyl amine,[67] etc. have also been utilized to prepare

membranes for gas separation. Few of these membranes follow solely the solution-diffusion mechanism, thus, suffer from truncated CO_2 separation factor and permeance as discussed by Robeson's "upper-bound" curve. Few of these membranes also lack mechanical, chemical and thermal stability.

Inorganic Membranes

Inorganic membranes are generally composite membranes composed of one or more types of inorganic materials. The most commonly used materials for inorganic membranes are Al_2O_3, SiO_2, TiO_2, ZrO_2, etc.[68] They usually have a microporous top (or dense) layer, mesoporous intermediate layers and macroporous support. The dense microporous layer is a selective membrane where separation occurs, the support layer is used to provide mechanical strength and the mesoporous intermediate layers bridge the pore size difference between the top layer and the support layer.

The primary transport mechanisms of gas mixtures through such membranes are Knudsen diffusion, bulk diffusion and viscous flow, with Knudsen transport dominating in the smaller pore regime. The main advantages of inorganic membranes are they can withstand high pressure and high temperature and are chemical resistant. Membranes are synthesized with various types of zeolites, such as Y-type, silicate, ZSM-5, etc., on a porous support. Zhilin et al. prepared a Y-type zeolite membrane and found that the permeation rate of CO_2 remained the same while for N_2 decreased, hence selectivity increased.[69] However, the major limitation of inorganic membranes is their brittle nature and high cost. Also, preparing a crack-free inorganic membrane for industrial purposes is still a big challenge.

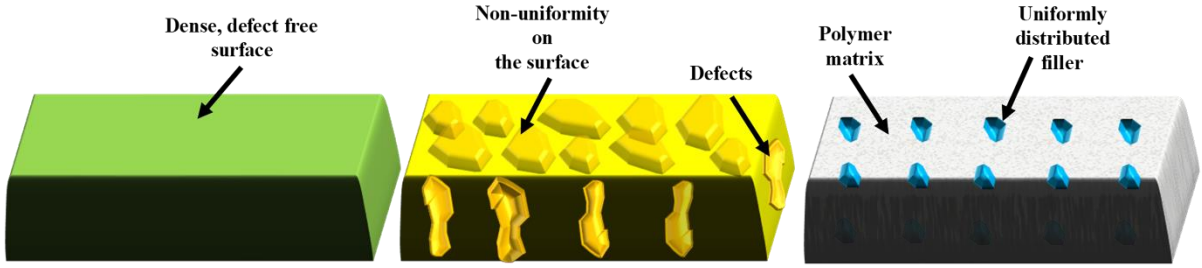

Figure 1.2. Morphological feature of (a) Polymeric membrane: Dense and Defect free, (b) Inorganic membranes: Defective and porous, (c) Mixed matrix membranes: Uniform distribution of fillers into the dense polymer matrix.

Mixed Matrix Membranes (MMMs)

Polymeric membranes face a crucial drawback concerning the balance between selectivity and permeability, which significantly hinders their practicality in flue gas separation applications. However, this limitation can be overcome by incorporating a suitable inorganic or organic-inorganic filler that is compatible with the polymer matrix. This incorporation leads to an enhanced membrane separation factor and creates a new frontier in the field of membranes known as mixed matrix membranes (MMMs), combining the advantages of both polymeric and inorganic materials. The key challenge lies in selecting the appropriate filler, as inadequate interactions between the polymer and filler can lead to issues such as pore blockage, filler agglomeration, void formation and membrane rigidity. These problems ultimately result in subpar gas separation performance. Therefore, careful consideration of the filler material is crucial to achieve optimal results in MMMs. Kulprathipanja et al. were the first who introduce the concept of mixed matrix membrane.[70] They incorporated silicalite filler into the cellulose acetate polymer and found that the CO_2/H_2 separation factor increased to 9.6, which was 0.7 for a plain cellulose acetate membrane. So far, various materials have been explored as fillers, such as zeolites, metal oxides, inorganic oxides, graphene oxide (GO), molecular sieves, activated alumina, carbon nanotubes, silica gel, metal-organic frameworks (MOFs), covalent-organic frameworks (COFs), etc.[71] In the past two decades, MOFs have drawn the attention of

many scientists as novel hybrid porous materials. Li et al. have developed a microporous MOF and found a CO_2/N_2 selectivity of 11.7. Asgharnejad et al.[72] have developed Ni-AG5 with 5% GO-based MOF and fabricated a mixed matrix membrane and got the CO_2/N_2 selectivity of 52 at 273 K and 1 bar feed pressure, i.e., three-fold higher than the selectivity of the parent MOF.

1.4. Literature Survey

The aim of this research work is the efficient separation of CO_2 from the CO_2/N_2 binary gas mixture using membrane separation technology. So far, various polymers, including polyvinyl alcohol (PVA),[73,74] poly(ether-block-amide) (Pebax),[112-118] poly(vinylamine) (PVAm),[119-126] polyethersulfone (PES),[75] polycarbonates (PC),[53] Chitosan (CS),[64,76–78] cellulose acetate, (CA)[59,79] polyimide (PI, such as Matrimid®),[66,80,81] polyetherimide (such as Ultem) and PIM-1,[82,83] etc. have been utilized in the CO_2 separation. Their gas permeation results are summarized in Table 1.1.

Table 1.1. CO_2 permeability/permeance and CO_2/N_2 selectivity of reported mixed matrix membranes (MMMs).

Polymer	Filler/Carrier	Operation Condition	P_{CO_2}	S_{CO_2/N_2}	Reference
Polyetherimide (Ultem® 1000)	ZIF-8	45 °C 100 psi	34 GPU	28	84
Matrimid	MIL-101	35 °C 10 bar	5.85 Barrer	42	81
Matrimid	Benzimidazole (RT BIPL-101)	35 °C 2 bar	27 Barrer	60	66
Carboxymethyl chitosan (CMC)	CNTs	90 °C 2 bar	43 GPU	45	66
CMC	Polyamidoamine	90 °C	100	149	85

	(PAMAM)	2 bar	GPU		
Polyvinyl alcohol (PVA)	PG/zeolite	80 °C 2 bar	82 GPU	370	[73]
PVA	PEG/ Silica gel	80 °C 2 bar	400 Barrer	210	[74]
PIM-1	UIO-66(Zr)	25 °C 1 bar	8000 Barrer	23	[83]
Polyurethane (PU)	SAPO-34	1.2 MPa	28 Barrer	58.59	[86]
PU	UIO-66(Zr)	25 °C 4 bar	75 Barrer	34	[87]
Polysulfone (PSF)	porous aromatic frameworks (PAF-56P)	80 °C 0.06 MPa	151 GPU	38.9	[88]
PU	MIL-101 (Cu)	25 °C 4 bar	83 Barrer	42	[87]
CS	Sericin	90 °C 2 bar	112 GPU	73	[78]
Cellulose acetate	Multiwalled carbon nanotubes (MWCNTs)	25 °C 2 bar	741 GPU*	40	[79]
Polydimethylsiloxane (PDMS)	Zeolite	25 °C	1245* GPU	11.1	[89]
Polyvinyl amine (PVAm)	-	57 °C 2 bar	213 Barrer	48	[90]
PVAm	HPEI-GO	25 °C 0.1 MPa	36 GPU	107	[67]
PVAm	PANI@CNTs-GO	25 °C 1 bar	264 GPU	149.8	[91]

A high-performance facilitated transport membrane for CO_2 separation was fabricated by incorporating amino-functionalized carbon nanotubes into the Pebax-1657 matrix and reported 743 Barrer and 108 CO_2 permeability and CO_2/N_2 selectivity, respectively, at 25 °C and 10 bar feed pressure.[92] The results showed that the PEG-CNT filler plays multiple roles in improving the membrane performance as for the pure PEBAX. It was observed that despite its good separation properties, many efforts are still needed to improve the thermal stability of PEBAX membranes to commercialize in the flue gas application.

Fortunately, through the reversible reactions between the targeted gas molecule-CO_2 and reactive carriers (amines), high CO_2/gas selectivity and high CO_2 permeance can be obtained. This inspires the selection of aminated polymers, e.g., polyvinyl amine (PVAm),[67] polyethyleneimine (PEI),[93] polyallylamine (PAAm),[64] tetraethylenepentamine (TEPA),[76] chitosan (CS) etc. to fabricate the fixed site carrier (FSC) membranes for CO_2 separation. A novel PVAm membrane was fabricated and tested for CO_2 separation performance at 57 °C temperature and 2 bar feed pressure.[90] They reported the CO_2 permeability of 213 Barrer and CO_2/N_2 selectivity of 57. The same group has also modified PVAm to Poly(N-methyl-N-vinylamine), sterically hindered amine by converting primary amines of PVAm to secondary amines and reported the CO_2 permeability of 264 Barrer and CO_2/N_2 selectivity of 55 at the same temperature and pressure which are higher than that reported for pure PVAm.[90] Further, PVAm- MMM loaded with 1 wt% polyaniline coated carbon nanotube in GO was prepared, which exhibited excellent long-term stability for over 300 h with CO_2 permeance of 264 GPU and a CO_2/N_2 selectivity of 149.8.

Chitosan (CS), derived from chitin, is a biopolymer characterized by the presence of a one hydroxyl and one amine group in its each ring, enables simple modifications for increasing CO_2 separation efficiency. These functional groups can also form hydrogen bonds with

absorbed moisture and introduce a swelling effect on the membrane resulting in enhanced CO_2 diffusivity and solubility. Besides that, CO_2 can react with amines reversibly in the presence of moisture, which was responsible for the facilitated transport of CO_2.[94,95] From an environmental standpoint, chitosan emerges as a favourable option for CO_2 capture, owing to its cost-effectiveness, film forming properties, ecological compatibility and the presence of advantageous functional groups such as $-NH_2$ and -OH. The amino activity of chitosan enables CO_2 to permeate through its active sites via facilitated transport mechanism more rapidly than other gases, making it a compelling choice for CO_2 permeation. Additionally, the chemical structure of chitosan lends itself well to easy modification, enabling the tailoring of its properties to specific requirements. By either functionalizing or blending it with other materials, we can optimize the permeability, selectivity, and stability of chitosan membranes to meet the demands of various separation processes. This adaptability allows for the customization of chitosan membranes to effectively tackle the challenges encountered in CO2 separation, including the need for high selectivity towards CO2 over other gases and resilience to harsh operating conditions. Moreover, the abundance of chitosan sourced from renewable outlets like shrimp and crab shells further enhances its appeal from an environmental sustainability standpoint. Leveraging this natural, renewable resource enables us to minimize the environmental footprint associated with the production and disposal of membrane materials.

This unique chemical composition imparts remarkable CO_2 separation capabilities to the material. Moreover, CS exhibits exceptional thermal stability in the absence of cross-linking, ensuring its suitability for high-temperature applications, the material enables the facilitated transport of CO_2 during separation processes, contributing to enhanced separation efficiency. Additionally, CS possesses commendable film-forming attributes, ensuring the fabrication of

thin, uniform films for flue gas separation applications.[96]

However, the presence of a limited amine group (only one amine in the CS ring structure) limits its efficacy towards CO_2 separation. So, CS blended or grafted with other polymers, amines, or fillers have been successfully used to separate CO_2 pure gas,[97] binary gas,[78] and ternary gas mixture.[77] Prasad et al. added Tetraethylenepentamine (TEPA) as a mobile into the CS matrix and the effect on CO_2 separation performance was studied at 90 °C and 2 bar feed pressure.[76] The results show that the CO_2 permeance has increased from 12.5 GPU to 24.7 GPU and selectivity increased from 54 to 80 compared to pure CS. A novel mixed matrix membrane has been fabricated by incorporating silk fibroin and graphene nanoparticles as mobile carriers and fillers into the CS matrix.[77] The fabricated membrane resulted in 159 GPU permeability and 98 selectivity at 90 °C and 2 bar feed pressure. The other modifications in the CS membrane and its CO_2 separation performance can be reviewed in Table 1.2.

Table 1.2. CO_2 permeability/permeance and CO_2/N_2 selectivity of chitosan based mixed matrix membranes.

Polymer	**Filler/Carrier**	**Operation Condition**	**P_{CO_2}**	**S_{CO_2/N_2}**	**Reference**
Chitosan (CS)	-	2 bar 90 °C	12.5 GPU	54	[76]
CS	Tetraethylenepentaamine (TEPA)	2 bar 90 °C	24.7 GPU	80	[76]
CS	Polyallyl amine (PAA)	2 bar 90 °C	44 GPU	260	[64]
CS	Silk fibroin (SF)	2 bar 90 °C	140 GPU	103	[98]
CS	SF/GNP	2 bar 90 °C	159 GPU	93	[77]

CS	[emim] [AC] (IL)/ZIF-8 (MOF)	25 °C	5413 Barrer	11.5	[97]
CS	[emim] [AC] (IL)/ HKUST-1 (MOF)	25 °C	1388 Barrer	19.3	[97]
CS	Trimesoyl chloride (TMC)	25 °C 2 bar	163 Barrer	42	[99]
CS-PEBA	-	85 °C 2 bar	2884 Barrer	65.3	[100]
CS-PEBA	-	65 °C 6 kgf/cm^2	150 Barrer	44.3	[65]
PVAm-CS	GO-HPEI	25 °C 0.1 MPa	36 GPU	107	[67]

1.5. The Objectives of This Research

The primary objectives of this research are as follows:

1. Selection of bio-based polymers with high affinity for CO_2 molecules.
2. Selection of suitable bio-based amine carriers for high affinity towards CO_2 molecules.
3. Selection of suitable inorganic fillers compatible with the polymer matrix to improve the transportation of CO_2 across the membranes.
4. Fabrication, characterization and utilization of the thin film composite membranes (TFCMs) and mixed matrix membranes (MMMs) for CO_2 separation from CO_2/N_2 binary gas mixture.

The following research works have been undertaken based on the above objectives:

1. A Strategical Improvement in the Performance of CO_2 Gas Permeation via Conjugation of L-Tyrosine onto Chitosan Membrane.

2. An Investigation on the Effects of Both Amine Grafting and Blending with Biodegradable

Chitosan Membrane for Enhanced CO_2 Separation.

3. Effects of L-Lysine-Conjugated-Graphene Oxide Nanosheets on the CO_2 Separation Performance of Mixed Matrix Chitosan Membrane

4. Green Synthesized Hf-Free Mil-100(Fe) Nanoparticles Infused Chitosan Mixed Matrix Membrane for Enhanced CO_2 Permeance.

5. Surface Engineering of Zr Bdc Nanoparticles via Conjugation with Lysine to Enhance CO_2 Separation Performance of Chitosan Mixed Matrix Membrane under Dry and Humid Conditions.

1.6. Thesis outline

On the basis of the above discussion, thesis work has been divided into eight chapters. A brief overview of each chapter is presented below.

Chapter 1: This chapter of the thesis shed light on the interrelationships between greenhouse gas (GHG) emissions, climate change and their detrimental effects on both human health and the environment. It specifically focused on the significant impact of CO_2 emissions on climate change and the need for CO_2 capture. Existing CO_2 capture technologies are also discussed, with an emphasis on the advantages of membrane separation technology. After a detailed analysis of various membrane types, the chapter highlighted the importance and benefits of mixed matrix membranes over other types of membranes. Finally, the research objectives were defined based on the gaps and challenges identified through a comprehensive literature review.

Chapter 2: The materials utilized to synthesize different filler materials and membranes are discussed in this section of the thesis. A step-by-step description of the membrane synthesis processes is provided, along with a detailed overview of the analytical techniques employed to

characterize the membranes and fillers. The gas permeation set-up is also explained, with accompanying illustrations and discussions.

Chapter 3: The study presented in this work involved the fabrication and analysis of a high-performing membrane synthesized from chitosan (CS) and L-tyrosine-conjugated-CS (Tyr-c-CS) for the purpose of separating CO_2 from CO_2/N_2 gas mixture. L-Tyrosine (Tyr), an amino acid containing an amine group, possesses elevated surface tension, a non-volatile nature, exceptional resistance to degradation in environments with high oxygen levels, environmentally friendly behavior and better CO_2 loading compared to alkonoalamines. These features make Tyr a promising candidate to be explored as a potential carrier for CO_2 separation applications. So far, the collective impact of the chitosan-tyrosine conjugate on the CO_2 separation performance has remained unexplored. The thermal, physical and chemical properties of the membrane were thoroughly examined using various techniques in the chapter. The research revealed that the addition of amino acid via conjugation to the CS backbone significantly improved the membrane's ability to separate CO_2 from N_2. The conjugated L-tyrosine's amine groups attract CO_2 molecules over N_2 due to the zwitterion mechanism of carbamate formation. The study also proposed a new technique to enhance CO_2 separation performance by inducing plasticization and swelling. The presence of amines carrier from L-tyrosine, along with those from the CS backbone, enables a combination of facilitated transport and the solution-diffusion mechanism. This unique combination significantly enhances the CO_2 separation performance of the Tyr-c-CS matrix when compared to the pure CS membrane. The CO_2 separation performance, including CO_2 permeance and CO_2/N_2 selectivity, was analyzed for both pure CS and Tyr-c-CS membranes by varying temperature under dry and humid conditions. Subsequently, the effects of varying moisture flow rates in sweep stream, pressures and selective layer thickness were studied for the Tyr-c-CS membrane.

Chapter 4: In this chapter we delve into a study focusing on the utilization of another amino acid Phenylalanine (Phe) in place of Tyr. Phenylalanine, being easily soluble in water (not requiring the use of strong acid (HCl) solutions as needed for dissolving tyrosine), consequently its better compatibility with CS, piqued our interest for its potential utilization in aiding the carrier in the chitosan backbone. Also, the absence of the phenolic -OH in phenylalanine resulted in more basicity in the composite membranes thereby facilitating better interaction of the acidic CO_2 with the membrane polymer. In our research, we used two different methods to modify the CS. The first method involved chemical grafting, where we used carbodiimide coupling agents. The second method was physical blending, where we varied the concentration of phenylalanine (Phe) in the material from 10 wt% to 40 wt%. By employing these techniques, we aimed to achieve specific modifications and their effects on the material's properties. Afterward, we proceeded to synthesize composite membranes on a polyethersulfone (PES) substrate using the solution casting approach. To thoroughly evaluate the performance of these membranes, we conducted multiple analysis by employing various analytical techniques, including XPS, NMR, FTIR, XRD, TGA, FESEM and AFM. These tests allowed us to assess the stability, mechanical strength and thermal resistance of the membranes, as well as their efficiency in selectively transporting CO_2 over N_2.

The results of our experiments revealed the formation of a thin, defect-free, CO_2-attractive and durable selective layer on the PES support. To determine their practical applicability, we tested the composite membranes on a gas separation module under different operating conditions. In a stability test lasting 400 hours, the Phe-g-CS membrane exhibited better consistency in CO_2 uptake capacity compared to the Phe-b-CS membrane and Tyr-c-CS membrane. Overall, this study offers valuable insights into the development of composite membranes for gas separation applications utilizing blending and grafting strategies.

Chapter 5: Although the amino acids incorporation into the polymer yielded high performing membranes for CO_2 separation, the Robeson curve is yet to be well-surpassed towards commercialization. As explained in Chapter 1, this chapter of the thesis explores the advances in membrane separation technology through the invention of mixed matrix membranes (MMMs). Here we synthesized graphene oxide (GO) nanosheets utilizing modified Hummer's method and modified their surface with L-lysine (Lys) amino acid to enhance their functionality. We have utilized the previously discussed conjugation method for the functionalization of GO nanosheets with Lys. Lys exhibits unique molecular interactions because it possesses two amino groups. One of these groups can form covalent bonds with various functional groups on the surface of GO (graphene oxide), while the other remains unchanged. The presence of the dual amino groups provides an advantage over tyrosine and phenylalanine amino acids. The modified nanosheets of GO were then added to a chitosan matrix to synthesize mixed matrix membrane and the study of CO_2 separation using these membranes is presented. The Lysine-conjugated-GO nanosheets had a positive synergistic effect on the gas separation performance of the MMMs. The amino groups attached to the GO sheets provided a pathway for high CO_2 selectivity. The selective barrier created by the amine, hydroxyl and carboxy groups of the nanosheets on the MMM surface also contributed to an increase in selectivity.

Chapter 6: Metal-organic frameworks (MOFs) have become a subject of intense interest among researchers exploring the formation of mixed matrix membranes (MMMs) for CO_2 separation applications. The interest in MOFs arises from their exceptional properties and potential benefits in improving CO_2 separation efficiency of membranes. In this chapter, we introduce a sustainable method for synthesizing MIL-100(Fe) MOF nanoparticles. These nanoparticles serve as nanofillers, integrated into a biodegradable CS matrix to create high-

performing mixed matrix membranes (MMMs) for effective CO_2 separation. Notably, the MIL-100(Fe) nanoparticles were created without the use of harsh hydrofluoric acid at room temperature and integrated into a biodegradable CS matrix. The CO_2 molecules were captured by the μ3-oxo-trimer of the MIL-100(Fe) NPs and the amine groups of the CS polymer, due to the affinity of the MOF NPs for CO_2 and zwitterionic mechanism, respectively. The nanoparticles' high surface area provided a specific channel for gas molecule passage. The MMMs underwent testing for CO_2 separation performance, with maximum filler incorporation limit and optimization of the MMM. The MMM's endurance and efficacy were tested under adverse conditions. The MMMs showed increased CO_2 permeance and CO_2/N_2 selectivity with increasing concentration of the MIL-100(Fe) up to 15 wt%. This technique could be applied to other nanofiller-matrix combinations to develop more efficient MMMs and enhance CO_2 separation performance even further.

Chapter 7: Inspired from the benefits of MOFs as filler in MMM synthesis and conjugation method to aid amino groups to polymer or filler, in this chapter of the thesis we describe the synthesis of Zr BDC (UIO-66) MOF nanoparticles and their functionalization with lysine amino acids via conjugation mechanism to create nanofillers for chitosan mixed matrix membranes (MMMs). The resulting lysine-conjugated Zr BDC MOF exhibits a strong affinity for CO_2 molecules, making it highly selective in capturing CO_2 over N_2. This selectivity is essential for efficient and targeted CO_2 separation. To fabricate the MMMs, we utilized the solution casting method, incorporating Zr BDC and lysine-conjugated-Zr BDC as nanofillers, with chitosan polymer as the compatible matrix due to its amphipathic structure. Successful conjugation of lysine with the nanoparticles was achieved through amide bond formation, which enhances CO_2 adsorption. By embedding various concentrations of the nanofillers in chitosan and casting them onto a porous support, we obtained a dense and thermally stable

selective layer for CO_2 separation.

Remarkably, the lysine-conjugated-Zr BDC embedded CS MMM displayed better CO_2 separation performance than the MIL or the Lys-c-GO embedded MMMs and successfully surpassed Robeson's upper bound curve. This promising result suggests that this approach holds great potential for CO_2 separation from flue gas and the development of high-performing gas separation membranes.

Chapter 8: In this chapter, the present study draws its well-founded overall conclusions drawn from the investigation. This section also offers valuable recommendations for future research in the relevant field.

Notably, all the research endeavour within this thesis have been acknowledged in international journals, namely Membranes (mdpi), Chemical Engineering Journal (Elsevier), Indian Chemical Engineers (Taylor & Francis), Industrial and Engineering Chemistry Research (ACS) and Applied Nano Materials (ACS). For specific publication details of journals and conferences, please refer to the research output section provided at the end of this thesis.

1.7. References

(1) Rubin, E. S. IPCC Special Report on Carbon Dioxide Capture and Storage Structure of the Intergovernmental Panel on Climate Change (IPCC). **2006**, 1–443.

(2) Reinmuth-Selzle, K.; Kampf, C. J.; Lucas, K.; Lang-Yona, N.; Fröhlich-Nowoisky, J.; Shiraiwa, M.; Lakey, P. S. J.; Lai, S.; Liu, F.; Kunert, A. T.; Ziegler, K.; Shen, F.; Sgarbanti, R.; Weber, B.; Bellinghausen, I.; Saloga, J.; Weller, M. G.; Duschl, A.; Schuppan, D.; Pöschl, U. Air Pollution and Climate Change Effects on Allergies in the Anthropocene: Abundance, Interaction and Modification of Allergens and Adjuvants. *Environ. Sci. Technol.* **2017**, *51* (8), 4119–4141.

https://doi.org/10.1021/acs.est.6b04908.

(3) de Richter, R.; Ming, T.; Davies, P.; Liu, W.; Caillol, S. Removal of Non-CO_2 Greenhouse Gases by Large-Scale Atmospheric Solar Photocatalysis. *Prog. Energy Combust. Sci.* **2017**, *60*, 68–96. https://doi.org/10.1016/j.pecs.2017.01.001.

(4) Ogurtsov, M.; Lindholm, M.; Jalkanen, R. On the Possible Contribution of Natural Climatic Fluctuations to the Global Warming of the Last 135 Years. *Atmos. Clim. Sci.* **2017**, *07* (03), 256–262. https://doi.org/10.4236/acs.2017.73018.

(5) Steingrube, A.; Voll, P. Selecting CO_2 Sources for CO_2 Utilization by Environmental-Merit- Order Curves. **2016**. https://doi.org/10.1021/acs.est.5b03474.

(6) Pöschl, U.; Shiraiwa, M. Multiphase Chemistry at the Atmosphere-Biosphere Interface Influencing Climate and Public Health in the Anthropocene. *Chem. Rev.* **2015**, *115* (10), 4440–4475. https://doi.org/10.1021/cr500487s.

(7) *Carbon Dioxide | Vital Signs – Climate Change: Vital Signs of the Planet*.

(8) Wang, S.; Li, X.; Wu, H.; Tian, Z.; Xin, Q.; He, G.; Peng, D.; Chen, S.; Yin, Y.; Jiang, Z.; Guiver, M. D. Advances in High Permeability Polymer-Based Membrane Materials for CO_2 Separations. *Energy Environ. Sci.* **2016**, *9* (6), 1863–1890. https://doi.org/10.1039/c6ee00811a.

(9) *Global Energy & CO_2 Status Report 2019 – Analysis - IEA*.

(10) Matthews, H. D.; Caldeira, K. Stabilizing Climate Requires Near-Zero Emissions. *Geophys. Res. Lett.* **2008**, *35* (4), 1–5. https://doi.org/10.1029/2007GL032388.

(11) Yang, H.; Xu, Z.; Fan, M.; Gupta, R.; Slimane, R. B.; Bland, A. E.; Wright, I. Progress in Carbon Dioxide Separation and Capture: A Review. *J. Environ. Sci.* **2008**, *20* (1), 14–

27. https://doi.org/10.1016/S1001-0742(08)60002-9.

(12) Singh, G.; Lakhi, K. S.; Ramadass, K.; Sathish, C. I.; Vinu, A. High-Performance Biomass-Derived Activated Porous Biocarbons for Combined Pre- and Post-Combustion CO_2 separation. *ACS Sustain. Chem. Eng.* **2019**, *7* (7), 7412–7420. https://doi.org/10.1021/acssuschemeng.9b00921.

(13) Güleç, F.; Meredith, W.; Sun, C. G.; Snape, C. E. A Novel Approach to CO_2 Capture in Fluid Catalytic Cracking—Chemical Looping Combustion. *Fuel* **2019**, *244*, 140–150. https://doi.org/10.1016/j.fuel.2019.01.168.

(14) Merkel, T. C.; Lin, H.; Wei, X.; Baker, R. Power Plant Post-Combustion Carbon Dioxide Capture: An Opportunity for Membranes. *J. Memb. Sci.* **2010**, *359* (1–2), 126–139. https://doi.org/10.1016/j.memsci.2009.10.041.

(15) Figueroa, J. D.; Fout, T.; Plasynski, S.; McIlvried, H.; Srivastava, R. D. Advances in CO_2 Capture Technology-The U.S. Department of Energy's Carbon Sequestration Program. *Int. J. Greenh. Gas Control* **2008**, *2* (1), 9–20. https://doi.org/10.1016/S1750-5836(07)00094-1.

(16) Luis Míguez, J.; Porteiro, J.; Pérez-Orozco, R.; Patiño, D.; Rodríguez, S. Evolution of CO_2 Capture Technology between 2007 and 2017 through the Study of Patent Activity. *Appl. Energy* **2018**, *211*, 1282–1296. https://doi.org/10.1016/j.apenergy.2017.11.107.

(17) Lv, B.; Guo, B.; Zhou, Z.; Jing, G. Mechanisms of CO_2 Capture into Monoethanolamine Solution with Different CO_2 Loading during the Absorption/Desorption Processes. *Environ. Sci. Technol.* **2015**, *49* (17), 10728–10735. https://doi.org/10.1021/acs.est.5b02356.

(18) Naji, S. Z.; Abd, A. A. Sensitivity Analysis of Using Diethanolamine Instead of Methyldiethanolamine Solution for GASCO'S Habshan Acid Gases Removal Plant. *Front. Energy* **2019**, *13* (2), 317–324. https://doi.org/10.1007/s11708-019-0622-2.

(19) Lin, G.; Jiang, S.; Zhu, C.; Fu, T.; Ma, Y. Mass-Transfer Characteristics of CO_2 Absorption into Aqueous Solutions of N-Methyldiethanolamine + Diethanolamine in a T-Junction Microchannel. *ACS Sustain. Chem. Eng.* **2019**, *7* (4), 4368–4375. https://doi.org/10.1021/acssuschemeng.8b06231.

(20) Yeh, J. T.; Pennline, H. W. Kevin P. **2004**, *4* (x), 89–104 https://doi.org/10.1021/es9032309.

(21) Li, K.; Yu, H.; Feron, P.; Tade, M.; Wardhaugh, L. Technical and Energy Performance of an Advanced, Aqueous Ammonia-Based CO_2 Capture Technology for a 500 MW Coal-Fired Power Station. *Environ. Sci. Technol.* **2015**, *49* (16), 10243–10252. https://doi.org/10.1021/acs.est.5b02258.

(22) Liu, J.; Wang, S.; Qi, G.; Zhao, B.; Chen, C. Kinetics and Mass Transfer of Carbon Dioxide Absorption into Aqueous Ammonia. *Energy Procedia* **2011**, *4*, 525–532. https://doi.org/10.1016/j.egypro.2011.01.084.

(23) Olajire, A. A. Synthesis of Bare and Functionalized Porous Adsorbent Materials for CO_2 Capture. *Greenhouse Gases: Science and Technology*. **2017**, 399–459. https://doi.org/10.1002/ghg.1657.

(24) Choi, S.; Drese, J. H.; Jones, C. W. Adsorbent Materials for Carbon Dioxide Capture from Large Anthropogenic Point Sources. *ChemSusChem*. **2009**, 796–854. https://doi.org/10.1002/cssc.200900036.

(25) Wawrzyńczak, D.; Majchrzak-Kucęba, I.; Srokosz, K.; Kozak, M.; Nowak, W.; Zdeb, J.; Smółka, W.; Zajchowski, A. The Pilot Dual-Reflux Vacuum Pressure Swing Adsorption Unit for CO_2 Capture from Flue Gas. *Sep. Purif. Technol.* **2019**, *209*, 560–570. https://doi.org/10.1016/j.seppur.2018.07.079.

(26) Park, J.; Seo, Y. T.; Lee, J. won; Lee, H. Spectroscopic Analysis of Carbon Dioxide and Nitrogen Mixed Gas Hydrates in Silica Gel for CO_2 Separation. *Catal. Today* **2006**, *115* (1–4), 279–282. https://doi.org/10.1016/j.cattod.2006.02.059.

(27) Subramanian Balashankar, V.; Rajendran, A. Process Optimization-Based Screening of Zeolites for Post-Combustion CO_2 Capture by Vacuum Swing Adsorption. *ACS Sustain. Chem. Eng.* **2019**, *7* (21), 17747–17755. https://doi.org/10.1021/acssuschemeng.9b04124.

(28) Shan, S. Y.; Ma, A. H.; Hu, Y. C.; Jia, Q. M.; Wang, Y. M.; Peng, J. H. Development of Sintering-Resistant CaO-Based Sorbent Derived from Eggshells and Bauxite Tailings for Cyclic CO_2 Capture. *Environ. Pollut.* **2016**, *208*, 546–552. https://doi.org/10.1016/j.envpol.2015.10.028.

(29) Pierre-Louis, A. M.; Hausner, D. B.; Bhandari, N.; Li, W.; Kim, J.; Kubicki, J. D.; Strongin, D. Adsorption of Carbon Dioxide on Al/Fe Oxyhydroxide. *J. Colloid Interface Sci.* **2013**, *400*, 1–10. https://doi.org/10.1016/j.jcis.2013.01.047.

(30) Creamer, A. E.; Gao, B.; Wang, S. Carbon Dioxide Capture Using Various Metal Oxyhydroxide-Biochar Composites. *Chem. Eng. J.* **2016**, *283*, 826–832. https://doi.org/10.1016/j.cej.2015.08.037.

(31) Xue, M.; Ma, S.; Jin, Z.; Schaffino, R. M.; Zhu, G. S.; Lobkovsky, E. B.; Qiu, S. L.; Chen, B. Robust Metal-Organic Framework Enforced by Triple-Framework

Interpenetration Exhibiting High H_2 Storage Density. *Inorg. Chem.* **2008**, *47* (15), 6825–6828. https://doi.org/10.1021/ic800854y.

(32) Zhuang, W.; Yuan, D.; Liu, D.; Zhong, C.; Li, J. R.; Zhou, H. C. Robust Metal-Organic Framework with an Octatopic Ligand for Gas Adsorption and Separation: Combined Characterization by Experiments and Molecular Simulation. *Chem. Mater.* **2012**, *24* (1), 18–25. https://doi.org/10.1021/cm2008889.

(33) Audus, H. Greenhouse Gas Mitigation Technology: An Overview of the CO_2 Capture and Sequestration Studies and Further Activities of the IEA Greenhouse Gas R and D Programme. *Energy* **1997**, *22* (2–3), 217–221. https://doi.org/10.1016/S0360-5442(96)00107-7.

(34) Hahn, M. W.; Jelic, J.; Berger, E.; Reuter, K.; Jentys, A.; Lercher, J. A. Role of Amine Functionality for CO_2 Chemisorption on Silica. *J. Phys. Chem. B* **2016**, *120* (8), 1988–1995. https://doi.org/10.1021/acs.jpcb.5b10012.

(35) *Handbook of Compressed Gases - Compressed Gas Association, Inc. - Google Books*.

(36) Song, C.; Liu, Q.; Ji, N.; Deng, S.; Zhao, J.; Kitamura, Y. Advanced Cryogenic CO_2 capture Process Based on Stirling Coolers by Heat Integration. *Appl. Therm. Eng.* **2017**, *114*, 887–895. https://doi.org/10.1016/j.applthermaleng.2016.12.049.

(37) Holmes, I. A. S.; Ryan, J. M. United States Patent (19) Holmes et Al. (54) (75). **1982**, No. 19.

(38) Denis Clodic, M. Y. Method and System for Extracting Carbon Dioxide by Anti-Sublimation for Storage Thereof. **2016**, *2* (12).

(39) Tuinier, M. J.; van Sint Annaland, M.; Kramer, G. J.; Kuipers, J. A. M. Cryogenic CO_2

Capture Using Dynamically Operated Packed Beds. *Chem. Eng. Sci.* **2010**, *65* (1), 114–119. https://doi.org/10.1016/j.ces.2009.01.055.

(40) Song, C.; Liu, Q.; Deng, S.; Li, H.; Kitamura, Y. Cryogenic-Based CO_2 Capture Technologies: State-of-the-Art Developments and Current Challenges. *Renew. Sustain. Energy Rev.* **2019**, *101*, 265–278. https://doi.org/10.1016/j.rser.2018.11.018.

(41) Bhatta, L. K. G.; Subramanyam, S.; Chengala, M. D.; Olivera, S.; Venkatesh, K. Progress in Hydrotalcite like Compounds and Metal-Based Oxides for CO_2 Capture: A Review. *J. Clean. Prod.* **2015**, *103*, 171–196. https://doi.org/10.1016/j.jclepro.2014.12.059.

(42) Uchida, T.; Goto, T.; Yamada, T.; Kiga, T.; Spero, C. Oxyfuel Combustion as CO_2 Capture Technology Advancing for Practical Use - Callide Oxyfuel Project. *Energy Procedia* **2013**, *37*, 1471–1479. https://doi.org/10.1016/j.egypro.2013.06.022.

(43) Scheffknecht, G.; Al-Makhadmeh, L.; Schnell, U.; Maier, J. Oxy-Fuel Coal Combustion-A Review of the Current State-of-the-Art. *Int. J. Greenh. Gas Control* **2011**, *5*, 16–35. https://doi.org/10.1016/j.ijggc.2011.05.020.

(44) Senior, C. L.; Morris, W.; Lewandowski, T. A. Emissions and Risks Associated with Oxyfuel Combustion: State of the Science and Critical Data Gaps. *J. Air Waste Manag. Assoc.* **2013**, *63* (7), 832–843. https://doi.org/10.1080/10962247.2013.791892.

(45) Aaron, D.; Tsouris, C. Separation of CO_2 from Flue Gas: A Review. *Sep. Sci. Technol.* **2005**, *40* (1–3), 321–348. https://doi.org/10.1081/SS-200042244.

(46) Ishida, M.; Yamamoto, M.; Ohba, T. Experimental Results of Chemical-Looping Combustion with $NiO/NiAl_2O_4$ Particle Circulation at 1200 °C. *Energy Convers.*

Manag. **2002**, *43* (9–12), 1469–1478. https://doi.org/10.1016/S0196-8904(02)00029-8.

(47) Moftakhari Sharifzadeh, M. M.; Ebadi Amooghin, A.; Zamani Pedram, M.; Omidkhah, M. Time-Dependent Mathematical Modeling of Binary Gas Mixture in Facilitated Transport Membranes (FTMs): A Real Condition for Single-Reaction Mechanism. *J. Ind. Eng. Chem.* **2016**, *39*, 48–65. https://doi.org/10.1016/j.jiec.2016.05.004.

(48) Böddeker, K. W. Commentary: Tracing Membrane Science. *J. Memb. Sci.* **1995**, *100* (1), 65–68. https://doi.org/10.1016/0376-7388(94)00223-L.

(49) *Polymeric Gas Separation Membranes - Donald R. Paul, Yuri P. Yampol'skii - Google Books*, 2018.

(50) Mitchell, J. K. On the Penetrativeness of Fluids. *J. Memb. Sci.* **1995**, *100* (1), 11–16. https://doi.org/10.1016/0376-7388(94)00227-P.

(51) Tabe-Mohammadi, A. A Review of the Applications of Membrane Separation Technology in Natural Gas Treatment. *Sep. Sci. Technol.* **1999**, *34* (10), 2095–2111. https://doi.org/10.1081/SS-100100758.

(52) Lonsdale, H. K. The Evolution of Ultrathin Synthetic Membranes. *J. Memb. Sci.* **1987**, *33* (2), 121–136. https://doi.org/10.1016/S0376-7388(00)80372-5.

(53) Ward, W. J.; Browall, W. R.; Salemme, R. M. Ultrathin Silicone/Polycarbonate Membranes for Gas Separation Processes. *J. Memb. Sci.* **1976**, *1* (C), 99–108. https://doi.org/10.1016/S0376-7388(00)82259-0.

(54) Wang, M.; Lawal, A.; Stephenson, P.; Sidders, J.; Ramshaw, C. Post-Combustion CO_2 Capture with Chemical Absorption: A State-of-the-Art Review. *Chem. Eng. Res. Des.* **2011**, *89* (9), 1609–1624. https://doi.org/10.1016/j.cherd.2010.11.005.

(55) Kentish, S. E.; Scholes, C. A.; Stevens, G. W. Carbon Dioxide Separation through Polymeric Membrane Systems for Flue Gas Applications. *Recent Patents on Chemical Engineering* **2008**, *1*(1), 52-66. http://dx.doi.org/10.2174/2211334710801010052.

(56) Matteucci, S.; Yampolskii, Y.; Freeman, B. D.; Pinnau, I. Transport of Gases and Vapors in Glassy and Rubbery Polymers. In *Materials Science of Membranes for Gas and Vapor Separation*; John Wiley & Sons, Ltd, **2006**; 1–47. https://doi.org/10.1002/047002903X.ch1.

(57) Robeson, L. M.; Smith, Z. P.; Freeman, B. D.; Paul, D. R. Contributions of Diffusion and Solubility Selectivity to the Upper Bound Analysis for Glassy Gas Separation Membranes. *J. Memb. Sci.* **2014**, *453*, 71–83. https://doi.org/10.1016/j.memsci.2013.10.066.

(58) Caplow, M. Kinetics of Carbamate Formation and Breakdown. *J. Am. Chem. Soc.* **1968**, *90* (24), 6795–6803. https://doi.org/10.1021/ja01026a041.

(59) Mubashir, M.; Yeong, Y. F.; Lau, K. K.; Chew, T. L.; Norwahyu, J. Efficient CO_2/N_2 and CO_2/CH_4 Separation Using NH_2-MIL-53(Al)/Cellulose Acetate (CA) Mixed Matrix Membranes. *Sep. Purif. Technol.* **2018**, *199*, 140–151. https://doi.org/10.1016/j.seppur.2018.01.038.

(60) Wu, S. Y.; Hsiao, I. C.; Liu, C. M.; Mt Yusuf, N. Y.; Wan Isahak, W. N. R.; Masdar, M. S. A Novel Bio-Cellulose Membrane and Modified Adsorption Approach in CO_2/H_2 Separation Technique for PEM Fuel Cell Applications. *Int. J. Hydrogen Energy* **2017**, *42* (45), 27630–27640. https://doi.org/10.1016/j.ijhydene.2017.05.148.

(61) Barrie, J. A. Materials Science of Synthetic Membranes. Edited by D. R. Lloyd, ACS Symposium Series, No. 269, American Chemical Society, Washington, D.C., 1985. Pp.

Ix+494, Price $79.95 (USA & Canada), $95.95 (Rest of World). ISBN 0-8412-0887-5. *Br. Polym. J.* **1986**, *18* (5), 351–351. https://doi.org/10.1002/pi.4980180520.

(62) Houde, A. Y.; Krishnakumar, B.; Charati, S. G.; Stern, S. A. Permeability of Dense (Homogeneous) Cellulose Acetate Membranes to Methane, Carbon Dioxide and Their Mixtures at Elevated Pressures. *J. Appl. Polym. Sci.* **1996**, *62* (13), 2181–2192. https://doi.org/10.1002.

(63) Aitken, C. L.; Koros, W. J.; Paul, D. R. Effect of Structural Symmetry on Gas Transport Properties of Polysulfones. *Macromolecules* **1992**, *25* (13), 3424–3434. https://doi.org/10.1021/ma00039a018.

(64) Prasad, B.; Mandal, B. Preparation and Characterization of CO_2-Selective Facilitated Transport Membrane Composed of Chitosan and Poly(Allylamine) Blend for CO_2/N_2 Separation. *J. Ind. Eng. Chem.* **2018**, *66*, 419–429. https://doi.org/10.1016/j.jiec.2018.06.009.

(65) Kim, S. H.; Hong, S. R. Gas Permeation Characteristics by Chitosan/Pebax Composite Membranes. *Membr. J.* **2017**, *27* (4), 319–327. https://doi.org/10.14579/membrane_journal.2017.27.4.319.

(66) Shan, M.; Seoane, B.; Pustovarenko, A.; Wang, X.; Liu, X.; Yarulina, I.; Abou-Hamad, E.; Kapteijn, F.; Gascon, J. Benzimidazole Linked Polymers (BILPs) in Mixed-Matrix Membranes: Influence of Filler Porosity on the CO_2/N_2 Separation Performance. *J. Memb. Sci.* **2018**, *566*, 213–222. https://doi.org/10.1016/j.memsci.2018.08.023.

(67) Shen, Y.; Wang, H.; Liu, J.; Zhang, Y. Enhanced Performance of a Novel Polyvinyl Amine/Chitosan/Graphene Oxide Mixed Matrix Membrane for CO_2 Capture. *ACS Sustain. Chem. Eng.* **2015**, *3* (8), 1819–1829.

https://doi.org/10.1021/acssuschemeng.5b00409.

(68) *Ceramic Membranes for Separation and Reaction - Kang Li - Google Books*. **2007**.

(69) Cheng, Z.; Han, S. Synthesis and Separation Performance of Y-Type Zeolite Membranes by Pre-Seeding Using Electrophoresis Deposition Method. *China Pet. Process. Petrochemical Technol.* **2015**, *17* (4), 62–70.

(70) Kulprathipanja, S.; Neuzil, R. W.; Li, N. N. Separation of Fluids by Means of Mixed-Matrix Membranes. *U.S. Pat.* **1988**, No. 19, 1–7.

(71) Ghanbari, T.; Abnisa, F.; Wan Daud, W. M. A. A Review on Production of Metal Organic Frameworks (MOF) for CO_2 Adsorption. *Sci. Total Environ.* **2020**, *707*, 135090. https://doi.org/10.1016/j.scitotenv.2019.135090.

(72) Eddaoudi, M.; Sava, D. F.; Eubank, J. F.; Adil, K.; Guillerm, V. Zeolite-like Metal-Organic Frameworks (ZMOFs): Design, Synthesis and Properties. *Chem. Soc. Rev.* **2015**, *44* (1), 228–249. https://doi.org/10.1039/c4cs00230j.

(73) Barooah, M.; Mandal, B. Synthesis, Characterization and CO_2 Separation Performance of Novel PVA/PG/ZIF-8 Mixed Matrix Membrane. *J. Memb. Sci.* **2019**, *572*, 198–209. https://doi.org/10.1016/j.memsci.2018.11.001.

(74) Barooah, M.; Mandal, B. Enhanced CO_2 Separation Performance by PVA/PEG/Silica Mixed Matrix Membrane. *J. Appl. Polym. Sci.* **2018**, *135* (28), 1–12. https://doi.org/10.1002/app.46481.

(75) Mohshim, D. F.; Mukhtar, H.; Man, Z. The Effect of Incorporating Ionic Liquid into Polyethersulfone-SAPO34 Based Mixed Matrix Membrane on CO_2 Gas Separation Performance. *Sep. Purif. Technol.* **2014**, *135*, 252–258.

https://doi.org/10.1016/j.seppur.2014.08.019.

(76) Prasad, B.; Mandal, B. CO_2 Separation Performance by Chitosan/Tetraethylenepentamine/Poly(Ether Sulfone) Composite Membrane. *J. Appl. Polym. Sci.* **2017**, *134* (34), 1–9. https://doi.org/10.1002/app.45206.

(77) Prasad, B.; Mandal, B. Graphene-Incorporated Biopolymeric Mixed-Matrix Membrane for Enhanced CO_2 Separation by Regulating the Support Pore Filling. *ACS Appl. Mater. Interfaces* **2018**, *10* (33), 27810–27820. https://doi.org/10.1021/acsami.8b09377.

(78) Prasad, B.; Thakur, R. M.; Mandal, B.; Su, B. Enhanced CO_2 Separation Membrane Prepared from Waste By-Product of Silk Fibroin. *J. Memb. Sci.* **2019**, *587*, 117170. https://doi.org/10.1016/j.memsci.2019.117170.

(79) Ahmad, A. L.; Jawad, Z. A.; Low, S. C.; Zein, S. H. S. A Cellulose Acetate/Multi-Walled Carbon Nanotube Mixed Matrix Membrane for CO_2/N_2 Separation. *J. Memb. Sci.* **2014**, *451*, 55–66. https://doi.org/10.1016/j.memsci.2013.09.043.

(80) Anjum, M. W.; Vermoortele, F.; Khan, A. L.; Bueken, B.; De Vos, D. E.; Vankelecom, I. F. J. Modulated UiO-66-Based Mixed-Matrix Membranes for CO_2 Separation. *ACS Appl. Mater. Interfaces* **2015**, *7* (45), 25193–25201. https://doi.org/10.1021/acsami.5b08964.

(81) Naseri, M.; Mousavi, S. F.; Mohammadi, T.; Bakhtiari, O. Synthesis and Gas Transport Performance of MIL-101/Matrimid Mixed Matrix Membranes. *J. Ind. Eng. Chem.* **2015**, *29*, 249–256. https://doi.org/10.1016/j.jiec.2015.04.007.

(82) Budd, P. M.; Msayib, K. J.; Tattershall, C. E.; Ghanem, B. S.; Reynolds, K. J.; McKeown, N. B.; Fritsch, D. Gas Separation Membranes from Polymers of Intrinsic

Microporosity. *J. Memb. Sci.* **2005**, *251* (1–2), 263–269. https://doi.org/10.1016/j.memsci.2005.01.009.

(83) Khdhayyer, M. R.; Esposito, E.; Fuoco, A.; Monteleone, M.; Giorno, L.; Jansen, J. C.; Attfield, M. P.; Budd, P. M. Mixed Matrix Membranes Based on UiO-66 MOFs in the Polymer of Intrinsic Microporosity PIM-1. *Sep. Purif. Technol.* **2017**, *173*, 304–313. https://doi.org/10.1016/j.seppur.2016.09.036.

(84) Dai, Y.; Johnson, J. R.; Karvan, O.; Sholl, D. S.; Koros, W. J. Ultem ®/ZIF-8 Mixed Matrix Hollow Fiber Membranes for CO_2/N_2 Separations. *J. Memb. Sci.* **2012**, *401–402*, 76–82. https://doi.org/10.1016/j.memsci.2012.01.044.

(85) Borgohain, R.; Prasad, B.; Mandal, B. Synthesis and Characterization of Water-Soluble Chitosan Membrane Blended with a Mobile Carrier for CO_2 Separation. *Sep. Purif. Technol.* **2019**, *222*, 177–187. https://doi.org/10.1016/j.seppur.2019.04.038.

(86) Sodeifian, G.; Raji, M.; Asghari, M.; Rezakazemi, M.; Dashti, A. Polyurethane-SAPO-34 Mixed Matrix Membrane for CO_2 /CH_4 and CO_2 /N_2 Separation. *Chinese J. Chem. Eng.* **2019**, *27*, 322–334. https://doi.org/10.1016/j.cjche.2018.03.012.

(87) Rodrigues, M. A.; Ribeiro, J. de S.; Costa, E. de S.; de Miranda, J. L.; Ferraz, H. C. Nanostructured Membranes Containing UiO-66 (Zr) and MIL-101 (Cr) for O_2/N_2 and CO_2/N_2 Separation. *Sep. Purif. Technol.* **2018**, *192*, 491–500. https://doi.org/10.1016/j.seppur.2017.10.024.

(88) Meng, L.; Zou, X.; Guo, S.; Ma, H.; Zhao, Y.; Zhu, G. Self-Supported Fibrous Porous Aromatic Membranes for Efficient CO_2/N_2 Separations. *ACS Appl. Mater. Interfaces* **2015**, *7* (28), 15561–15569. https://doi.org/10.1021/acsami.5b04148.

(89) Wang, B.; Dutta, P. K. Influence of Cross-Linking, Temperature and Humidity on CO_2/N_2 Separation Performance of PDMS Coated Zeolite Membranes Grown within a Porous Poly(Ether Sulfone) Polymer. *Ind. Eng. Chem. Res.* **2017**, *56* (20), 6065–6077. https://doi.org/10.1021/acs.iecr.7b00850.

(90) Tong, Z.; Ho, W. S. W. New Sterically Hindered Polyvinylamine Membranes for CO_2 Separation and Capture. *J. Memb. Sci.* **2017**, *543*, 202–211. https://doi.org/10.1016/j.memsci.2017.08.057.

(91) Wang, Y.; Li, L.; Zhang, X.; Li, J.; Liu, C.; Li, N.; Xie, Z. Polyvinylamine/Graphene Oxide/PANI@CNTs Mixed Matrix Composite Membranes with Enhanced CO_2/N_2 Separation Performance. *J. Memb. Sci.* **2019**, *589*, 117246. https://doi.org/10.1016/j.memsci.2019.117246.

(92) Wang, S.; Liu, Y.; Huang, S.; Wu, H.; Li, Y.; Tian, Z.; Jiang, Z. Pebax-PEG-MWCNT Hybrid Membranes with Enhanced CO_2 Capture Properties. *J. Memb. Sci.* **2014**, *460*, 62–70. https://doi.org/10.1016/j.memsci.2014.02.036.

(93) Zhu, H.; Yuan, J.; Zhao, J.; Liu, G.; Jin, W. Enhanced CO_2 /N_2 Separation Performance by Using Dopamine/Polyethyleneimine-Grafted TiO_2 Nanoparticles Filled PEBA Mixed-Matrix Membranes. *Sep. Purif. Technol.* **2019**, *214*, 78–86. https://doi.org/10.1016/j.seppur.2018.02.020.

(94) Khor, E.; Lim, L. Y. Implantable Applications of Chitin and Chitosan. *Biomaterials* **2003**, *24* (13), 2339–2349. https://doi.org/10.1016/S0142-9612(03)00026-7.

(95) Rinaudo, M. Chitin and Chitosan: Properties and Applications. *Prog. Polym. Sci.* **2006**, *31* (7), 603–632. https://doi.org/10.1016/j.progpolymsci.2006.06.001.

(96) Tong, Z.; Ho, W. S. W. Facilitated Transport Membranes for CO_2 Separation and Capture. *Sep. Sci. Technol.* **2017**, *52* (2), 156–167. https://doi.org/10.1080/01496395.2016.1217885.

(97) Casado-Coterillo, C.; Fernández-Barquín, A.; Zornoza, B.; Téllez, C.; Coronas, J.; Irabien, Á. Synthesis and Characterisation of MOF/Ionic Liquid/Chitosan Mixed Matrix Membranes for CO_2/N_2 Separation. *RSC Adv.* **2015**, *5* (124), 102350–102361. https://doi.org/10.1039/c5ra19331a.

(98) Prasad, B.; Mandal, B. Moisture Responsive and CO_2 Selective Biopolymer Membrane Containing Silk Fibroin as a Green Carrier for Facilitated Transport of CO_2. *J. Memb. Sci.* **2018**, *550*, 416–426. https://doi.org/10.1016/j.memsci.2017.12.061.

(99) Xiao, S.; Feng, X.; Huang, R. Y. M. Trimesoyl Chloride Crosslinked Chitosan Membranes for CO_2/N_2 Separation and Pervaporation Dehydration of Isopropanol. *J. Memb. Sci.* **2007**, *306* (1–2), 36–46. https://doi.org/10.1016/j.memsci.2007.08.021.

(100) Liu, Y.; Yu, S.; Wu, H.; Li, Y.; Wang, S.; Tian, Z.; Jiang, Z. High Permeability Hydrogel Membranes of Chitosan/Poly Ether-Block-Amide Blends for CO_2 Separation. *J. Memb. Sci.* **2014**, *469*, 198–208. https://doi.org/10.1016/j.memsci.2014.06.050.

CHAPTER 2

Experimental Section

In this section of the thesis, the materials that were used to synthesize various filler materials and membranes are discussed. A detailed, step-by-step description of the processes utilized to produce various membranes is provided. Moreover, numerous analytical techniques were addressed for characterizing the membranes and filler. Lastly, the illustration and discussion are provided regarding the gas permeation set-up.

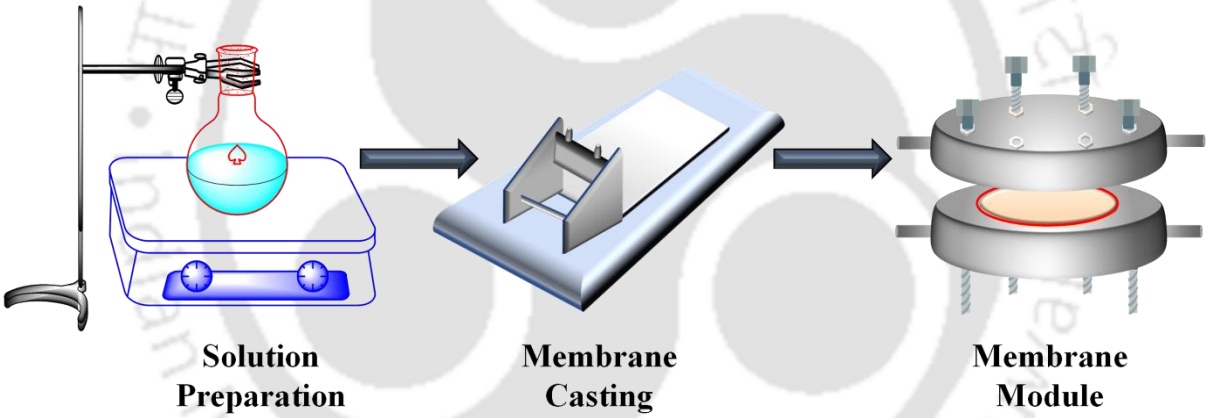

2.1. Reagents and Chemicals used

Except where otherwise noted, all obtained reagents and solvents were used without further purification.

The following chemicals were procured from Sigma Aldrich, USA: chitosan flakes (high molecular weight: 310−375 kDa, % deacetylated), $ZrCl_4$ (purity ≥ 99.9%), graphite powder, acetic acid (AA) (ACS grade, purity ≥ 99.9%), N-Dimethylformamide (GC grade, ≥ 99.9%), hydrochloric acid (ACS grade, 37%), sulphuric acid (H_2SO_4, 98 wt %, Merck), orthophosphoric acid (H_3PO_4, 88 wt%), hydrogen peroxide (H_2O_2, 30 wt%), potassium permanganate ($KMnO_4$), 4-morpholineethanesulfonic acid (MES), iron (II) sulfate heptahydrate ($FeSO_4.7H_2O$, 99%), Trimesic acid (BTC), sodium hydroxide pellets (NaOH, 98%), ethanol (C_2H_5OH), methanol (CH_2OH) and terephthalic acid (purity ≥ 99%). L-tyrosine, L-lysine, L-phenylalanine, 1-(3-dimethyl aminopropyl)-3-ethyl carbodiimide hydrochloride (EDC) and N-hydroxysuccinimide (NHS) were purchased from Hi-media, India. Helium (purity ≥ 99.99%), Argon (purity ≥ 98%), 20% CO_2 and 80% N_2 binary mixture gas (purity ≥ 99.995%) were purchased from Vadilal gases Ltd. India. In industrial flue gas, the composition typically includes varying percentages of carbon dioxide (CO2) and nitrogen (N2), typically ranging between 14-15% CO2 and 86-85% N2 by volume. However, for certain real-world applications and to ensure an adequate CO2 driving force across the membrane, adjustments may be necessary. To address this, a gas mixture containing 20% CO2 and 80% N2 has been employed. Membrane support (Polyethersulfone: PES) with a pore size of 0.03 μm and thickness of 150 μm was purchased from Sterlitech in the USA. Demineralized Millipore water (>18 MΩ.cm) was used during all the experiments.

2.2. Characterization of As-synthesized Fillers and Membranes

Various analytical techniques utilized to characterize synthesized nanofiller materials and fabricated membranes are discussed listed below:

1. To investigate the electronic environment around the elements, valence state and the possible interactions for the synthesized nanofillers and membranes X-ray photoelectron spectroscopy (XPS, Thermo Fisher Scientific, ESCALAB Xi+) was used with a monochromatic Al K_α X-ray source. Fitting and deconvolution of the obtained data were done using XPSPEAK 4.1 software.

2. To investigate the interaction between functional groups of constituent materials of synthesized nanofillers and membranes, the Fourier transform infrared spectra (FTIR, SHIMADZU, IR Affinity 1, Japan) were recorded in the range of 4000-400 cm^{-1}.

3. To characterize the ordered crystal structure of the nanofillers (GO and MIL-100(Fe)), Raman spectra (Horiba LabRam HR spectrometer) were taken at an excitation wavelength of 488 nm.

4. To study the crystallography and phase purity of all the samples X-ray Diffractometer (XRD, Rigaku SMARTLAB) was used with 9kW power in the scanning range of 2θ between 3º and 60º, using Cu K_α as the radiation source.

5. To investigate the specific surface area and porous structure, of the nanofillers (MIL-100(Fe) and UIO-66(Zr)), Brunauer-Emmett- Teller (BET, Beckman-Coulter SA 3100 N_2 adsorption apparatus) was used under a nitrogen atmosphere (77.3 K).

6. The surface morphology of the nanofillers and membranes (cross-section and top surface) was visualized using advanced microscopic techniques of field emission scanning electron microscope (FESEM, Zeiss, Sigma).

7. Morphology and selected area electron diffraction (SAED) patterns of nanofillers were taken using field emission transmission electron microscope (FETEM, JEM-2100F).

8. The topographical images and roughness of the membranes were recorded using atomic force microscopy (AFM, Innova, Bruker) under tapping mode at 0.8 MHz scan rate. The required images and data were extracted using WSxM 5.0 software.

9. The elemental analysis of as-prepared samples was done using an energy-dispersive spectroscopy (EDS, Zeiss, Sigma) analyzer under vacuum conditions.

10. The thermal behavior of samples was investigated using thermogravimetric (TGA, Shimadzu TGA-50) analysis in N_2 atmosphere under dynamic and isotherm mode.

11. The successful grafting of material onto the chitosan backbone was proved using 400 MHz resonance for ^1H nuclear magnetic resonance (NMR) spectroscopy. The sample was dissolved in the solution of DCl and D_2O and piped into the NMR tubes.[1]

12. Contact angle measurements were also conducted for all the fabricated membranes using the Kruss Drop Shape Analyser-DSA-25 instrument under ambient conditions.

2.3. Membrane Fabrication Method

Solution casting, also known as the wet processing method, has outperformed competing production techniques due to its simplicity and lack of sophisticated equipment requirements over other membrane fabrication methods like phase inversion, electrospinning, stretching, interfacial polymerization, track-etching, etc.[2,3] In this study, we used a Stokes' law principle-based "solution casting technique" to fabricate membranes with the desired thickness. Usually, a polymer solution is prepared by dissolving polymer material into a suitable solvent under continuous stirring till homogeneity is achieved. The solvent selection is determined by

the solubility of the polymer. After that, the solution was centrifuged to remove bubbles and unreacted particles. Meanwhile, a suspension of fillers or solution amino acids was prepared. Then, both solutions were intermixed and left to achieve possible interaction under continuous agitation via mechanical stirring. Meanwhile, the PES support was cleaned by soaking it in Millipore water for several hours. Finally, the solution was cast onto the porous PES utilizing a microfilm applicator (GARDCO, Paul N. Gardner, USA) support. The standard solution casting process utilized in this research is illustrated in Scheme 2.1.

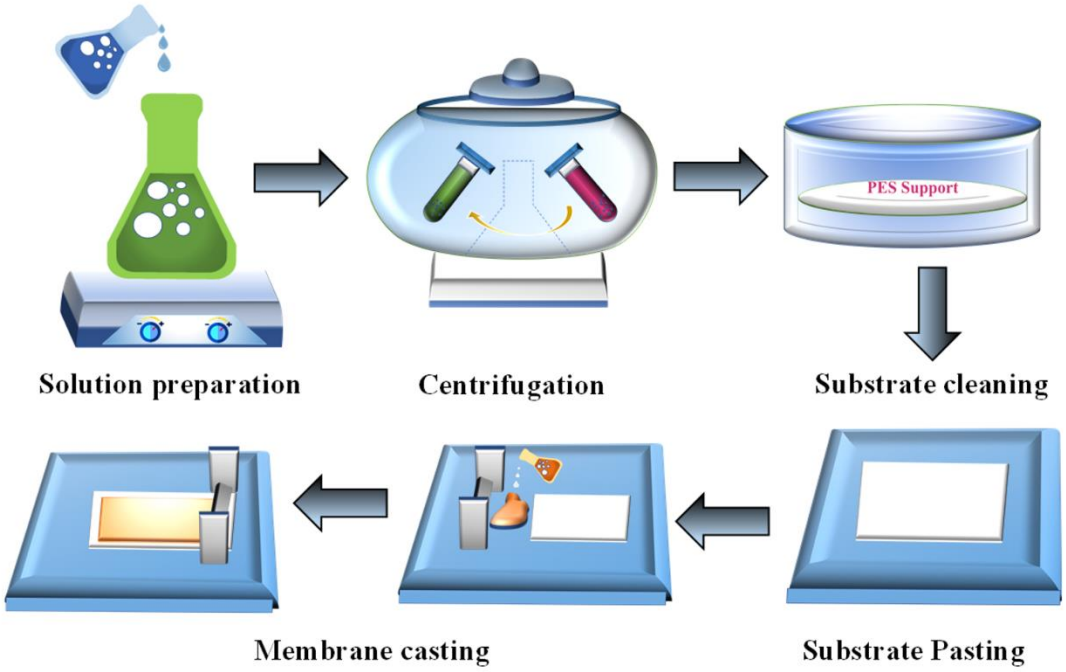

Scheme 2.1. Step-by-step illustration of thin film composite membrane synthesis procedure using solution casting method.

The thickness of the selective layer was maintained by assuming the following equation (Equation 2.1);[4]

$$l_2 \times r_2 = 0.5 \times c_1 \times r_1 \times \mathrm{l}_{gap} \qquad (2.1)$$

Where c_1 is the total solid weight concentration and r_1 is the density of the selective

layer solution, l_{gap} is the gap between the support and the casting knife, l_2 and r_2 denote the dried coated selective layer's thickness and density.

Afterward, the membranes were dried initially in the laminar hood chamber for 24 hours, followed by further drying in a hot air oven at 110 °C overnight. The as-prepared membranes were then stored in a desiccator to prevent any bacterial or moisture-related effects and ensured they are thoroughly dried before conducting any characterization study.

2.4. CO_2/N_2 Gas Separation Study Set-up

A schematic of a gas permeation set-up design is shown in Scheme 2.2. The fabricated membranes were cut into a circular shape with an active surface area of ~8 cm^2 and placed within a temperature-programmable oven fitted with a counter-current permeation cell. Two distinct AALBORG digital mass flow controllers were used to regulate the flow of the feed gas mixture (20% CO_2 and 80% N_2) and sweep (Ar) gas to the permeation cell. For feed and sweep

gas, the gas flow rates were maintained at 55 mL/min and 50 mL/min, respectively.

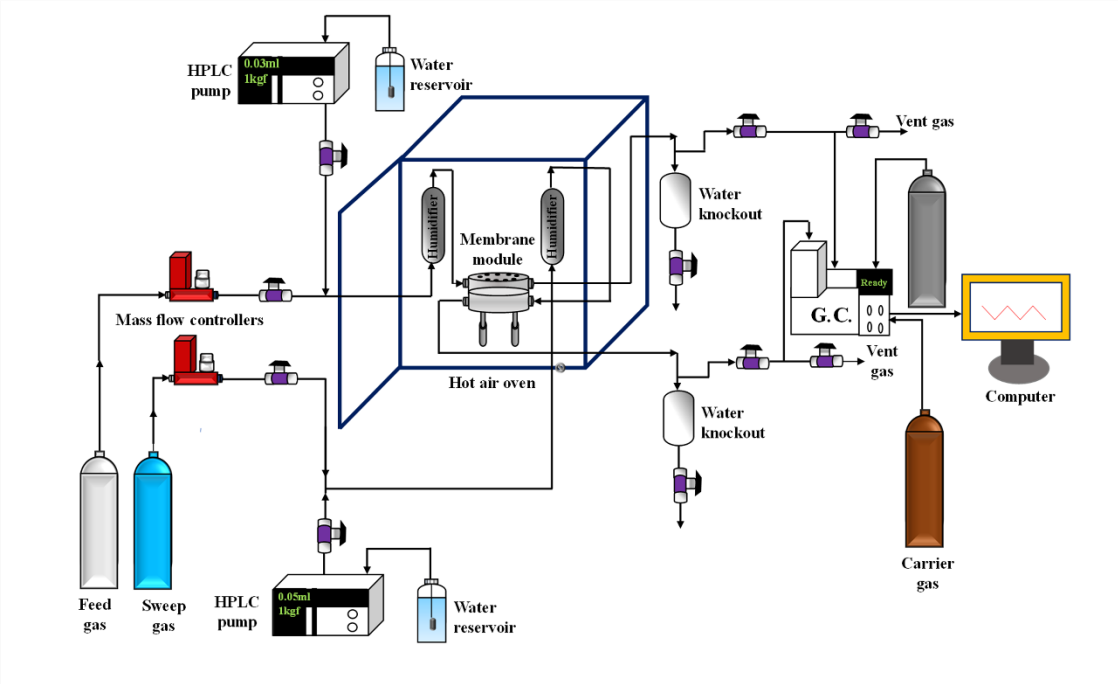

Scheme 2.2. Schematic representation of CO_2/N_2 gas permeation study setup.

Back-pressure regulators and Shimadzu HPLC pumps were used to keep the pressure and humidity inside the cell under check, respectively. Feed side pressure is kept at 2.21 bar and sweep side pressure is kept at 1.21 bar. Moisture flow rates were maintained at 0.03 mL/min in the feed gas stream and 0.05 mL/min in the sweep gas stream using HPLC pumps. Water knockout drums installed at leaving streams are used to dehumidify moisture of the permeation cell's outflow gases. With the aid of a bubble flow meter, the gas flow rates of the permeate and retentate streams discharged from the cell were determined. Finally, Agilent 7890B gas chromatography (GC) outfitted with a thermal conductivity detector (TCD) was used to record the compositions of CO_2 and N_2 in the permeate and retentate streams and the calculations of crucial gas separation parameters: CO_2/N_2 selectivity; CO_2, N_2 permeance and CO_2, N_2 flux was done using equations presented in Appendix A1. The analysis was carried out by adjusting various parameters, such as temperature, feed pressure and sweep-side

moisture flow rates and selective layer thickness. Before taking any readings, the operating conditions were maintained for 7-9 hours to achieve a steady state. Each reading was taken three times to assess reproducibility and the average of the three readings was considered the final value.

2.5. References

(1) Heras, A. N-Methylene Phosphonic Chitosan: A Novel Soluble Derivative. *Carbohydr. Polym.* **2001**, *44* (1), 1–8. https://doi.org/10.1016/S0144-8617(00)00195-8.

(2) Das, R.; Pattanayak, A. J.; Swain, S. K. Polymer Nanocomposites for Sensor Devices. In *Polymer-based Nanocomposites for Energy and Environmental Applications*; Elsevier, 2018; 205–218. https://doi.org/10.1016/B978-0-08-102262-7.00007-6.

(3) Singh, S.; Ghorai, M. K.; Kar, K. K. Fly Ash-Reinforced Epoxy Composites. In *Handbook of Fly Ash*; Elsevier, 2022; 335–356. https://doi.org/10.1016/B978-0-12-817686-3.00002-5.

(4) Barooah, M.; Mandal, B. Enhanced CO_2 Separation Performance by PVA/PEG/Silica Mixed Matrix Membrane. *J. Appl. Polym. Sci.* **2018**, *135* (28), 1–12. https://doi.org/10.1002/app.46481.

CHAPTER 3

A Strategical Improvement in the Performance of CO_2 Gas Permeation via Conjugation of L-Tyrosine onto Chitosan Membrane

This chapter discusses the CO_2 separation performance of neat chitosan (CS) and the covalently conjugated L-tyrosine (Tyr) onto CS using carbodiimide as a coupling agent membranes. Here, the amino acid, Tyr, was utilized to aid carriers into the CS matrix due to the formation of additional cross-linking points within the CS matrix, enhancing its overall structural integrity and mechanical strength. Tyr helped in boosting the CO_2 permeance and CO_2/N_2 selectivity across the membrane. This research work is scientifically acknowledged in ***"Membranes"****.*

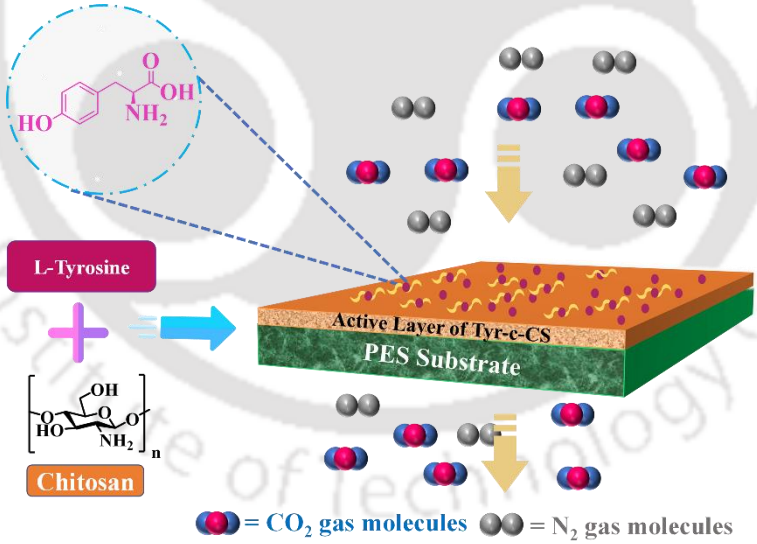

DOI: https://doi.org/10.3390/membranes13050487

3.1. Introduction

Rubbery polymeric membranes containing amine carriers have received much attention in CO_2 separation as they offer facilitated transport of CO_2 across the membrane. These membranes not only allow CO_2 to pass through more easily but also offer a simple and cost-effective method of synthesis. As a result, they have garnered significant interest in the field of CO_2 separation. In the pursuit of finding a cost-effective yet efficient polymeric material for CO_2 separation, chitosan (CS), a biodegradable polysaccharide, has emerged as a promising candidate.[1,2] and has been selected as a base material in the current research. Membranes, in general, rely on the solution-diffusion mechanism and work on the condensing ability of the various molecules. However, when it comes to the transport of carbonic acid gas across the CS membrane, it is achieved through a group of hydroxyl radicals and its high primary amine-content. As a result, it encompasses both the solution-diffusion and facilitated transport mechanism.[3]

The membrane performance efficiency is obtained by optimizing and tuning the CO_2 permeability and CO_2/N_2 selectivity, as discussed by Robeson "upper-bound".[4] Researchers have utilized several methods to minimize this "trade-off" by modifying the existing polymer, using blending,[5] crosslinking,[6] filler addition,[7,8] and thermal/chemical conjugation,[9] etc.

In this chapter of the thesis, we used a conjugation strategy to enhance the overall properties of the CS membrane. By incorporating amines into the CS matrix, we aimed to improve the efficiency of CO_2 separation. Additionally, our goal was to overcome the limitations posed by the Robeson "upper bound" trade-off observed in the neat CS membrane. L-Tyrosine (Tyr), an amino acid containing primary amine group, possesses elevated surface tension, a non-volatile nature, exceptional resistance to degradation in environment and environmentally friendly behavior. These features make Tyr a promising candidate to be

explored as a potential carrier for carbon dioxide (CO_2) capture applications. So far, the collective impact of the chitosan-tyrosine conjugate on the CO_2 separation performance has remained unexplored. The key novelty of this research study is the successful conjugation of L-tyrosine onto chitosan, which has aided CO_2-philic functional groups and improvised the amorphousness of the membrane along with other properties. This novel approach has turned the membrane into a highly promising material for better CO_2 separation from N_2, outperforming the traditional neat CS membrane. Apart from this, the influence of important operating variables such as temperature under dry and humid conditions, was analyzed for both pure CS and Tyr-c-CS membranes. Subsequently, the effects of varying moisture flow rates in sweep stream, pressures and selective layer thickness were studied for the Tyr-c-CS membrane.

3.2. Experimental Section

3.2.1. Synthesis of l-tyrosine-conjugated-chitosan (Tyr-c-CS)

Tyr-c-CS preparation method is outlined in Scheme 3.1. 500 mg CS flakes dissolved in 1 vol % of 50 mL acetic acid solution in two separate flasks and stirred at room temperature till the homogenous solution is obtained. The experiment was performed considering maximum conjugation (bond formation) by calculating the maximum amount of Tyr that can be conjugated to the free amine group of the high molecular weight CS. The average molecular weight of the CS is ~310-375 kDa which will carry an average of 1694 monomeric units or free amine groups for conjugation (considering 100% deacetylation-for maximum conjugation). Thus, by reacting 1694 mole equivalent of Tyr to CS, maximum conjugation can be achieved. So, for the reaction 485 mg Tyr were first dissolved into a certain amount of a dilute HCl acid solution and to activate the carboxyl group of amino acid, NHS (1.2 mol equivalent to Tyr) and EDC (1.2 mol equivalent to Tyr) were introduced using sonication. To one homogeneous solution of CS, activated Tyr solution and HOBt (1.2 mol equivalent to Tyr)

were added and kept for stirring at 4 °C for 30 min followed by 24 h stirring at room temperature and the other CS solution was kept aside. The dialysis of the prepared Tyr-c-CS solution was done against demineralized water in a dialysis tube (MW limit value 13 kDa) for 3 days. Both the solutions were centrifuged for 10 mins at 10,000 rpm to remove all unreacted species.

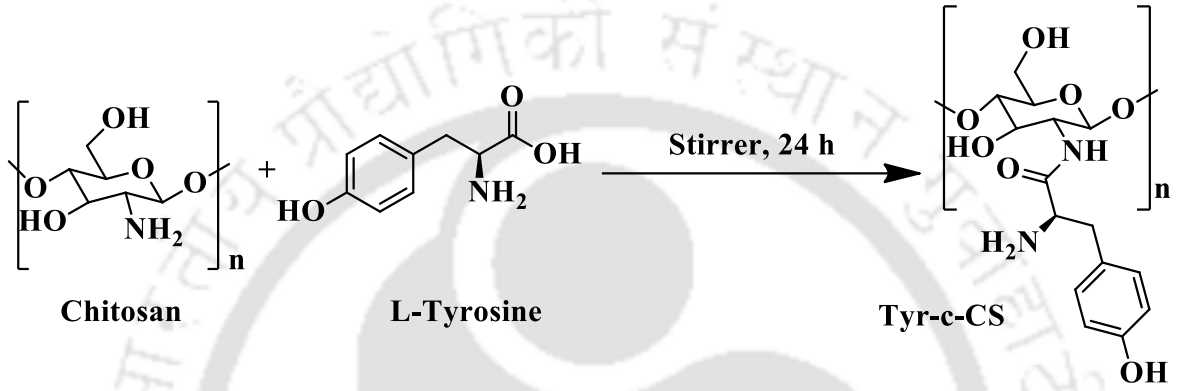

Scheme 3.1. Schematic representation of the preparation of Tyr-c-CS in the presence of EDC, NHS and HOBt.

3.2.2. Neat CS and Tyr-c-CS membrane fabrication

The solution casting method was used to cast both neat CS and Tyr-c-CS solutions as shown in scheme 3.2. Before casting, the polyethersulfone (PES) support was soaked in water for several hours to eliminate unwanted particles. Once cleaned, it was carefully attached to a glass plate. The solutions were then poured onto the PES support and a GARDCO micrometric film applicator (Paul N. Gardner, USA) was employed to spread the solution evenly. The detailed schematic representation of the process is shown in Scheme 2.1. The resulting membrane was placed in a laminar airflow for 24 hours, allowing the solvent to evaporate and form a thin, defect-free selective layer on the PES support. Subsequently, it was dried in a hot air oven, with the temperature gradually increasing from ambient to 110 °C at a heating rate of 1 °C/min and left overnight. After cooling to room temperature, the circular membrane with a

diameter of ~32 mm was cut and accommodated in the flat sheet membrane module to conduct the CO_2/N_2 gas permeation test. The detailed schematic representation of the gas permeation set-up is shown in Scheme 2.2.

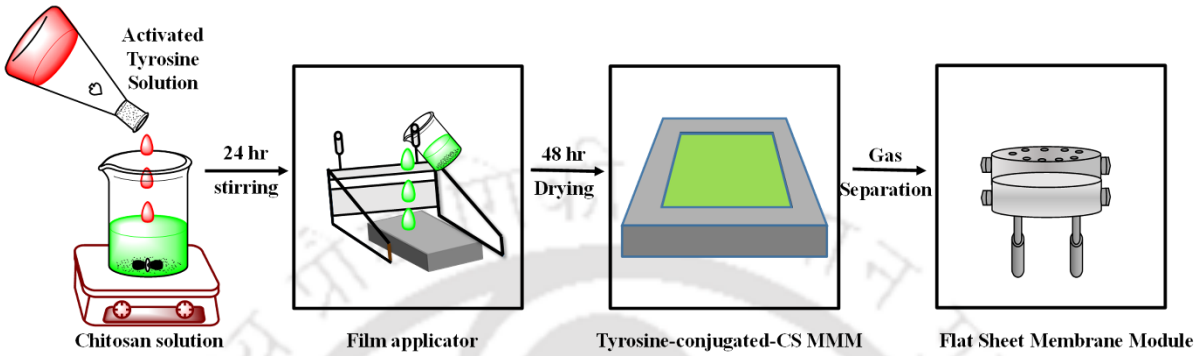

Scheme 3.2. Development of Tyr-c-CS flat sheet membrane for CO_2 separation.

3.3. Results and Discussions

3.3.1. Spectroscopic Analysis

To investigate the molecular structure changes resulting from the conjugation of CS, Fourier transmission infrared (FT-IR) spectra (Figure 3.1a) and X-ray diffraction (XRD) spectra (Figure 3.1b) were recorded and analyzed for four samples: CS powder, Tyr powder, CS film and the Tyr-c-CS film. In Figure 3.1a from 3100-3500 cm^{-1}, the CS film exhibited a medium broad peak and the Tyr-c-CS film exhibited a broad but strong peak. These peaks are assigned to hydroxyl and secondary amine stretch.[10] The increment in the intensity of O-H and N-H peaks for Tyr-c-CS partially proves the successful grafting of Tyr onto CS (Scheme 3.1).[11]

Also, in the FTIR spectrum in the C-H stretch region, the lower intensity peak shift is observed from 2887 cm^{-1} for CS film to 2951 cm^{-1} for Tyr-c-CS film, suggesting a possible interaction between CS and Tyr molecules. In the Tyr-c-CS film, the presence of Tyr was confirmed by a weak aromatic C-H peak at 1697 cm^{-1}, a medium aromatic C=C peak at 1555 cm^{-1} and N-H bends at 1613 cm^{-1}. An amide bond (C=O-N-H) peak formed due to the

interaction of CS and Tyr molecules was observed at 1646 cm^{-1} in the Tyr-c-CS film spectrum. The strong C-O stretch at 1053 cm^{-1} was observed for the Tyr-c-CS film, as was seen for both powder CS and CS film.[12] Strong N-H bending vibrations of primary amines are assigned for the peaks at 1559 cm^{-1} and 1599 cm^{-1} arising from the inherent chemical structure of CS and conjugated tyrosine. Due to -CH_2 scissoring, which occurred at 1465 cm^{-1} for CS, the band was broadened in conjugated CS. However, two new peaks were observed in the fingerprint region of the Tyr-c-CS film spectrum at 1394 cm^{-1} and 721 cm^{-1} due to phenolic OH and benzene ring, which further confirms the conjugation of Tyr with chitosan.[13,14]

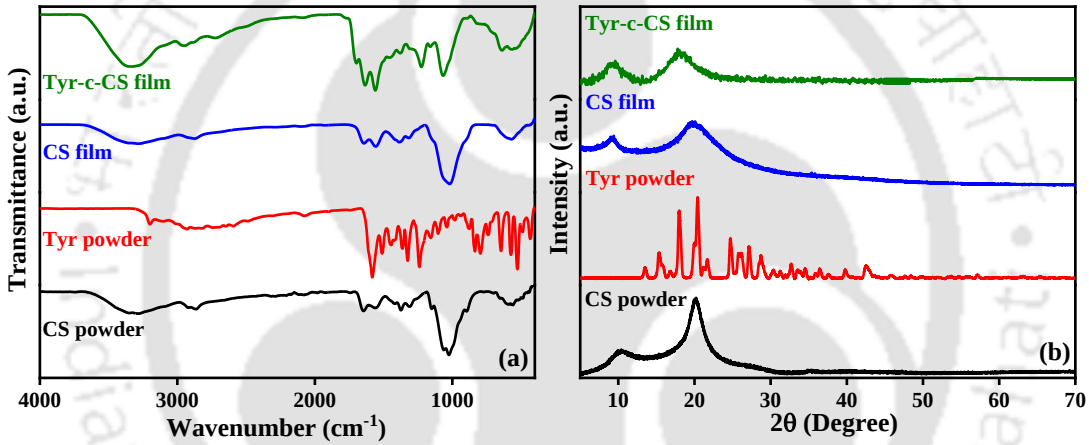

Figure 3.1. (a) FTIR and (b) XRD spectra of CS powder, Tyr powder, CS film and Tyr-c-CS film.

Material crystallinity analysis is usually performed using the XRD technique. As shown in Figure 3.1b, the XRD pattern of CS powder demonstrates a weak and a strong diffraction peak that appeared at 2θ values of 10.25° and 20.21°, respectively. The initial peak indicates the amorphous region and the second peak represents the crystalline structure. Therefore, as expressed in the reported literature, CS creates a semi-crystalline structured polymer.[15] Unlike the CS powder, the neat CS film exhibited a lower amplitude peak in the 2θ range of 10-20°. This suggests an increase in disarray in chain alignment compared to the CS powder. As perceived in Figure 3.1b, Tyr-c-CS film exhibited comparatively broader hump with low-

intensity peaks, which is an indication of a highly amorphous region due to the conjugation of Tyr.[16]

3.3.2. Thermal Stability Analysis

A thermal stability test of CS powder, Tyr powder, CS selective layer and Tyr-c-CS selective layer was performed using the thermogravimetric analyzer (TGA). Specimens 5-10 mg were heated at 10 °C/min in nitrogen flow post-evacuation in ceramic cans. The weight loss profiles for each of them are shown in Figure 3.2. As observed from the TGA spectra shown in Figure 3.2a, the temperature at the onset of thermal degradation is ~300 °C for Tyr powder and 244 °C for CS powder.[17,18] In Figure 3.2b thermal degradation trend is shown for both the prepared membranes. The CS membrane showed 8.21 % loss between 25-114 °C in the first stage due to the removal of unbound free moisture, followed by 15 % loss up to 227 °C in the second stage due to the evaporation of bound free moisture content. High temperatures may induce plastic deformation within the polymer matrix, even with a minor weight reduction of 5-8% at 100°C. Despite the seemingly small weight loss, nanoscale plastic deformation begins at this temperature, affecting the material's mechanical properties and performance. This insight into thermal behavior is crucial for designing polymers suited to specific environments and applications. In the third stage, the membrane experienced a sudden weight drop from 15% to 55% between 215-358 °C, which can be ascribed to the thermal degradation of the polymer structure. On the other hand, the Tyr-c-CS membrane represents only 5% loss up to 212 °C and later experienced a sudden weight drop of 30% up to 250 °C followed by 48% weight loss up to 410 °C in the third stage. It has been observed that the thermal stability has a trend following the order of Tyr powder > CS powder > Tyr-c-CS membrane > CS membrane. Apart from this, the weight loss is lower in the Tyr-c-CS selective layer by 8% compared to the CS selective layer. Hence, CS modified with Tyr via chemical

conjugation has shown better thermal stability, which can be ascribed as the advantage of using covalent conjugation instead of blending compared with available literature.[19] The amide bond formation upon conjugation of the two moieties resulted in the increased chemical stability of the molecule, which in turn enhanced the thermal stability. According to the TGA analysis, the fabricated Tyr-c-CS membrane is well-suitable for CO_2 separation processes.

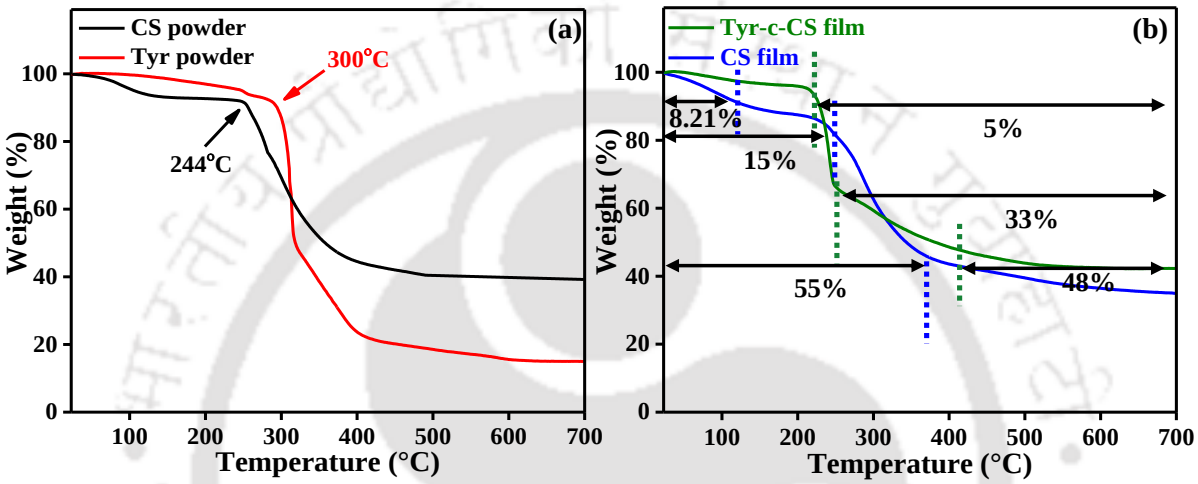

Figure 3.2. TGA profile of (a) CS powder, Tyr powder and (b) CS film, Tyr-c-CS film.

3.3.3. Morphological Analysis

The cross-sectional and surface images of the PES support, neat CS and Tyr-c-CS membranes are shown in Figure 3.3. The commercial PES support provides mechanical strength to the CS and Tyr-c-CS selective layer in the harsh environment, which is required for CO_2 separation. Moreover, the porous structure (average pore size ~30 nm) imparts resistance-free transport of gas molecules across the membrane after penetrating through a dense selective layer (Figure 3.3a). The formation of defect-free dense selective layers of CS and Tyr-c-CS onto PES support required for facilitated transport of CO_2 molecules along with solution–diffusion[20] is confirmed in Figure 3.3b and c. The cross-sectional view of the fabricated membranes (Figure 3.3d and e) clearly shows the selective layer formed with average thickness of ~600 nm and 4 μm (Figure 3.3f) on PES support. The cross-sectional view indicates no pore

filling of PES support by selective layer solution.[21] The pore filling of the support layer is undesirable as it reduces the available diffusion space and consequently, hinders the transport of gas molecules.[22]

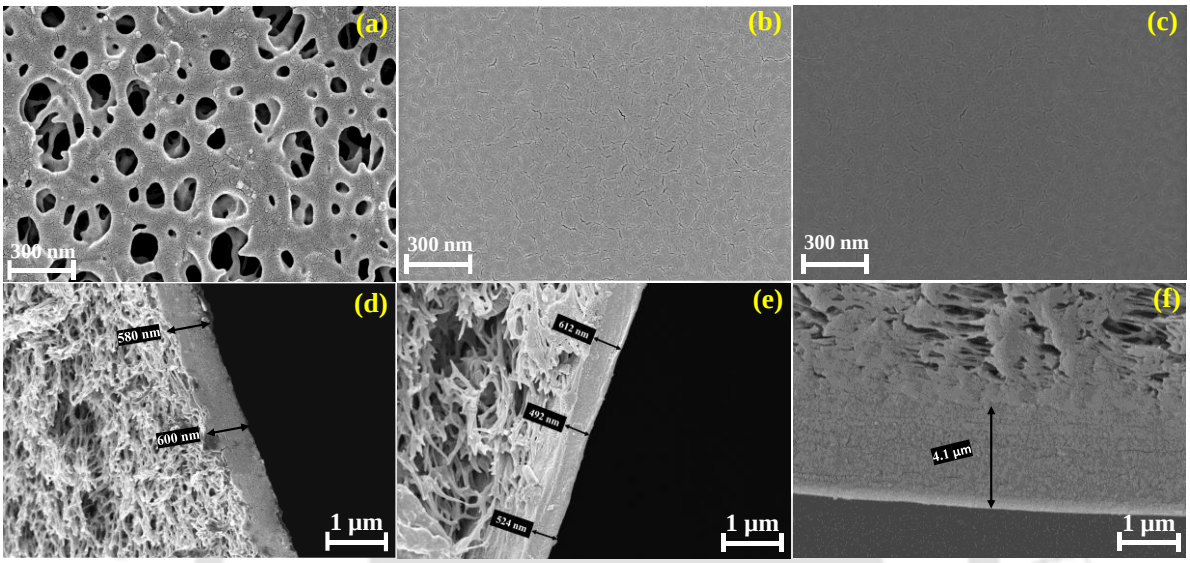

Figure 3.3. FESEM image obtained for the top section of (a) PES support, (b) neat CS, (c) Tyr-c-CS membrane and the cross surface of (d) neat CS, (e,f) Tyr-c-CS membrane, respectively.

3.3.4. Surface Roughness Analysis

A more detailed surface analysis of the CS and the Tyr-c-CS membrane was conducted using atomic force microscopy (AFM). The typical two-dimensional, three-dimensional and height profiling of the membrane images obtained from the AFM analysis is shown in Figure 3.4. The images represent distinct peak and valley regions. The average roughness of the CS membrane was 5.72 nm, whereas Tyr-c-CS was 10.22 nm. The enhanced roughness in Tyr-c-CS can be observed from heavier bumps and valleys (Figure 3.4b) which is due to the conjugation of amino acid in the polymeric chain of CS, which is crucial for CO_2 separation, as it may increase the effective area for molecular transport.[23]

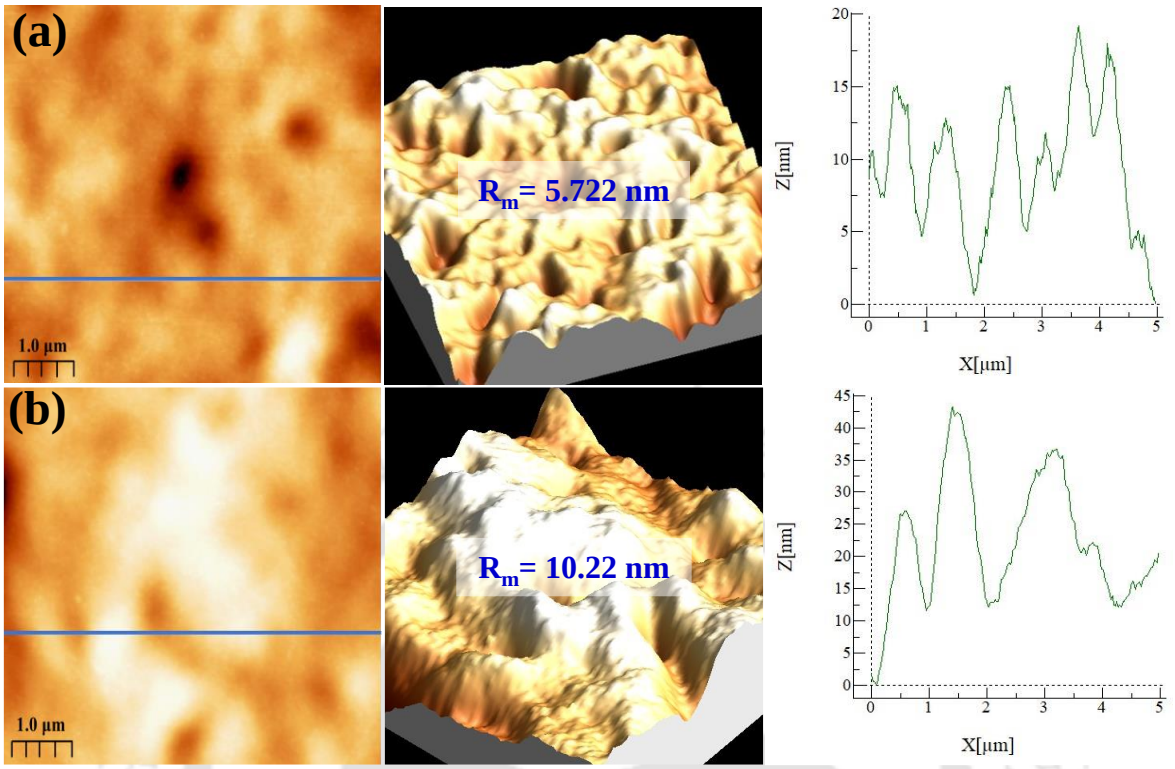

Figure 3.4. AFM images (a,b) were obtained for the top surface of the CS membrane and Tyr-c-CS membrane, respectively.

3.4. CO_2/N_2 Gas Permeation Study

Flue gas mixture (20% CO_2 and 80% N_2) is separated using a gas permeation setup design, explained in Section 2.4 and illustrated in Scheme 2.2, at different operating conditions such as temperature under dry and humid conditions, sweep side moisture flow, feed pressure, test run time and selective layer thickness etc.

3.4.1. Effect of temperature on the CO_2 separation efficiency of dry CS and Tyr-c-CS membrane

Initially, the study of the CO_2 separation performance of the neat CS membrane was performed in dry conditions (moisture flow in both feed and sweep gas streams: 0 ml/min) in the temperature range of 25 °C to 115 °C, feed pressure 32 psi and sweep pressure 17 psi as

shown in Figure 3.5a, b and compared to that of Tyr-c-CS membrane, shown in Figure 3.5c, d. As expected, the CO_2/N_2 selectivity was increased by ~4-folds, from 1.2 to 5.2 and CO_2 permeance by ~3-folds, from 7.92 GPU to 27 GPU for Tyr-c-CS membrane, when the temperature raised from room temperature to 85 °C. Whereas, neat CS membrane showed the CO_2 permeance of 16 GPU and CO_2/N_2 selectivity of 4.3 under similar operating conditions.

From equation 1.1, the gas permeability (P) is a product of the contribution of both the diffusion and sorption of the gas molecules in the membrane. At lower temperature, the sorption effect dominates due to higher affinity of CO_2 towards $-NH_2$, forming the carbamate, while the diffusion of the gas molecules is much less, resulting in low CO_2 permeance of the membrane at lower temperature. With increase in temperature (up to 85 °C), the diffusion of CO_2 through the membrane advances owing to the increase in diffusion coefficient (Fick's law) and flexibility of the membrane with temperature. This causes the enhancement in the CO_2 permeance of the membrane up to 85 °C. Beyond 85 °C, the sorption effect reduces due to the dominance of backward reaction of carbamate formation (equation 1.4-1.5), resulting in less solubility of the gas into the membrane. Due to this effect, the reduction in the solubility at higher temperature (>85 °C), there occurs a sharp decrease in the CO_2 permeance of the membrane at higher temperature.

Facilitated transport membranes use a carrier molecule to selectively transport CO_2 over N_2 by binding to CO_2 and facilitating its transport across the membrane. The effect of temperature on CO_2/N_2 selectivity may differ between facilitated transport membranes and traditional membranes that rely on gas diffusion rates.[27] In CS and Tyr-c-CS facilitated transport membranes, CO_2/N_2 selectivity increases with temperature up to a certain point. This is because the carrier molecule used in the facilitated transport mechanism can have temperature-dependent binding properties for CO_2, which can impact the overall CO_2 transport

rate. The reaction of CO_2 with amine ($-NH_2$) functional group is a reversible exothermic reaction. Thus, up to a certain temperature, the forward reaction dominates forming the carbamate, while, at higher temperature, the backward reaction predominates, resulting in the decrease in the carbamate formation.[13,24–26]

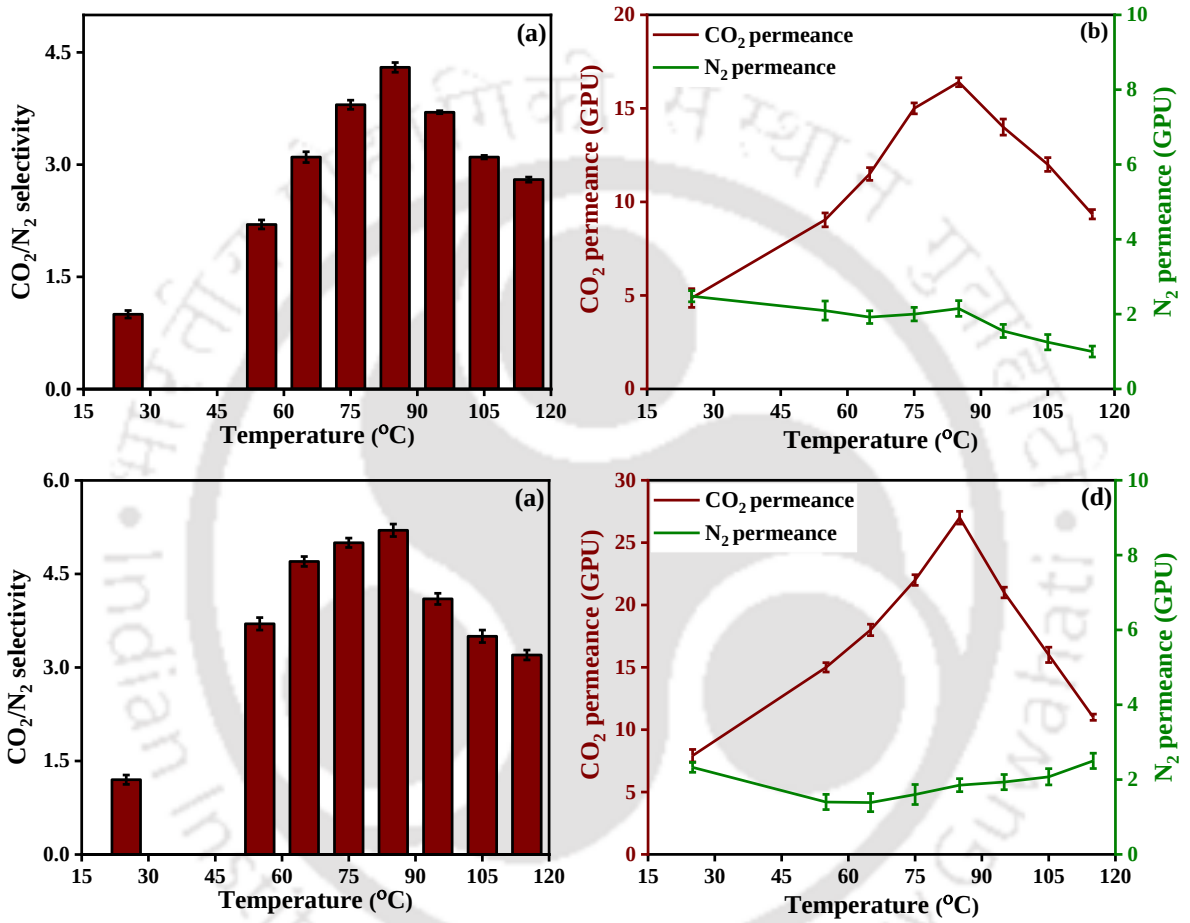

Figure 3.5. Effect temperature on (a) CO_2/N_2 selectivity and (b) CO_2, N_2 permeance of dry CS membranes; Effect temperature on (c) CO_2/N_2 selectivity and (d) CO_2, N_2 permeance of dry Tyr-c-CS membranes.

3.4.2. Effect of temperature on the CO_2 separation efficiency of swollen CS and Tyr-c-CS membrane

In practical applications, moisture in the form of water vapor is a common constituent of flue gas. The hydrophilic selective layer of CS and its composite (Tyr-c-CS) are susceptible

to swelling phenomena when exposed to this moisture. Therefore, it is essential for the membrane to maintain higher efficiency even under swollen conditions. This requirement ensures that the membrane performs effectively and consistently in real-world flue gas separation processes where moisture is present. The impact of temperature on the separation performance of CS and Tyr-c-CS membranes for CO_2 and N_2 gas mixture was examined under humid conditions. The investigation was conducted in oven, temperatures ranging from 25 °C to 115 °C and a feed absolute pressure of 32 psi. Controlled moisture flow rates of 0.03 mL/min and 0.05 mL/min were maintained in the feed and sweep gas flow streams, respectively. These conditions were optimized by previous research group.[2]

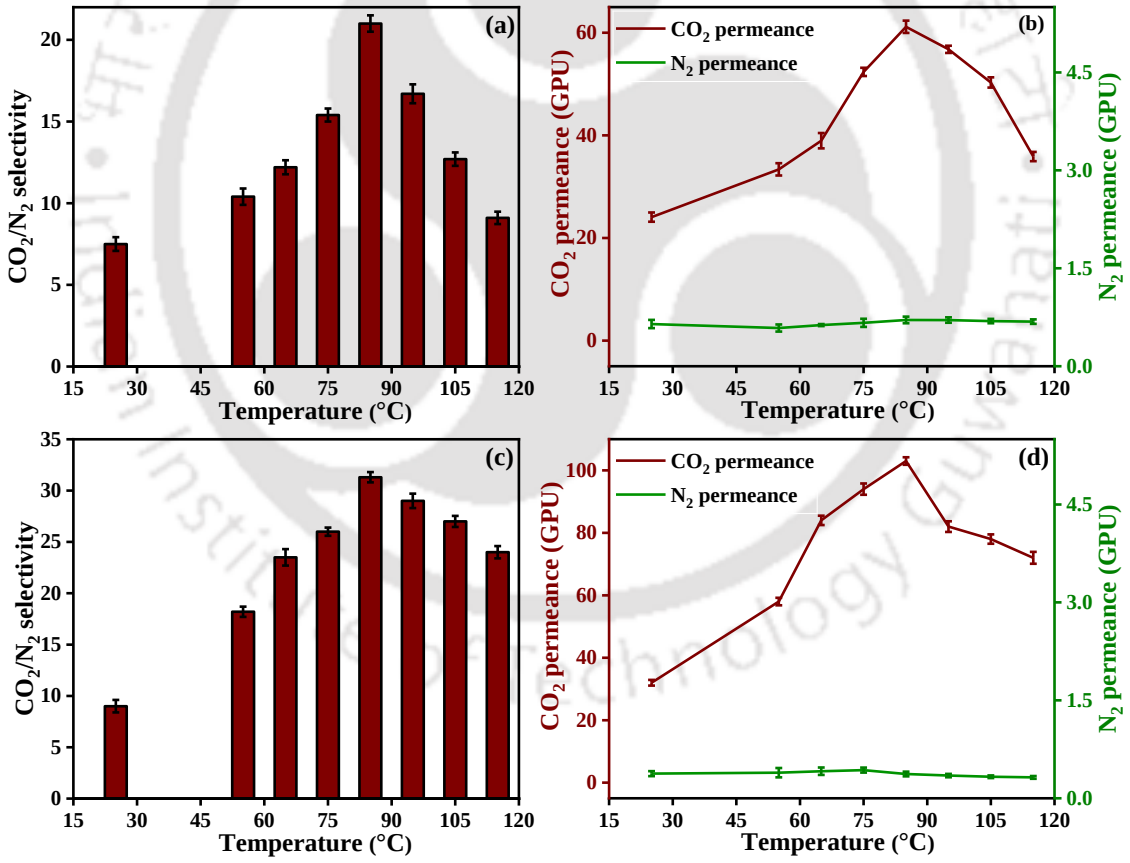

Figure 3.6. Effect temperature on (a) CO_2/N_2 selectivity and (b) CO_2, N_2 permeance of swollen CS membranes; Effect temperature on (c) CO_2/N_2 selectivity and (d) CO_2, N_2 permeance of swollen Tyr-c-CS membranes.

As depicted in Figure 3.6a and b, neat CS membrane showed the CO_2 permeance of 60 GPU

and CO_2/N_2 selectivity of 21 at 85 °C temperature. Whereas, for Tyr-c-CS membrane the CO_2 permeance increased from 32 GPU to 103 GPU and CO_2/N_2 selectivity increased from 9 to 31.3 when the temperature increased from 25 to 85 °C under swollen conditions as shown in Figure 3.6c and d.

The CO_2 in the CO_2/N_2 mixture is separated through a facilitated transport mechanism. The amine functional group-rich membrane (Lys-c-CS) interacts with more incoming CO_2 molecules in the presence of water due to the zwitterion mechanism described by Caplow in reactions 1.6-1.7. Consequently, the rate of CO_2 adsorption on the membrane is enhanced, benefiting from the 1:1 CO_2-NH_2 interaction, which represents the maximum CO_2 loading of amines in the presence of a water molecule.[24,28] Due to the reversible formation reaction of the zwitterion mechanism, the adsorbed CO_2 is desorbed. It then immediately reacts with the neighbouring -NH_2 group of the Lys-c-CS polymer and travels across the membrane through a facilitated transport mechanism involving simultaneous reversible carbamate formation. This process effectively separates CO_2 from the CO_2/N_2 gas mixture.[29]

This increase in CO_2 permeance and CO_2/N_2 selectivity can be attributed to the additional free amines provided by the conjugation of Tyr onto chitosan. These free amines actively facilitate the transport reaction and promote carbamate formation in the presence of water molecules. As for N_2 transport, similar to the trend observed in dry conditions, there was not much change with an increase in temperature. However, with further increases in temperature from 85–115 °C, the separation performances declined due to the reduction of gas molecule sorption and diffusion through the membrane, resulting from the deterioration of the moisture-holding capacity at higher temperature ranges.

3.4.3. Effect of moisture supply in sweep side stream on the CO_2 separation efficiency of swollen Tyr-c-CS membrane

The effect of moisture flow on the sweep side gas stream on the CO_2 separation performance of the membrane was studied in the range of 0-0.09 mL/min at an absolute pressure of 32 psi for feed, the temperature of 85 °C and feed side moisture of 0.03 mL/min. The conditions were chosen based on the study conducted on the chitosan/silk fibroin membrane by our previous group.[30] As shown in Figure 3.7a, b, for 0 mL/min moisture flow rate on the sweep side, CO_2 permeance and selectivity were 27.9 GPU and 5.2, respectively. At 0.05 mL/min sweep moisture flow rate, the CO_2 permeance and selectivity were amplified by ~267% and ~496% to 103 GPU and 31.3, respectively. N_2 permeance was reduced from 5.5 GPU to 4 GPU with an increase in moisture content in sweep flow from 0 to 0.05 mL/min. As observed in Figure 3.7a, b, the separation performance of the membrane improved with increasing moisture flow on the sweep side and then decreased after 0.05 mL/min. The findings suggest that water plays a beneficial role in CO_2 separation by aiding in the formation of CO_2-carrier complexes. The reaction between CO_2 and the carrier leads to the formation of bicarbonate (HCO_3^-) in the high-pressure feed region, which dissociates in the low-pressure permeate region to release CO_2 and water. The diffusivity of the HCO_3^- complex is greater than that of CO_2 alone, which improves the CO_2 flux or permeance compared to non-reacting gases, such as N_2. Water-induced swelling of the membranes increases the free volume and reduces mass transfer resistance to gas molecules. Water also acts as a plasticizing agent, inducing chain relaxation and increasing membrane flexibility. CO_2/N_2 selectivity increases with sweep water flow rate up to 0.05 mL/min, beyond which further improvement is not observed due to carrier saturation.[24,31] At 0.07 mL/min and more sweep-side moisture flow, due to excessive swelling effect mass transfer resistance to N_2, gas decreases further. As a result, the CO_2/N_2 selectivity decreased at higher sweep moisture flow and, due to carrier saturation phenomena.

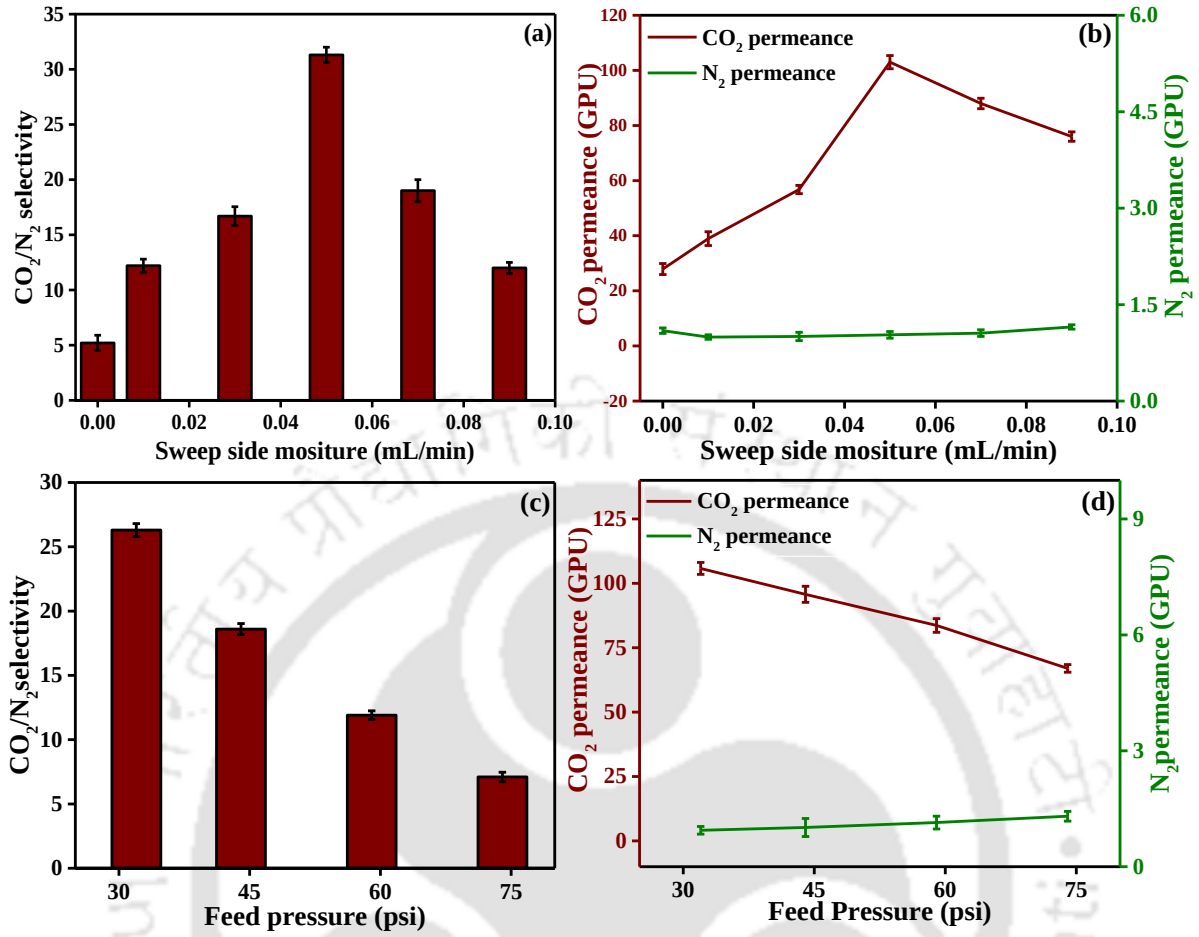

Figure 3.7. Effect of moisture flow in sweep side stream on (a) CO_2/N_2 selectivity and (b) CO_2, N_2 permeance of Tyr-c-CS membranes; Effect of Feed pressure on (c) CO_2/N_2 selectivity and (d) CO_2, N_2 permeance of Tyr-c-CS membranes.

3.4.4. Effect of feed pressure on the CO_2 separation efficiency of swollen Tyr-c-CS membrane

To investigate the effect of pressure difference across the membrane, gas permeation tests were conducted at the different feed pressures of 32 psi, 44 psi, 59 psi and 74 psi while keeping sweep side pressure constant at 17 psi at an operating temperature of 85 °C sweep moisture flow rate at 0.05 mL/min and feed moisture flow rate at 0.03 mL/min. For binary CO_2/N_2 gases, as shown in Figure 3.7c, d, CO_2 permeance and selectivity decreased from 105 GPU to 66 GPU and 31 to 7.1, respectively, when feed pressure in the membrane increased

from 32 psi to 74 psi. As known, at high pressure, the facilitated transport of CO_2 leads to the formation of complexes with amino groups. This increased formation of complexes inhibits the interaction of active sites with coming CO_2 molecules, leading to reduced CO_2 separation performances.[2] Thus, the decreased CO_2 permeance and selectivity are due to the carrier saturation phenomena that hamper the efficiency of facilitated transport of CO_2 molecules.

3.4.5. Effect of selective layer thickness on CO_2 separation efficiency of swollen Tyr-c-CS membrane

There is not a lot of information currently available in the literature about the effects of selective layer thickness effects on CO_2 permeance and CO_2/N_2 selectivity. This behaviour can be attributed to the intricate gas transport system that exists within a facilitated transport membrane, which includes both solution-diffusion and reversible reactions between amine and CO_2 molecules. The first step occurs in the bulk CO_2 transport process when CO_2 molecules are absorbed and react with amine carriers at the feed gas/membrane interface. The reaction products then diffuse across the membrane, moving towards the permeate side along their corresponding concentration gradients. Through reversible zwitterion reaction mechanism, CO_2 molecules are released into the sweep gas on the permeate side. Additionally, a lesser amount of CO_2 simultaneously passes through the membrane via the solution-diffusion mechanism as well.

The impact of varying selective layer thickness (shown in Figure 3.3e and f) on CO_2 permanence and CO_2/N_2 selectivity was investigated using neat CS and Tyr-c-CS membranes. Table 3.1 presents the separation performance obtained from different selective layer thicknesses. It was observed that a membrane with selective layer thickness of approximately 600 nm exhibited higher CO_2 permeance but lower CO_2/N_2 selectivity. Conversely, when the membrane thickness was around 4.5 μm, the CO_2/N_2 selectivity increased, although the

permeance did not meet the desired standard. The increase in CO_2 permeance with a decrease in selective layer thickness indicates that Tyr-c-CS membranes operate based on a combination of the solution-diffusion mechanism and facilitated transport.

Table 3.1. Comparison of the performance of the CO_2 separation performance of Tyr-c-CS membranes with different selective layer thickness.

	Tyr-c-CS Membrane	
Selective layer Thickness (µm)	**CO_2 Permeance (GPU)**	**S_{CO_2/N_2}**
0.5-0.6	103	31
4-4.5	44	67

3.4.6. Prolonged CO_2 separation test of Tyr-c-CS membrane

Durability under harsh prolonged conditions for separation performance is a vital necessity to be an efficient membrane. CO_2 separation performance of the fabricated Tyr-c-CS membrane was analyzed for over 150 h at 85 °C temperature, 32 psi feed pressure, 17 psi sweep pressure and feed to sweep side moisture flow ratio of 1.67. Due to the covalent link formed between the molecules of chitosan and tyrosine during conjugation, the membrane retains its CO_2 separation performance over a period of 150 h with barely any fluctuation, exhibiting the remarkable stability of the membrane performance, as shown in Figure 3.9. After the gas separation test, the Tyr-c-CS membrane was demounted from the module, dried in an oven and tested with various analytical techniques, such as FESEM, XRD, FTIR. AFM, etc. and shown in Figure 3.10. The FT-IR and XRD spectra of the Tyr-c-CS membrane (after stability test) confirmed that the crystal and electronic structure remained intact. The FESEM and AFM images inferred the constancy of the surface features. The obtained results demonstrate the stability of the membrane after passing through harsh environment provided during the

experiment. Thus, we can say that the membrane is stable and re-usable.

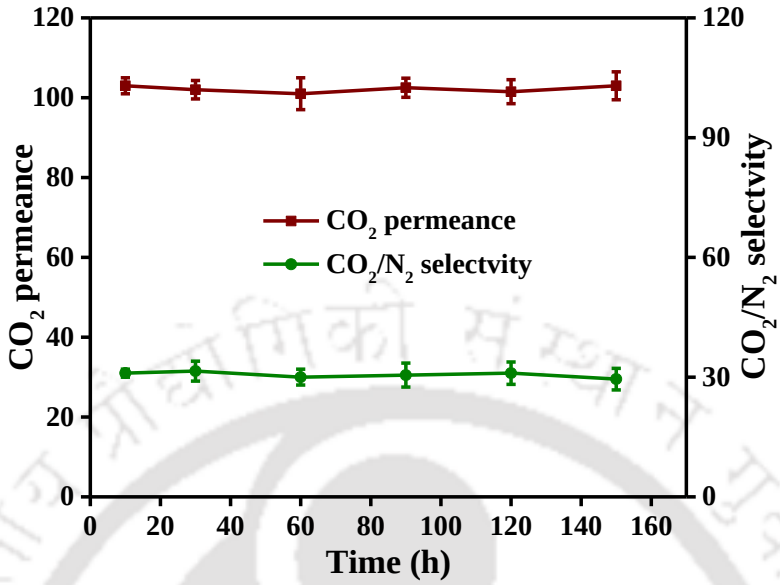

Figure 3.8. CO_2 separation performance of Tyr-c-CS membrane continuously run for 150 h at optimum operating conditions.

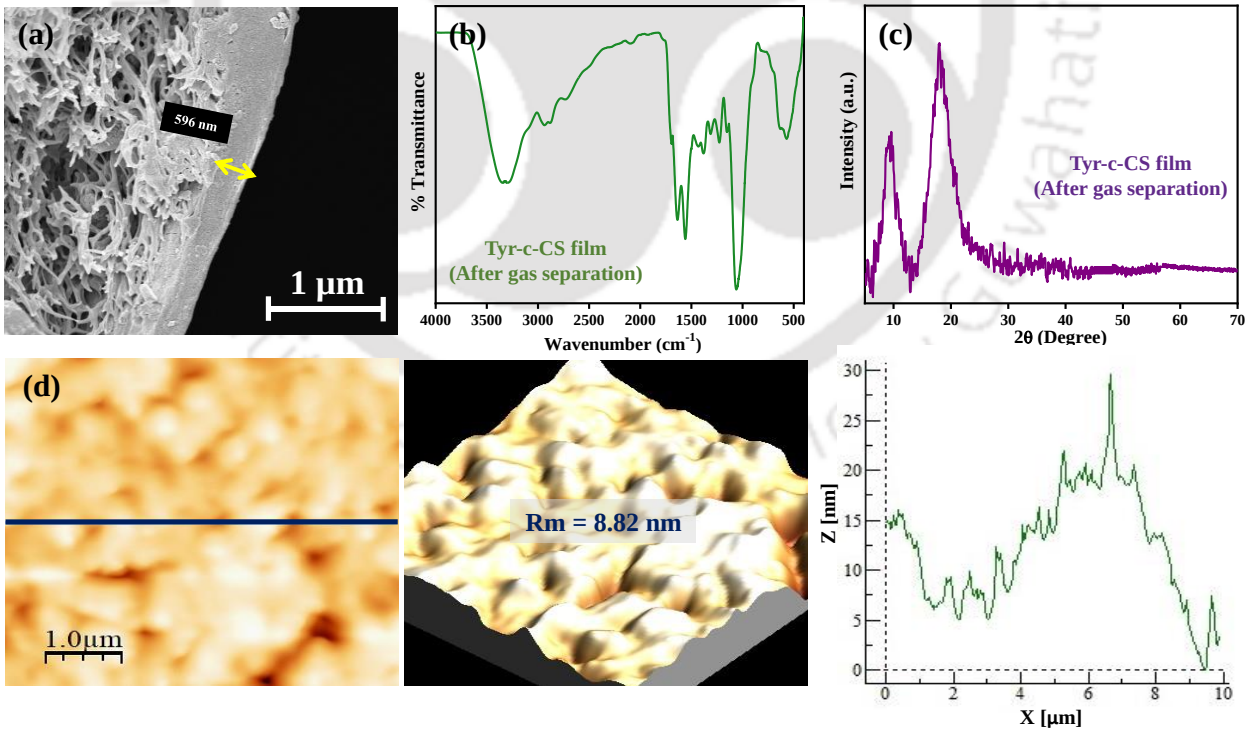

Figure 3.9. (a) FESEM image of cross section, (b) FTIR spectra, (c) XRD and (d) AFM image of top section of Tyr-c-CS membrane analysed after the gas separation experiments to

confirm the stability and reusability of the membrane.

3.4.7. Comparative study of the obtained results with the reported literature

Robeson's upper bound curve illustrates the trade-off between CO_2 permeability and CO_2/N_2 selectivity on a logarithm plot for polymeric membranes. CO_2 permeability is reported in Barrer units and can be calculated by multiplying permeance with selective layer thickness. To better understand the upgraded performance of the fabricated Tyr-c-CS membrane and to support the utilized strategy of conjugation of amino acid onto chitosan polymer, the results are meticulously compared with the well-established contemporary studies on gas separation with FTM, presented in Table 3.2. In this comparative study, the performance of the fabricated membrane is evaluated from the Robeson upper bound curve (Figure 3.11) and other available literature.[21,30,32–35] The curve clearly indicated that when compared to neat CS membrane, Tyr-c-CS membrane showed better separation performance in both dry and wet conditions. This is due to the facts that, conjugation of tyrosine onto CS matrix enhanced the available amine active sites and also increased the roughness of the membrane. A pure CS membrane has a rather smooth surface, but when Tyr is conjugated, the topology of the membrane surface is significantly changed.[36,37] Little projecting bumps with a height of 10–30 nm are created, enhancing the membrane's surface roughness and contributed in high CO_2 permeance.[38] Moreover, Tyr-c-CS is more stable membrane than other amine blended CS membranes due to the conjugation.

Table 3.2. A comparative account of the CO_2 separation performance of the optimized CS and Tyr-c-CS composite membrane with available literature.

Polymer	Carrier	T_{op} (°C), P (psi)	Thickness (µm)	CO_2 Permeance (GPU)	S_{CO_2/N_2}	Reference

CS	TEPA	90, 32	3.5	24.7	80[a]	[32]
CS	PAA	90, 32	4.5	39	260[a]	[21]
CS	SF	90, 32	3	140	103[a]	[30]
CMC	PAMAM	90, 32	2.6	100	149[a]	[1]
CS	PAMAM	40, 14	0.1	61	230[a]	[33]
PVA/PVP	PEI	25, 32	0.5	183	35[b]	[34]
PVA	SC	25, 32	25	2.16	54[c]	[35]
CS	-	85, 32	0.6	60	21[a]	This work
CS	L-Tyr	85, 32	0.6	103	31[a]	This work

Gas mixture composition-[a]: CO_2/N_2:20/80; [b]: CO_2/N_2:10/80; [c]: Pure gas mixture.

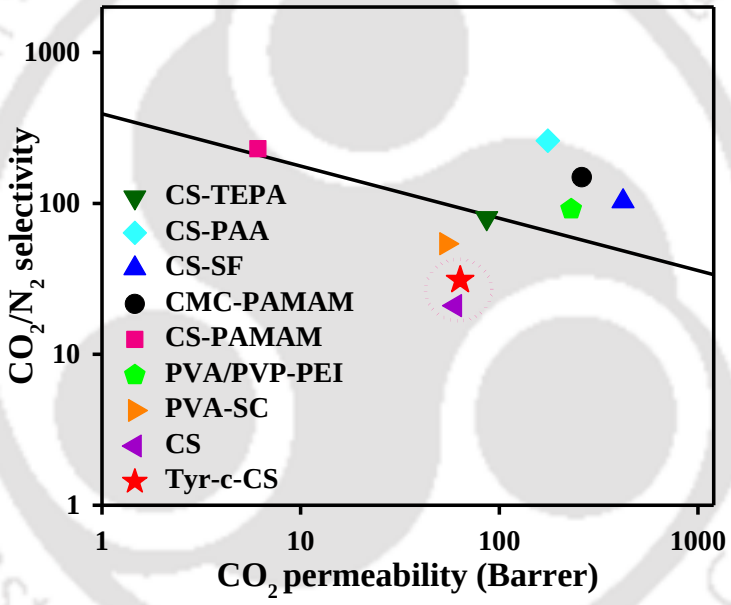

Figure 3.10. Robeson upper bound curve: Comparison of CO_2 separation performance of the synthesized CS and Tyr-c-CS membrane with the reported literature.

3.5. Conclusions

In conclusion, a high-performing Tyr-c-CS membrane was fabricated and thoroughly characterized for flue gas separation. The conjugated membrane, with an average thickness of 600 nm, exhibited remarkable CO_2 separation properties. It demonstrated a high CO_2 permeance of 103 GPU and a reasonably good CO_2/N_2 selectivity of 31 at 85 °C and 32 psi

absolute feed pressure. The successful incorporation of amino acid conjugation on polymer backbones played a crucial role in enhancing CO_2 separation performance. The amine groups from L-tyrosine facilitated CO_2 attraction while excluding N_2 through the zwitterion mechanism for carbamate formation. Moreover, the study proposed a novel method to enhance membrane performance by inducing plasticization and swelling. The results highlight the potential of this approach in designing effective membranes for CO_2 separation applications.

Although the as-synthesized membrane's overall performance has significantly improved, it still has the scope for improvisation by incorporating other amine-carriers containing molecules.

3.6. References

(1) Borgohain, R.; Mandal, B. PH Responsive Carboxymethyl Chitosan/Poly(Amidoamine) Molecular Gate Membrane for CO_2/N_2 Separation. *ACS Appl. Mater. Interfaces* **2019**, *11* (45), 42616–42628. https://doi.org/10.1021/acsami.9b15044.

(2) Prasad, B.; Mandal, B. Graphene-Incorporated Biopolymeric Mixed-Matrix Membrane for Enhanced CO_2 Separation by Regulating the Support Pore Filling. *ACS Appl. Mater. Interfaces* **2018**, *10* (33), 27810–27820. https://doi.org/10.1021/acsami.8b09377.

(3) Wijmans, J. G.; Baker, R. W. The Solution-Diffusion Model: A Review. *J. Memb. Sci.* **1995**, *107*, 1–21. https://doi.org/10.1016/0376-7388(95)00102-I

(4) Robeson, L. M. Correlation of Separation Factor versus Permeability for Polymeric Membranes. *J. Memb. Sci.* **1991**, *62* (2), 165–185. https://doi.org/10.1016/0376-7388(91)80060-J.

(5) Reijerkerk, S. R.; Wessling, M.; Nijmeijer, K. Pushing the Limits of Block Copolymer

Membranes for CO_2 Separation. *J. Memb. Sci.* **2011**, *378* (1–2), 479–484. https://doi.org/10.1016/j.memsci.2011.05.039.

(6) Mondal, A.; Barooah, M.; Mandal, B. Effect of Single and Blended Amine Carriers on CO_2 Separation from CO_2/N_2 Mixtures Using Crosslinked Thin-Film Poly(Vinyl Alcohol) Composite Membrane. *Int. J. Greenh. Gas Control* **2015**, *39*, 27–38. https://doi.org/10.1016/j.ijggc.2015.05.002.

(7) Zhang, H.; Guo, R.; Hou, J.; Wei, Z.; Li, X. Mixed-Matrix Membranes Containing Carbon Nanotubes Composite with Hydrogel for Efficient CO_2 Separation. *ACS Appl. Mater. Interfaces* **2016**, *8* (42), 29044–29051. https://doi.org/10.1021/acsami.6b09786.

(8) Borgohain, R.; Jain, N.; Prasad, B.; Mandal, B.; Su, B. Carboxymethyl Chitosan/Carbon Nanotubes Mixed Matrix Membranes for CO_2 Separation. *React. Funct. Polym.* **2019**, *143*, 104331. https://doi.org/10.1016/j.reactfunctpolym.2019.104331.

(9) Xia, J.; Liu, S.; Chung, T. S. Effect of End Groups and Grafting on the CO_2 Separation Performance of Poly(Ethylene Glycol) Based Membranes. *Macromolecules* **2011**, *44* (19), 7727–7736. https://doi.org/10.1021/ma201844y.

(10) Hu, Y.; Zhan, C.; Zhou, A.; Zhang, S.; Chen, J.; Huang, X. Synthesis and Characterization of L-Tyrosine-Conjugated Quaternary Ammonium Salt Chitosan and Their Cytocompatibility as a Potential Tissue Engineering Scaffold. *J. Biomater. Sci. Polym. Ed.* **2020**, *31* (7), 833–848. https://doi.org/10.1080/09205063.2020.1712174.

(11) Purwanto, M.; Atmaja, L.; Mohamed, M. A.; Salleh, M. T.; Jaafar, J.; Ismail, A. F.; Santoso, M.; Widiastuti, N. Biopolymer-Based Electrolyte Membranes from Chitosan Incorporated with Montmorillonite-Crosslinked GPTMS for Direct Methanol Fuel Cells. *RSC Adv.* **2016**, *6* (3), 2314–2322. https://doi.org/10.1039/C5RA22420A.

(12) Yoksan, R.; Akashi, M. Low Molecular Weight Chitosan-g-l-Phenylalanine: Preparation, Characterization and Complex Formation with DNA. *Carbohydr. Polym.* **2009**, *75* (1), 95–103. https://doi.org/10.1016/j.carbpol.2008.07.001.

(13) Takara, E. A.; Vega-Hissi, E. G.; Garro-Martinez, J. C.; Marchese, J.; Ochoa, N. A. About Endothermic Sorption of Tyrosine on Chitosan Films. *Carbohydr. Polym.* **2019**, *206*, 57–64. https://doi.org/10.1016/j.carbpol.2018.10.102.

(14) Cassano, R.; Trapani, A.; Luisa, M.; Gioia, D.; Mandracchia, D.; Pellitteri, R.; Tripodo, G.; Trombino, S.; Di, S.; Conese, M. Synthesis and Characterization of Novel Chitosan-Dopamine or Chitosan- Tyrosine Conjugates for Potential Nose-to-Brain Delivery. *Int. J. Pharm.* **2020**, *589*, 119829. https://doi.org/10.1016/j.ijpharm.2020.119829.

(15) Rai, S.; Dutta, P. K.; Mehrotra, G. K. Lignin Incorporated Antimicrobial Chitosan Film for Food Packaging Application. *J. Polym. Mater.* **2017**, *34* (1), 171–183.

(16) Liu, B.; Ye, H. bin; Liang, Q. yan; Jiang, L. liang; Chen, M. miao; Yang, S. bin. Development and Characterization of Pectin and Chitosan Films Incorporated with a New Cross-Linking Agent. *J. Sci. Food Agric.* **2022**, https://doi.org/10.1002/jsfa.12395.

(17) Mehta, R.; Kumari, R.; Das, P.; Bhowmick, A. K. Synthesis and Characterization of a Biocompatible Monotyrosine-Based Polymer and Its Interaction with DNA. *J. Mater. Chem. B* **2014**, *2* (37), 6236–6248. https://doi.org/10.1039/C4TB00854E.

(18) S. B, S.; Roy, P.; R. N. Sailaja, R.; Sengupta, C. Encapsulation And Release Characteristics Of Marigold Oleoresin In Chitosan Grafted Sodium Acrylate-Acrylate-Co-Acrylamide. *Adv. Mater. Lett.* **2016**, *7* (10), 795–801. https://doi.org/10.5185/amlett.2016.6342.

(19) Shen, J. N.; Yu, C. C.; Zeng, G. N.; van der Bruggen, B. Preparation of a Facilitated Transport Membrane Composed of Carboxymethyl Chitosan and Polyethylenimine for CO_2/N_2 Separation. *International Journal of Molecular Sciences*. **2013**, 3621–3638. https://doi.org/10.3390/ijms14023621.

(20) Prasad, B.; Thakur, R. M.; Mandal, B.; Su, B. Enhanced CO_2 Separation Membrane Prepared from Waste By-Product of Silk Fibroin. *J. Memb. Sci.* **2019**, *587*, 117170. https://doi.org/10.1016/j.memsci.2019.117170.

(21) Prasad, B.; Mandal, B. Preparation and Characterization of CO_2-Selective Facilitated Transport Membrane Composed of Chitosan and Poly(Allylamine) Blend for CO_2/N_2 Separation. *J. Ind. Eng. Chem.* **2018**, *66*, 419–429. https://doi.org/10.1016/j.jiec.2018.06.009.

(22) Liu, M.; Xie, K.; Nothling, M. D.; Gurr, P. A.; Siew, S.; Tan, L.; Fu, Q.; Webley, P. A.; Qiao, G. G.; Tan, S. S. L.; Fu, Q.; Webley, P. A.; Qiao, G. G. Ultrathin Metal-Organic Framework Nanosheets as a Gutter Layer for Flexible Composite Gas Separation Membranes. *ACS Nano* **2018**, *12* (11), 11591–11599. https://doi.org/10.1021/acsnano.8b06811.

(23) Sanaeepur, H.; Ahmadi, R.; Ebadi Amooghin, A.; Ghanbari, D. A Novel Ternary Mixed Matrix Membrane Containing Glycerol-Modified Poly(Ether-Block-Amide) (Pebax 1657)/Copper Nanoparticles for CO_2 Separation. *J. Memb. Sci.* **2019**, *573*, 234–246. https://doi.org/10.1016/j.memsci.2018.12.012.

(24) Tong, Z.; Ho, W. S. W. New Sterically Hindered Polyvinylamine Membranes for CO_2 Separation and Capture. *J. Memb. Sci.* **2017**, *543*, 202–211. https://doi.org/10.1016/j.memsci.2017.08.057.

(25) Hampe, E. M.; Rudkevich, D. M. Exploring Reversible Reactions between CO_2 and Amines. *Tetrahedron* **2003**, *59* (48), 9619–9625. https://doi.org/10.1016/j.tet.2003.09.096.

(26) Penny, D. E.; Ritter, T. J. Kinetic Study of the Reaction between Carbon Dioxide and Primary Amines. *J. Chem. Soc. Faraday Trans. 1 Phys. Chem. Condens. Phases* **1983**, *79* (9), 2103–2109. https://doi.org/10.1039/F19837902103.

(27) Li, P.; Pramoda, K. P.; Chung, T.-S. CO_2 Separation from Flue Gas Using Polyvinyl-(Room Temperature Ionic Liquid)–Room Temperature Ionic Liquid Composite Membranes. *Ind. Eng. Chem. Res.* **2011**, *50* (15), 9344–9353. https://doi.org/10.1021/ie2005884.

(28) Lv, B.; Guo, B.; Zhou, Z.; Jing, G. Mechanisms of CO_2 Capture into Monoethanolamine Solution with Different CO_2 Loading during the Absorption/Desorption Processes. *Environ. Sci. Technol.* **2015**, *49* (17), 10728–10735. https://doi.org/10.1021/acs.est.5b02356.

(29) *Energy for a Sustainable World: From the Oil Age to a Sun-Powered Future - Vincenzo Balzani, Nicola Armaroli - Google Books*.

(30) Prasad, B.; Mandal, B. Moisture Responsive and CO_2 Selective Biopolymer Membrane Containing Silk Fibroin as a Green Carrier for Facilitated Transport of CO_2. *J. Memb. Sci.* **2018**, *550*, 416–426. https://doi.org/10.1016/j.memsci.2017.12.061.

(31) Borgohain, R.; Prasad, B.; Mandal, B. Synthesis and Characterization of Water-Soluble Chitosan Membrane Blended with a Mobile Carrier for CO_2 Separation. *Sep. Purif. Technol.* **2019**, *222*, 177–187. https://doi.org/10.1016/j.seppur.2019.04.038.

(32) Prasad, B.; Mandal, B. CO_2 Separation Performance by Chitosan/Tetraethylenepentamine/Poly(Ether Sulfone) Composite Membrane. *J. Appl. Polym. Sci.* **2017**, *134* (34), 1–9. https://doi.org/10.1002/app.45206.

(33) Duan, S.; Kouketsu, T.; Kazama, S.; Yamada, K. Development of PAMAM Dendrimer Composite Membranes for CO_2 Separation. *J. Memb. Sci.* **2006**, *283* (1–2), 2–6. https://doi.org/10.1016/j.memsci.2006.06.026.

(34) Lilleby Helberg, R. M.; Dai, Z.; Ansaloni, L.; Deng, L. PVA/PVP Blend Polymer Matrix for Hosting Carriers in Facilitated Transport Membranes: Synergistic Enhancement of CO_2 Separation Performance. *Green Energy Environ.* **2019**, *5* (1), 59–68. https://doi.org/10.1016/j.gee.2019.10.001.

(35) Kim, S. J. Gas Permeation through Water-Swollen Sericin / PVA Membranes. **2007**, Doctoral thesis, University of Waterloo, Ontario, Canada.

(36) Yoshida, W.; Cohen, Y. Topological AFM Characterization of Graft Polymerized Silica Membranes. *J. Memb. Sci.* **2003**, *215* (1–2), 249–264. https://doi.org/10.1016/S0376-7388(03)00019-X.

(37) Fernández, L.; Sánchez, M.; Carmona, F. J.; Palacio, L.; Calvo, J. I.; Hernández, A.; Prádanos, P. Analysis of the Grafting Process of PVP on a Silicon Surface by AFM and Contact Angle. *Langmuir* **2011**, *27* (18), 11636–11649. https://doi.org/10.1021/la201683p.

(38) Dong, G.; Zhang, J.; Wang, Z.; Wang, J.; Zhao, P.; Cao, X.; Zhang, Y. Interfacial Property Modulation of PIM-1 through Polydopamine-Derived Submicrospheres for Enhanced CO_2/N_2 Separation Performance. *ACS Appl. Mater. Interfaces* **2019**, *11* (21), 19613–19622. https://doi.org/10.1021/acsami.9b02281.

CHAPTER 4

An Investigation on the Effects of Both Amine Grafting and Blending with Biodegradable Chitosan Membrane for Enhanced CO_2 separation

In this chapter of the thesis, comparison of the effects of two approaches: amine blending and grafting with polymer matrix and their contribution to gas separation (GS) performance is presented. A facilitated transport-cum-solution diffusion-based chitosan membranes were prepared by using 2-Amino-3-phenylpropanoic acid, also called phenylalanine and the solution casting method was used to fabricate grafted and blended membranes on PES support. All the fabricated membranes were utilized for CO_2 separation (GS) application. This work is scientifically acknowledged in ***"Chemical Engineering Journal"****.*

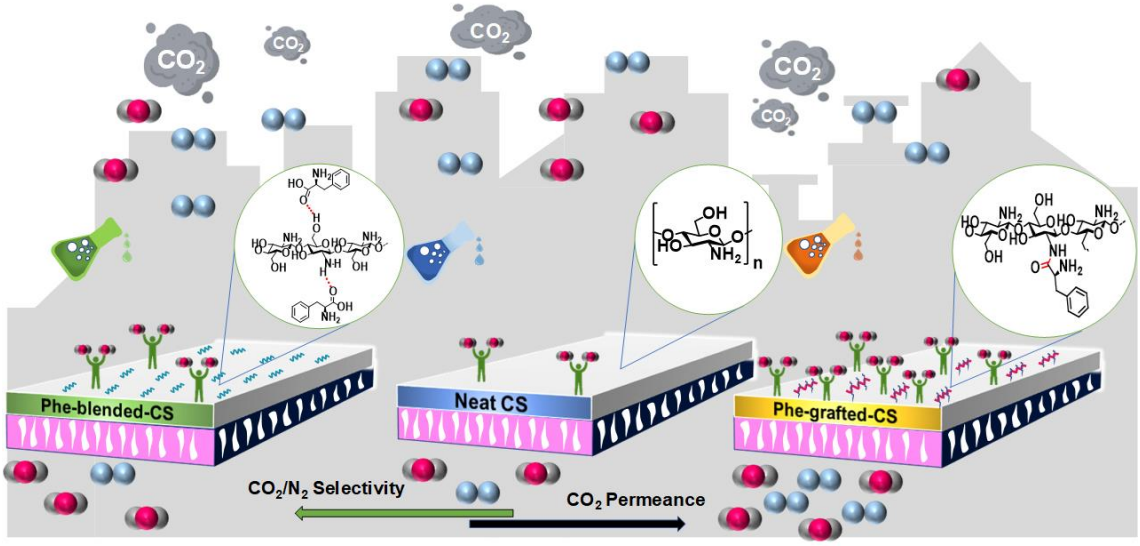

DOI: https://doi.org/10.1016/j.cej.2023.143215

4.1. Introduction

In this chapter, we address the limitations of earlier fabricated neat CS and Tyr-c-CS polymeric membranes, which exhibit subpar performances, specifically the trade-off between selectivity and permeability as described by Robeson's upper bound. To overcome these limitations, we explored the use of Phenylalanine (Phe) amino acid as an alternative to Tyr. Phenylalanine, being easily soluble in water (not requiring the use of strong acid (HCl) solutions as needed for dissolving tyrosine), consequently its better compatibility with CS, piqued our interest for its potential utilization in aiding the carrier in the CS backbone.[1–3] Also, the absence of the phenolic -OH in phenylalanine resulted in more basicity in the composite membranes thereby facilitating better interaction of the acidic CO_2 with the membrane polymer. Both mobile and fixed carriers within the facilitated transport process demonstrate superior CO_2 separation capabilities. However, mobile carriers suffer from reduced stability over time due to a leach out problem, whereas fixed carriers are more stable. [4–6]

To address these challenges, the current study concentrates on increasing the gas permeance of the chitosan-based membranes because CS has naturally low gas permeance. Two approaches grafting and blending, have been researched in which a low molecular weight sacrificial component was added into the CS, as shown in Scheme 4.1. The 2-Amino-3-phenylpropanoic acid (Phe) short-chain (MN = 165.19 Da) was grafted onto the CS backbone using a "chemical grafting" technique in the presence of 1-ethyl-3-(3-dimethylamino-propyl) carbodiimide (EDC) and N-hydroxy-succinimide (NHS).[8] As an alternative, the Phe amino acid was also blended with the CS with 10-40 wt% amount to investigate the effects of both strategies.

4.2. Experimental Section

4.2.1. Amino-3-phenylpropanoic acid-*blended*-Chitosan (Phe-*b*-CS) solution preparation

The weight% of the Phe to be blended into CS matrix was decided based on the previous literature where amine-containing low molecular weight components were introduced into the CS polymer matrix for the preparation of thin film composite membranes.[9,10] 1 wt% CS was added to 100 ml of 1 vol% acetic acid (AA) solution first, followed by the addition of calculated amounts of Phe into the solution. The prepared solution is continuously stirred for 24 h to attain desired bonding and homogeneity. Finally, the blended solutions were centrifuged to remove bubbles and non-interacted material before being cast onto the polyethersulfone (PES) support. The selective layer solutions have four different weight ratios of blends of CS and Phe, such as 90 wt% CS + 10 wt% Phe [Phe-*b*-CS (10)], 80 wt% CS + 20 wt% Phe [Phe-*b*-CS (20)], 70 wt% CS + 30 wt% Phe [Phe-*b*-CS (30)] and 60 wt% CS + 40 wt% Phe [Phe-*b*-CS (40)] were prepared successfully. The basic chemical reaction undergoing during the blending procedure has been demonstrated in Scheme 4.1a.

4.2.2. 2-Amino-3-phenylpropanoic acid-*grafted*-Chitosan (Phe-*g*-CS) solution preparation

The grafting reaction of Phe onto CS was conducted under normal conditions, i.e., water-based system and room temperature, using carbodiimide (EDC) as a coupling agent and NHS as a catalyst.[11] The experiment was performed considering analysis discussed in section 3.2.1. Thus, for the reaction, 6.26 moles of Phe were first dissolved into a certain amount of 1 vol% AA solution and then 1.5 mol equivalent of EDC was added to activate the carboxyl groups of the Phe, followed by a 1.5 mol equivalent addition of NHS to get a stable ester. The activation reaction was carried out at a constant temperature of 4 °C for 30 mins. The step-by-step chemical reactions undergoing during the grafting procedure has been demonstrated in

Scheme 4.1b. Separately, the CS solution was prepared as mentioned in Section 3.2.2 The activated Phe solution was then slowly added to the CS solution and kept stirring at room temperature for 36 h. The as prepared Phe-*g*-CS solution was dialyzed against millipore water for three days to remove the catalyst and unreacted impurities.

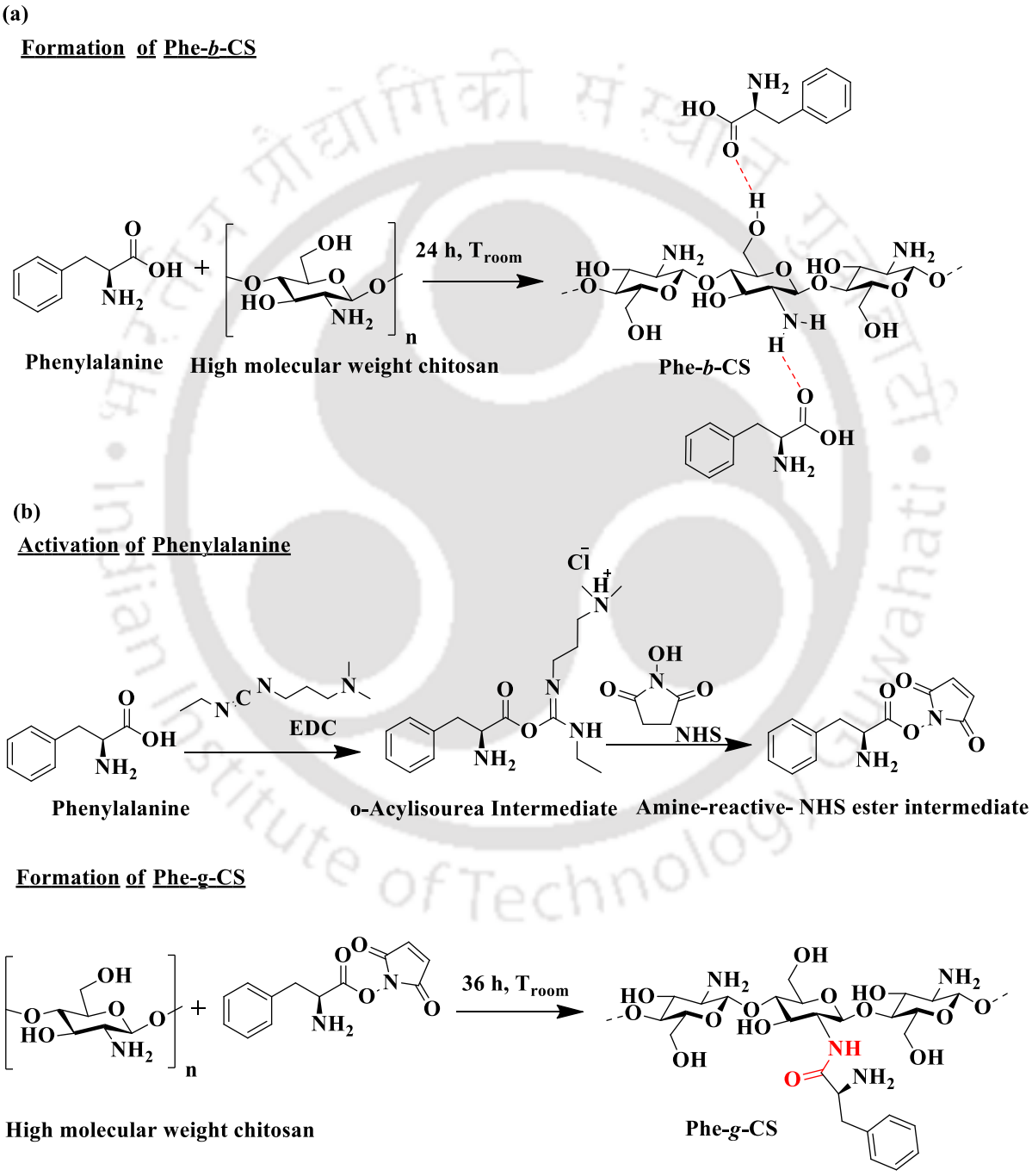

Scheme 4.1. (a) Synthesis of Phe-*b*-CS and (b) Phe-*g*-CS

4.2.3 Membrane fabrication

Before casting the as-prepared solutions, the PES support was immersed in water for several hours to remove any unwanted particles. Subsequently, it was delicately pasted onto a cleaned glass plate. Using a casting knife, all the prepared solutions were then cast onto the porous support. In order to comprehend the impact of blending and grafting on the enhancement of CO_2 separation performance, we also casted a neat CS membrane with a similar thickness. All the membranes were dried in a laminar hood chamber for 24 hours, followed by overnight drying in a hot air oven at 110 °C. Finally, the membranes were kept in a desiccator for further characterization and gas separation studies.

4.3. Results and Discussions

4.3.1. Electronic State Characterization

The electronic structure of the constituent elements of the fabricated membranes was determined using the X-ray photoelectron spectroscopy (XPS) technique. Figure 4.1a show the survey spectra of the three materials confirming the presence of all three elements: carbon, oxygen and nitrogen. To get an insight into the electronic structures of the respective materials, XPS was performed to obtain the core level spectra of C1s, N1s and O1s for bare, blended and grafted chitosan. Figure 4.1b shows the C1s core-level spectra, deconvoluted into three individual spectra. For bare CS, three peaks were obtained at binding energy (B.E.) of 284.82, 286.45 and 288.11 eV corresponding to the C-C/C-H, C-N/C-O and C=O bonds in the chitosan backbone.[12] For Phe-*b*-CS (20), the corresponding peaks appear at 284.88, 286.38 and 288 eV, while for Phe-*g*-CS, the corresponding peaks appear at 284.81, 286.40 and 288.14 eV. The negligible shift in C-C/C-H peaks for both confirms the integrity of the CS backbone. The shift in the C-N peak is due to the formed interaction between the CS and Phenylalanine (Phe). The

red shift of ~0.1 eV in the C=O peak for Phe-*b*-CS (20) is due to the formation of an H-bond between the carbonyl group of Phe and the amine group of CS, resulting in the increase in electron density around carbonyl C of the Phe molecule. But the negligible shift in the C=O peak for grafted-CS compared to bare CS is due to the formation of an amide bond between Phe and CS. Figure 4.1c shows the N1s core-level spectra deconvoluted into two major peaks for the 2°-N atom (-NH-) and 1°-N atom ($-NH_2$). For bare CS, the peaks were obtained at 399.57 and 401.67 eV, for Phe-*b*-CS (20) at 399.46 and 401.12 eV and for Phe-*g*-CS at 399.75 and 401.57 eV, corresponding to the respective peaks. Due to only the formation of the H-bond between the carbonyl of Phe and amine of CS for Phe-*b*-CS (20), there is a negligible shift in peaks for 2°-N, confirming the integrity of the CS backbone. But in the Phe-*g*-CS, there is the formation of amide bonds between CS and Phe, resulting in a shift in the 2°-N peak position. But in the case of $-NH_2$ peak for Phe-*b*-CS (20), there is a decrease in BE of ~0.5eV due to the formation of H-bond between the NH_2 group of CS and carbonyl group of Phe resulting in an increase in electron density around the N-atom. Finally, in Figure 4.1d, the O1s core-level spectra are deconvoluted into three peaks corresponding to C=O, C-O and surface-adsorbed H_2O molecules. For bare CS, the respective peaks were obtained at 531.42, 532.55 and 533.28 eV; for blended-CS at 531.82, 532.73 and 533.48 eV and Phe-*g*-CS at 531.49, 532.57 and 533.36 eV, respectively. The blue shift of the C=O peak for Phe-*b*-CS (20) compared to bare CS is due to the formation of an H-bond between the carbonyl of Phe and amine of CS, resulting in a decrease in the electron density of the carbonyl O atom. Similarly, due to the H-bond formation between the carbonyl of Phe and hydroxyl of CS, there is a decrease in BE of C-O for blended-CS. The C=O and C-O peaks for grafted-CS showed negligible shifts confirming the formation of an amide bond between CS and Phe.

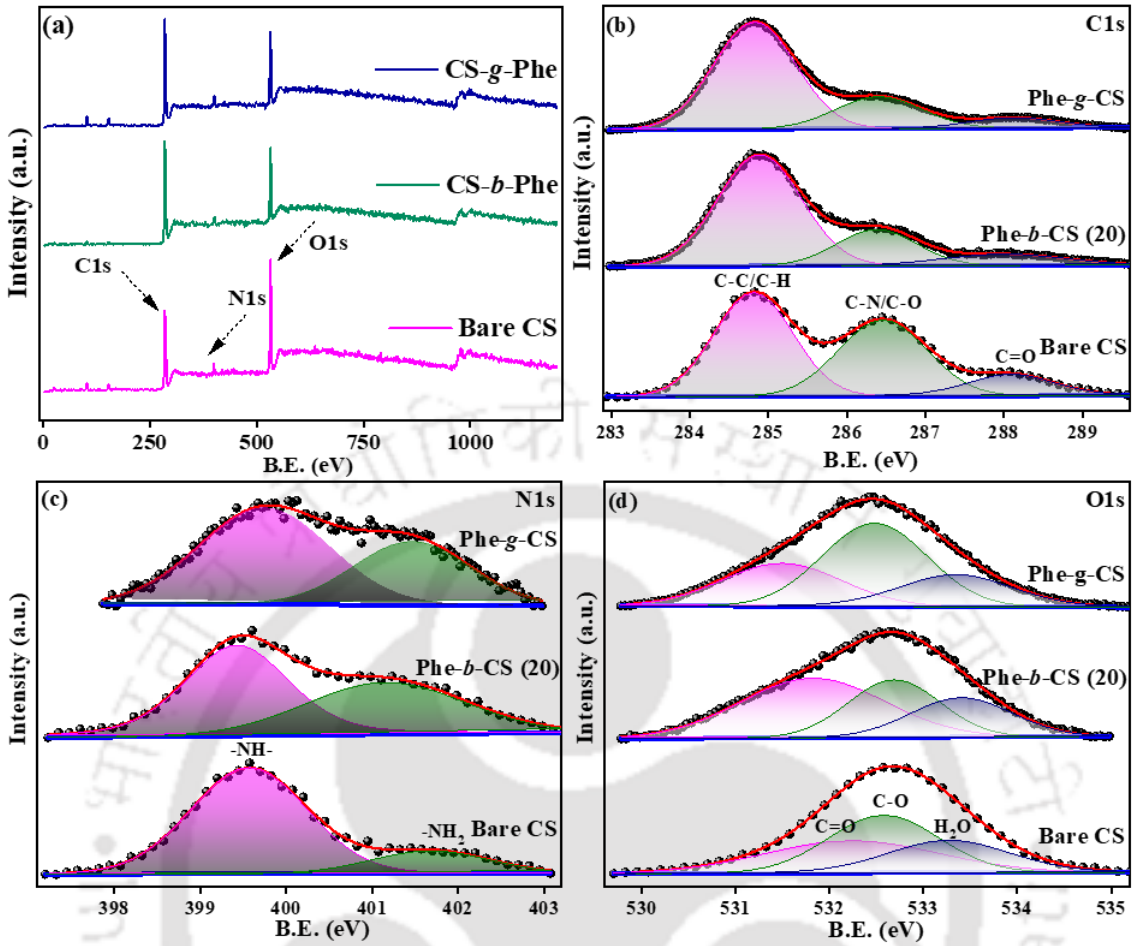

Figure 4.1. (a) Survey spectra of C1s, N1s and O1s (b) High resolution spectra of C1s, (c) High resolution spectra of N1s, (d) High resolution spectra of O1s of all three: bare CS, Phe-*g*-CS and Phe-*b*-CS (20) membranes.

4.3.2. ^{1}H-Nuclear Magnetic Resonance Spectroscopy Analysis

Proton (^{1}H) nuclear magnetic resonance (^{1}H NMR) spectroscopy technique was used to validate the successful bond formation between the Phe and CS molecules upon grafting. ^{1}H NMR was recorded for Phe, CS and Phe-*g*-CS using a 600 MHz spectrometer by dissolving all three samples in 1% DCl/D_2O solvent at 25 °C, as shown in Figure 4.2. Addressing Phe-*g*-CS, the proton-containing N-acetyl glucosamine units of CS were responsible for the solitary peak at 2.08 ppm.[13] The protons on the glycan ring of CS are responsible for the single peak at 2.89 ppm and several peaks at approximately 3.30-3.60 ppm. The successful grafting of Phe

onto CS can be confirmed with the presence of benzene ring (5H, C_6H_5) peaks observed at δ (ppm): 7.37,7.37, 7.34, 7.34, 7.33, 7.33 in ^{1}H MNR spectra of Phe shift to: 7.83,7.83, 7.57,7.57, 7.56, 7.56 in ^{1}H NMR of Phe-*g*-CS.[11] Meanwhile, a secondary amine bond peak that arises during amide bond formation between CS and Phe is also observed at δ (ppm): 7.33 in Phe-*g*-CS.

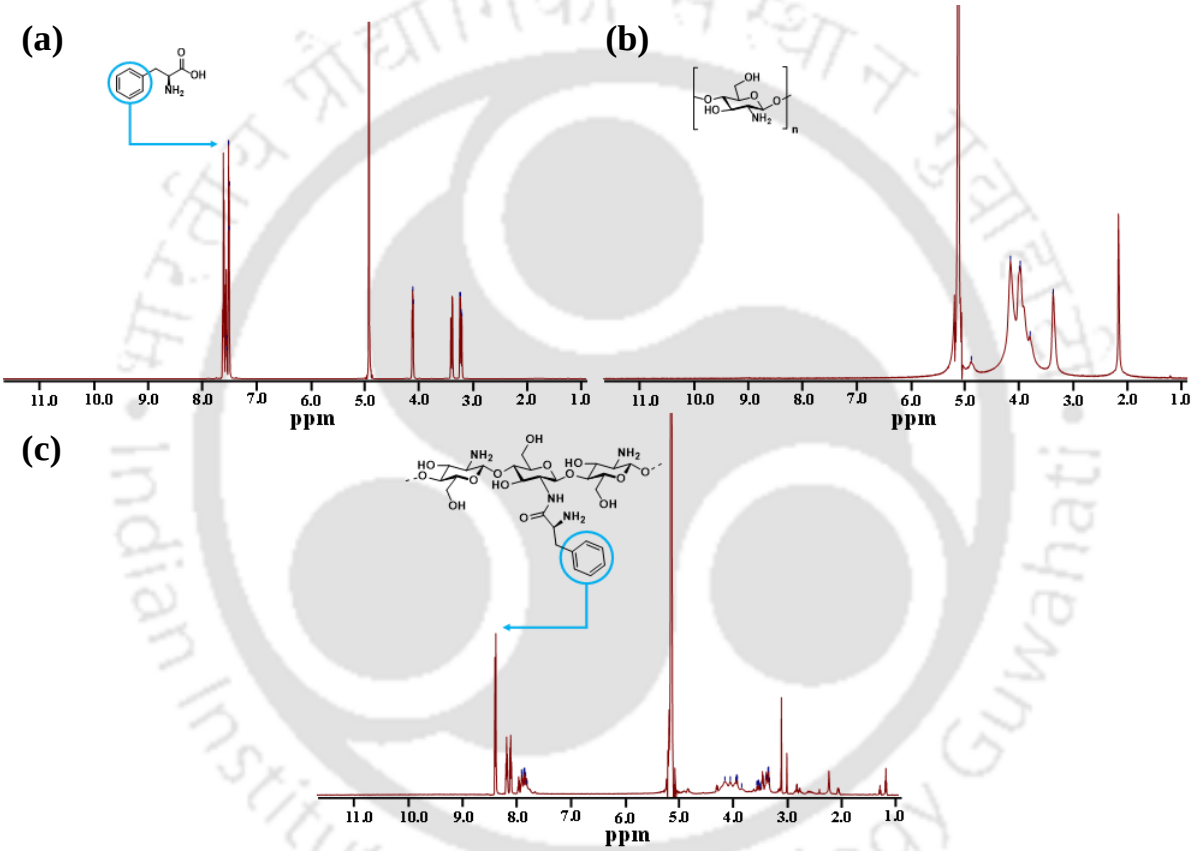

Figure 4.2. NMR spectra of (a) Phe (b) CS and (c) Phe-*g*-CS

4.3.3. Structural and Thermal Stability Analysis

To identify the chemical bonds, functional groups and to confirm the successful interaction between the Phe and CS molecules upon blending and grafting, Fourier transform infrared (FTIR) spectroscopy technique was employed. The FTIR spectra of pure Phe, CS membrane and fabricated composite membranes are shown in Figure 4.3a. For CS membrane,

the absorption band in the range of 3400-3100 cm^{-1} is assigned to the N-H and O-H stretching vibration. The appearance of peaks in the range of 2936-2881 cm^{-1} are ascribed to the symmetric stretching vibration of $–CH_3$ and asymmetric stretching vibration of $–CH_2$, respectively. The peaks at 1647 cm^{-1} and 1554 cm^{-1} has been assigned to the C=O stretching and N-H bending vibration. Upon blending CS with phenylalanine, a significant variation in the peaks was observed. A new peak at 2122 cm^{-1} has appeared, the characteristic peak of L-amino acid, signifying the presence of phenylalanine.[14] The FTIR analysis of the CS-Phe blends also revealed notable shifts in the primary amine peaks around 1563 cm^{-1}, along with changes in peak intensities for OH and N-H stretching vibrations (3400-3100 cm^{-1}). These alterations signify the formation of hydrogen bonds between CS and Phe within the blend. Additionally, the new peaks at 1416 cm^{-1} and between 745-600 cm^{-1} are attributed to the aromatic C=C stretching and aromatic C-H bending vibration of phenylalanine. The intensity of the peaks has increased with increasing the percentage of blending from 10% to 40%. The FTIR spectra of phenylalanine grafted chitosan is also displayed in Figure 4.3a, showing the characteristic peaks of chitosan and phenylalanine along with the appearance of distinct new peaks, which attributed to the formation of new covalent bonds between chitosan and phenylalanine. The new peak at 1704 cm^{-1} is due to the ester bond. The increase in the peak intensity at 1554 cm^{-1} can be assigned to amide II, confirming the formation of a new amide bond between the carboxyl group of phenylalanine and the amino group of chitosan.[11]

To investigate the crystallinity, phase behavior and crystal structure of all the materials powder X-ray diffractometer (XRD) technique was utilized. The powder XRD pattern of chitosan displayed in Figure 4.3b shows two diffraction peaks $2\theta = 9.75°$ and 20.21°, which are attributed to the amorphous and crystalline nature of chitosan, respectively. The powder XRD pattern of phenylalanine demonstrated in Figure 4.3b displays diffraction peaks at 5.85°,

17.02°, 22.91°, 28.65° and 34.5° which matches with the earlier reported data of the anhydrous phase.[11,15] The Phe-*b*-CS membranes show peaks at 6.74°, 15.18° and 20.80°, whose intensity increases upon increasing the blending percentage.[16–18] The new observed peaks correspond to the monohydrate phase of the phenylalanine.[19,20] The phase change of Phe from anhydrous to monohydrate form confirms the successful blending, i.e., the formation of H-bonds between the Phe and CS molecules, as shown in Scheme 4.1. The Phe-*g*-CS shows peaks at 5.73°, 16.95°, 17.83°, 22.75°, 25.48° and 34.32° corresponding to the anhydrous form of the phenylalanine.[21,22] The presence of the peaks verifies the presence of Phe in the CS polymer. Both, the grafted and blended membranes show the broad peak of amorphous chitosan, ascertaining the polymeric structure of the CS molecule.[23]

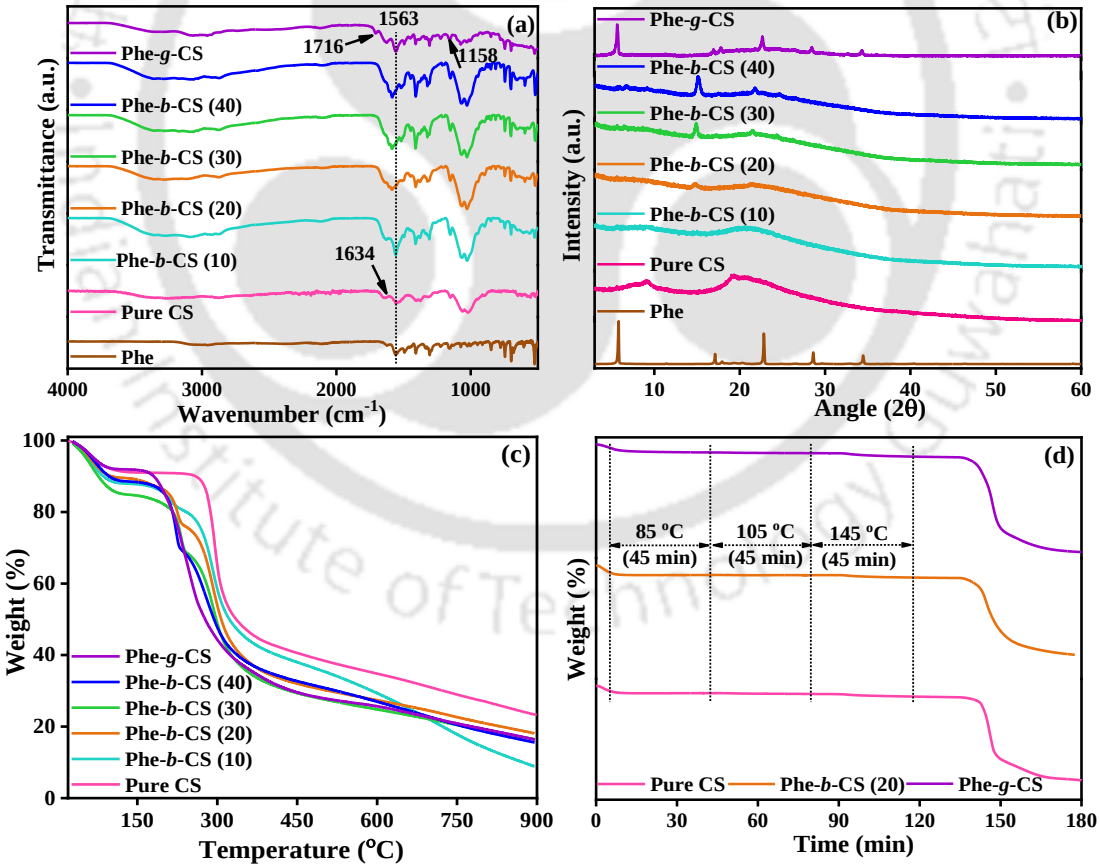

Figure 4.3. (a) FTIR spectra and (b) XRD spectra of Phe and all the fabricated composite membranes, (c) Dynamic TGA study of all the fabricated membranes, and (d) TGA isotherm

of neat CS, Phe-*g*-CS and Phe-*b*-CS (20) membranes.

Thermogravimetric analysis (TGA) accessed to study thermal degradation and stability of the pure CS, Phe-*g*-CS and Phe-*b*-CS membranes is shown in Figure 4.3c. The TGA profile of neat chitosan shows three consecutive weight loss steps. The first weight loss of about 6% occurs between 30-150 °C due to moisture loss. The second weight loss of about 40% occurs from 260 °C due to the scission of the ether linkage. The third weight loss of about 26 % occurs from 338 °C due to the degradation of glucosamine residue. While in the profile of Phe-*g*-CS, shown in Figure 4.3c, the second weight loss starts earlier at about 154 °C. The early weight loss might be due to the formation of a new covalent bond between the polymer and the amino acid, which blocks the chitosan's free amino group, leading to a decrease in the intermolecular polymeric chain interaction.[24,25] The residue percentage of the conjugate has also been reduced compared to the pristine polymer, indicating a decrease in the conjugated compound's thermal stability. The TGA profile of the blended membranes shows three consecutive weight losses, with the second and third weight losses starting much earlier than chitosan.[13] A minor decrease in the degradation temperature was observed with increasing phenylalanine percentage. The decrease in the thermal stability might be due to the decrease in the intermolecular chain attraction occurring due to the formation of hydrogen bonds between the amino group of chitosan and the hydroxyl group of phenylalanine.

TGA isotherm tests on the pure CS, Phe-*g*-CS and Phe-*b*-CS (20) membranes demonstrated their thermal stability at the experimental temperature range. When the membrane was held at 85 °C for 30 minutes, a loss of 2.01 % was observed, as shown in Figure 4.3d. This minute loss was caused by eliminating moisture from the membrane matrix. Further, when the membrane was heated for 30 minutes at 105 °C and 145 °C, respectively, another 1.2 % and 0.95 % loss was noticed. The slight losses to 145 °C may have resulted from the total

moisture removed from the membrane.[26] Later, the melting of Phe in the selective layer was the cause of the weight loss. Therefore, it is possible to ensure the membrane is stable under the experimental operating conditions.

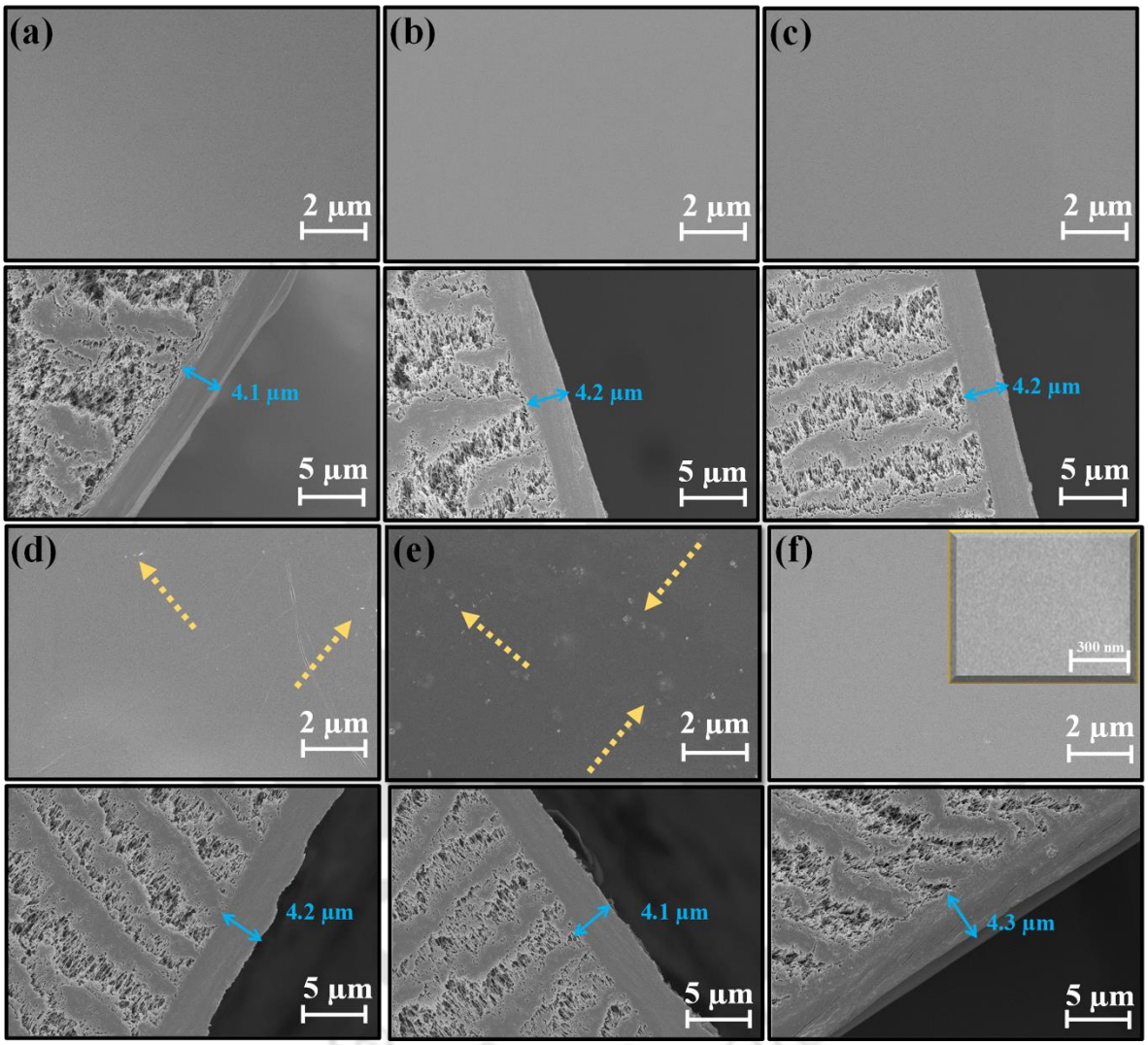

Figure 4.4. FESEM images of cross section and top surface of (a) Pure CS, (b) Phe-*b*-CS (10), (c) Phe-*b*-CS (20), (d) Phe-*b*-CS (30), (e) Phe-*b*-CS (40) and (f) Phe-*g*-CS membranes.

4.3.4. Morphological Analysis

To visualize the surface texture and to elucidate the actual thickness of the fabricated membranes, field emission scanning electron microscopy (FESEM) technique was employed. As perceived in the FESEM images in Figure 4.4, the top surfaces of Phe-*b*-CS (10 & 20) and

Phe-*g*-CS, when compared to that of pure CS, have similar smooth-homogeneous surfaces, suggesting proper interaction of Phe with the CS matrix. The magnified image of Phe-*g*-CS shows the defect-free selective layer is made-up of Phe-*g*-CS. Phe gets aggregated on the membrane surface when its content in the CS matrix is increased to 30 % and 40 %. Instead of offering an alternative pathway for CO_2 molecules, the aggregated Phe may impede their passage across the membrane.

4.3.5. Surface Roughness Analysis

The variation in the surface roughness of CS membrane upon interaction with Phe due to blending and grafting has been demonstrated using the atomic force microscopy (AFM) technique. The AFM images and the obtained roughness values (R_a) of the neat CS membrane and all the composite membranes are shown in Figure 4.5. The increase in the roughness for blended and grafted membranes revealed the development of interaction between Phe and the CS matrix. The calculated surface roughness demonstrated that the grafting led to greater roughness of the composite CS membranes than the blending, which might benefit the CO_2 molecule passage across the composite membrane. In blending, the weaker interaction of Phe and CS at high loading of Phe, leads to non-uniform and agglomerated distribution of the amino acid that lead to marginal increment in roughness values compared to neat CS membrane.[27–29]

Upon grafting, the formation of a strong amide bond between Phe and CS chain led increased immobilization of Phe on the membrane surface.[30,31] The high modification of the CS upon grafting with Phe resulted in the formation of hills and valleys that uniformly covered the entire surface (visible from Figure 4.5f) and resulted in significantly higher roughness compared to neat and blended CS membranes.[32,33] The top surface view of the various casted membranes with varied Phe content in CS, such as Phe-*b*-CS (0-40%) and Phe-*g*-CS presented

in the Figure 4.4 confirm the similar smoother topology. Hence, we can say that the AFM results are in good agreement with FESEM results.

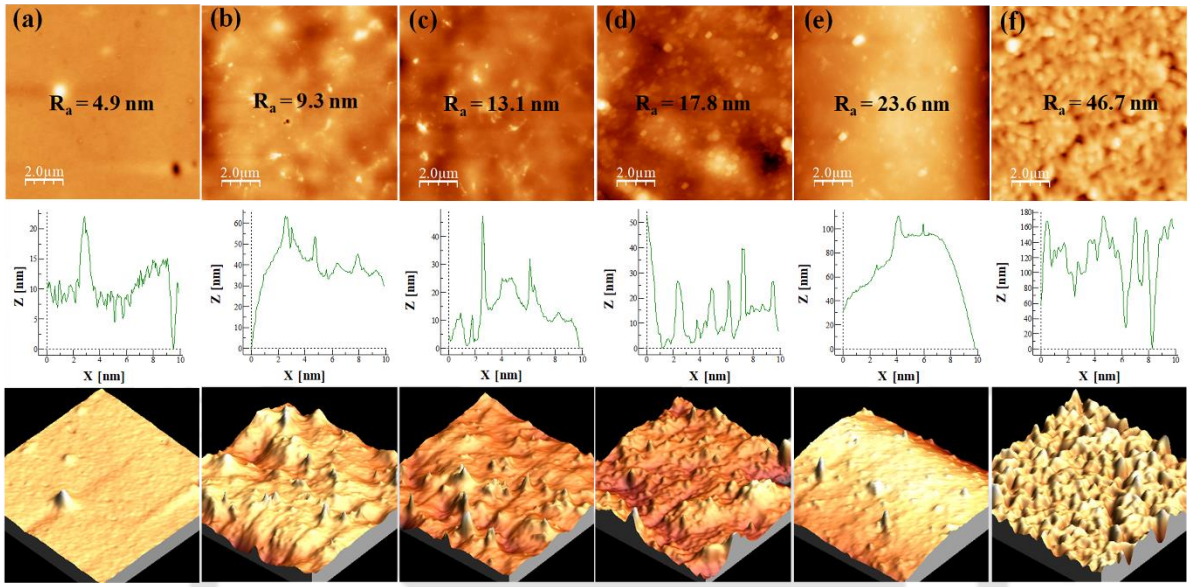

Figure 4.5. AFM images of (a) Pure CS, (b) Phe-*b*-CS (10), (c) Phe-*b*-CS (20), (d) Phe-*b*-CS (30), (e) Phe-*b*-CS (40) and (f) Phe-*g*-CS membranes.

4.4. Gas separation (GS) performance of the membrane

Flue gas mixture (20% CO_2 and 80% N_2) is separated using a gas permeation setup design, explained in Section 2.4 and illustrated in Scheme 2.2, at different operating conditions such as blending and grafting approaches, the temperature and run time under humid conditions.

4.4.1. Effect of Phe blending and grafting on CO_2 separation

The gas separation performance of the fabricated membranes was studied at an optimum temperature of 85 °C with a constant moisture flow ratio of feed/sweep as 0.667 at an absolute pressure of 2.21/1.21 bar (feed/sweep). To boost the carrier in the selective layer,

Phe was blended into the CS matrix at various weights % ranging from 10% to 40%. The gas separation results in Figure 4.6 show that the blending of Phe with CS boosted CO_2 selectivity and permeance compared to that for the neat CS membrane. The enhancement in performance upon blending is due to the availability of an additional mobile carrier that helps in providing an additional pathway for CO_2 gas molecules and, consequently, improves the rate of facilitated CO_2 transport across the composite membrane. Among all the Phe-*b*-CS (10, 20, 30 and 40) membranes, the addition of 20 wt% Phe into CS showed the highest CO_2 permeance and CO_2/N_2 selectivity. The neat CS membrane showed a CO_2 permeance of 15 GPU and CO_2/N_2 selectivity of 48 and that for the best performing Phe blended CS (Phe-*b*-CS (20)) is 72(±0.5) GPU and 97, respectively. This enhancement in the separation performance of the synthesized composite membrane [Phe-*b*-CS (20)], when compared to neat CS, can be explained by the zwitterion reversible reaction between CO_2 and -NH_2 groups.[34,35] As per the zwitterion reaction, CO_2 is first taken up by an amine functional group, which then produces zwitterionic intermediates. These intermediates subsequently combine with another amine functional group to make carbamate. Therefore, for amino acids containing one amine group and two amine groups, the theoretical maximal absorptions are 0.5 mol CO_2/mol amine and 1 mol CO_2/mol amine. The blending of lower wt% (10) may be unable to provide sufficient CO_2 carriers and the blending of a higher amount creates a barrier in the CO_2 molecule pathway, consequently responsible for the deterioration in separation performance.

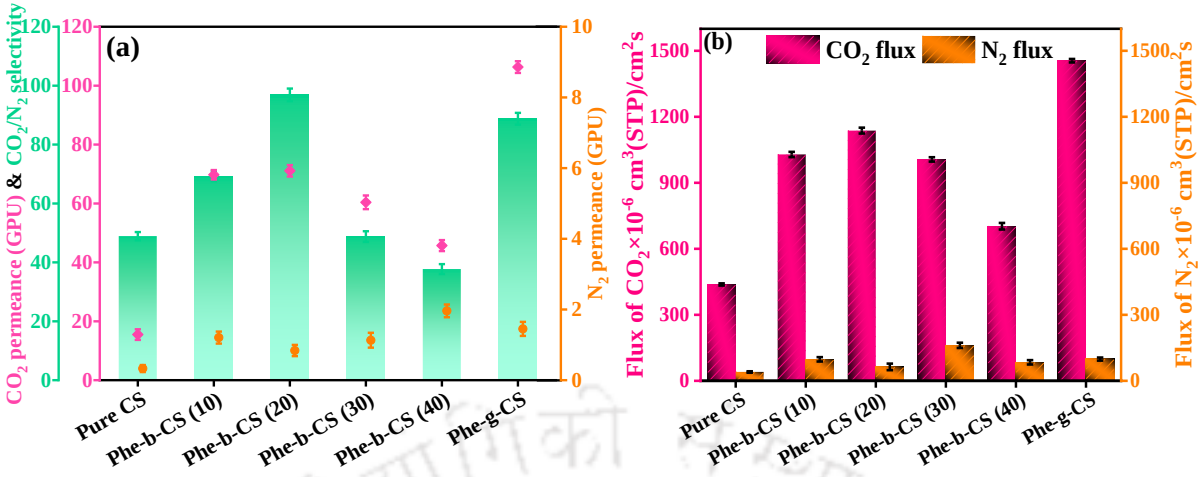

Figure 4.6. Effect of Phe grafting and blending on (a) CO_2/N_2 selectivity and CO_2, N_2 permeance and (b) CO_2, N_2 flux of all the fabricated membranes at 85 °C temperature, 2.21 bar feed pressure under humid condition.

To understand the effect of stronger interaction (amide bond formation) between CS and amino acid towards its activity for CO_2 separation, the grafting methodology was employed. Interestingly, even at the same operating conditions: temperature of 85 °C with a constant water flow ratio of feed/sweep as 0.667 at an absolute pressure of 2.21/1.21 bar (feed/sweep), the uptake capacity reached 106 GPU CO_2 permeance and 89 CO_2/N_2 selectivity when Phe is grafted onto the CS matrix; similar results are obtained by Xia et al.[21] This can be explained as the covalent tethering of amines onto polymer matrix is an effective way of increasing CO_2 separation capacity and selectivity because CO_2 has a higher affinity towards polar amine or amide groups than other flue gases like N_2. The amide bond formation contributes to a larger quadruple moment and Polaris ability. The X-ray photoelectron and Fourier transform infrared spectra revealed a high density of amide groups in the polymer matrix after grafting, which enabled high permeance to CO_2. Also, the grafted membrane displays improved membrane hydrophilicity and surface roughness (as shown by AFM) because of amide bond formation, which also contributed to membrane CO_2 separation performance enhancement. Therefore, as the results show, the polymers retained polar amide

groups of Phe intact; thus, there was no need for any secondary chemical modification to make them selective to CO_2. As a result, we may conclude that adding pendant amide (-CONH-) groups to polymers is seen to be a potential way to increase CO_2 uptake because amides act as both donors and acceptors of hydrogen bonds (through C=O) (via N-H).[36]

4.4.2. Effect of temperature on CO_2 separation performance of Phe-*b*-CS (20)

The CO_2 separation performance of the 20 wt% loaded, optimized Phe-*b*-CS was examined at different operating temperatures. As shown in Figure 4.7a and b the CO_2 gas permeance and the flux increased significantly from 48.6 GPU to 100.1 GPU and 976 $\times 10^{-6}$ $cm^3(STP)/cm^2s$ to 1470 $\times 10^{-6}$ $cm^3(STP)/cm^2s$ with an increase in operating temperature from 65 to 95 °C and the selectivity of CO_2 improved from 37.3 to 97 with an increase in operating temperature from 65 to 85 °C. Also, a minor increment from 1.1 GPU to 1.9 GPU is observed for N_2 gas permeance and 71.6 $\times 10^{-6}$ $cm^3(STP)/cm^2s$ to 162.4 $\times 10^{-6}$ $cm^3(STP)/cm^2s$ with an increase in operating temperature from 65 to 105 °C is observed.

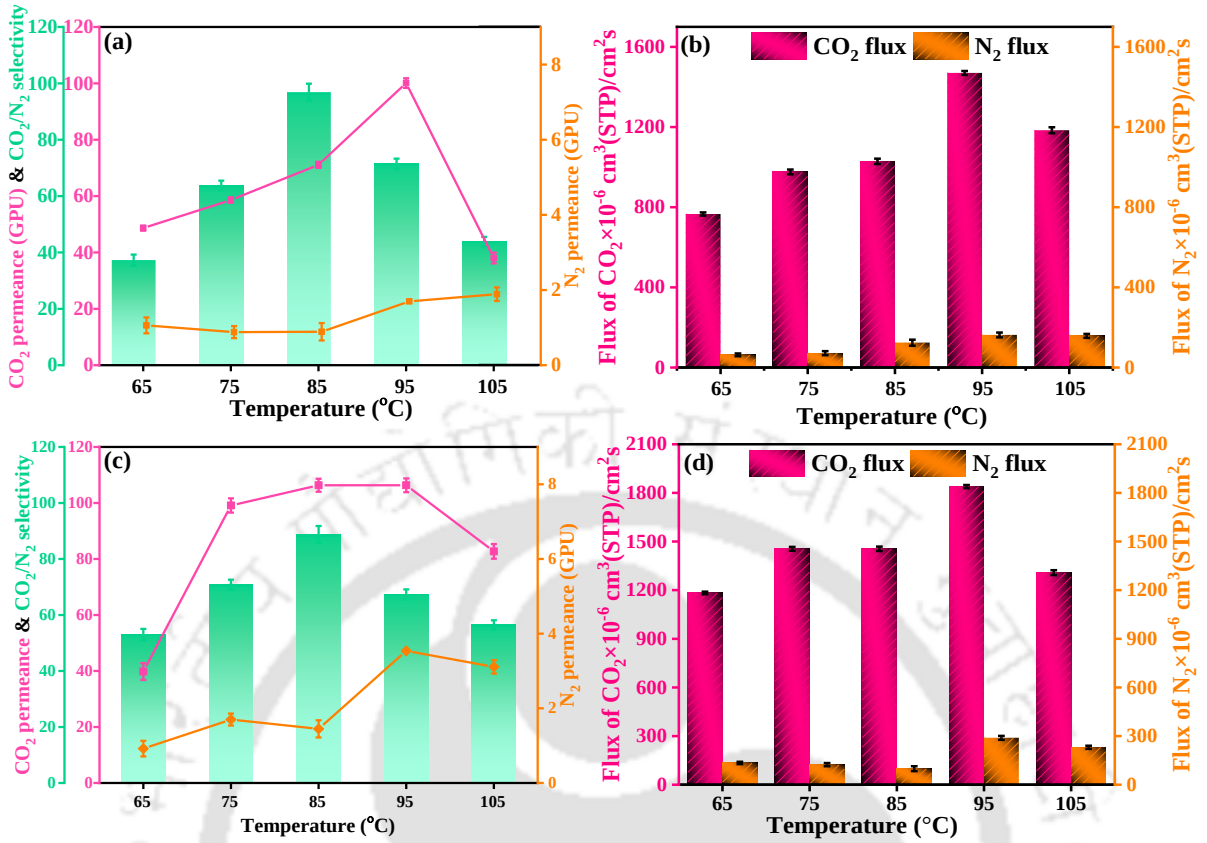

Figure 4.7. Temperature effects on CO_2/N_2 selectivity and CO_2, N_2 permeance of (a) Phe-*b*-CS membrane and (c) Phe-*g*-CS membrane; Temperature effects on CO_2, N_2 flux of (b) Phe-*b*-CS membrane and (d) Phe-*g*-CS membrane at 2.21 bar feed pressure under humid conditions.

This increase in CO_2 and N_2 permeance and flux up to a certain temperature is consistent with the literature.[10,37] This significant rise in CO_2 transport properties and minor rise in the N_2 transport properties across the Phe-*b*-CS (20) composite membrane can be explained by the fact that, at higher temperature, the enhanced polymer chain mobility raises the diffusion coefficients for both CO_2 and N_2, as well as accelerates the rate at which CO_2 molecules and amine carriers react and consequently CO_2 molecules can be transported more easily than N_2 molecules.

However, N_2 with a larger molecular size is less impacted than CO_2; hence higher temperatures up to 85 °C enhance N_2 permeance and increase CO_2/N_2 selectivity. Further, rise in the operating temperature to 105 °C results in a significant loss of CO_2 permeance and

selectivity. This can be explained by the fact that when the temperature rises, the moisture retention capacity of the membrane decreases, lowering the facilitated transport rate of CO_2 molecules across the membrane and consequently responsible for the decline in the separation performance of the membrane.[38]

4.4.3. Effect of temperature on the CO_2 separation performance of Phe-*g*-CS

Temperature effects on CO_2 flux, N_2 flux, CO_2 permeance, N_2 permeance and CO_2/N_2 selectivity for the Phe-*g*-CS membrane were studied by ranging the temperature from 65 to 105 °C. The absolute pressures on the feed and sweep sides were kept constant at 2.21 bar and 1.21 bar, respectively. In addition, the feed/sweep side water flow ratio was held constant at 0.667. Figure 4.7c demonstrates the influence of temperature on CO_2 and N_2 permeance and CO_2/N_2 selectivity, while Figure 4.7d shows the CO_2 and N_2 fluxes for the membrane. The representation of the data points in Figure 4.7c indicates that temperature differences do not affect the films' permeance performance significantly between 75-95 °C. As can be observed from the permeance (Figure 4.7c) and flux (Figure 4.7d) graph, grafting improved the temperature effects of the membrane when compared to blending, as the permeance increased from 40 to 99 GPU when the temperature rose from 65 to 75 °C, then it remained constant at 106 GPU at 85 °C and 95 °C. The CO_2 permeance decreased to 89 GPU at 105 °C on the further rise in the temperature. The results clearly show that the grafting has removed the effect of high temperature on the CO_2 separation performance of the membrane, as can be validated with TGA results too, when compared to the blended membrane, thus giving scope for operating at temperatures up to 95 °C. Grafting has demonstrated superior separation performance compared to blended membranes, which can be attributed to the introduction of pendant amide (-CONH-) groups into the polymer structure. The incorporation of these amide groups is considered a promising strategy for enhancing CO_2 uptake, primarily because they facilitate

the formation of hydrogen bonds. Amides act as both hydrogen bond acceptors (through the C=O moiety) and donors (via the N-H group), which leads to improved gas selectivity and permeability in the membrane. Amide groups have the same positive effect on the adsorption of CO_2 as the widely reported amine ($-NH_2$) groups by facilitating dipole-quadruple interactions. However, these two analogous functional groups have different structural and chemical characteristics.[39]

4.4.4. Effect of experiment run time

The Phe-*g*-CS and Phe-*b*-CS (20) membranes' stability was tested for 400 h at the optimal operating conditions of 85 °C, 2.21 bar feed pressure, 1.21 bar sweep side pressure and 0.667 feed-flow ratios of feed/sweep and represented in Figure 4.9. It was discovered that the Phe-*g*-CS membrane has better consistency of CO_2 uptake capacity than the Phe-*b*-CS (20) membrane. This is clear from the fact that although grafting produces the greatest covalent bond formation between amino acid and polymer functional groups, blending produces the weakest H-bond formation. A number of techniques, like physical blending and chemical grafting, are used to introduce Phe to CS. Physical blending can be the preferred option due to its simplicity. However, Phe frequently migrates out of the CS materials during material aging, impairing their characteristics. As an alternative, (graft) copolymers may stop polyether migration and provide the opportunity to change the final product's soft/hard segment ratio to modify its mechanical capabilities, hydrophilic/hydrophobic traits and rate of degradation.

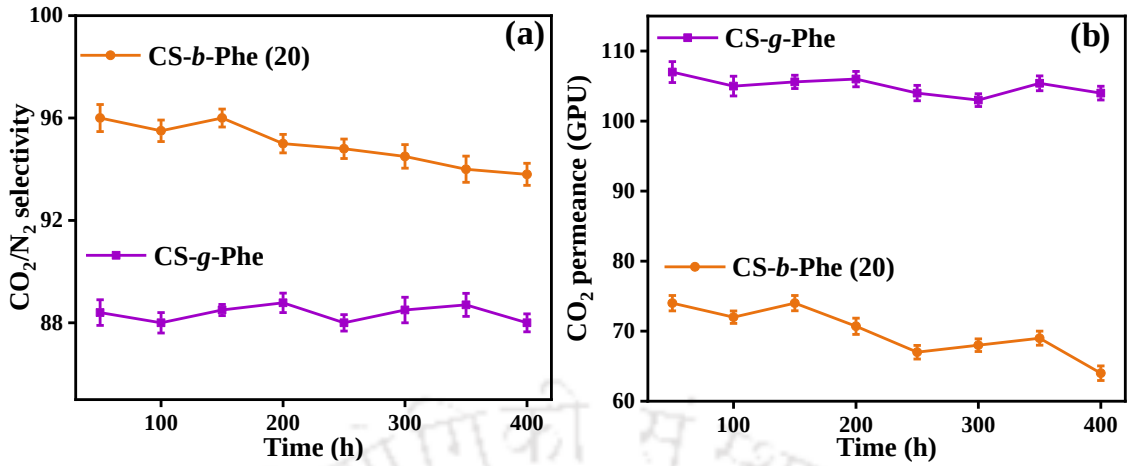

Figure 4.8. Effect of the experiment run time on (a) CO_2 permeance and (b) CO_2/N_2 selectivity of both Phe-*b*-CS (20) membrane and Phe-*g*-CS membrane.

4.4.5. Comparative study of the obtained results with the reported literature

The Robeson upper bound curve, which assesses the trade-off between selectivity and permeability in each membrane, is typically used to measure the separation performance of polymeric membranes.[40] The as-synthesized membrane's selective layer thickness is multiplied by the acquired CO_2 permeance to attain CO_2 permeability in barrer. The Robeson upper bound curve (2008) (Figure 4.10) and other high-performing composite membranes as the fixed and mobile site carriers (Table 4.2) were used to compare the performance of the as-prepared bare CS, Phe-*b*-CS (20) and Phe-*g*-CS membranes in this work. In addition, we have also compared the obtained performances with earlier published similar work for CO_2 separation from our previous groups.[6,9,26,29,39,41–43] The obtained results for Phe-*g*-CS and Phe-*b*-CS (20) membranes showed significant improvements in terms of CO_2/N_2 selectivity, CO_2 permeance, reproducibility and stability in the performance when compared to neat CS and many of the earlier reported works from our group. Grafting has contributed to improving the permeance by providing additional pathways for CO_2 to transport, whereas blending contributed to CO_2/N_2 selectivity enhancement by providing aided mobile carriers.

Table 4.1. A comparative account of the CO_2 separation Performance of the optimized Phe-*b*-CS (20) and Phe-*g*-CS membranes with available literature.

Polymer/ Carrier	Temperature (°C)	Thickness (µm)	Feed absolute pressure (bar)	CO_2 Permeance (GPU)	S_{CO_2/N_2}	Ref.
CS/ TEPA	90	3.5	2.21	24.7	80	[1]
CS/PAA	90	4.5	2.21	39	260	[29]
CMC/ PAMAM	90	2.6	2.21	100	149	[26]
PVA-PVP/PEI	25	0.5	2.21	183	35	[22]
PVA/SC	25	25	2.21	2.16	54	[44]
PVAm/PG	57	0.17	1.11	1100	140	[45]
Pebax®MH 1657/SG	25	0.12	75-100	1023[a]	91	[46]
PVAm-CH_3/ PZEA-Sar	57	0.17	0.17	1071	183	[47]
Pebax/amino-PDMS/PAN	25	-	5	147	62	[48]
PVC/PEG[b]	25	-	20	5.82[a]	109	[49]
PVA/PVP/PEI/ TEPA	100	45	2.8	30.44	270	[41]
CS/SF	90	3	2.21	140	103	[42]
CS/SC	90	3	2.21	164	52	[6]
CS/Phe (grafted)	85	~ 4	2.21	106	89	This work
CS/Phe (blended)	85	~ 4	2.21	72	97	This work

[a] barrer, [b] pure gas permeation test.

Abbreviations: *TEPA - Tetraethylenepentamine, PAA - Poly(allylamine), PAMAM - poly(amidoamine), PVP - Poly (vinylpyrrolidone), PEI - Polyethylenimine, SC - sericin, PZEA-*

Sar - 2-(1-piperazinyl)ethylamine sarcosinate, PDMS - Polydimethylsiloxane, PAN – Polyacrylonitrile, PVC – Polyvinylchloride, PEG – Polyethyleneglycol.

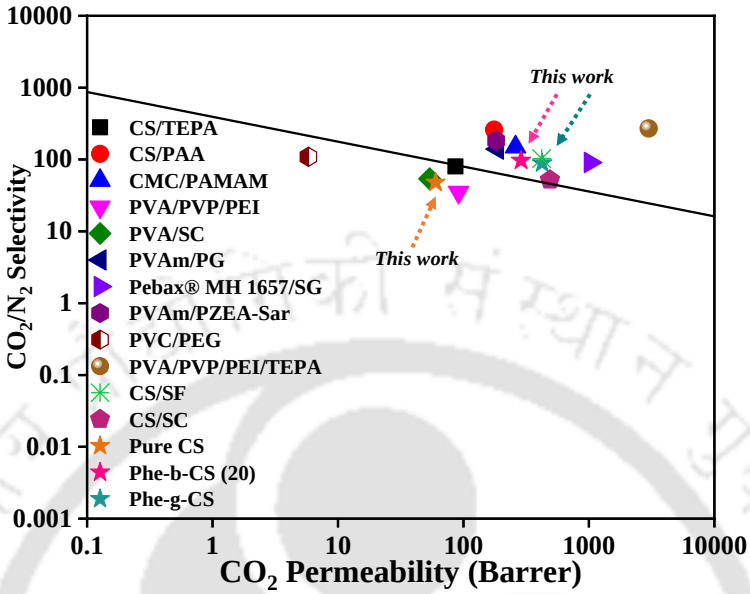

Figure 4.9. Robeson upper bound curve: Comparison of the CO_2 separation performance of the synthesized bare CS, Phe-*b*-CS and Phe-*g*-CS membrane with the reported literature.

4.5. Conclusions

In this research, various graft copolymers and polymer blends were developed to create membranes with labile thermal, mechanical and chemical properties for efficient CO_2 gas movement. Phenylalanine was incorporated as a sacrificed element using physical blending and chemical grafting approaches. Membrane stability and separation performances were compared effectively. Under optimal conditions (85 °C, 2.21 bar feed pressure, 1.21 bar sweep side pressure and 0.667 feed/sweep moisture flow ratio), the Phe-g-CS membrane (4.5 µm thickness) exhibited CO_2/N_2 selectivity of 89 and CO_2 permeance of 106 GPU, while the Phe-b-CS (20) membrane showed 97 selectivity and 72 GPU permeance. The Phe-g-CS membrane demonstrated better CO_2 uptake consistency, attributed to stronger covalent bonds between functional groups of the polymer and amino acids compared to blending, which results in

weaker H-bond formation.

The as-synthesized membrane shows a notable improvement in performance compared to neat CS and Tyr-c-CS membranes. However, there is still room for further enhancement through the incorporation of filler materials.

4.6. References

(1) Dong, G.; Zhang, J.; Wang, Z.; Wang, J.; Zhao, P.; Cao, X.; Zhang, Y. Interfacial Property Modulation of PIM-1 through Polydopamine-Derived Submicrospheres for Enhanced CO_2/N_2 Separation Performance. *ACS Appl. Mater. Interfaces* **2019**, *11* (21), 19613–19622. https://doi.org/10.1021/acsami.9b02281.

(2) Dai, Z.; Ansaloni, L.; Deng, L. Recent Advances in Multi-Layer Composite Polymeric Membranes for CO_2 Separation: A Review. *Green Energy Environ.* **2016**, *1* (2), 102–128. https://doi.org/10.1016/j.gee.2016.08.001.

(3) Wang, S.; Li, X.; Wu, H.; Tian, Z.; Xin, Q.; He, G.; Peng, D.; Chen, S.; Yin, Y.; Jiang, Z.; Guiver, M. D. Advances in High Permeability Polymer-Based Membrane Materials for CO_2 Separations. *Energy Environ. Sci* **2016**, *9*, 1863. https://doi.org/10.1039/c6ee00811a.

(4) Olajire, A. A. Synthesis of Bare and Functionalized Porous Adsorbent Materials for CO_2 Capture. *Greenhouse Gases: Science and Technology*. Blackwell Publishing Ltd June 1, 2017, pp 399–459. https://doi.org/10.1002/ghg.1657.

(5) Liu, Y.; Yu, S.; Wu, H.; Li, Y.; Wang, S.; Tian, Z.; Jiang, Z. High Permeability Hydrogel Membranes of Chitosan/Poly Ether-Block-Amide Blends for CO_2 Separation. *J. Memb. Sci.* **2014**, *469*, 198–208. https://doi.org/10.1016/j.memsci.2014.06.050.

(6) Prasad, B.; Thakur, R. M.; Mandal, B.; Su, B. Enhanced CO_2 Separation Membrane Prepared from Waste By-Product of Silk Fibroin. *J. Memb. Sci.* **2019**, *587*, 117170. https://doi.org/10.1016/j.memsci.2019.117170.

(7) Ashtiani, S.; Khoshnamvand, M.; Bouša, D.; Šturala, J.; Sofer, Z.; Shaliutina-Kolešová, A.; Gardenö, D.; Friess, K. Surface and Interface Engineering in CO_2-Philic Based UiO-66-NH_2-PEI Mixed Matrix Membranes via Covalently Bridging PVP for Effective Hydrogen Purification. *Int. J. Hydrogen Energy* **2021**, *46* (7), 5449–5458. https://doi.org/10.1016/j.ijhydene.2020.11.081.

(8) Xie, J.; Qin, D.; Han, Y.; Wang, L. Synthesis and Characterization of a Novel Hydroxypropyl Chitosan-Graft-β-Cyclodextrin Copolymer as Potential Drug Carrier. *J. Carbohydr. Chem.* **2019**, *38* (5–6), 383–397. https://doi.org/10.1080/07328303.2019.1630837.

(9) Prasad, B.; Mandal, B. CO_2 Separation Performance by Chitosan/Tetraethylenepentamine/Poly(Ether Sulfone) Composite Membrane. *J. Appl. Polym. Sci.* **2017**, *134* (34), 1–9. https://doi.org/10.1002/app.45206.

(10) Borgohain, R.; Mandal, B. PH Responsive Carboxymethyl Chitosan/Poly(Amidoamine) Molecular Gate Membrane for CO_2/N_2 Separation. *ACS Appl. Mater. Interfaces* **2019**, *11* (45), 42616–42628. https://doi.org/10.1021/acsami.9b15044.

(11) Yoksan, R.; Akashi, M. Low Molecular Weight Chitosan-g-l-Phenylalanine: Preparation, Characterization and Complex Formation with DNA. *Carbohydr. Polym.* **2009**, *75* (1), 95–103. https://doi.org/10.1016/j.carbpol.2008.07.001.

(12) Han, D.; Yan, L.; Chen, W.; Li, W. Preparation of Chitosan/Graphene Oxide Composite

Film with Enhanced Mechanical Strength in the Wet State. *Carbohydr. Polym.* **2011**, *83* (2), 653–658. https://doi.org/10.1016/j.carbpol.2010.08.038.

(13) Wang, Y.; Han, Q.; Wang, Y.; Qin, D.; Luo, Q.; Zhang, H. Self-Assembly, Rheological Properties and Antioxidant Activities of Chitosan Grafted with Tryptophan and Phenylalanine. *Colloids Surfaces A Physicochem. Eng. Asp.* **2020**, *597*, 124763. https://doi.org/10.1016/j.colsurfa.2020.124763.

(14) Mallakpour, S.; Abdolmaleki, A.; Borandeh, S. Covalently Functionalized Graphene Sheets with Biocompatible Natural Amino Acids. *Appl. Surf. Sci.* **2014**, *307*, 533–542. https://doi.org/10.1016/j.apsusc.2014.04.070.

(15) Kee, N. C. S.; Arendt, P. D.; Tan, R. B. H.; Braatz, R. D. Selective Crystallization of the Metastable Anhydrate Form in the Enantiotropic Pseudo-Dimorph System of L-Phenylalanine Using Concentration Feedback Control. *Cryst. Growth Des.* **2009**, *9* (7), 3052–3061. https://doi.org/10.1021/cg8006537.

(16) Nafisi, V.; Hägg, M. Gas Separation Properties of ZIF-8 / 6FDA-Durene Diamine Mixed Matrix Membrane. *Sep. Purif. Technol.* **2014**, *128*, 31–38. https://doi.org/10.1016/j.seppur.2014.03.006.

(17) Xin, Q.; Zhao, M.; Guo, J.; Huang, D.; Zeng, Y.; Zhao, Y.; Zhang, T.; Zhang, L.; Wang, S.; Zhang, Y. Light-Responsive Metal-Organic Framework Sheets Constructed Smart Membranes with Tunable Transport Channels for Efficient Gas Separation. *RSC Adv.* **2021**, *12* (1), 517–527. https://doi.org/10.1039/d1ra06814h.

(18) Moi, R.; Ghorai, A.; Banerjee, S.; Biradha, K. Amino- A Nd Sulfonate-Functionalized Metal-Organic Framework for Fabrication of Proton Exchange Membranes with

Improved Proton Conductivity. *Cryst. Growth Des.* **2020**, *20* (8), 5557–5563. https://doi.org/10.1021/acs.cgd.0c00732.

(19) Ike, Y.; Hirasawa, I. Polymorph Control of L-Phenylalanine in Cooling Crystallization by Ultrasonication. *Chem. Eng. Technol.* **2018**, *41* (6), 1093–1097. https://doi.org/10.1002/ceat.201700662.

(20) Lu, J. Characterization and Pseudopolymorphism of L-Phenylalanine Anhydrous and Monohydrate Forms. *African J. Pharm. Pharmacol.* **2012**, *6* (4), 269–277. https://doi.org/10.5897/ajpp11.842.

(21) Xia, J.; Liu, S.; Chung, T. S. Effect of End Groups and Grafting on the CO_2 Separation Performance of Poly(Ethylene Glycol) Based Membranes. *Macromolecules* **2011**, *44* (19), 7727–7736. https://doi.org/10.1021/ma201844y.

(22) Lilleby Helberg, R. M.; Dai, Z.; Ansaloni, L.; Deng, L. PVA/PVP Blend Polymer Matrix for Hosting Carriers in Facilitated Transport Membranes: Synergistic Enhancement of CO_2 Separation Performance. *Green Energy Environ.* **2019**, *5* (1), 59–68. https://doi.org/10.1016/j.gee.2019.10.001.

(23) Gutiérrez-Serpa, A.; Kundu, T.; Pasán, J.; Jiménez-Abizanda, A. I.; Kaskel, S.; Senkovska, I.; Pino, V. Zirconium-Based Metal–Organic Framework Mixed-Matrix Membranes as Analytical Devices for the Trace Analysis of Complex Cosmetic Samples in the Assessment of Their Personal Care Product Content. *ACS Appl. Mater. Interfaces* **2022**, *14* (3), 4510–4521. https://doi.org/10.1021/acsami.1c21284.

(24) Dalhatu, S. N.; Modu, K. A.; Mahmoud, A. A.; Zango, Z. U.; Umar, A. B.; Usman, F.; Dennis, J. O.; Alsadig, A.; Ibnaouf, K. H.; Aldaghri, O. A. L-Arginine Grafted Chitosan

as Corrosion Inhibitor for Mild Steel Protection. *Polymers (Basel).* **2023**, *15* (2). https://doi.org/10.3390/polym15020398.

(25) Prasad, B.; Mandal, B. Graphene-Incorporated Biopolymeric Mixed-Matrix Membrane for Enhanced CO_2 Separation by Regulating the Support Pore Filling. *ACS Appl. Mater. Interfaces* **2018**, *10* (33), 27810–27820. https://doi.org/10.1021/acsami.8b09377.

(26) Borgohain, R.; Mandal, B. Thermally Stable and Moisture Responsive Carboxymethyl Chitosan/Dendrimer/Hydrotalcite Membrane for CO_2 Separation. *J. Memb. Sci.* **2020**, *608* (May), 118214. https://doi.org/10.1016/j.memsci.2020.118214.

(27) Sarasam, A. R.; Krishnaswamy, R. K.; Madihally, S. V. Blending Chitosan with Polycaprolactone: Effects on Physicochemical and Antibacterial Properties. *Biomacromolecules* **2006**, *7* (4), 1131–1138. https://doi.org/10.1021/bm050935d.

(28) Didden, J.; Thür, R.; Volodin, A.; Vankelecom, I. F. J. Blending PPO-Based Molecules with Pebax MH 1657 in Membranes for Gas Separation. *J. Appl. Polym. Sci.* **2018**, *135* (27), 1–12. https://doi.org/10.1002/app.46433.

(29) Prasad, B.; Mandal, B. Preparation and Characterization of CO_2-Selective Facilitated Transport Membrane Composed of Chitosan and Poly(Allylamine) Blend for CO_2/N_2 Separation. *J. Ind. Eng. Chem.* **2018**, *66*, 419–429. https://doi.org/10.1016/j.jiec.2018.06.009.

(30) Freger, V.; Gilron, J.; Belfer, S. TFC Polyamide Membranes Modified by Grafting of Hydrophilic Polymers: An FT-IR/AFM/TEM Study. *J. Memb. Sci.* **2002**, *209* (1), 283–292. https://doi.org/10.1016/S0376-7388(02)00356-3.

(31) Yoshida, W.; Cohen, Y. Topological AFM Characterization of Graft Polymerized Silica

Membranes. *J. Memb. Sci.* **2003**, *215* (1–2), 249–264. https://doi.org/10.1016/S0376-7388(03)00019-X.

(32) Shen, L.; Feng, S.; Li, J.; Chen, J.; Li, F.; Lin, H.; Yu, G. Surface Modification of Polyvinylidene Fluoride (PVDF) Membrane via Radiation Grafting: Novel Mechanisms Underlying the Interesting Enhanced Membrane Performance. *Sci. Rep.* **2017**, *7* (1), 1–13. https://doi.org/10.1038/s41598-017-02605-3.

(33) Fernández, L.; Sánchez, M.; Carmona, F. J.; Palacio, L.; Calvo, J. I.; Hernández, A.; Prádanos, P. Analysis of the Grafting Process of PVP on a Silicon Surface by AFM and Contact Angle. *Langmuir* **2011**, *27* (18), 11636–11649. https://doi.org/10.1021/la201683p.

(34) Danckwerts, P. V. The Reaction of CO_2 with Ethanolamines. *Chem. Eng. Sci.* **1979**, *34* (4), 443–446. https://doi.org/10.1016/0009-2509(79)85087-3.

(35) Lv, B.; Guo, B.; Zhou, Z.; Jing, G. Mechanisms of CO_2 Capture into Monoethanolamine Solution with Different CO_2 Loading during the Absorption/Desorption Processes. *Environ. Sci. Technol.* **2015**, *49* (17), 10728–10735. https://doi.org/10.1021/acs.est.5b02356.

(36) Ji, D.; Luo, Z.; He, M.; Shi, Y.; Gu, X. Effect of Both Grafting and Blending Modifications on the Performance of Lignosulphonate-Modified Sulphanilic Acid-Phenol-Formaldehyde Condensates. *Cem. Concr. Res.* **2012**, *42* (9), 1199–1206. https://doi.org/10.1016/j.cemconres.2012.05.010.

(37) de Richter, R.; Ming, T.; Davies, P.; Liu, W.; Caillol, S. Removal of Non-CO_2 Greenhouse Gases by Large-Scale Atmospheric Solar Photocatalysis. *Prog. Energy*

Combust. Sci. **2017**, *60*, 68–96. https://doi.org/10.1016/j.pecs.2017.01.001.

(38) Barooah, M.; Mandal, B. Synthesis, Characterization and CO_2 Separation Performance of Novel PVA/PG/ZIF-8 Mixed Matrix Membrane. *J. Memb. Sci.* **2019**, *572*, 198–209. https://doi.org/10.1016/j.memsci.2018.11.001.

(39) Mondal, A.; Barooah, M.; Mandal, B. Effect of Single and Blended Amine Carriers on CO_2 Separation from CO_2/N_2 Mixtures Using Crosslinked Thin-Film Poly(Vinyl Alcohol) Composite Membrane. *Int. J. Greenh. Gas Control* **2015**, *39*, 27–38. https://doi.org/10.1016/j.ijggc.2015.05.002.

(40) Robeson, L. M. Correlation of Separation Factor versus Permeability for Polymeric Membranes. *J. Memb. Sci.* **1991**, *62* (2), 165–185. https://doi.org/10.1016/0376-7388(91)80060-J.

(41) Mondal, A.; Mandal, B. CO_2 Separation Using Thermally Stable Crosslinked Poly(Vinyl Alcohol) Membrane Blended with Polyvinylpyrrolidone/Polyethyleneimine/Tetraethylenepentamine. *J. Memb. Sci.* **2014**, *460*, 126–138. https://doi.org/10.1016/j.memsci.2014.02.040.

(42) Prasad, B.; Mandal, B. Moisture Responsive and CO_2 Selective Biopolymer Membrane Containing Silk Fibroin as a Green Carrier for Facilitated Transport of CO_2. *J. Memb. Sci.* **2018**, *550*, 416–426. https://doi.org/10.1016/j.memsci.2017.12.061.

(43) Borgohain, R.; Prasad, B.; Mandal, B. Synthesis and Characterization of Water-Soluble Chitosan Membrane Blended with a Mobile Carrier for CO_2 Separation. *Sep. Purif. Technol.* **2019**, *222*, 177–187. https://doi.org/10.1016/j.seppur.2019.04.038.

(44) Kim, S. J. Gas Permeation through Water-Swollen Sericin / PVA Membranes. **2007**.

(45) Chen, Y.; Ho, W. S. W. High-Molecular-Weight Polyvinylamine/Piperazine Glycinate Membranes for CO_2 Capture from Flue Gas. *J. Memb. Sci.* **2016**, *514*, 376–384. https://doi.org/10.1016/j.memsci.2016.05.005.

(46) Zhang, H.; Tian, H.; Zhang, J.; Guo, R.; Li, X. Facilitated Transport Membranes with an Amino Acid Salt for Highly Efficient CO_2 Separation. *Int. J. Greenh. Gas Control* **2018**, *78*, 85–93. https://doi.org/10.1016/j.ijggc.2018.07.014.

(47) Chen, T. Y.; Deng, X.; Lin, L. C.; Ho, W. S. W. New Sterically Hindered Polyvinylamine-Containing Membranes for CO_2 Capture from Flue Gas. *J. Memb. Sci.* **2022**, *645*, 120195. https://doi.org/10.1016/j.memsci.2021.120195.

(48) Wang, L.; Ji, P.; Li, Y.; Di, M.; Lv, Q.; Li, S. Design of Poly(Ether Block Amide)/Polyacrylonitrile Composite Membrane for Carbon Dioxide Capture. *Funct. Mater. Lett.* **2015**, *08* (04), 1550045. https://doi.org/10.1142/S1793604715500459.

(49) Ben Hamouda, S.; Nguyen, Q. T.; Langevin, D.; Roudesli, S. Poly(Vinylalcohol)/Poly(Ethyleneglycol)/Poly(Ethyleneimine) Blend Membranes - Structure and CO_2 Facilitated Transport. *Comptes Rendus Chim.* **2010**, *13* (3), 372–379. https://doi.org/10.1016/j.crci.2009.10.009.

CHAPTER 5

Effects of L-Lysine-Conjugated-Graphene Oxide Nanosheets on the CO_2 Separation Performance of Chitosan Mixed Matrix Membrane

The invention of mixed matrix membranes has opened a new dimension in the field of membrane separation technology and this chapter of the thesis discusses the same. We have synthesized highly functional layers of graphene oxide sheets and utilized L-lysine for their surface modification. The modified nanosheets of GO are incorporated into the chitosan matrix and their CO_2 separation study is presented. This research work is scientifically acknowledged in ***"Indian Chemical Engineer"****.*

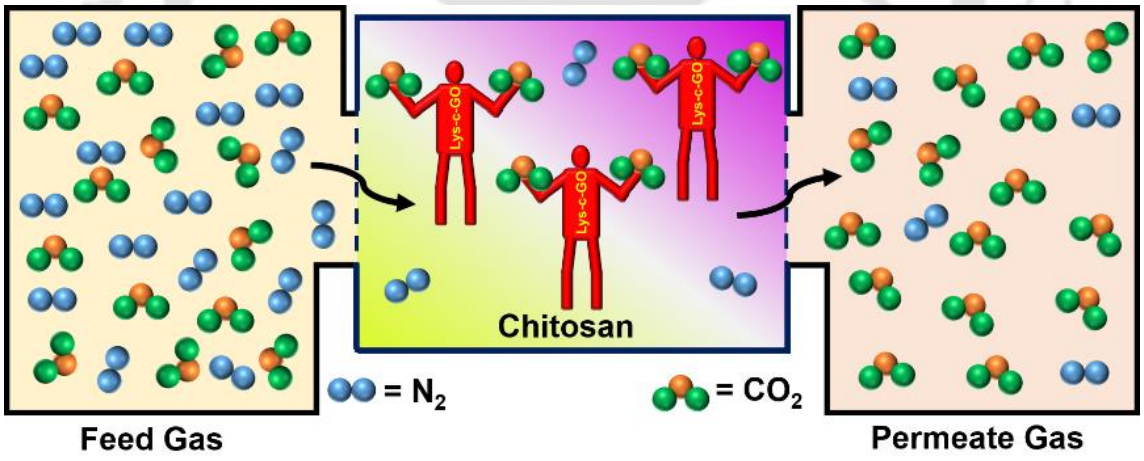

DOI: https://doi.org/10.1080/00194506.2022.2119895

5.1. Introduction

Swollen and dry polymeric membranes have significantly different CO_2 separation performances, yet in any of the conditions, the majority of polymeric membranes fail to meet the expectations. Despite decades of research on the carefully optimized polymer backbone structure, the Robeson upper bound, a trade-off between gas permeability and selectivity, is still a problem for polymeric membranes.[1]

Mixed matrix membranes (MMMs), formed of a polymer matrix as continuous phase and inorganic particles as the dispersion phase, have exceptional permeability and selectivity. They illustrate the benefits of polymers and inorganic particles and have received tremendous attention in recent years.[2] Membrane-based gas separation is in desperate need of new membrane materials with better gas separation capabilities. In membrane fabrication, it is common to use traditional inorganic fillers like silica gel and zeolites, which are non-porous solid fillers. However, researchers have also explored a newer class of porous solid fillers, including carbon nanotubes, activated carbon, graphene oxides and metal-organic frameworks (MOFs). These novel fillers offer unique properties and open up exciting possibilities for enhancing the performance of membranes.[3–6] Regarding gas separation, one of the most popular choices has been the standard two-dimensional (2D) nanosheet materials: graphene oxide (GO). Because GO is formed by oxidizing natural graphene, it is one of the 2D laminar materials containing many different oxygen-containing groups. The resultant material show promise in terms of thinness, flexibility, mechanical strength, chemical stability and the capacity to build an atom-thick 2D carbon nanomaterial, thereby opening several prospects for nanomaterials science and technology study.[7] Unlike conventional filler materials (e.g., zeolite), GOs are soluble in water and can be easily processed with polymeric materials.[8] The surface modification of GO sheets with CO_2-philic functional groups has been demonstrated to

significantly improve the separation performance of membranes, as evidenced in the study by Prasad et al.[31] Building upon this finding, we have opted to employ L-lysine (Lys) amino acids, a distinct biomaterial, for the functionalization of GO sheets. The reason behind this choice stems from the presence of two amine groups within the molecular structure of Lys, which indicates a higher CO_2-philicity compared to Tyr or Phe. This heightened CO_2-philicity characteristic has piqued our interest in using L-lysine amino acids as a potential carrier material. Hence, this work aims to develop a stable, proficient and compatible Lysine-conjugated-Graphene Oxide (Lys-c-GO) incorporated mixed matrix membrane for efficient CO_2 separation. The key novelty of this research study is the successful synthesis and impregnation of Lys-c-GO filler into the CS matrix, which has increased the stability, amorphousness and mechanical strength of the membrane and proven to be a promising membrane material for the effective separation of CO_2 from CO_2/N_2 gas mixture.

5.2. Experimental Section

5.2.1. Preparation of GO and Lysine-Conjugated-GO (Lys-c-GO)

The GO and Lys-c-GO preparation method is outlined in Scheme 5.1. A modified Hummers' method was used to make GO from graphite flakes. Briefly, 0.5 g of graphite powder was disseminated and swirled in a solution of H_2SO_4 and H_3PO_4 in a ratio of 63:7 for 30 minutes at room temperature. Then, $KMnO_4$ was slowly added to the solution in an ice bath; the solution was agitated for an hour to ensure the temperature change was less than 5 °C. The reaction temperature (oxidation) was raised to 30 °C and the mixture was agitated for another 12 hours. After that, 150 mL of water was added to the solution, followed by H_2O_2 (4 mL) and kept for stirring for a few hours. To remove unreacted graphite from the obtained solution, the mixture was centrifuged at 10,000 rpm. Then obtained gel was washed three times with a dilute HCl solution. Finally, the supernatant was washed with water to obtain neutral pH and the vacuum

dried to obtain GO sheets.

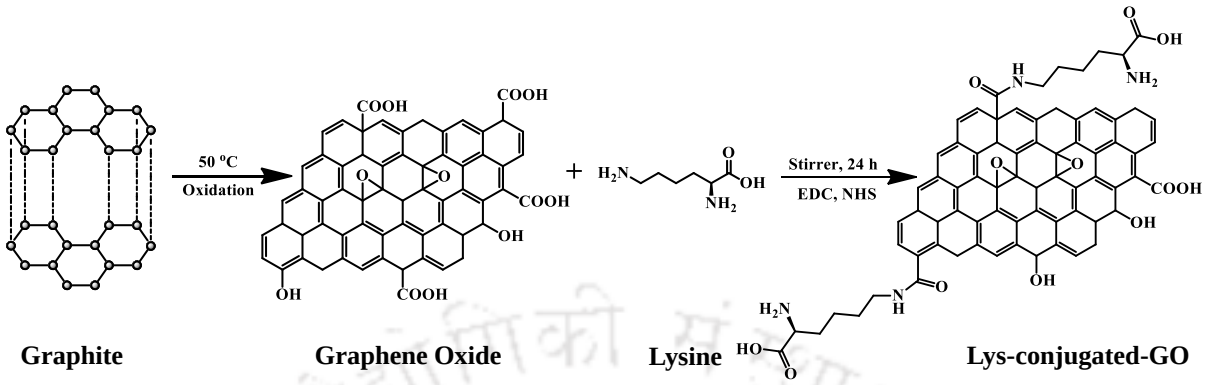

Scheme 5.1. Schematic representation of GO and Lys-c-GO synthesis.

The Lys functionalization of GO was carried out according to a previously published approach with minor changes.[9] An aqueous solution of GO was prepared (100 mL, 7.5 mg/mL) and mixed with Lys solution (7.5 g, 75 mmol), which was catalyzed by EDC (4.79 g, 25 mmol) and NHS (2.475 g, 22 mmol) and stirred for 24 hours at room temperature. Subsequently, the resulting solution was centrifuged for 5 minutes at 5,000 rpm and rinsed with ultrapure water to remove any unreacted impurities. The obtained product was then dried overnight at 60 °C in a vacuum oven and labeled as Lys-c-GO sheets for further studies.

5.2.2. Fabrication of Lys-c-GO filled CS MMMs

The fabrication process for the Lys-c-GO filled CS mixed matrix membrane (MMM) is illustrated in Figure 5.1. Firstly, 1 wt% CS flakes were dissolved in a 1 vol% acetic acid solution. Simultaneously, Lys-c-GO solutions with filler concentrations of 0.5 wt%, 1 wt% and 2 wt% were prepared, following previous research findings by our group. The CS and Lys-c-GO solutions were then thoroughly mixed and continuously agitated for 12 hours at 200 rpm. Afterward, the resulting solution was centrifuged for 5 minutes at 5,000 rpm to remove undissolved particles and bubbles (Model: Sigma 3-30k). Then each sample was spread on a polyethersulfone (PES) support pasted onto a glass plate. An adjustable micrometer casting

knife was used to cast the membranes with the desired thickness. Subsequently, the casted membranes were dried in a laminar hood chamber for 24 hours, followed by drying in an hot air oven for 12 hours at 110 °C. The resultant membranes were labeled as Lys-c-GO@CS(0.5), Lys-c-GO@CS(1) and Lys-c-GO@CS(2) for 0.5, 1 and 2 wt% of Lys-c-GO filler. We have also prepared neat CS membranes as described in section 3.2.2 to gain a better understanding of the changes that occur during MMM fabrication.

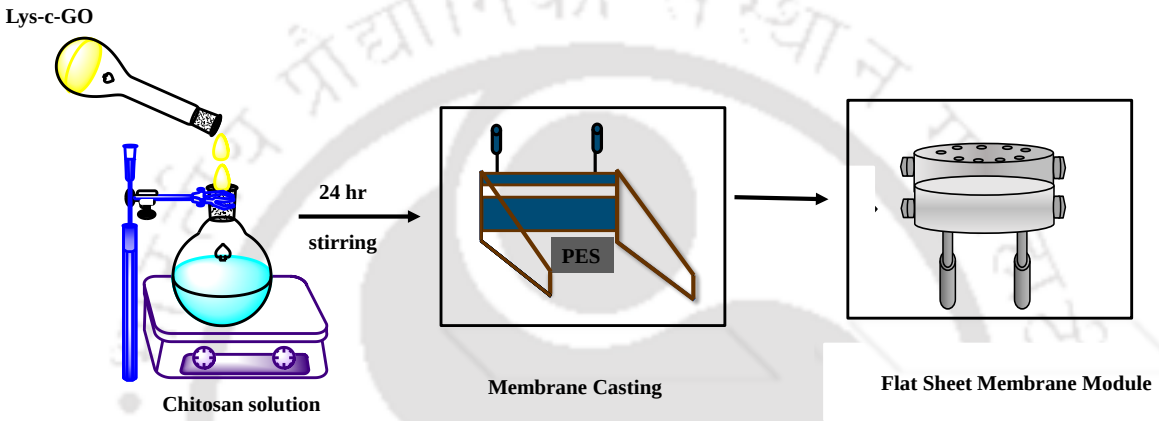

Figure 5.1. Development of Lys-c-GO embedded CS MMMs for CO_2 separation.

5.3. Results and Discussions

5.3.1. Characterization of GO and Lys-c-GO

5.3.1.1 Structural Analysis

The XRD patterns of graphite, GO and Lys-c-GO are shown in Figure 5.2a. The (002) reflection plane produces a diffraction peak in graphite powder at 2θ = 26.53º. When graphite oxidizes to GO, the peak at 26.53º disappears and a new peak arises at 2θ value of 11.18° corresponding to the (001) plane, indicating the 2D nature of the GO due to the existence of oxygen-containing functional groups connected to GO sheet.[10] For Lys-c-GO, the peak at 2θ = 11.55º corresponds to the (001) plane of GO. The change in the *d*-spacing confirms the presence of additional functional groups brought by Lys molecules in the composite.

The bending and stretching of functional groups present in the GO and Lys-c-GO, were

studied using FTIR measurement and shown in Figure 5.2b. The distinctive peaks at 3361 cm^{-1} and 1723 cm^{-1} correspond to O-H and C=O bending, respectively, from the -OH and -COOH functionalities of GO. The additional peaks at 1617 cm^{-1} and 1043 cm^{-1}, respectively, correspond to C=C bending and phenolic C-O-C stretching. Due to the conjugation of Lys with GO, additional peaks at 3364 cm^{-1} and 1629 cm^{-1} were generated in the lys-c-GO spectra, matching the $-NH_2$ and amide groups, respectively.[11] The intensity of the -OH peak went down after Lys was conjugated. This is because oxygen-containing functionalities were lost. These findings demonstrate that Lys has been effectively conjugated onto GO.

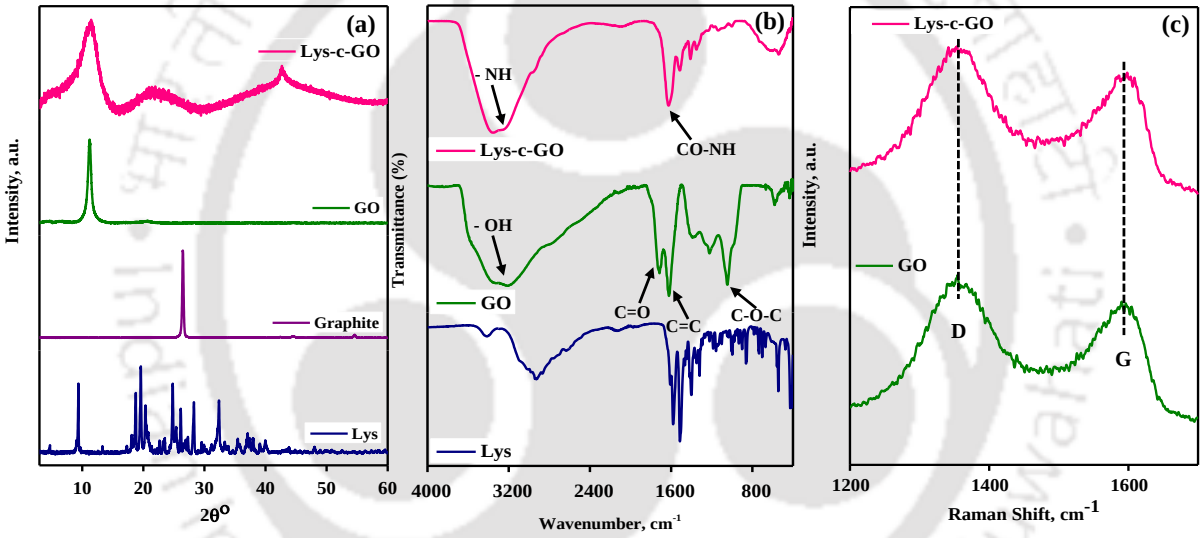

Figure 5.2. (a) XRD, (b) FTIR and (c) Raman spectra of GO and Lys-c-GO, respectively.

Raman spectroscopy was used to investigate the crystal structure of GO and Lys-c-GO, as shown in Figure 5.2c. D-band for carbon atom vibration was detected at 1353 cm^{-1} in disordered graphite, while a G-band was detected at 1591 cm^{-1} in GO, indicating the change in the electronic structure of graphite after oxidation. After conjugating Lys onto the GO surface, both D and G-bands shifted down to 1355 cm^{-1} and 1598 cm^{-1}, compared to bare GO.[12] This could be because there were more sp^3 carbon atoms on the surface of GO after conjugation. The intensity ratio of the D and G-bands (I_D/I_G) for GO is 0.48 and rises to 0.51 for Lys-c-GO, which is attributable to the formation of covalent bonds between Lys and GO. Consistent with

previously described GO functionalization systems, these results indicate that the functional Lys has been well adsorbed on GO after the conjugation.

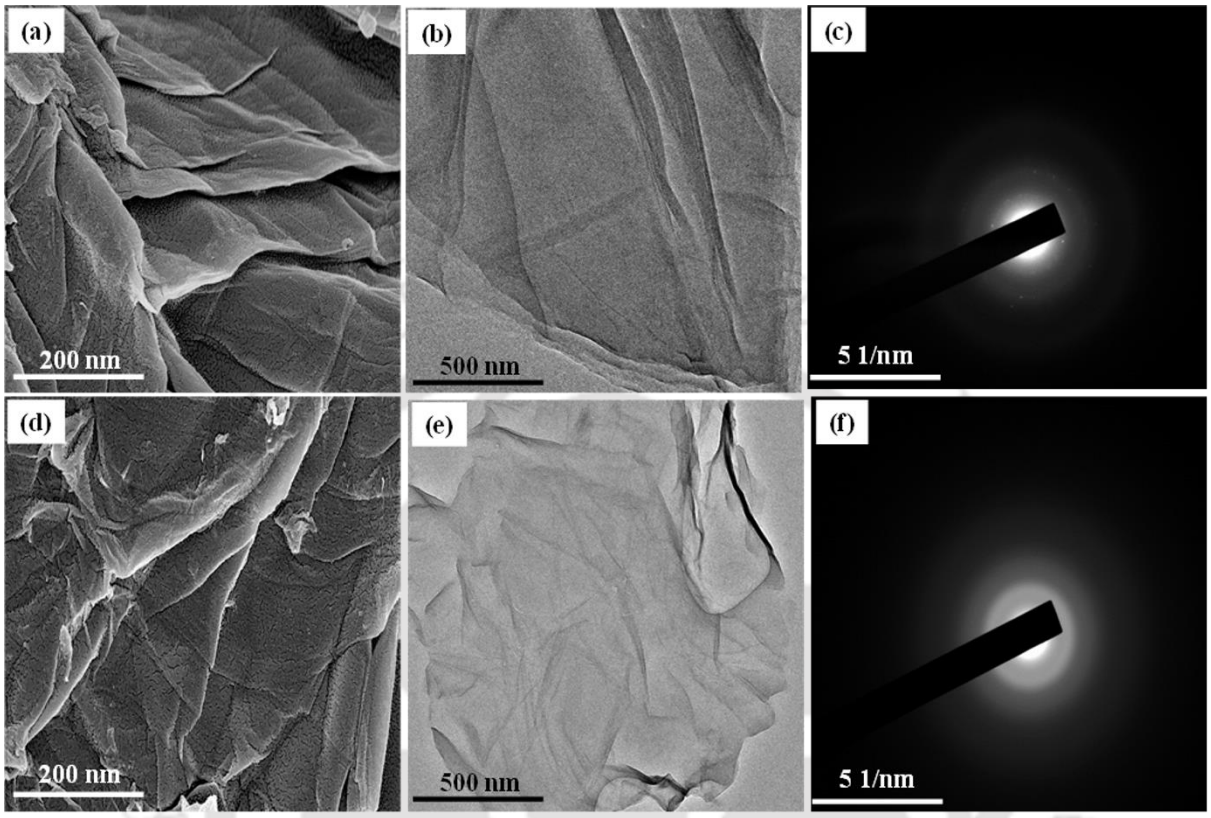

Figure 5.3. (a), (b) and (c) are FESEM, FETEM and SAED images of GO and (d), (e) and (f) are FESEM, FETEM and SAED images of Lys-c-GO, respectively.

5.3.1.2. Morphological Analysis

To study the morphological structure of GO and Lys-c-GO, FESEM and FETEM measurements were performed, as shown in Figure 5.3. We can clearly see that in its native state, GO has a flake-like and wrinkled appearance. This might be attributed to the presence of various chemically active functional groups on their basal planes, such as epoxy, carboxyl and hydroxyl, as GO has a natural tendency to unfold and present wrinkled morphology. Compared to GO, more transparent, wrinkled and folded nanosheets were observed for Lys-c-GO. This might be due to Lys's multifunctionality resulting in the interaction between the functionalized GO sheets and the polar groups attached to Lys.[13,14] The microscopic images confirm that the

morphology of the GO sheets has not been affected after conjugation with Lys. In addition, Figure 5.3c and f, display the SAED pattern of Lys-c-GO, which shows the amorphous nature of GO and Lys-c-GO.

5.3.1.3. Thermal Stability Analysis

The thermal stability of GO and Lys-c-GO was investigated using TGA analysis and the findings are presented in Figure 5.4a. For the GO curve, weight loss of 16.13 % up to 166 ºC is observed due to the evaporation of residual water. At around 213 ºC, a weight loss of 32.19 % is observed due to the removal of bounded moisture content from GO layers. Finally, a gradual weight loss was observed due to the decomposition of remaining oxygenated functional groups.[15] For the Lys-c-GO, a weight loss of 10.45% was observed upto 160 °C, then 28.7% loss between 158 ºC and 220 ºC was observed and finally, a gradual weight loss indicating a decrease in the amount of oxygen-containing functional groups in Lys-c-GO. The weight loss in the Lys-c-GO sample is observed to be smaller than those of GO, which indicates that the thermal stability has enhanced and Lys has been well adsorbed on GO after the conjugation reaction.[16]

5.3.2. Characterization of Lys-c-GO@CS(x) MMMs

5.3.2.1. Thermal Stability Analysis

The thermal stability test of the neat CS membrane and Lys-c-GO embedded MMMs was conducted using TGA analysis (Figure 5.4b). The primary weight loss for all the membranes occurred at around 115 ºC, attributed to the loss of unbound moisture content. Subsequently, weight loss at approximately 198 ºC was observed, corresponding to the depolymerization and decomposition of polymer units. Finally, a significant weight loss was observed at around 290 ºC, which was attributed to the saccharide ring degradation of the CS matrix. For neat chitosan and Lys-c-GO blended chitosan, the total weight loss was 43.1%,

40.66% (Lys-c-GO@CS(0.5)), 40% (Lys-c-GO@CS(1)) and 35.89% (Lys-c-GO@CS(2)), respectively. This weight loss was due to the pyrolysis of organic moieties, as confirmed by other literature.[17,18]

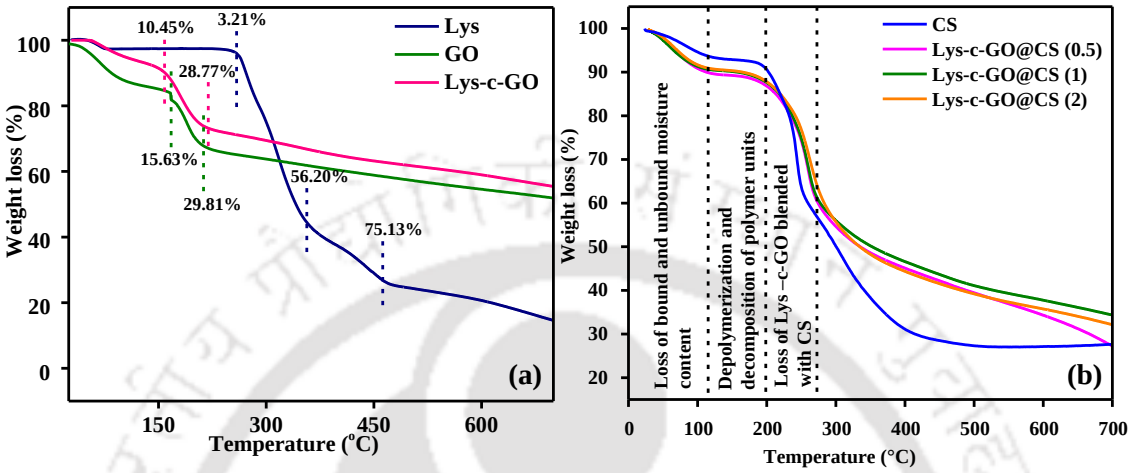

Figure 5.4. (a) TGA analysis of Lys, GO and Lys-c-GO, respectively and (b) TGA analysis of Lys-c-GO incorporated MMMs.

5.3.2.2. Structural Analysis

Figure 5.5a depicts the FTIR spectra of a neat CS membrane and Lys-c-GO embedded MMMs. For chitosan, the peak at 1361 cm^{-1} and 1557 cm^{-1} corresponds to -NH bending of -NH_3 and strong N-O carbon stretching of the nitro group, respectively. The peaks at 1637 cm^{-1} represent the C=C stretching vibrations of alkene groups. Additionally, the peak observed in chitosan at 3321 cm^{-1} results from the overlapping of weak -NH and -OH stretching vibrations. All of these peaks are present in the chitosan membrane, as confirmed by other literature.[19,20] With the addition of Lys-c-GO onto the chitosan membrane, three new peaks were discovered. For CS-lys-GO, the peak at 1647 cm^{-1} corresponds to the C=O stretching band of carboxylic acid and the peak at 1147 cm^{-1} corresponds to C-O stretching, revealing the presence of GO on the chitosan membrane.[21,22]

To study the effects of Lys-c-GO on chitosan structure, the XRD pattern of chitosan

membrane with different weight % of Lys-c-GO has been recorded and showed in Figure 5.5b. There are two distinct types of XRD patterns persist in the pristine CS: crystalline and amorphous phases. The strong and wide distinctive peak at 2θ = 10.25º and 2θ = 20.75º were generated by the coexistence of the crystalline and non-crystalline phases. The peak intensity rapidly reduces with the addition of Lys-c- GO. This shows that the crystalline segment of the CS is inhibited by the addition of uniformly distributed Lys-c-GO. Hence more transport networks are created when the crystalline phase of the polymer decreases, which is expected to enhance the CO_2 permeance of membrane.[23]

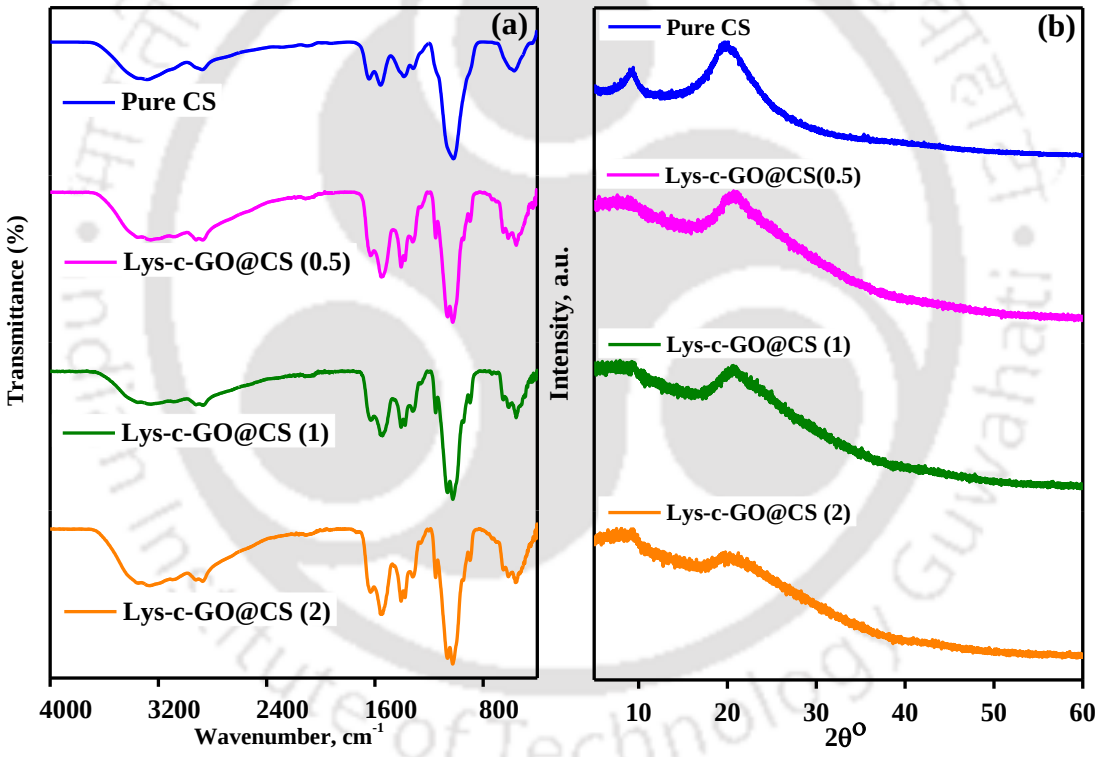

Figure 5.5. (a) FTIR and (b) XRD spectra of CS, Lys-c-GO@CS(0.5), Lys-c-GO@CS(1) and Lys-c-GO@CS(2) MMMs, respectively.

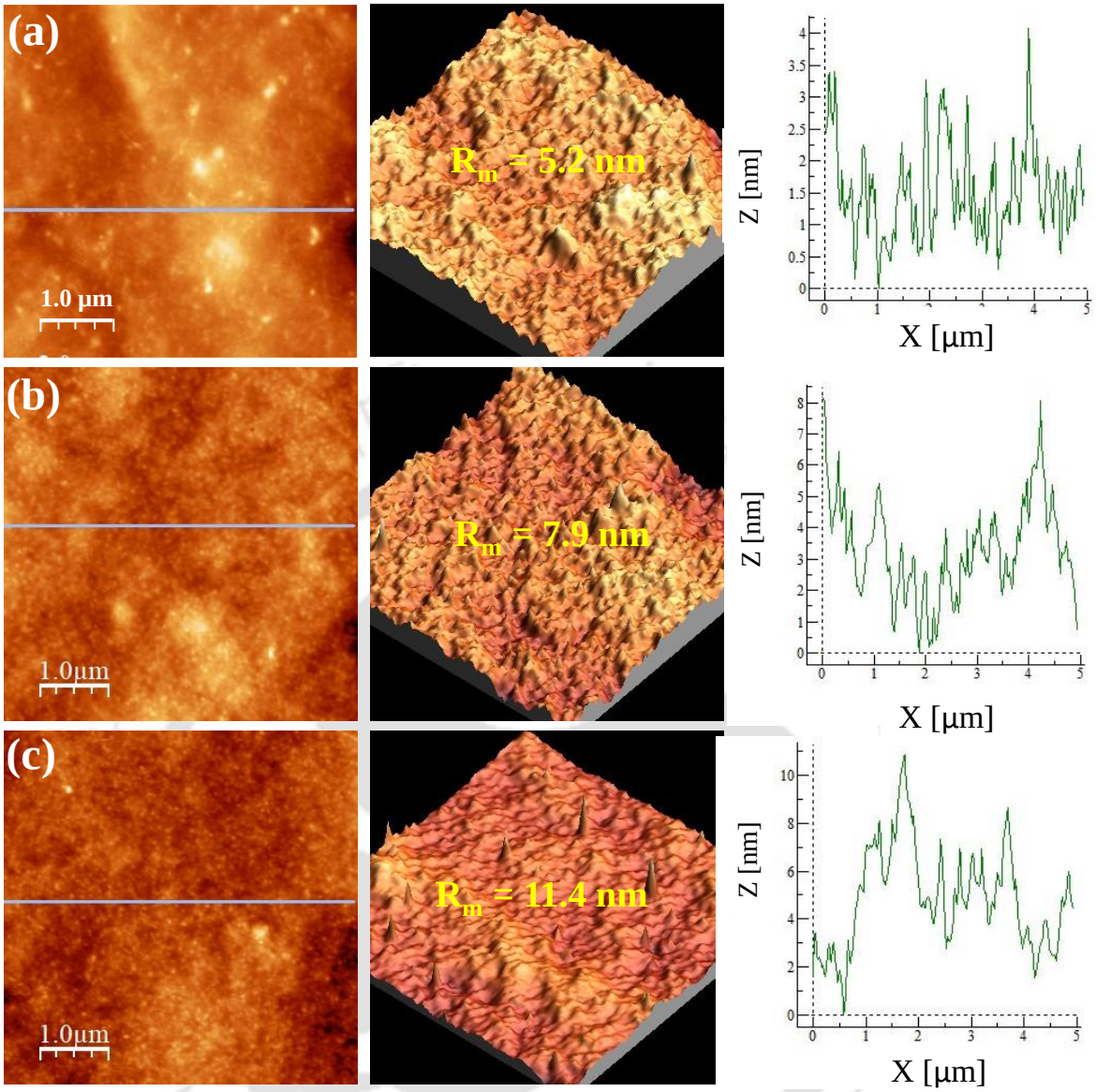

Figure 5.6. AFM images of top surfaces of (a) Lys-c-GO@CS(0.5), (b) Lys-c-GO@CS(1) and (c) Lys-c-GO@CS(2) MMMs, respectively.

5.3.2.3. Surface Roughness Analysis

The formation of a complete mixing of Lys-c-GO sheets with the CS matrix for the dense selective layer of the membranes was confimed by AFM images in Figure 5.6. When the filler concentration was increased from 0.5 to 2 wt%, the expected increment in the surface roughness was observed[24] and showed in Figure 5.6. The degree of surface roughness has been indicated by the obtained R_m values.

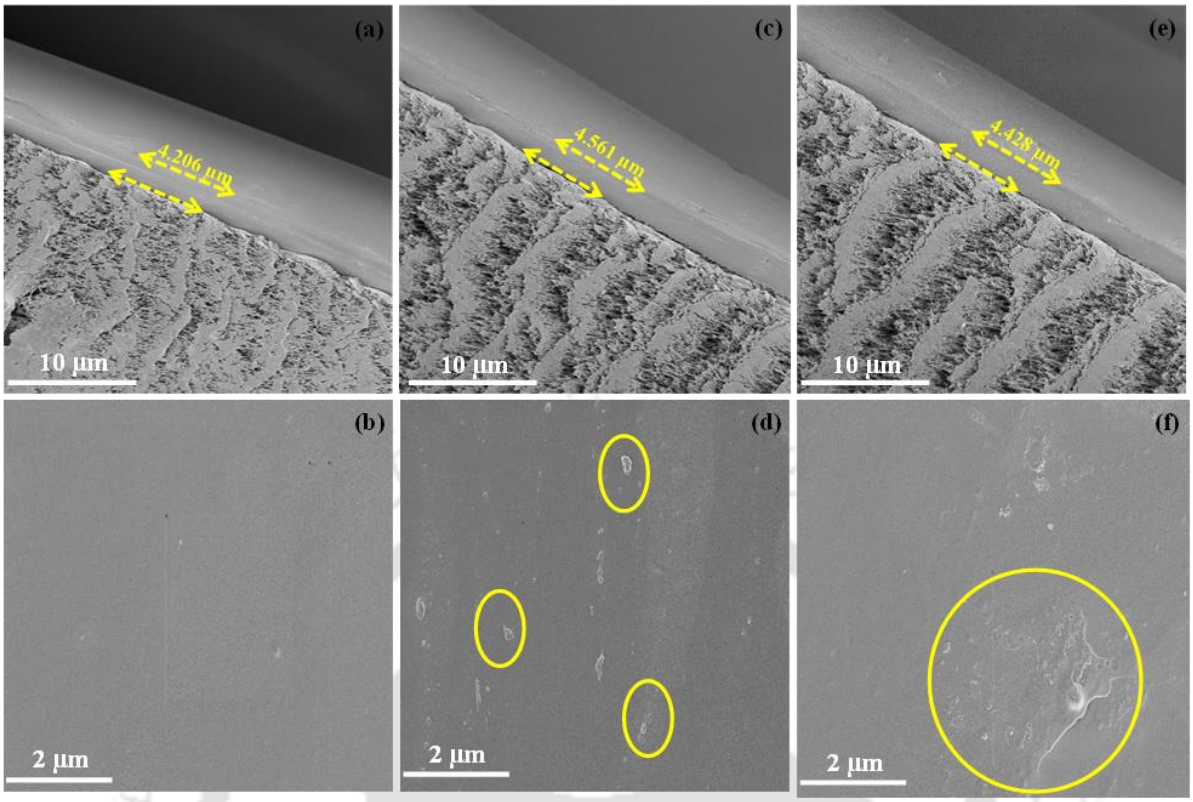

Figure 5.7. FESEM images obtained for the cross-section and top surfaces of (a), (b) Lys-c-GO@CS(0.5); (c), (d) Lys-c-GO@CS(1) and (e), (f) Lys-c-GO@CS(2) MMMs respectively.

5.3.2.4. Morphological Analysis

The top surface and cross-sectional morphologies of the neat CS membrane and Lys-c-GO filled CS MMMs were investigated using FESEM as shown in the Figure 5.7. For all the fabricated membranes, thin dense layer of around 4.5 µm was observed. Since the viscosity of casting solution was maintained above 1200 cp, the selective layer has not penetrated into the pores and thus well casted on PES support.[25] From Figure 5.7b, d and f, it can be observed that the CS with 1 wt% Lys-c-GO loading has the smooth and homogeneous surface. In contrast, as the loading of the Lys-c-GO increases the agglomeration of nanosheets on the matrix of the membrane increases. The surface of the Lys-c-GO loaded membrane is found to be more uniform depicting the good interface compatibility of filler with the polymer.

5.4. CO_2/N_2 Gas permeation study

The binary gas mixture of 20% CO_2 and 80% N_2 is separated using a gas permeation setup design, explained in Section 2.4 and illustrated in Scheme 2.2 and the influence of important operating variables such as Lys-c-GO content, temperature and transmembrane pressure is investigated precisely.

5.4.1. Effect of Lys-c-GO loading (wt%) on CO_2 separation performance of MMMs

To gain insight into the effect of Lys-c-GO content on the CO_2 separation performance, gas permeation studies of neat CS, Lys-c-GO@CS (x) MMMs were performed at the optimized operating conditions: temperature 85 °C, sweep to feed water supply ratio of 1.67, sweep absolute pressure 1.21 bar and feed absolute pressure 2 bar and shown in Figure 5.8. As the Lys-c-GO content rises, the membrane gas permeance performance increases at first, then declines at higher loading, which is consistent with the literature. [26,27,28] The reduction might be attributed to filler aggregation at increased loading, which reduces filler effective surface area.

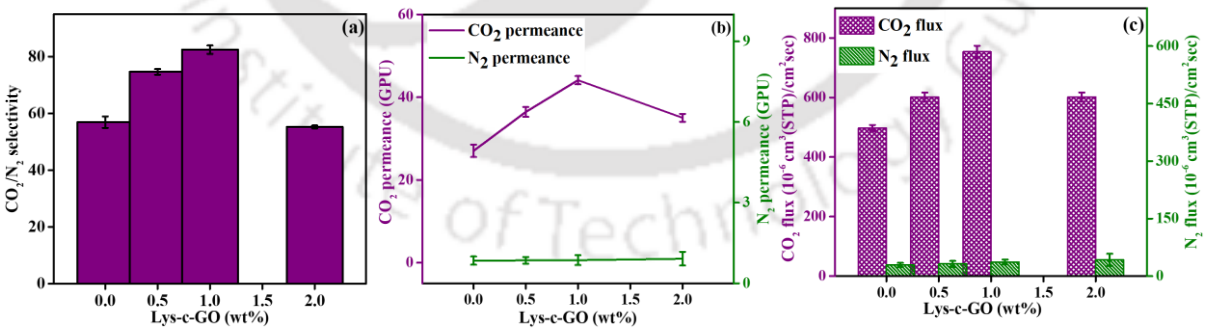

Figure 5.8. Effect of Lys-c-GO content on the gas separation performance of MMMs: (a) CO_2/N_2 selectivity, (b) CO_2, N_2 permeance and (c) CO_2, N_2 flux, respectively.

Lys-c-GO@CS(1) has showed the best performance as CO_2 permeance of 44.04 GPU and a CO_2/N_2 selectivity of 82.5. The CO_2 permeance of the Lys-c-GO@CS(1) membrane

increased from 15 GPU to 44 GPU compared to the pristine CS membrane, while the CO_2/N_2 selectivity rises from 48 to 82.5. The reduction in the separation performance at 2 wt% loading of Lys-c-GO is due to the poor interfacial compatibility of the Lys-c-GO with CS at higher loading that caused some interfacial defects and aggregation, which hindered the gas transport across the membrane.

5.4.2. Effect of operating temperature on CO_2 separation performance of optimized Lys-c-GO@CS(1) MMMs

Operating temperature and pressure have a major impact on the gas separation process. Initially, the influence of operating temperature on the gas permeation properties was examined as shown in Figure 5.9. In the temperatures between 25 and 115 °C with a sweep-to-feed water supply ratio of 1.67, an absolute pressure of 2 bar for feed gas and a 1.21 bar for sweep gas, CO_2 flux, CO_2 permeance and CO_2/N_2 selectivity were studied. At 25 °C, CO_2 flux, CO_2 permeance and CO_2/N_2 selectivity were 251 $cm^3(STP)/cm^2s$, 17.29 GPU and, 32.8, respectively. These values increased to 753 $cm^3(STP)/cm^2s$, 44.10 GPU and 82.5 at 85 °C, respectively. When the membrane's temperature increases, the polymer chains become more flexible, resulting in an increase in their diffusivity.[29] CO_2 permeance increased rapidly with temperature as the membrane showed much faster CO_2 transport. There is less energy barrier for the Lys-c-GO@CS(1) membrane, which is more evidence that the CO_2 separation efficiency was improved by using GO laminates rather than just bare CS membrane.

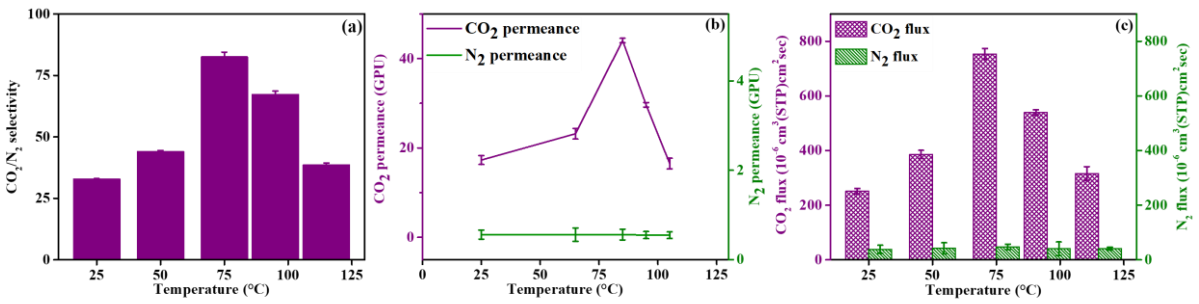

Figure 5.9. Effect of operating temperature on the gas separation performance of Lys-c-GO@CS(1) MMM: (a) CO_2/N_2 selectivity, (b) CO_2, N_2 permeance and (c) CO_2, N_2 flux, respectively.

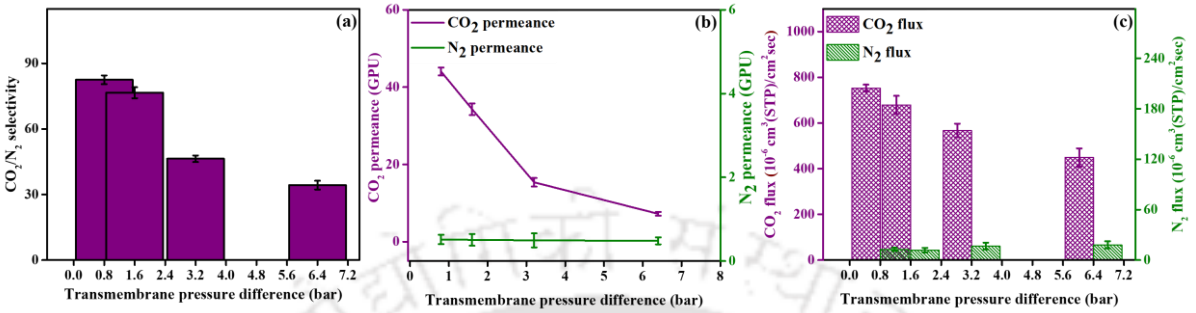

Figure 5.10. Effect of transmembrane pressure difference on the gas separation performance of Lys-c-GO@CS (1) MMM: (a) CO_2/N_2 selectivity, (b) CO_2, N_2 permeance and (c) CO_2, N_2 flux, respectively.

5.4.3. Effect of transmembrane pressure difference on CO_2 separation performance of optimized Lys-c-GO@CS(1) MMMs

To observe how pressure conditions can affect gas separation performance of Lys-c-GO@CS(1) MMM, transmembrane pressure across the membrane was varied from 0.8 bar to 6.4 bar. While other operating conditions were retained constant at 85 °C temperature, 1.67 sweep-to-feed water supply ratio. The obtained CO_2 permeance and CO_2/N_2 selectivity of the CO_2 permeance are shown in Figure 5.10. The CO_2/N_2 selectivity declines from 82.5 to 34.3 and the CO_2 permeance declines from 44.04 GPU to 15.38 GPU when the transmembrane pressure difference increases from 0.8 bar to 6.4 bar. Compaction of the polymeric matrix and GO sheets result in a smaller interlayer gap between layers, increasing gas transport resistance and consequently responsible for reduction in CO_2 permeation and CO_2/gas selectivity.[30]

5.4.4. Comparative study of the obtained results with the reported literature

The microstructures, physicochemical characteristics and gas transport behaviors of MMMs are all influenced by amino acid modified GO sheets. With the Lys-c-GO loading, the

effective molecular transport area was varying and higher loading of Lys-c-GO caused a polymer to become stiffer. The obtained results for Lys-c-GO@CS(1) were compared with literature and shown in Figure 5.12 and Table 5.2. The Lys-c-GO@CS membranes demonstrated a clear increment in the CO_2 separation performance after introducing Lys-c-GO sheets, breaking the trade-off relationship. Transcending Robeson' 2008 upper bound curve.

Table 5.1. A comparative account of the CO_2 separation Performance of the optimized Lys-c-GO@CS (1) MMM with available literature.

Polymer	**Filler**	**Operating conditions**	**CO_2 permeability (Barrer)**	**CO_2/N_2 selectivity**	**References**
CS	-	85 °C, 2.21 bar	60	48	This work
CS	Silk fibroin/Graphene Oxide	90 °C, 2.21 bar	93	81	[31]
Pebax	Polyethylene Glycol–polyethylenimine – GO	30 °C, 2 bar	1330	120	[27]
PVAm/CS	GO	25 °C, 1 bar	81	107	[32]
PEBAX MH1657	Aminated-GO	25 °C, 4 bar	47.5	83.2	[33]
PEBAX MH1657	Aligned-GO	25 °C, 4 bar	83.2	28.1	[34]
PEBAX MH1657	Random-GO	25 °C, 4 bar	29.6	142.9	[34]
CS	**Lys-c-GO**	**85°C, 2.21 bar**	**176**	**82.5**	**This Work**

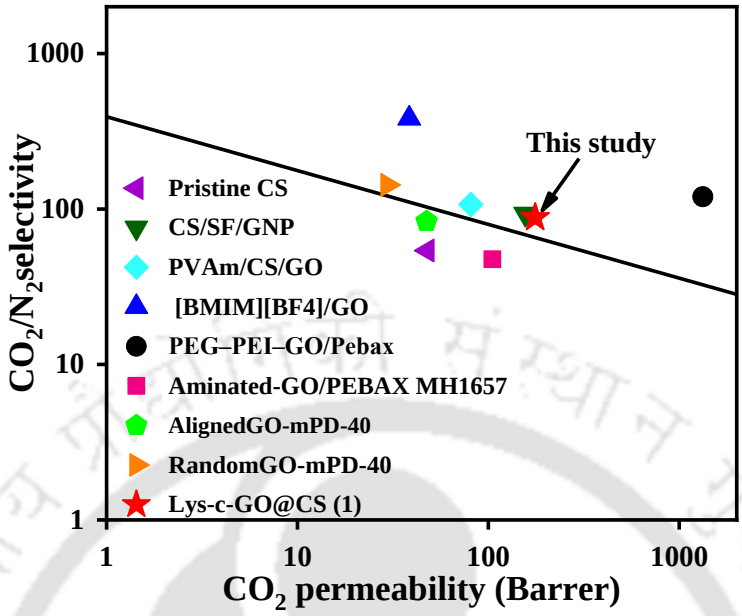

Figure 5.11. Robeson upper bound curve: Comparison of the CO_2 separation performance of the optimized Lys-c-GO@CS (1) MMM with the reported literature.

5.5. Conclusion

To enhance the separation efficiency of chitosan (CS), we successfully synthesized Lysine-functionalized graphene oxide embedded mixed matrix membranes (MMMs) by incorporating Lys-c-GO nanosheets into the CS matrix. Among the various Lys-c-GO concentrations studied, MMMs doped with 1 wt% Lys-c-GO demonstrated superior CO_2 separation performance compared to those with 0.5 wt% and 2 wt% Lys-c-GO. The CO_2 separation results revealed that MMMs containing 1 wt% Lys-c-GO exhibited commendable CO_2 permeance and CO_2/N_2 selectivity, achieving values of 44 GPU and 82.5, respectively. The presence of Lys-c-GO had a positive synergistic effect on the gas separation performance, significantly contributing to enhanced CO_2 selectivity. The introduction of amino groups linked to the GO sheets within the MMM structure played a pivotal role in facilitating high CO_2 selectivity. These amino groups acted as efficient pathways, allowing for preferential CO_2 transport through the membrane. Moreover, the selective barrier provided by the amine,

hydroxyl and carboxy groups of the Lys-c-GO nanosheets on the MMM surface contributed to the increased selectivity of the membrane.

Overall, our findings demonstrate the promising potential of Lys-c-GO@CS MMMs as efficient membranes for CO_2 separation, driven by the favorable interactions between Lys-c-GO nanosheets and the chitosan matrix, paving the way for advanced gas separation applications.

5.6. References

(1) Dai, Z.; Ansaloni, L.; Deng, L. Recent Advances in Multi-Layer Composite Polymeric Membranes for CO_2 Separation: A Review. *Green Energy Environ.* **2016**, *1* (2), 102–128. https://doi.org/10.1016/j.gee.2016.08.001.

(2) Zahri, K.; Wong, K. C.; Goh, P. S.; Ismail, A. F. Graphene Oxide/Polysulfone Hollow Fiber Mixed Matrix Membranes for Gas Separation. *RSC Adv.* **2016**, *6* (92), 89130–89139. https://doi.org/10.1039/c6ra16820e.

(3) Zhang, H.; Guo, R.; Hou, J.; Wei, Z.; Li, X. Mixed-Matrix Membranes Containing Carbon Nanotubes Composite with Hydrogel for Efficient CO_2 Separation. **2016**. https://doi.org/10.1021/acsami.6b09786.

(4) Goh, P. S.; Ismail, A. F.; Sanip, S. M.; Ng, B. C.; Aziz, M. Recent Advances of Inorganic Fillers in Mixed Matrix Membrane for Gas Separation. *Sep. Purif. Technol.* **2011**, *81* (3), 243–264. https://doi.org/10.1016/j.seppur.2011.07.042.

(5) Gutiérrez-Serpa, A.; Kundu, T.; Pasán, J.; Jiménez-Abizanda, A. I.; Kaskel, S.; Senkovska, I.; Pino, V. Zirconium-Based Metal–Organic Framework Mixed-Matrix Membranes as Analytical Devices for the Trace Analysis of Complex Cosmetic Samples in the Assessment of Their Personal Care Product Content. *ACS Appl. Mater. Interfaces* **2022**, *14* (3), 4510–4521. https://doi.org/10.1021/acsami.1c21284.

(6) Li, X.; Ma, L.; Zhang, H.; Wang, S.; Jiang, Z.; Guo, R.; Wu, H.; Cao, X. Z.; Yang, J.; Wang, B. Synergistic Effect of Combining Carbon Nanotubes and Graphene Oxide in Mixed Matrix Membranes for Efficient CO_2 Separation. *J. Memb. Sci.* **2015**, *479*, 1–10. https://doi.org/10.1016/j.memsci.2015.01.014.

(7) Cheng, L.; Liu, G.; Jin, W. Recent Progress in Two-Dimensional-Material Membranes for Gas Separation. *Wuli Huaxue Xuebao/ Acta Phys. - Chim. Sin.* **2019**, *35* (10), 1090–1098. https://doi.org/10.3866/PKU.WHXB201810059.

(8) Ahmadi, M.; Janakiram, S.; Dai, Z.; Ansaloni, L.; Deng, L. Performance of Mixed Matrix Membranes Containing Porous Two-Dimensional (2D) and Three-Dimensional (3D) Fillers for CO_2 Separation: A Review. *Membranes (Basel).* **2018**, *8* (3). https://doi.org/10.3390/membranes8030050.

(9) Ma, J.; Wang, X.; Wu, T.; Liu, Y.; Guo, Y.; Li, R.; Sun, X.; Wu, F.; Li, C.; Gao, J.; Liu, Y. Reduction of Graphene Oxide with L-Lysine to Prepare Reduced Graphene Oxide Stabilized with Polysaccharide Polyelectrolyte. *J. Mater. Chem. A* **2013**, *1* (6), 2192–2201. https://doi.org/10.1039/c2ta00340f.

(10) Das, P.; Mandal, B.; Gumma, S. L-Tyrosine Grafted Palladium Graphite Oxide and Sulfonated Poly(Ether Ether Ketone) Based Novel Composite Membrane for Direct Methanol Fuel Cell. *Chem. Eng. J.* **2021**, *423*, 130235. https://doi.org/10.1016/j.cej.2021.130235.

(11) Sapner, V. S.; Chavan, P. P.; Sathe, B. R. L -Lysine-Functionalized Reduced Graphene Oxide as a Highly Efficient Electrocatalyst for Enhanced Oxygen Evolution Reaction. *ACS Sustain. Chem. Eng.* **2020**, *8* (14), 5524–5533. https://doi.org/10.1021/acssuschemeng.9b06918.

(12) Zhou, X.; Huang, H.; Zhu, R.; Sheng, X.; Xie, D.; Mei, Y. Facile Modification of Graphene Oxide with Lysine for Improving Anti-Corrosion Performances of Water-

Borne Epoxy Coatings. *Prog. Org. Coatings* **2019**, *136*, 105200. https://doi.org/10.1016/j.porgcoat.2019.06.046.

(13) Zhang, X.; Li, K.; Li, H.; Lu, J.; Fu, Q.; Chu, Y. Graphene Nanosheets Synthesis via Chemical Reduction of Graphene Oxide Using Sodium Acetate Trihydrate Solution. *Synth. Met.* **2014**, *193*, 132–138. https://doi.org/10.1016/j.synthmet.2014.04.007.

(14) Zhang, Q.; Wu, B.; Song, R.; Song, H.; Zhang, J.; Hu, X. Preparation, Characterization and Tribological Properties of Polyalphaolefin with Magnetic Reduced Graphene Oxide/Fe3O4. *Tribol. Int.* **2020**, *141*, 105952. https://doi.org/10.1016/j.triboint.2019.105952.

(15) Aliabadian, E.; Sadeghi, S.; Rezvani Moghaddam, A.; Maini, B.; Chen, Z.; Sundararaj, U. Application of Graphene Oxide Nanosheets and HPAM Aqueous Dispersion for Improving Heavy Oil Recovery: Effect of Localized Functionalization. *Fuel* **2020**, *265*, 116918. https://doi.org/10.1016/j.fuel.2019.116918.

(16) Li, J.; Zhu, W.; Zhang, S.; Gao, Q.; Li, J.; Zhang, W. Amine-Terminated Hyperbranched Polyamide Covalent Functionalized Graphene Oxide-Reinforced Epoxy Nanocomposites with Enhanced Toughness and Mechanical Properties. *Polym. Test.* **2019**, *76*, 232–244. https://doi.org/10.1016/j.polymertesting.2019.03.017.

(17) Rajendiran, R.; Patchaiyappan, A.; Harisingh, S.; Balla, P.; Paari, A.; Ponnala, B.; Perupogu, V.; Lassi, U.; Seelam, P. K. Synergistic Effects of Graphene Oxide Grafted Chitosan & Decorated MnO_2 Nanorods Composite Materials Application in Efficient Removal of Toxic Industrial Dyes. *J. Water Process Eng.* **2022**, *47*, 102704. https://doi.org/10.1016/j.jwpe.2022.102704.

(18) Joseph R.M.; Merrick M.M.; Liu R.; Fraser A.C.; Moon J.D.; Choudhury S.R.; Lesko J; Freeman B.D.; Riffle J.S.; Synthesis and Characterization of Polybenzimidazole Membranes for Gas Separation with Improved Gas Permeability: A Grafting and

Blending Approach. *J. Memb. Sci.* **2018**, *10*, 1–14. https://doi.org/10.1016/j.seppur.2018.03.028.

(19) Gong, Y.; Yu, Y.; Kang, H.; Chen, X.; Liu, H.; Zhang, Y.; Sun, Y.; Song, H. Synthesis and Characterization of Graphene Oxide/Chitosan Composite Aerogels with High Mechanical Performance. *Polymers (Basel).* **2019**, *11* (5), 777. https://doi.org/10.3390/polym11050777.

(20) Kamal, S.; Khan, F.; Kausar, H.; Khan, M. S.; Ahmad, A.; Ishraque Ahmad, S.; Asim, M.; Alshitari, W.; Nami, S. A. A. Synthesis, Characterization, Morphology and Adsorption Studies of Ternary Nanocomposite Comprising Graphene Oxide, Chitosan and Polypyrrole. *Polym. Compos.* **2020**, *41* (9), 3758–3767. https://doi.org/10.1002/pc.25673.

(21) Khan, Y. H.; Islam, A.; Sarwar, A.; Gull, N.; Khan, S. M.; Munawar, M. A.; Zia, S.; Sabir, A.; Shafiq, M.; Jamil, T. Novel Green Nano Composites Films Fabricated by Indigenously Synthesized Graphene Oxide and Chitosan. *Carbohydr. Polym.* **2016**, *146*, 131–138. https://doi.org/10.1016/j.carbpol.2016.03.031.

(22) Shamekhi, M. A.; Mirzadeh, H.; Mahdavi, H.; Rabiee, A.; Mohebbi-Kalhori, D.; Baghaban Eslaminejad, M. Graphene Oxide Containing Chitosan Scaffolds for Cartilage Tissue Engineering. *Int. J. Biol. Macromol.* **2019**, *127*, 396–405. https://doi.org/10.1016/j.ijbiomac.2019.01.020.

(23) Yadav, M.; Ahmad, S. Montmorillonite/Graphene Oxide/Chitosan Composite: Synthesis, Characterization and Properties. *Int. J. Biol. Macromol.* **2015**, *79*, 923–933. https://doi.org/10.1016/j.ijbiomac.2015.05.055.

(24) Prasad, B.; Mandal, B. CO_2 Separation Performance by Chitosan/Tetraethylenepentamine/Poly(Ether Sulfone) Composite Membrane. *J. Appl. Polym. Sci.* **2017**, *134* (34), 1–9. https://doi.org/10.1002/app.45206.

(25) Barooah, M.; Mandal, B. Synthesis, Characterization and CO_2 Separation Performance of Novel PVA/PG/ZIF-8 Mixed Matrix Membrane. *J. Memb. Sci.* **2019**, *572*, 198–209. https://doi.org/10.1016/j.memsci.2018.11.001.

(26) Prasad, B.; Mandal, B. Preparation and Characterization of CO_2-Selective Facilitated Transport Membrane Composed of Chitosan and Poly(Allylamine) Blend for CO_2/N_2 Separation. *J. Ind. Eng. Chem.* **2018**, *66*, 419–429. https://doi.org/10.1016/j.jiec.2018.06.009.

(27) Li, X.; Cheng, Y.; Zhang, H.; Wang, S.; Jiang, Z.; Guo, R.; Wu, H. Efficient CO_2 Capture by Functionalized Graphene Oxide Nanosheets as Fillers To Fabricate Multi-Permselective Mixed Matrix Membranes. *ACS Appl. Mater. Interfaces* **2015**, *7* (9), 5528–5537. https://doi.org/10.1021/acsami.5b00106.

(28) Dai, Y.; Ruan, X.; Yan, Z.; Yang, K.; Yu, M.; Li, H.; Zhao, W.; He, G. Imidazole Functionalized Graphene Oxide/PEBAX Mixed Matrix Membranes for Efficient CO_2 Capture. *Sep. Purif. Technol.* **2016**, *166*, 171–180. https://doi.org/10.1016/j.seppur.2016.04.038.

(29) Singh, S.; Varghese, A. M.; Reddy, K. S. K.; Romanos, G. E.; Karanikolos, G. N. Polysulfone Mixed-Matrix Membranes Comprising Poly(Ethylene Glycol)-Grafted Carbon Nanotubes: Mechanical Properties and CO_2 Separation Performance. *Ind. Eng. Chem. Res.* **2021**, *60* (30), 11289–11308. https://doi.org/10.1021/acs.iecr.1c02040.

(30) Prasad, B.; Mandal, B. Moisture Responsive and CO_2 Selective Biopolymer Membrane Containing Silk Fibroin as a Green Carrier for Facilitated Transport of CO_2. *J. Memb. Sci.* **2018**, *550*, 416–426. https://doi.org/10.1016/j.memsci.2017.12.061.

(31) Prasad, B.; Mandal, B. Graphene-Incorporated Biopolymeric Mixed-Matrix Membrane for Enhanced CO_2 Separation by Regulating the Support Pore Filling. *ACS Appl. Mater. Interfaces* **2018**, *10* (33), 27810–27820. https://doi.org/10.1021/acsami.8b09377.

(32) Shen, Y.; Wang, H.; Liu, J.; Zhang, Y. Enhanced Performance of a Novel Polyvinyl Amine/Chitosan/Graphene Oxide Mixed Matrix Membrane for CO_2 Capture. *ACS Sustain. Chem. Eng.* **2015**, *3* (8), 1819–1829. https://doi.org/10.1021/acssuschemeng.5b00409.

(33) Mohammed, S. A.; Nasir, A. M.; Aziz, F.; Kumar, G.; Sallehhudin, W.; Jaafar, J.; Lau, W. J.; Yusof, N.; Salleh, W. N. W.; Ismail, A. F. CO_2/N_2 Selectivity Enhancement of PEBAX MH 1657/Aminated Partially Reduced Graphene Oxide Mixed Matrix Composite Membrane. *Sep. Purif. Technol.* **2019**, *223*, 142–153. https://doi.org/10.1016/j.seppur.2019.04.061.

(34) Mehdinia Lichaei, M.; Pazani, F.; Aroujalian, A.; Rodrigue, D. Two-Step Surface Functionalization/Alignment Strategy to Improve CO_2/N_2 Separation from Mixed Matrix Membranes Based on PEBAX and Graphene Oxide. *Process Saf. Environ. Prot.* **2022**, *163*, 36–47. https://doi.org/10.1016/j.psep.2022.05.024.

CHAPTER 6

Green Synthesized HF-free MIL-100(Fe) Nanoparticles Infused Chitosan Mixed Matrix Membrane for Enhanced CO_2 Permeance

In this chapter of the thesis, we adopted a green route to synthesis MIL-100(Fe) MOF. The MOF nanoparticles are utilized as nanofiller to synthesize CS MMM. The advantages of the zwitterion mechanism via amine groups of CS and the high surface area and CO_2 affinity via open-metal sites of MIL-100(Fe) nanoparticles are exploited in the study. The effect of MOF addition on the chemical, physical, thermal structure and CO_2 separation performance of synthesized MMMs are presented and compared with the pristine CS membrane. This research work is scientifically acknowledged in ***"ACS Industrial & Engineering Chemistry Research"****.*

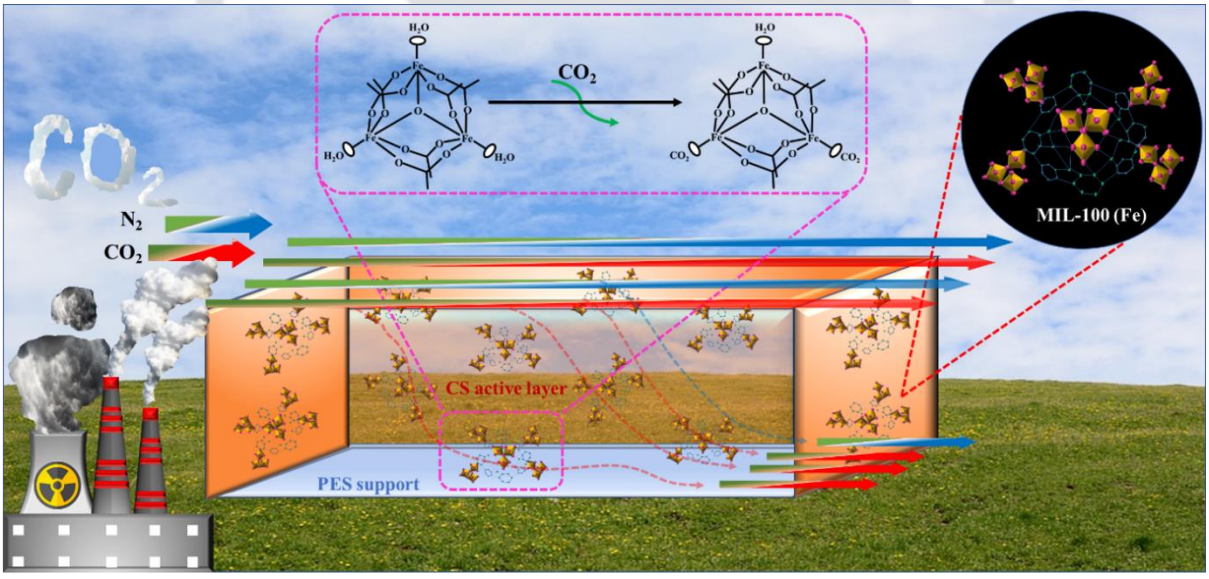

DOI: https://doi.org/10.1021/acs.iecr.3c01648

6.1. Introduction

Metal-organic frameworks (MOFs), an emerging class of porous crystalline nanomaterials, have seen a surge in interest in employing fillers to construct MMMs for gas separation over the last decade due to the synergistic effect of both organic ligand and metal center.[1,2] The partial organic nature reduces the solubility difficulty of fillers into a polymeric matrix while the high oxidation state of the metal center adds to the acid stability during the CO_2 separation.[3] Furthermore, MOF materials offer enhanced versatility in their structure, allowing for the synthesis of a wide range of shapes and sizes, surpassing the capabilities of graphene oxide (GO). Therefore, nano-sized MOF material adds on intrinsic properties towards the enhanced CO_2 separation activity. In this regard, a variety of MOFs were developed to utilize as nanofiller for MMMs, such as Cu-BPY-HFS,[4] HKUST-1,[5] ZIF-8,[6] UiO-66,[7-8] Mil-53,[9] MIL-100, including MIL-100(Fe, Al, Cr, Ni, etc.) for gas separation.[10–12]

The green synthesis route for producing filler and mixed matrix membranes (MMMs) to capture CO_2 from the gaseous mixture is highly recommendable. Taking this into account, out of the countless MOFs available, we have chosen MIL-100 (Fe) as nanofiller. The synthesis of MIL-100(Fe) nanoparticles at ambient conditions with the usage of low-cost green chemicals and the absence of corrosive inorganic acids establish a sustainable approach for the development of the MMM.

MIL-100(Fe) is one of the few thermodynamically stable MOFs with high surface area and strong adsorption separation properties especially at humid conditions.[13] In MIL-100(Fe), the μ3-Oxo-bridged trinuclear metal nodes have three terminal coordination sites occupied by water or solvent molecules used in the synthesis process. At high temperature these terminal water molecules are eliminated resulting into formation of open-metal sites that have the potential to interact with the incoming guest molecules. The presence of Fe, as an earth

abundant element, makes the MIL-100(Fe) environmentally friendly nano-material compared to other MOFs with Cr, Ni, Cu and Co as the central ions. Additionally, the synthesis of MIL-100(Fe) nanoparticles at ambient conditions with the usage of low-cost green chemicals and the absence of corrosive inorganic acids establish a sustainable approach for the development of the MMM.

The MMMs developed by Nabais et al. with various loading percentages (10 wt%, 20 wt% and 30 wt%) of Fe(BTC) as a nanofiller into Matrimid®5218 polymer surpassed the known Robeson upper-bound correlation at 80 °C, making them a good choice for CO_2 separation.[14] Dorosti et al. reported a PEBAX/Fe-BTC membrane with the highest CO_2 permeability of 425.4 Barrer at 40% loading and a selectivity of 22.19. He also noticed that a 25% loading into the membrane increased CO_2 permeability and selectivity by 50% and 9% at 7 bar compared to the base polymer.[15]

Even though MIL-100(Fe) nanoparticles (NPs) and CS have been the subject of several application-based studies independently and jointly, their combined performance in the CO_2 separation application has not yet been investigated. In this contribution, we focused on the development of MIL-100(Fe) MOF as a nanofiller via a green synthetic route, with chitosan (CS) as a base material. Both materials are combined in different weight ratios to fabricate the mixed matrix membrane with optimum filler loading. Furthermore, the CO_2 separation over the N_2 study is also evaluated with the different conditions.

6.2. Experimental Section

6.2.1. Synthesis of HF-free MIL-100(Fe) Nanoparticles

MIL-100(Fe) nanoparticles were synthesized via HF-free route at room temperature, as shown in Scheme 6.1, according to the previously reported literature with some

modifications.[16] 11 mmol of iron (II) sulfate heptahydrate ($FeSO_4.7H_2O$) was dissolved in 100 mL of Millipore water and named Solution-I and 8 mmol of Trimesic acid was dissolved in 25 mL of 1 M NaOH solution and named Solution-II. Solution-II was added dropwise to Solution-I and stirred for 24 hours at room temperature. The obtained product was repeatedly washed with water and ethanol and later recovered via centrifugation at 4000 rpm. The recovered product was activated in methanol solution for 3 days and then kept for vacuum drying at 120 ºC for 10 h. The final product was weighed, labeled as HF-free MIL-100(Fe) and kept in a desiccator for further characterization and experimental studies.

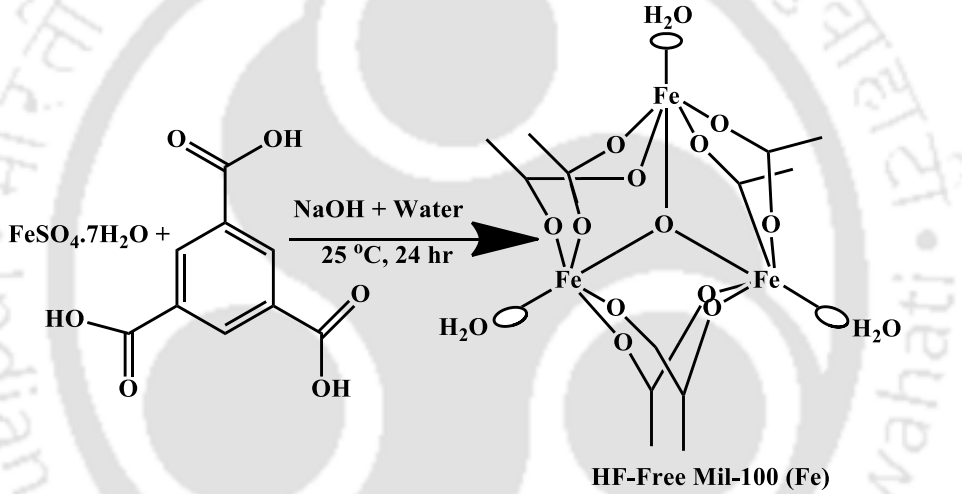

Scheme 6.1. Schematic representation of the HF-free route of MIL-100(Fe) NPs synthesis.

6.2.2. Fabrication of MIL-100(Fe) embedded CS (CSM) MMMs

1 wt% of chitosan solution (aqueous) was prepared by dissolving chitosan flakes into a 100 mL of 1 vol% acetic acid (AA) solution. The MIL-100(Fe) nanoparticles (5, 10, 15 and 20 wt%) were dispersed in AA solution and sonicated for a few minutes to obtain a homogeneous MOF suspension. The MOF suspension was mixed with the prepared chitosan solution and stirred overnight. Undissolved particles and formed bubbles (due to continuous stirring) from the solution were removed via centrifuging for 4-5 minutes at 5,000 rpm. The solution casting

method was used to cast the membranes on polyethersulfone (PES) support and their thickness was monitored using a film-casting blade. The casted membranes were then dried in a laminar hood for 24 hours. To completely remove all the moisture, the membranes were dried in a hot air oven for 12 hours at 110 °C. To support the enhancement of properties upon incorporation of MOF particles into the CS matrix, a neat CS membrane was also prepared under the same experimental conditions onto the PES support. The prepared membranes with 0, 5, 10, 15 and 20 wt% HF free MIL-100(Fe) nanoparticles (NPs) in the CS matrix were named CS, CSM-5, CSM-10, CSM-15 and CSM-20, respectively. The digital images of the prepared membranes are shown the Figure 6.1. Finally, the prepared membranes were cut to modular size for the CO_2 separation study.

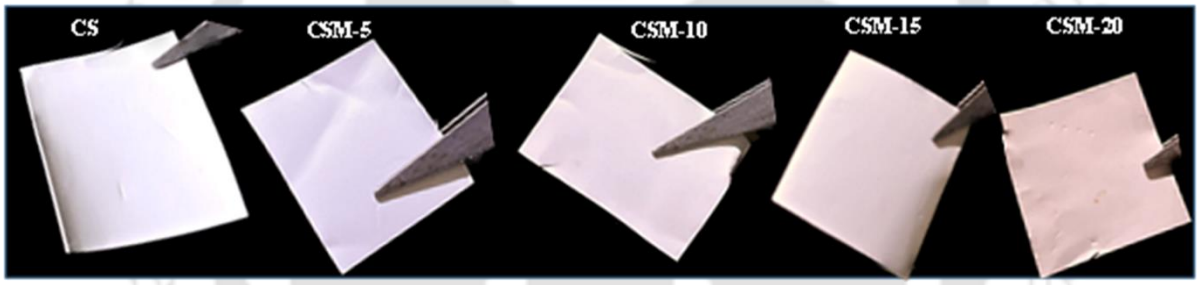

Figure 6.1: The digital images of the membranes: (a) CS, (b) CSM-5, (c) CSM-10, (d) CSM-15 and (e) CSM-20.

6.3. Results and Discussions

6.3.1. Characterization of synthesized HF-free MIL-100(Fe) NPs

6.3.1.1. Electronic State Analysis

The state of different elements of HF-free MIL-100(Fe) MOF was examined using X-ray photoelectron spectroscopy (XPS) and shown in Figure 6.2. The survey scan, as shown in Figure 6.2a, demonstrates the formation of the MOF nanoparticles as they comprise the three

elements Fe, O and C. High-resolution core-level spectra of all three elements Fe, C and O are displayed in Figure 6.2b, c and d, respectively.

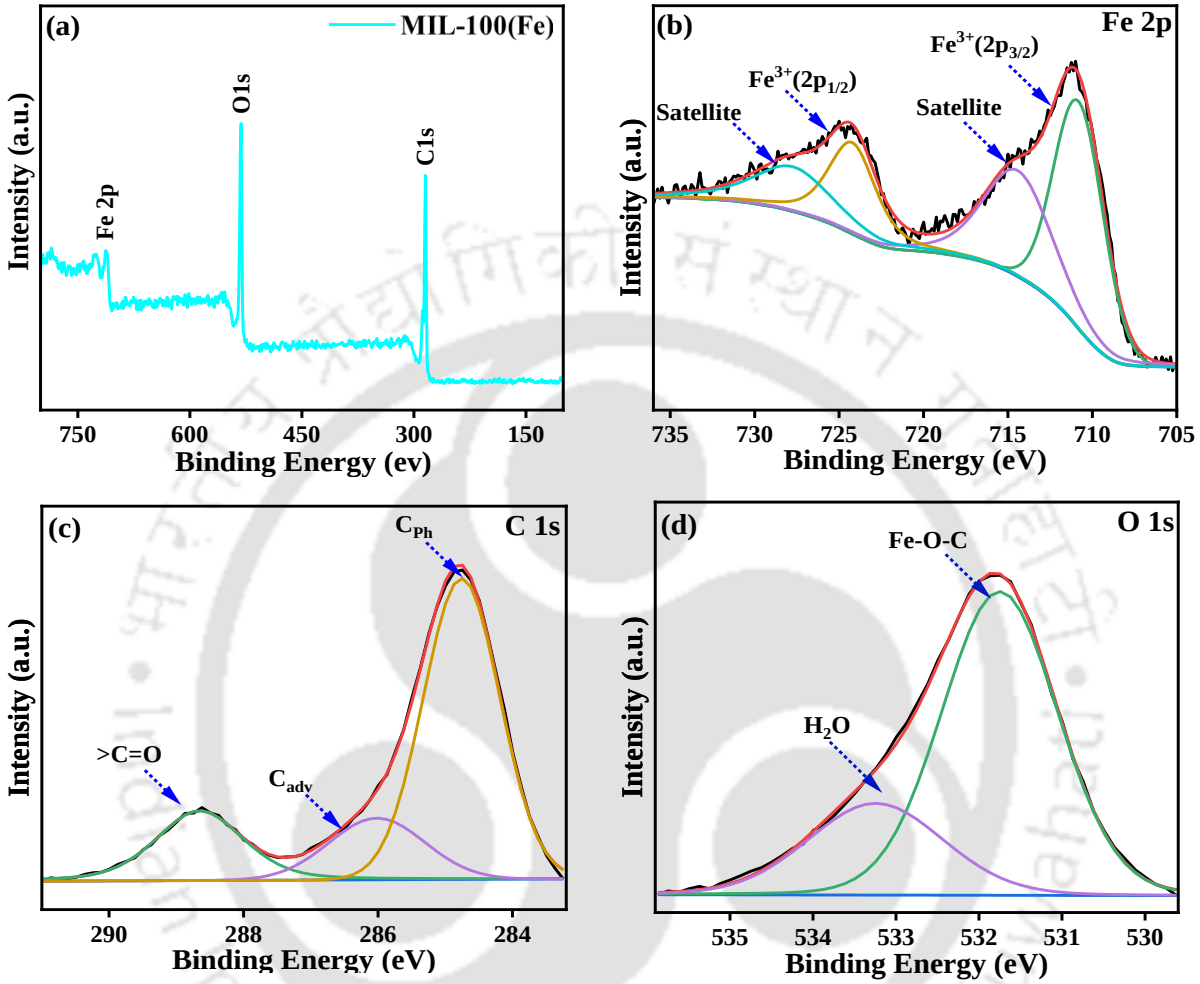

Figure 6.2. XPS spectra of HF free MIL-100(Fe) NPs: (a) survey spectra, (b) Fe 2p, (c) C 1s and (d) O 1s.

The four deconvoluted peaks from the high-resolution Fe 2p spectra are shown in Figure 6.2b. Those four peaks at binding energies (B.E.) of 710.81 eV, 714.41 eV, 724.21 eV and 727.7 eV, are related to the Fe^{3+} ($2p_{3/2}$) and Fe^{3+} ($2p_{1/2}$) peaks. It confirms the presence of Fe metal in +3 oxidation state formed during the synthesis of MOF.[17] As displayed in Figure 6.2c, the high-resolution spectra of C 1s have three peaks at B.E. of 284.75 eV, 286.01 eV and 288.64 eV; these peaks are associated with phenyl, surface and carboxyl signals.[18] Figure 6.2d

displays the XPS core level 1s spectrum of oxygen, which can be deconvoluted into two peaks at B.E. of 531.75 eV and 533.25 eV that correspond to Fe-O-C species in the crystal lattice and adsorbed water molecules.[17,18] XPS spectra amply support the effective formation of HF-free MIL-100(Fe) nanoparticles.

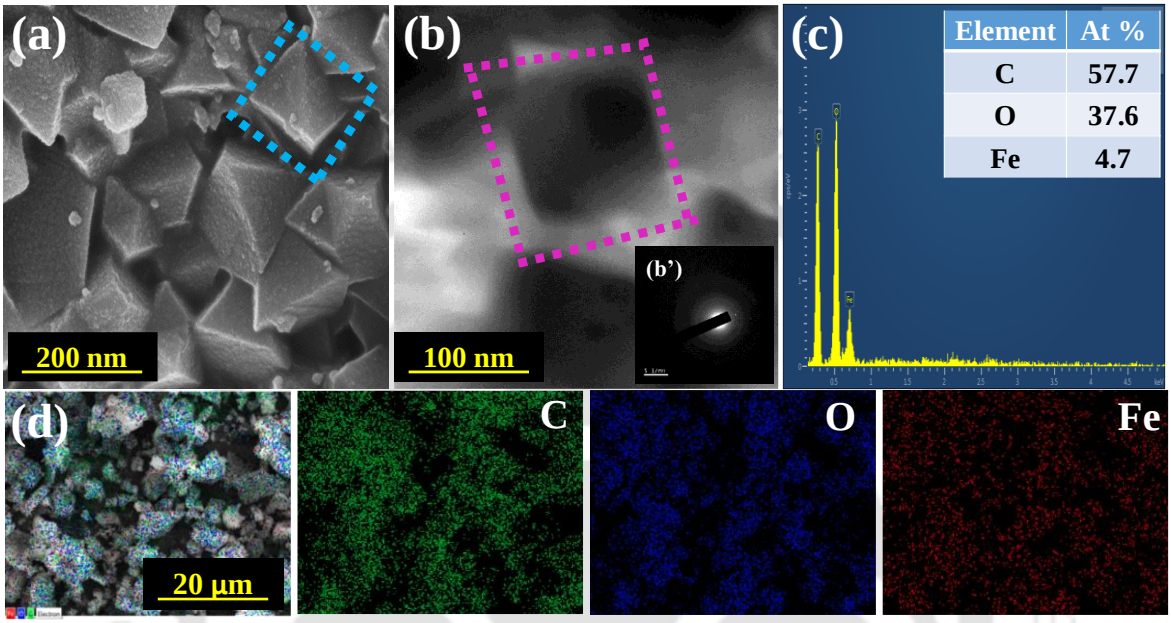

Figure 6.3. (a) SEM images, (b, b') TEM images, (c) EDX spectra and (d) EDX mapping of the synthesized HF-free MIL-100(Fe) NPs showing the uniform distribution of carbon (green), oxygen (blue) and iron (red).

6.3.1.2. Morphological and Elemental Analysis

The scanning electron microscopy (SEM), transmission electron microscopy (TEM) and energy dispersive X-ray spectroscopy (EDX) images of the fabricated HF-free MIL-100(Fe) nanoparticles are displayed in Figure 6.3. MIL-100(Fe) has irregular octahedron morphologies with particle size in the range of 50-150 nm, as evidenced in SEM images in Figure 6.3a and TEM images in Figure 3b, which is consistent with earlier findings in the literature.[19] The EDX spectra and elemental mapping as shown in Figure 6.3c and d,

respectively, confirm the presence of the primary constituents (Fe, C and O) of MIL-100(Fe) nanoparticles.

6.3.1.3. Structural Analysis

Figure 6.4a display the Fourier transform infrared **(**FTIR) spectra of the synthesized HF-free MIL-100(Fe) NPs. The vibration of the O-H group causes a broad peak at 3000-3300 cm^{-1} in the MIL-100(Fe) spectra. Strong peaks at 755 cm^{-1} and 701 cm^{-1} are indicative of the 1,3,5-tri-substitution of the benzene ring. The peaks at 1635 cm^{-1}, 1453 cm^{-1} and 1378 cm^{-1} are attributable to the asymmetrical and symmetrical vibrations of the complementary carboxyl group. The characteristic peak of NPs is seen at 618 $cm^{-1,}$ which depicts the vibration of the Fe-O bond in MIL-100(Fe).[20] The aforementioned results showed that although the carboxyl group of BTC has lost its bond, the BTC base frame is still present in the MIL-100(Fe) structure. This is in line with earlier studies and supports the creation of bonds between Fe metal ions and the BTC organic ligand.

The crystal purity of the synthesized Hf-free Mil-10(Fe) NPs was confirmed from the X-ray diffraction (XRD) spectra as shown in Figure 6.4b. The diffraction planes found at 2θ values of 5.18°, 10.09°, 19.05°, 23.03° and 27.29° was matched with the crystallographic database (CCDC standard no. 640536)[13,21,22] which corresponds to the cubic (isometric) crystal.[23,24] The XRD spectra of the MOF confirms the successful formation of MIL-100(Fe) NPs, synthesized under ambient-temperature and HF-free conditions.

As shown in the Raman spectra in Figure 6.4c, the unique MIL-100(Fe) peaks in the 0-1800 cm^{-1} region can be seen in typical MOF.[23] Peaks between 165-225 cm^{-1} are related to the ordered crystalline iron-based structure, while the band at about 496 cm^{-1} is assigned to lattice vibrations and network binding modes. The key peaks are the two aromatic ring peaks at 810

cm^{-1} and 1001 $cm^{-1,}$ which are the fingerprints of the trimesate linker. The C-O-Fe stretching of Fe-trimesate generates the peak at 1226 cm^{-1}; however, the H-O-H bonding vibrations in the F bands from 1368 cm^{-1} to 1606 cm^{-1} show that the Fe-trimesate network contains coordinated water.[25]

6.3.1.4. Thermal Stability Analysis

The thermal stability of the synthesized MIL-100(Fe) NPs was demonstrated utilizing thermogravimetric analysis (TGA). Figure 6.4d depicts three stages of the weight loss profile during the thermal stability test of HF-free MIL-100(Fe) NPs. The first stage of the 8 % weight loss in the temperature range of 25-149 °C is the elimination of physically adsorbed water molecules that were entrapped inside MIL-100(Fe) pores. The second stage exhibits weight loss of 7 % at 149-301 °C, which demonstrates the stability of MIL-100(Fe) in this temperature range. This weight loss is attributed to the removal of chemically adsorbed water molecules and carboxylic groups. At temperatures between 301 °C and 486 °C, a weight loss of 33% is observed in the third stage. When ligand degradation occurs at temperatures greater than 349 °C, MIL-100(Fe) structural collapse results from BTC degradation, MOF structure disintegration and organic matter evaporation.[26] As the framework continues to disintegrate and the amount of organic ligand in the structure decreases, a noticeable weight loss begins at 486 °C. The third stage's degradation ends at 486 °C, demonstrating that MIL-100(Fe) NPs have completely decomposed into Fe_2O_3. As a result, it is concluded that the synthesized MIL-100(Fe) NPs are thermally stable below 301 °C and suitable for its use in CO_2 separation application.

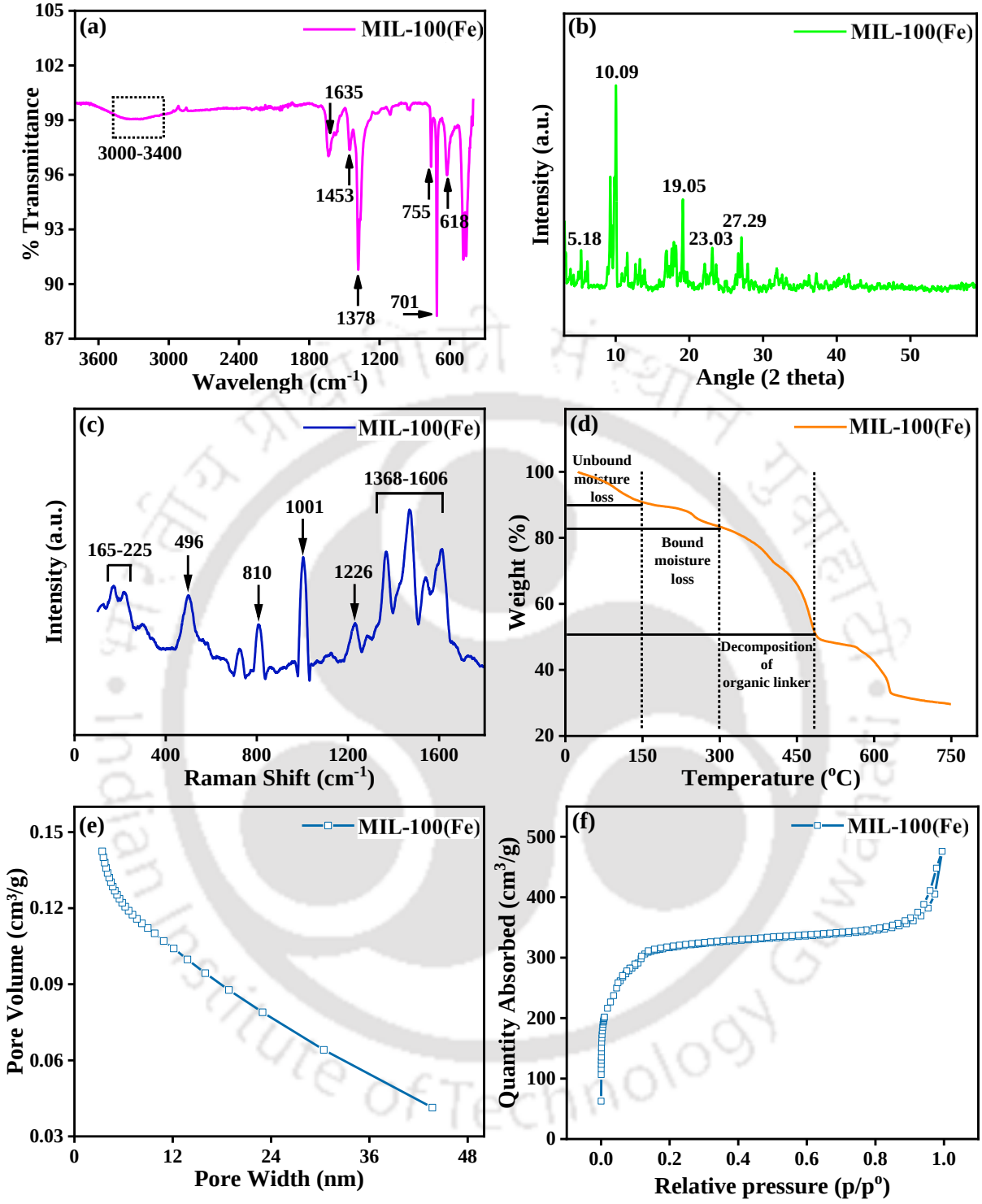

Figure 6.4. (a) FTIR spectra, (b) XRD pattern, (c) Raman spectra, (d) TGA profile and (e,f) N_2 adsorption-desorption isotherms at 77 K of synthesized HF-free MIL-100(Fe) MOF NPs.

6.3.1.5. Surface Area Analysis

According to the IUPAC classification of porous nano-materials, the isotherm pattern of MIL-100(Fe) NPs belongs to type I and type II shapes, which are linked to materials having a wide range of pore sizes, including broader micropores and narrower mesopores.[12,14] Figure 6.4e and f show the Brunauer–Emmett–Teller (BET) analysis of the synthesized HF-free MIL-100(Fe) NPs and shows a highly porous structure and type II adsorption isotherms. Types I and II are sought-after isotherms because they provide high removal at low pressure and concentration and lack hysteresis. The N_2 adsorption-desorption isotherms can be used to calculate the porosity of metal-organic framework. The complete merging of the N_2 adsorption-desorption isotherms for MIL-100(Fe) shows that the adsorbed N_2 was completely desorbed and that a sizeable amount of N_2 adsorption took place below the relative pressure of 0.1. When the pore width increases, the available surface area inside the pores decreases relative to the volume due to which with increasing the pore width, pore volume is decreasing. The textural properties are listed in Table 6.1 which include specific surface area, total pore volume and average pore size.

Table 6.1. N_2 adsorption-desorption study of HF-free MIL-100(Fe) NPs.

Material	**BET Surface Area**	**Total pore volume**	**Average Pore diameter**
HF-free MIL-100(Fe)	1288 m^2/g	0.78 cm^3/g	2.42 nm

6.3.2. Characterization of CSM-x MMMs

6.3.2.1. Structural Analysis

To characterize the synthesized membranes, we have performed the FTIR analysis. Figure 6.5a display the FTIR spectra of the synthesized neat CS membrane and CSM MMMs. The broad peak between 3400-3200 cm^{-1} confirms the -OH and -NH bending of CS polymer. The peaks at 2873 cm^{-1}, 1652 cm^{-1}, 1549 cm^{-1} and 1369 cm^{-1} correspond to the C-H, C-N, N-H and C=O stretching respectively. Figure 6.5b shows the zoomed in X-axis of the FTIR spectra for all the membranes. The peaks at 760 cm^{-1} and 711 cm^{-1} corresponding to the C-H benzene stretching and at 616 cm^{-1} corresponding to the Fe-O stretching, confirms the presence of MIL-100(Fe) NPs in the CS matrix.

Further, the XRD study is conducted and shown in Figure 6.5c to check the influence of MIL-100(Fe) NPs on the crystallinity of all the CS matrix. The CS membrane and CSM MMMs showed broad peaks at 2θ value of 9.4° and 20.1° attributable to crystalline and non-crystalline phase, respectively of CS.[27] The presence of MIL-100(Fe) nanoparticles in the CSM MMMs is shown by the new peak of MIL-100(Fe) nanoparticles that appear at about 10.9° (2θ) in the XRD spectra.[25] The intensity of the peak at 10.9° increases with increase in the filler concentration (5-20 wt%) and becomes much prominent in CSM-20 MMM which may be due to the agglomeration of the MIL-100(Fe) NPs in CS matrix can be observed from FESEM images (Figure 6.6f).

6.3.2.2. Thermal Stability Analysis

The thermal stability of the membrane is very crucial in CO_2 separation applications. TGA was used to test the thermal degradation of CS membrane and all CSM MMMs in a nitrogen environment between 25 °C and 800 °C and the outcomes are displayed in Figure 6.5d. The TGA curves show the typical three stage curves of thermal degradation: removal of unbound or free water from embedded MOF nanoparticles and CS at 114 °C, removal of bound moisture from embedded MOF nanoparticles at around 200 °C and the onset of deacetylation

of the CS matrix and breakdown of organic linkers of embedded MOF nanoparticles at around 400 °C. The weight loss before 114 °C is ~2% for CS and ~5% for CSM MMMs since the incorporation of MOF NPs into the CS matrix resulted more water adsorption owing to the large surface area of 1228 m^2/g (seen in Figure 6.4e and f) of the synthesized MIL-100(Fe) NPs. The third stage degradation at 460 °C confirms that the thermal stability of the CS membrane is not affected with the incorporation of MOF NPs.

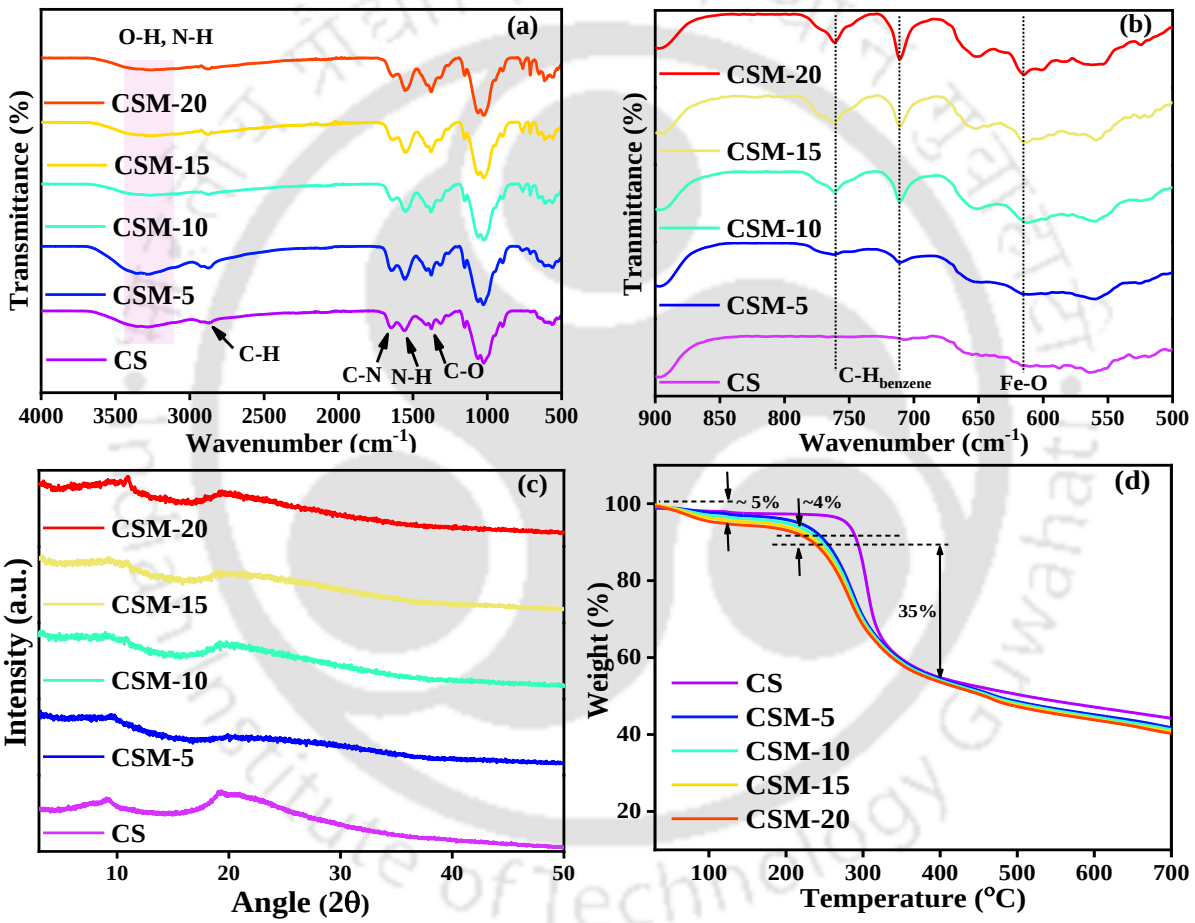

Figure 6.5. (a) and (b) FTIR spectra, (c) XRD patterns, (d) TGA profiles of CS membrane and all the CSM MMMs.

6.3.2.3. Morphological and Elemental Analysis

Figure 6.6 represents the top surface images of the, PES support, fabricated CS membrane and CSM MMMs along with EDX data. Figure 6.6a display the porous structure of the PES support and Figure 6.6b. displays the formation of defect free layer of CS onto the PES support. MIL-100(Fe) NPs are uniformly dispersed at loadings of 5 wt% to 15 wt%, respectively, as can be observed from Figure 6.6c, d and e. At higher loading of MOF, i.e., 20 wt%, non-uniform and agglomerated MOF clusters were observed, respectively, as shown in Figure 6.6f. The saturation of the gaps of the polymer matrix led to the particles' agglomeration at higher loading levels.

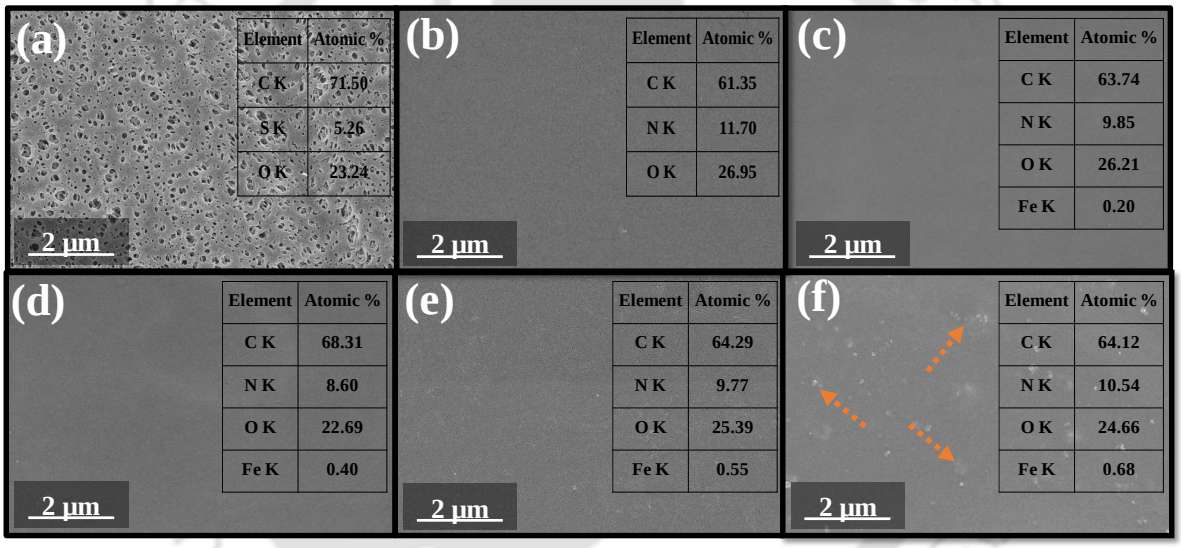

Figure 6.6. Top surface images and EDX data of (a) PES support, (b) CS membrane, (c) CSM-5, (d) CSM-10, (e) CSM-15 and (f) CSM-20 MMMs, respectively.

The obtained EDX results match the experimental approach; that is, increasing the amount of MIL-100(Fe) in the CS matrix, its atomic % is also increasing, as proven by obtained EDX data. Due to the limit of loading of MOF NPs at 15 wt%, we have chosen the CSM-15 as the optimized MMM for further studies.

The cross-section images of the MMMs, made by embedding MIL-100(Fe) NPs into the CS polymer matrix, are shown in Figure 6.7. PES support, CS membrane and all the CSM MMMs showed uniform surfaces and comparable cross-sections. The thickness of the selective layer of the produced membranes ranges between 1.2 and 1.5 µm, as shown in Figure 6.7. The cross-sectional images also demonstrate the strong adhesion between the support and selective layer and no pore filling.

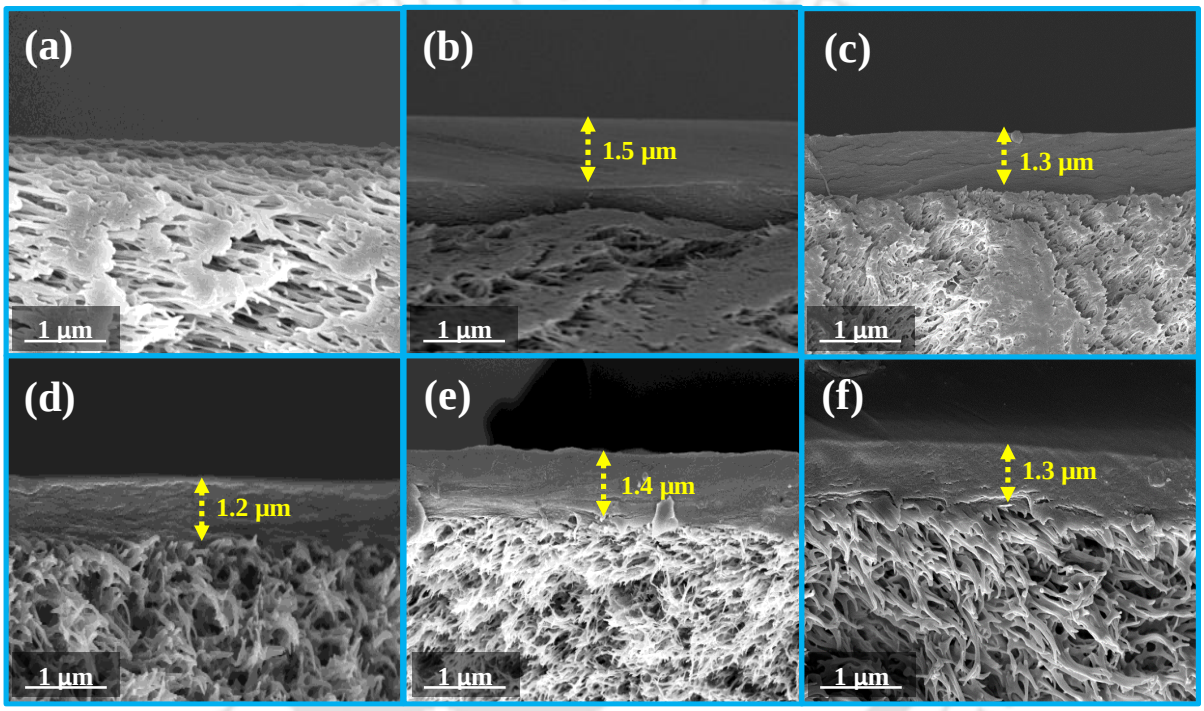

Figure 6.7. Cross-sectional images (a) PES support, (b) CS membrane, (c) CSM-5, (d) CSM-10, (e) CSM-15 and (f) CSM-20 MMMs, respectively.

6.3.2.4. Electronic State Analysis of optimized CSM-15 MMM

Based on the CSM characterizations and the CO_2 separation performance, 15 wt% is considered the optimum filler concentration in the CSM MMMs. Thus, the electronic structure of the bare CS and optimized CSM-15 MMM was examined by utilizing the XPS analysis, , to understand the filler-matrix interactions and shown in Figure 6.8. The survey spectra of CSM-

15 MMM shown in Figure 6.8a, confirm the presence of C, O, N, Fe at B.E. of 285 eV, 532 eV, 400 eV and 710 eV, respectively. The Fe 2p core level spectrum has been deconvoluted into Fe $2p_{1/2}$ and Fe $2p_{3/2}$ centered at B.E. of 724.04 eV and 710.68 eV, respectively as shown in Figure 6.8b. The B.E. of Fe $2p_{3/2}$ at 711.43 eV proves that Fe is present in a tri-valence

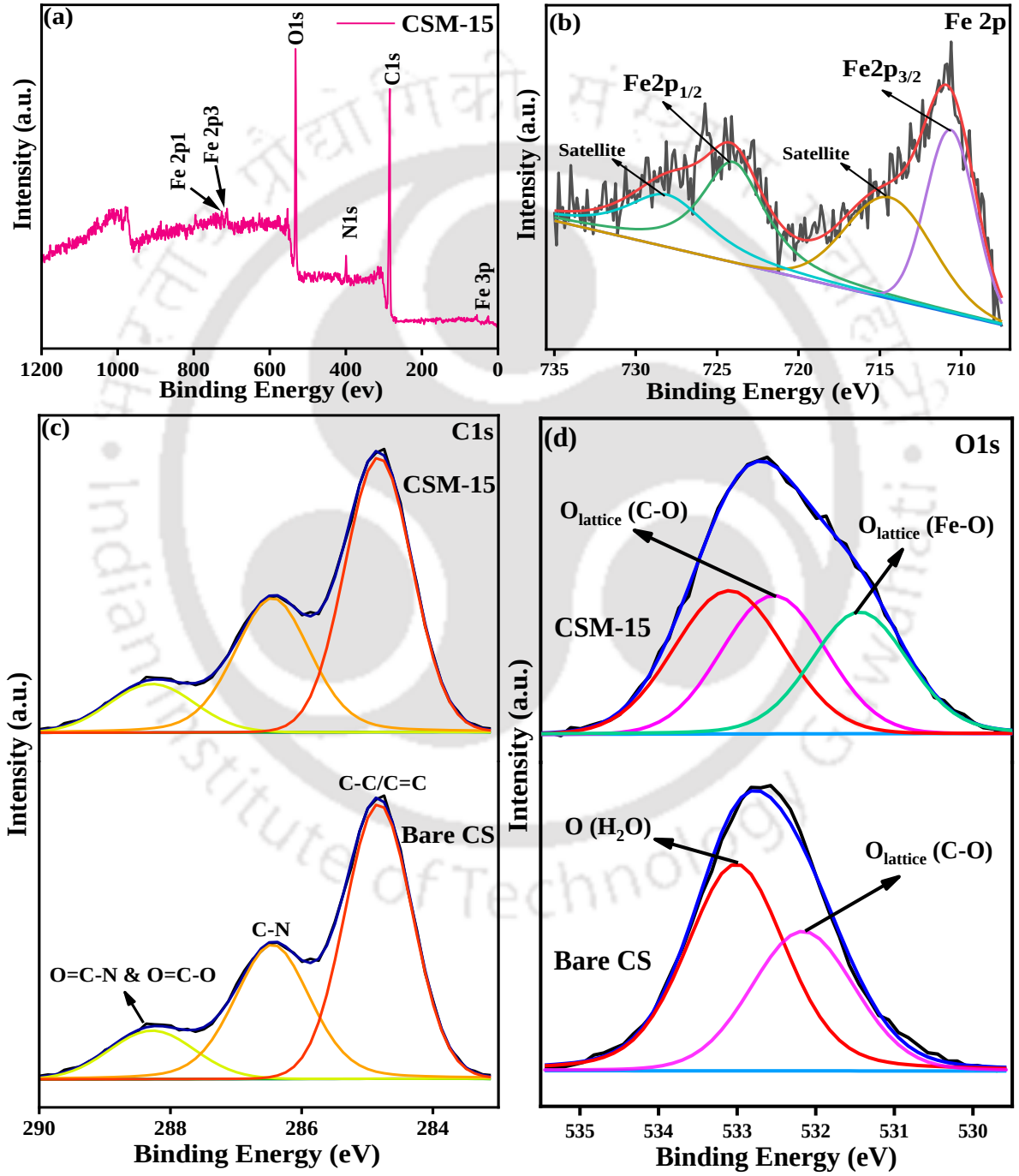

Figure 6.8. XPS spectra: (a) survey spectra of CSM-15 MMM, (b) Fe 2p spectra of CSM-15 MMM, (c) C 1s spectra of CS membrane and CSM-15 MMM; (d) O 1s spectra of CS membrane and CSM-15 MMM.

oxidation state in the fabricated CSM-15 MMM.[30] The peaks at B.E. of 287.92 eV, 286.49 eV and 284.86 eV in the high-resolution XPS spectra of C 1s are attributed to the carbons in the O=C-N and O=C-O; C-N and C-C or C=C bonds of bare CS membrane, respectively depicted in Figure 6.8c. For the CSM-15 MMM the respective peaks are obtained at B.E. of 287.87 eV, 286.44 eV and 284.83 eV in the high-resolution XPS spectra of C 1s. The shift in the peak validate the interaction of the CS and MIL-100(Fe) NPs. In Figure 6.8d the peak at B.E. of 531.82 eV is attributed to lattice oxygen in the CS polymer and the peak at B.E. of 532.16 eV is attributed to surface adsorbed water. For the CSM-15 MMM the peak at B.E. of 531.45 eV and 532.45 eV corresponds to the lattice oxygen present in the CS and the MIL-100(Fe), respectively, while the peak at 533.08 eV is attributed to water molecules as shown in Figure 6.8d.[30,31] The shift in the peak in O 1s spectra also validate the strong interaction of the CS and MIL-100(Fe) NPs.

6.4. CO_2/N_2 Gas permeation study

The systematic study of the separation of a Mixture of 20 % CO_2 and 80% N_2 gas is conducted in the gas permeation cell (as shown in Scheme 2.2) by varying the following parameters: Loading of MIL-100(Fe) NPs from 0-20 wt%, temperature from 65-105 °C and sweep side humidity from 0.01-0.09 mL/min. and thickness of selective layer ~ 0.5 μm to ~ 4 μm. A detailed explanation of the gas permeation cell was discussed in the Section 2.4.

6.4.1. Effect of MIL-100(Fe) NPs content on CO_2 separation performances of CSM MMMs

Prior to the CO_2/N_2 gas permeation study, all the fabricated membranes were cut into the equal dimension of ~8 cm^2 surface area and mounted in the membrane module, as shown in Scheme 2.2. The temperature of the module is upheld at 85 °C, feed gas pressure (20% CO_2 and 80% N_2) and sweep gas (Ar) pressure were kept at 2.21 bar and 1.21 bar. The humid conditions (introduced through HPLC pump) were maintained in the feed gas and sweep gas with 0.03 mL/min and 0.05 mL/min. Table 6.2 displays the mixed gas selectivity, CO_2 permeance, N_2 permeance, CO_2 flux and N_2 flux of the bare CS membrane and CSM MMMs. In the current study, for the neat CS membrane we have achieved 24 GPU CO_2 permeance and 29 CO_2/N_2 selectivity as mentioned in chapter 3. With increasing the loading of the MIL-100(Fe) NPs, the CO_2 separation performance enhanced and for CSM-15 MMM maximum permeance of up to 85 GPU and CO_2/N_2 selectivity of 59 for the CSM-15 MMM were achieved. Produced MMMs with MIL-100(Fe) in the current research exhibit significant increases in CO_2 and N_2 permeances compared to bare polymeric membranes.

The gas separation mechanism is explained based on the reactivity of the MOF NPs and the amine groups of the CS matrix. The high surface and strong adsorption separation property of MIL-100(Fe) due to presence of μ3-Oxo-bridged trinuclear metal nodes.[28] These metal nodes have terminal coordination sites occupied by water molecules which at high temperature are eliminated leaving open-metal sites. These open-metal sites have affinity towards CO_2 molecules thus separating them from the CO_2/N_2 gas mixture. Moreover, the chitosan matrix has amine functional groups which also has the tendency to interact with the incoming CO_2 molecules (reversible zwitterion reaction described by Caplow) via facilitated transport mechanism as discussed in section 1.3.6.2 (eqn 1.4-1.7).[29]

Thus, the contemporary increase in CO_2 and N_2 permeance concerning the bare polymer membrane is due to combinational effects of both CS (facilitated transport mechanism) and MIL-100(Fe) (open-metal sites) as represented in Scheme 6.2.

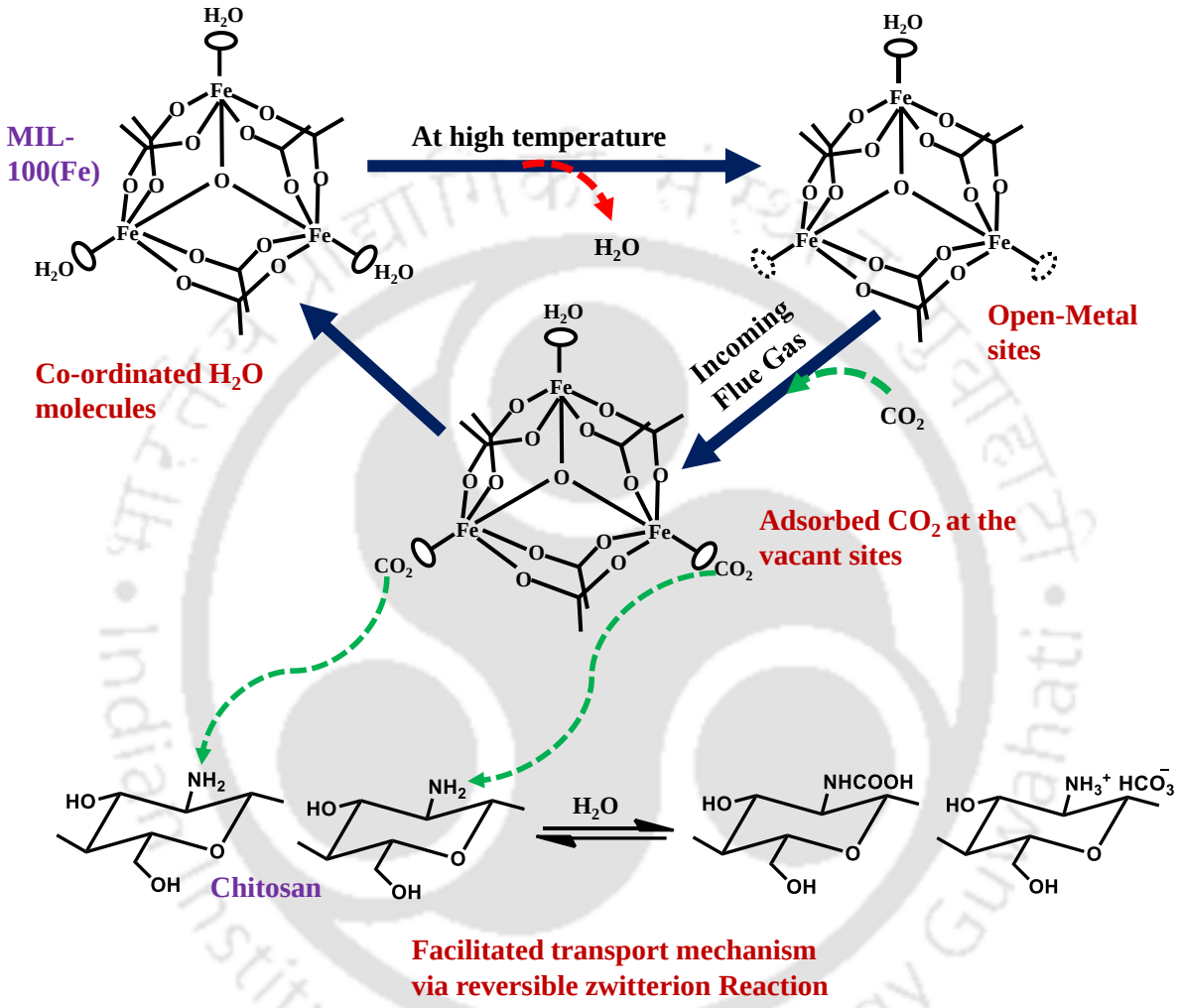

Scheme 6.2. Schematic representation of the plausible mechanism of the CO_2 separation from CO_2/N_2 mixture via dual effects of CS and MIL-100(Fe) in CSM MMMs.

With increasing the MOF concentration, the available open metal sites also increase thereby enhancing the CO_2 permeance and CO_2/N_2 selectivity. On further increment of the MOF loading in CS matrix up to 20 wt% the decline in the separation performance was observed. This can be attributed to the filler agglomeration as confirmed by the top surface

SEM images of the membranes (Figure 6.6f). The aggregation of NPs causes reduction in the active surface area and thus obstructs the CO_2 to travel across the membrane. Additionally, the cluster formation at higher loading causes steric hindrance for the open-metal sites to efficiently bind to the incoming CO_2 gas molecules, thereby ~1.5-fold reduction in the CO_2 permeance and ~2-fold reduction in CO_2/N_2 selectivity was observed.

Table 6.2. CO_2 separation performances of CSM MMMs at different MOF loadings.

MIL-100(Fe) content (wt%)	**CO_2/ N_2 Selectivity**	**CO_2 Permeance (GPU)**	**N_2 Permeance (GPU)**	**CO_2 Flux ($\times 10^{-6}$ cm^3 (STP)/cm^2s)**	**N_2 Flux ($\times 10^{-6}$ cm^3 (STP)/cm^2s)**
0	29	24	0.9	307	47
5	36	44	1.2	650	111 94
10	44	61	1.6	1004	135
15	59	85	1.9	1086	108
20	37	48	1.6	705	115

6.4.2. Effect of Temperature on CO_2 separation performances of optimized CSM-15 MMM

To assess the endurance and performance under adverse conditions, we utilized the optimized CSM-15 MMM for further studies. Particularly for high-temperature applications like flue gas separation, it is crucial to analyse how temperature affects the membrane absorption capacity and identify the ideal operating temperature range.[24,32] Therefore, the temperature effects on CO_2 separation performance of the optimized CSM-15 MMM were determined by varying the membrane module temperature from 65 °C to 105 °C, while feed

side pressure and moisture flow were maintained at 2.21 bar and 0.03 mL/min, respectively along with 1.21 bar sweep side pressure and 0.05 mL/min sweep side moisture flow.

According to Figure 6.9a and b, the CO_2 permeance, CO_2/N_2 selectivity and CO_2 flux increased from 42 GPU to 85 GPU, 37 to 59 and 998×10^{-6} cm^3 (STP)/cm^2s to 1086×10^{-6} cm^3 (STP)/cm^2s, respectively when the temperature was raised from 65 °C to 85 °C. This can be attributed to the dual contribution of the matrix and the filler. In CS matrix, firstly, the reversible zwitterion reaction between amine molecules of the polymer matrix and CO_2 molecules, which increases as the temperature increases (according to facilitated transport mechanism), contributing to CO_2 separation enhancement; and secondly, the enhancement in the flexibility of polymer chain at high temperature increases the mobility of the CO_2 gas molecules through the embedded highly porous MIL-100(Fe) MOF particles. While in case of filler the high surface and strong adsorption separation property of MIL-100(Fe) due to presence of μ3-Oxo-bridged trinuclear metal nodes regulates the gas separation performance of the MMMs. These metal nodes have terminal coordination sites occupied by water molecules which at high temperature are eliminated leaving open-metal sites. These open-metal sites have strong affinity towards CO_2 molecules thus separating them from the CO_2/N_2 gas mixture. At high temperature more open-metal sites are made available for the incoming CO_2 molecules, thereby increasing the active centers which increases the separation performance of the MMMs due to more gas adsorption onto its surface. The CO_2 separation performances of the CSM-15 MMM initially increased as the operating temperature raised from 65 to 85 °C, reached its optimum value and then again began to decline when the temperature went to 105 °C.[33] The observed gas permeability trend with rise in temperature can be deconvoluted to solubility and diffusivity coefficients. The permeability (P) of gas in the membrane is determined by the combined effects of gas diffusion and gas sorption.[34]

$$P = D \times S \quad (6.1)$$

where, D and S are the diffusivity and solubility coefficients, respectively.

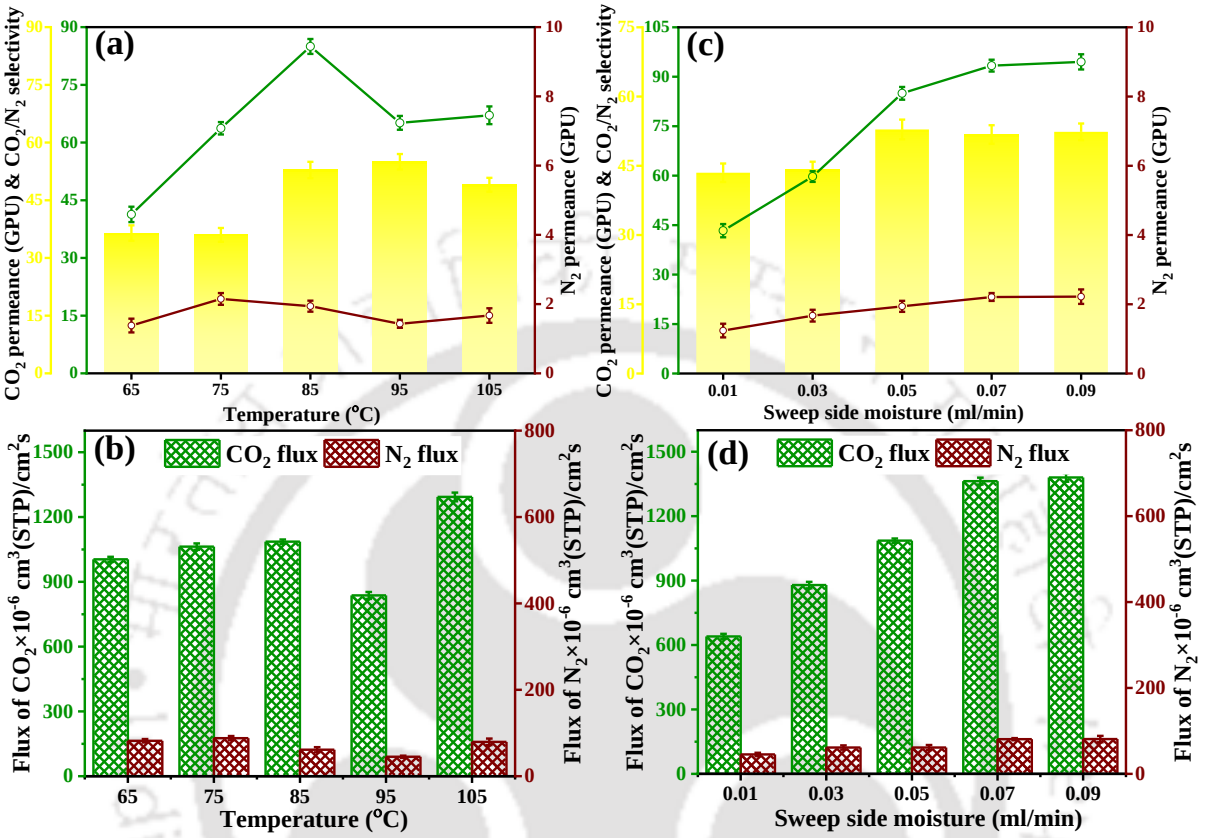

Figure 6.9. Operating temperature and sweep side moisture flow effects on (a), (c) CO_2 permeance, N_2 permeance and CO_2/N_2 selectivity and (b), (d) CO_2 flux, N_2 flux at 0.03 mL/min feed moisture flow, 2.21 bar feed pressure and 1.21 bar sweep side pressure.

The dominance of the sorption effect at lower temperatures is attributed to the higher affinity of CO_2 towards $-NH_2$, leading to the formation of carbamate. Consequently, the diffusion of gas molecules is significantly limited, resulting in a low permeance of CO_2 through the membrane. As the temperature increases (up to 85 °C), the diffusion of CO_2 improves due to the higher diffusion coefficient (Fick's law) and increased flexibility of the membrane with temperature. This leads to an enhancement in the membrane's CO_2 permeance up to 85 °C. However, beyond 85 °C, the sorption effect diminishes as the backward reaction of carbamate

formation becomes dominant, resulting in reduced gas solubility within the membrane. Consequently, the solubility decreases at higher temperatures (> 85 °C) causing a decline in the membrane's CO_2 permeance.

6.4.3. Effect of sweep side moisture flow on CO_2 separation performance of optimized CSM-15 MMM

In order to conduct further research, the stability and CO_2 and N_2 gas transport behaviour of the optimised CSM-15 MMM was tested by varying the sweep moisture flow rate from 0.01 to 0.09 mL/min as shown in Figure 6.9c and d. During the test, the operating temperature was upheld at 85 °C, absolute pressure of 2.21/1.21 bar (feed/sweep) and the feed gas humidity was maintained with 0.03 mL/min moisture flow. It has been discovered that as moisture flow of the sweep gas increased from 0.01 mL/min to 0.09 mL/min, CO_2 permeance improved from 43 GPU to 95 GPU and N_2 permeance increased from ~1 GPU to ~3 GPU. The enhancement in the CO_2 and N_2 permeance can be attributed to the increased moisture content inside the membrane matrix thereby inducing flexibility in the polymeric chains by plasticization effect which reduced the mass transport resistance for the gas molecules across the membrane.[49] Moreover, the difference in the water content across the membrane (feed to sweep side: 0.03 to 0.05 mL/min) dilutes the concentration of the permeated CO_2 thus increasing the driving force of CO_2 transport.[35-36] At the same time, the increment in the CO_2/N_2 selectivity from 43 to 59 was observed when sweep moisture flow was raised from 0.01 to 0.05 mL/min, this resulted from the enhanced facilitated transportation of CO_2 molecules due to reversible zwitterion reaction. The CO_2/N_2 selectivity reached its maximum value at 0.05 mL/min of moisture flow with further no significant changes upon rise in the sweep side moisture flow. This may be due to carrier saturation phenomena and competitive N_2 transport across the membrane.

6.4.4. Effect of selective layer thickness on CO_2 separation performance of optimized CSM-15 MMM

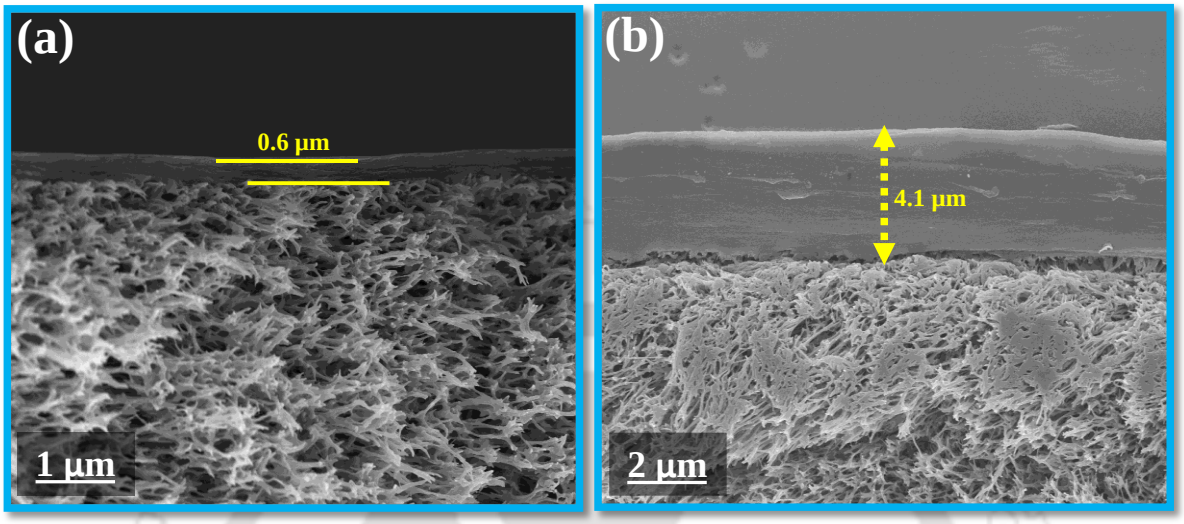

Figure 6.10. FESEM images of cross section optimized CSM-15 MMMs with different selective layer thickness.

The selective layer thickness (shown in Figure 6.7e and Figure 6.10) significantly influences the separation performance of the membranes for CO_2 and N_2. Increasing the coating layer thickness to around 4-4.5 µm considerably enhances the selectivity of CO_2 over N_2. Conversely, a thicker selective layer reduces the permeance of CO_2 as demonstrated in in Table 6.3. When the selective layer thickness is reduced from 1-1.5 µm to around 0.5 µm, the CO_2 permeance increased from 85 to 139 GPU, while the CO_2 selectivity decreased significantly from 59 to 36. The relationship between CO_2/N_2 selectivity and CO_2 permeance, along with the increasing selective layer thickness, supports the hypothesis that CO_2 transport in this membrane is primarily governed by the CO_2-carrier reaction rate and the diffusion of the CO_2-carrier complex, with the contribution of CO_2 molecule solution-diffusion being less significant than in solution-diffusion governed membranes.

Table 6.3. Comparison of the CO_2 separation performance of the CSM-15 MMM with different selective layer thickness.

	CSM-15 MMM	
Selective layer Thickness (µm)	**CO_2 Permeance (GPU)**	S_{CO_2/N_2}
0.5-0.6	139	36
1-1.5	85	59
4-4.5	59	65

6.4.5. Comparative study of obtained results with reported literature

Concerning the Robeson trade-off line, the separation performance of our membranes for the CO_2/N_2 gas pair is compared to that of existing MMMs in the literature shown in Figure 6.11 and Table 6.4. The performance of CSM MMMs lies near the 2008 upper bound for polymeric membrane performance. Specifically, CSM-15 with MIL-100(Fe) NPs loading of 15 wt% exhibits excellent CO_2 permeance of 85 GPU and reasonably good CO_2/N_2 selectivity of 59. As can be analysed from the comparative Table 6.4, the as-fabricated CSM-15 MMM shows comparable permeance and reasonably good CO_2/N_2 selectivity for CO_2 separation from flue gases than other reported MMMs containing MOFs, CNT, GO, or other filler materials and can be utilized for other application as well like biogas or field natural gas.

Table 6.4. A comparative account of the CO_2 separation performance of the synthesized CSM-15 MMM with available literature.

Material	Filler	Operating conditions	CO_2 Permeance (GPU)	CO_2/N_2 Selectivity	References
Bare CS	-	85 °C, 2.21 bar	24	29	This work
Carboxymethyl CS	Hydro-talcite	80 °C, 2.21 bar	70	13	[35]
Carboxymethyl CS	Carbon nanotubes (CNT)	80 °C, 2.21 bar	43	45	[36]
Matrimid ®5218	Fe(BTC)	90 °C, 0.7 bar	80	218[a]	[14]
Polyvinyl amine/CS	Modified Graphene oxide (GO)	1 bar, 25 °C	36	107	[37]
Pebax	Modified CNT	2 bar, 40 °C	369.1[b]	110.8	[38]
Polysulfone	Vertically aligned ZIF-8	3 bar, 30 °C	89.7 [b]	30	[38]
CS	HF-free MIL-100(Fe) NPs	85 °C, 2.21 bar	85	59	This work

[a] an ideal gas selectivity, [b] barrer units.

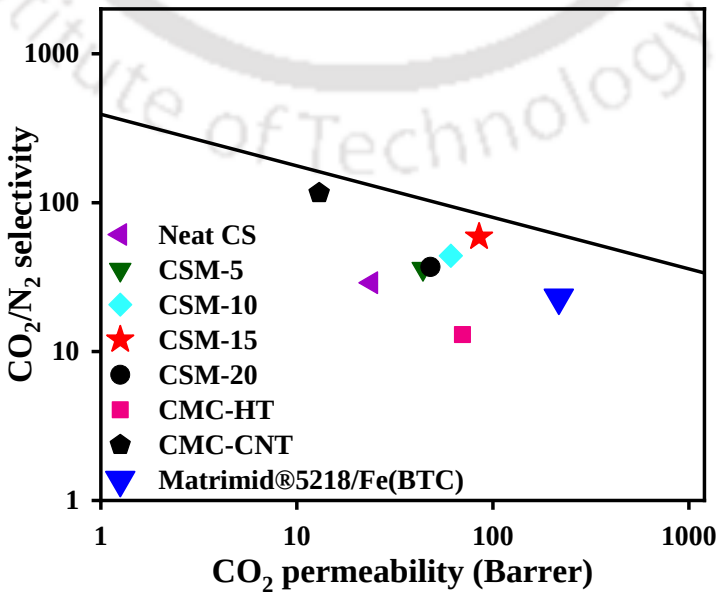

Figure 6.11. Robeson upper bound curve: Comparison of the CO_2 separation performance of the synthesized CSM MMMs with the reported literature.

6.5. Conclusions

This article presents high-performance MMMs synthesized with the green route for effective CO_2 separation. MIL-100(Fe) with average particle size of ~100 nm, were synthesized under HF-free circumstances at ambient conditions and incorporated into a biodegradable CS matrix. The μ3-oxo-trimer of the MIL-100(Fe) NPs aided the diffusion mechanism along with the amine groups of CS polymer for the capture of CO_2 molecules. The dual advantages of the zwitterion mechanism via amine groups and the CO_2 affinity via open-metal sites of the MOF NPs were exploited in this study. The high surface area of the nanoparticles also added the specific channel for the passage of the gas molecules. The prepared MMMs were characterized and tested for the CO_2 separation performance and compared with those for the neat CS membrane. The maximum limit of filler incorporation into the CS matrix was also evaluated and the optimized MMM was subjected to adverse test conditions to examine its endurance and efficacy. The CO_2 permeance and CO_2/N_2 selectivity were in trend with the increasing concentration of the MIL-100(Fe) up to 15 wt%; thereafter, a fall in the performance was observed. The CSM-15 demonstrated a CO_2 permeance of 85 GPU and CO_2/N_2 selectivity of 59; thus, a ~4-fold increment in permeance and ~15-fold increment in selectivity were obtained for the MMM compared to the neat CS membrane. The demonstrated technique may be utilized for various other nanofiller-matrix combinations to develop more efficient MMMs and further enhance CO_2 separation performance.

References

(1) Wang, M.; Wang, Z.; Zhao, S.; Wang, J.; Wang, S. Recent Advances on Mixed Matrix

Membranes for CO_2 Separation. *Chinese J. Chem. Eng.* **2017**, *25* (11), 1581–1597. https://doi.org/10.1016/j.cjche.2017.07.006.

(2) Kang, Z.; Peng, Y.; Hu, Z.; Qian, Y.; Chi, C.; Yeo, L. Y.; Tee, L.; Zhao, D. Mixed Matrix Membranes Composed of Two-Dimensional Metal-Organic Framework Nanosheets for Pre-Combustion CO_2 Capture: A Relationship Study of Filler Morphology versus Membrane Performance. *J. Mater. Chem. A* **2015**, *3* (41), 20801–20810. https://doi.org/10.1039/c5ta03739e.

(3) Venna, S. R.; Lartey, M.; Li, T.; Spore, A.; Kumar, S.; Nulwala, H. B.; Luebke, D. R.; Rosi, N. L.; Albenze, E. Fabrication of MMMs with Improved Gas Separation Properties Using Externally-Functionalized MOF Particles. *J. Mater. Chem. A* **2015**, *3* (9), 5014–5022. https://doi.org/10.1039/c4ta05225k.

(4) Zhang, Y.; Musselman, I. H.; Ferraris, J. P.; Jr, K. J. B. Gas Permeability Properties of Matrimid ® Membranes Containing the Metal-Organic Framework Cu – BPY – HFS. **2008**, *313*, 170–181. https://doi.org/10.1016/j.memsci.2008.01.005.

(5) Yang, C.; Li, W.; Samarasinghe, S. A. S. C.; Sethunga, G. S. M. D. P.; Bae, T. Microporous and Mesoporous Materials Enhancing the CO_2 Separation Performance of Polymer Membranes via the Incorporation of Amine-Functionalized HKUST-1 Nanocrystals. *Microporous Mesoporous Mater.* **2019**, *290* (April), 109680. https://doi.org/10.1016/j.micromeso.2019.109680.

(6) Meshkat, S.; Kaliaguine, S.; Rodrigue, D. Comparison between ZIF-67 and ZIF-8 in Pebax® MH-1657 Mixed Matrix Membranes for CO_2 Separation. *Sep. Purif. Technol.* **2020**, *235* (May 2019), 116150. https://doi.org/10.1016/j.seppur.2019.116150.

(7) Anjum, M. W.; Vermoortele, F.; Khan, A. L.; Bueken, B.; De Vos, D. E.; Vankelecom,

I. F. J. Modulated UiO-66-Based Mixed-Matrix Membranes for CO_2 Separation. *ACS Appl. Mater. Interfaces* **2015**, *7* (45), 25193–25201. https://doi.org/10.1021/acsami.5b08964.

(8) Katare, A.; Mandal, B. Surface Engineering of Zr BDC Nanoparticles via Conjugation with Lysine to Enhance the CO_2 /N_2 Separation Performance of Chitosan Mixed Matrix Membranes under Dry and Humid Conditions. *ACS Appl. Nano Mater.* **2023**. https://doi.org/10.1021/acsanm.3c00534.

(9) Wahyu, W.; Burhan, L.; Rahman, F.; Hermayanti, J.; Desi, P.; Handayani, S. Fabrication of Hybrid Membranes Based on Poly (Ether - Sulfone)/ Materials Institute Lavoisier (MIL - 53)(Al) and Its Enhanced - CO_2 Gas Separation Performance. *Chem. Pap.* **2021**, *75* (12), 6519–6530. https://doi.org/10.1007/s11696-021-01816-3.

(10) Lestari, W. W.; Al Adawiyah, R.; Khafidhin, M. A.; Wijiyanti, R.; Widiastuti, N.; Handayani, D. S. CO_2gas Separation Using Mixed Matrix Membranes Based on Polyethersulfone/MIL-100(Al). *Open Chem.* **2021**, *19* (1), 307–321. https://doi.org/10.1515/chem-2021-0033.

(11) Wang, L.; Zhang, F.; Wang, C.; Li, Y.; Yang, J.; Li, L.; Li, J. Separation and Puri Fi Cation Technology Ethylenediamine-Functionalized Metal Organic Frameworks MIL-100 (Cr) for e Ffi Cient CO_2 / N_2O Separation. *Sep. Purif. Technol.* **2020**, *235* (July 2019), 116219. https://doi.org/10.1016/j.seppur.2019.116219.

(12) Mutyala, S.; Yakout, S. M.; Ibrahim, S. S.; Jonnalagadda, M.; Mitta, H. Enhancement of CO_2 Capture and Separation of CO_2/N_2 Using Post-Synthetic Modified MIL-100(Fe). *New J. Chem.* **2019**, *43* (24), 9725–9731. https://doi.org/10.1039/c9nj02258a.

(13) Lestari, W. W.; Yunita, L.; Saraswati, T. E.; Heraldy, E.; Khafidhin, M. A.; Krisnandi,

Y. K.; Arrozi, U. S. F.; Kadja, G. T. M. Fabrication of Composite Materials MIL-100(Fe)/Indonesian Activated Natural Zeolite as Enhanced CO_2 Capture Material. *Chem. Pap.* **2021**, *75* (7), 3253–3263. https://doi.org/10.1007/s11696-021-01558-2.

(14) Nabais, A. R.; Ribeiro, R. P. P. L.; Mota, J. P. B.; Alves, V. D.; Esteves, I. A. A. C.; Neves, L. A. CO_2/N_2 Gas Separation Using Fe(BTC)-Based Mixed Matrix Membranes: A View on the Adsorptive and Filler Properties of Metal-Organic Frameworks. *Sep. Purif. Technol.* **2018**, *202* (March), 174–184. https://doi.org/10.1016/j.seppur.2018.03.028.

(15) Dorosti, F.; Alizadehdakhel, A. Fabrication and Investigation of PEBAX/Fe-BTC, a High Permeable and CO_2 Selective Mixed Matrix Membrane. *Chem. Eng. Res. Des.* **2018**, *136*, 119–128. https://doi.org/10.1016/j.cherd.2018.01.029.

(16) Sontakke, A. D.; Bhattacharjee, A.; Fopase, R.; Pandey, L. M.; Purkait, M. K. One-Pot, Sustainable and Room Temperature Synthesis of Graphene Oxide-Impregnated Iron-Based Metal-Organic Framework (GO/MIL-100(Fe)) Nanocarriers for Anticancer Drug Delivery Systems. *J. Mater. Sci.* **2022**, *57* (40), 19019–19049. https://doi.org/10.1007/s10853-022-07773-w.

(17) Zhang, F.; Shi, J.; Jin, Y.; Fu, Y.; Zhong, Y.; Zhu, W. Facile Synthesis of MIL-100(Fe) under HF-Free Conditions and Its Application in the Acetalization of Aldehydes with Diols. *Chem. Eng. J.* **2015**, *259*, 183–190. https://doi.org/10.1016/j.cej.2014.07.119.

(18) Zhang, F.; Jin, Y.; Shi, J.; Zhong, Y.; Zhu, W.; El-shall, M. S. Polyoxometalates Confined in the Mesoporous Cages of Metal – Organic Framework MIL-100 (Fe): Efficient Heterogeneous Catalysts for Esterification and Acetalization Reactions. *Chem. Eng. J.* **2015**, *269*, 236–244. https://doi.org/10.1016/j.cej.2015.01.092.

(19) Vo, T. K.; Bae, Y. S.; Chang, B. J.; Moon, S. Y.; Kim, J. H.; Kim, J. Highly CO Selective Cu(I)-Doped MIL-100(Fe) Adsorbent with High CO/CO_2 Selectivity Due to Π Complexation: Effects of Cu(I) Loading and Activation Temperature. *Microporous Mesoporous Mater.* **2019**, *274* (July 2018), 17–24. https://doi.org/10.1016/j.micromeso.2018.07.024.

(20) Basu, S.; Cano-Odena, A.; Vankelecom, I. F. J. MOF-Containing Mixed-Matrix Membranes for CO_2/CH_4 and CO_2/N_2 Binary Gas Mixture Separations. *Sep. Purif. Technol.* **2011**, *81* (1), 31–40. https://doi.org/10.1016/J.SEPPUR.2011.06.037.

(21) Elharony, N. E.; El Sayed, I. E. T.; Al-Sehemi, A. G.; Al-Ghamdi, A. A.; Abou-Elyazed, A. S. Facile Synthesis of Iron-Based MOFs MIL-100(Fe) as Heterogeneous Catalyst in Kabachnick Reaction. *Catalysts* **2021**, *11* (12), 1451. https://doi.org/10.3390/catal11121451.

(22) Zhang, F.; Shi, J.; Jin, Y.; Fu, Y.; Zhong, Y.; Zhu, W. Facile Synthesis of MIL-100 (Fe) under HF-Free Conditions and Its Application in the Acetalization of Aldehydes with Diols. *Chem. Eng. J.* **2015**, *259*, 183–190. https://doi.org/10.1016/j.cej.2014.07.119.

(23) Lv, H.; Zhao, H.; Cao, T.; Qian, L.; Wang, Y.; Zhao, G. Efficient Degradation of High Concentration Azo-Dye Wastewater by Heterogeneous Fenton Process with Iron-Based Metal-Organic Framework. *J. Mol. Catal. A Chem.* **2015**, *400* (January 2018), 81–89. https://doi.org/10.1016/j.molcata.2015.02.007.

(24) Tang, P. H.; So, P. B.; Li, W. H.; Hui, Z. Y.; Hu, C. C.; Lin, C. H. Carbon Dioxide Enrichment Pebax/Mof Composite Membrane for CO_2 Separation. *Membranes (Basel).* **2021**, *11* (6). https://doi.org/10.3390/membranes11060404.

(25) Li, X.; Lachmanski, L.; Safi, S.; Sene, S.; Serre, C.; Grenèche, J. M.; Zhang, J.; Gref, R.

New Insights into the Degradation Mechanism of Metal-Organic Frameworks Drug Carriers. *Sci. Rep.* **2017**, *7* (1), 1–12. https://doi.org/10.1038/s41598-017-13323-1.

(26) Wang, X.; Xu, J.; Yang, D.; Sun, C.; Sun, Q.; He, F.; Gai, S.; Zhong, C.; Li, C.; Yang, P. Fe_3O_4@MIL-100(Fe)-UCNPs Heterojunction Photosensitizer: Rational Design and Application in near Infrared Light Mediated Hypoxic Tumor Therapy. *Chem. Eng. J.* **2018**, *354* (August), 1141–1152. https://doi.org/10.1016/j.cej.2018.08.070.

(27) Hidalgo, T.; Giménez-Marqués, M.; Bellido, E.; Avila, J.; Asensio, M. C.; Salles, F.; Lozano, M. V.; Guillevic, M.; Simón-Vázquez, R.; González-Fernández, A.; Serre, C.; Alonso, M. J.; Horcajada, P. Chitosan-Coated Mesoporous MIL-100(Fe) Nanoparticles as Improved Bio-Compatible Oral Nanocarriers. *Sci. Rep.* **2017**, *7* (January), 1–14. https://doi.org/10.1038/srep43099.

(28) Gargiulo, V.; Alfè, M.; Raganati, F.; Lisi, L.; Chirone, R.; Ammendola, P. BTC-Based Metal-Organic Frameworks: Correlation between Relevant Structural Features and CO_2 Adsorption Performances. *Fuel* **2018**, *222* (March), 319–326. https://doi.org/10.1016/j.fuel.2018.02.093.

(29) Huang, J.; Zou, J.; Ho, W. S. W. Carbon Dioxide Capture Using a CO_2-Selective Facilitated Transport Membrane. *Ind. Eng. Chem. Res.* **2008**, *47* (4), 1261–1267. https://doi.org/10.1021/ie070794r.

(30) Gnanasekaran, G.; Sudhakaran, M. S. P.; Kulmatova, D.; Han, J.; Arthanareeswaran, G.; Jwa, E.; Mok, Y. S. Efficient Removal of Anionic, Cationic Textile Dyes and Salt Mixture Using a Novel CS/MIL-100 (Fe) Based Nanofiltration Membrane. *Chemosphere* **2021**, *284* (December 2020), 131244. https://doi.org/10.1016/j.chemosphere.2021.131244.

(31) Wang, Y.; Wang, K.; Lin, J.; Xiao, L.; Wang, X. The Preparation of Nano-MIL-101(Fe)@chitosan Hybrid Sponge and Its Rapid and Efficient Adsorption to Anionic Dyes. *Int. J. Biol. Macromol.* **2020**, *165*, 2684–2692. https://doi.org/10.1016/j.ijbiomac.2020.10.073.

(32) Cheng, J.; Zhu, Y.; Li, K.; Lu, H.; Shi, Z. Calcinated MIL-100(Fe) as a CO_2 Adsorbent to Promote Biomass Productivity of Arthrospira Platensis Cells. *Sci. Total Environ.* **2020**, *699*. https://doi.org/10.1016/j.scitotenv.2019.134375.

(33) Vo, T. K.; Vu, P. Van; Nguyen, V. C.; Kim, J. Construction of OH Sites within MIL-101(Cr)-NH_2 Framework for Enhanced CO_2 Adsorption and CO_2/N_2 Selectivity. *Korean J. Chem. Eng.* **2021**, *38* (8), 1676–1685. https://doi.org/10.1007/s11814-021-0799-z.

(34) Li, T.; Pan, Y.; Peinemann, K. V.; Lai, Z. Carbon Dioxide Selective Mixed Matrix Composite Membrane Containing ZIF-7 Nano-Fillers. *J. Memb. Sci.* **2013**, *425–426*, 235–242. https://doi.org/10.1016/j.memsci.2012.09.006.

(35) Borgohain, R.; Mandal, B. High-Speed CO_2 Transport Channel Containing Carboxymethyl Chitosan/Hydrotalcite Membrane for CO_2 Separation. *J. Appl. Polym. Sci.* **2019**, *48715*, 1–9. https://doi.org/10.1002/app.48715.

(36) Borgohain, R.; Jain, N.; Prasad, B.; Mandal, B.; Su, B. Carboxymethyl Chitosan/Carbon Nanotubes Mixed Matrix Membranes for CO_2 Separation. *React. Funct. Polym.* **2019**, *143* (July), 104331. https://doi.org/10.1016/j.reactfunctpolym.2019.104331.

(37) Shen, Y.; Wang, H.; Liu, J.; Zhang, Y. Enhanced Performance of a Novel Polyvinyl Amine/Chitosan/Graphene Oxide Mixed Matrix Membrane for CO_2 Capture. *ACS Sustain. Chem. Eng.* **2015**, *3* (8), 1819–1829. https://doi.org/10.1021/acssuschemeng.5b00409.

(38) Dai, Z.; Deng, J.; Peng, K. J.; Liu, Y. L.; Deng, L. Pebax/PEG Grafted CNT Hybrid Membranes for Enhanced CO_2/N_2 Separation. *Ind. Eng. Chem. Res.* **2019**, *58* (27), 12226–12234. https://doi.org/10.1021/acs.iecr.9b01466.

CHAPTER 7

Surface Engineering of Zr BDC Nanoparticles via Conjugation with Lysine to Enhance CO_2 Separation Performance of Chitosan Mixed Matrix Membrane under Dry and Humid Conditions

This chapter focuses on synthetization of Zr BDC (UIO-66) nanoparticles and their conjugation with L-lysine amino acid. The conjugation of NPs was done in the presence of carbodiimide to produce the CO_2 selective nanofillers with better compatibility into CS matrix. The effects and degree of conjugation on the properties of Zr BDC is confirmed using various characterization techniques. For the comparative study and to better understand the effect of conjugation, we have also prepared Zr BDC embedded CS MMMs and neat CS membrane with identical thickness. This research work is scientifically acknowledged in ***"ACS Applied Nano Materials"****.*

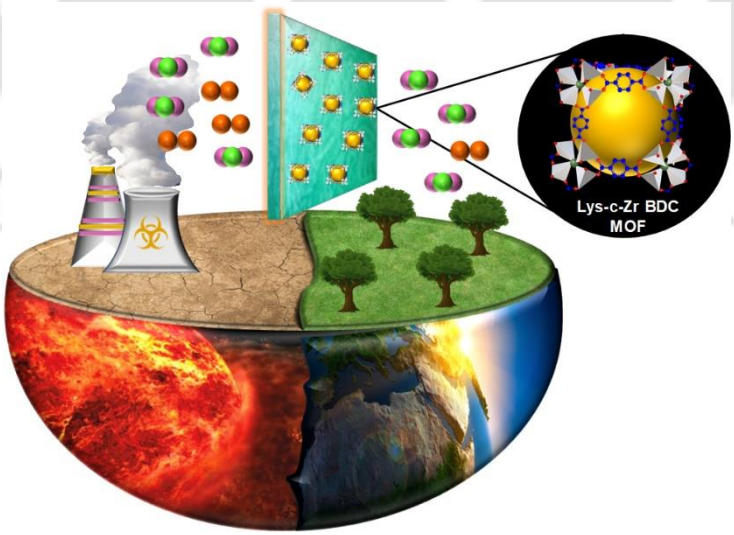

DOI: https://doi.org/10.1021/acsanm.3c00534

7.1. Introduction

Among all the metal-organic frameworks (MOFs) studied in the past two decades, Zr-MOFs, specifically ZrBDC (UiO-66), have been widely utilized as filler due to their robustness, cost-effectiveness, superior thermal and chemical stability, exceptionally high surface area and non-toxic nature.[1] Its stronger affinity for CO_2 makes it more efficient for CO_2 separation compared to GO and MIL-100(Fe).

Despite ongoing efforts, challenges related to poor polymer-MOF affinity, interfacial defects and gas leakage persist. To address these issues, researchers have explored functionalizing the ligand of UiO-66 with polar groups such as $-NH_2$, $-Br$, $-NO_2$, $-(CF_3)_2$, $-SO_3H$ and $-CO_2H$. Among these functional groups, controlled and appropriate functionalization of UiO-66 with the use of amino groups has shown particular promise in enhancing CO_2 adsorption selectivity and polymer binding affinity while maintaining the stability. MOFs with alkyl amine-functionalized (R_1NHR_2 or RNH_2) surfaces or/and pores have proven to be efficient for selective CO_2 sorption.[2] In line with these concept, biomaterial amino acids can be employed for engineering Zr BDC MOFs via conjugation approach. The presence of amine groups in amino acid, such as lysine, makes it a suitable candidate to introduce nitrogen source in the composite thereby increasing the CO_2 adsorption capacity via the zwitterion reaction mechanism.

In this view, CO_2-philic zirconium-based MOF nanoparticles (NPs) (Zr BDC or UIO-66) were synthesized and decorated with L-lysine (Lys) amino acids to incorporate into chitosan (CS) polymer matrix. The high porosity and surface area of the MOF NPs aided to the CO_2 separation permeance while the selectivity was addressed by amine functional groups present in Lys. The covalently bonded Lys onto Zr BDC NPs has a greater CO_2 affinity due to the dangling amine groups. Additionally, the amine conjugation strengthened the hydrogen

bonds between MOF and the CS matrix thereby improving the dispersibility of MOF in the polymer matrix. The importance of this work lies in the fact that appropriate combination of highly stable Zr BDC MOF and Lys amino acid enhanced the overall performance of the mixed matrix membrane (MMM).

7.2. Experimental Section

7.2.1. Synthesis of Zr BDC and Lysine-conjugated-Zr-BDC (Lys-c-Zr BDC) Nanofillers

Zr BDC nanoparticles were produced using the hydrothermal method[2] with HCl serving as modulator. In a typical preparation procedure, equal amounts (10 mmol each) of zirconium chloride and terephthalic acid (TPA) were dissolved in a solution of N,N-dimethylformamide and HCl (DMF, 58 mL+ HCl 4 mL) using ultrasonic waves until they completely dissolved. Then, the zirconium chloride and TPA solutions were combined and sonicated for an additional 10 minutes. The resulting solution was subjected to a hydrothermal treatment at 120 °C for 24 hours. Once the treatment was completed, the sample was allowed to cool to room temperature and then separated using a centrifuge. To eliminate any remaining unreacted metal salts and organic components, the sample was thoroughly rinsed with methanol multiple times. Finally, it was centrifuged again after being soaked in methanol for 72 hours to activate the pores of the material.

The conjugation of as-synthesized nanoparticles was done using the previously reported method.[3] In the typical preparation method described in Scheme 7.1, the process began by combining 25 mL of MES buffer with 8 mmol of EDC and 4 mmol of NHS. To this solution, 4 mmol of Lys was added. Subsequently, a certain amount of Zr BDC was introduced into the mixture. The entire solution was subjected to vigorous stirring for a duration of 12 hours, allowing the reaction to take place effectively. Once the reaction was complete, the amino acid-

conjugated Zr BDC nanoparticles (referred to as Lys-c-Zr BDC) were obtained from the reaction mixture. To remove any excess reagents and impurities, the Lys-c-Zr BDC nanoparticles were repeatedly washed using deionized water. After thorough washing, the nanoparticles were subjected to vacuum drying to yield the final product. The main objective of this method was to successfully conjugate Lys with Zr BDC nanoparticles and each step was carefully executed to ensure the efficient attachment of the amino acid onto the surface of the nanoparticles.

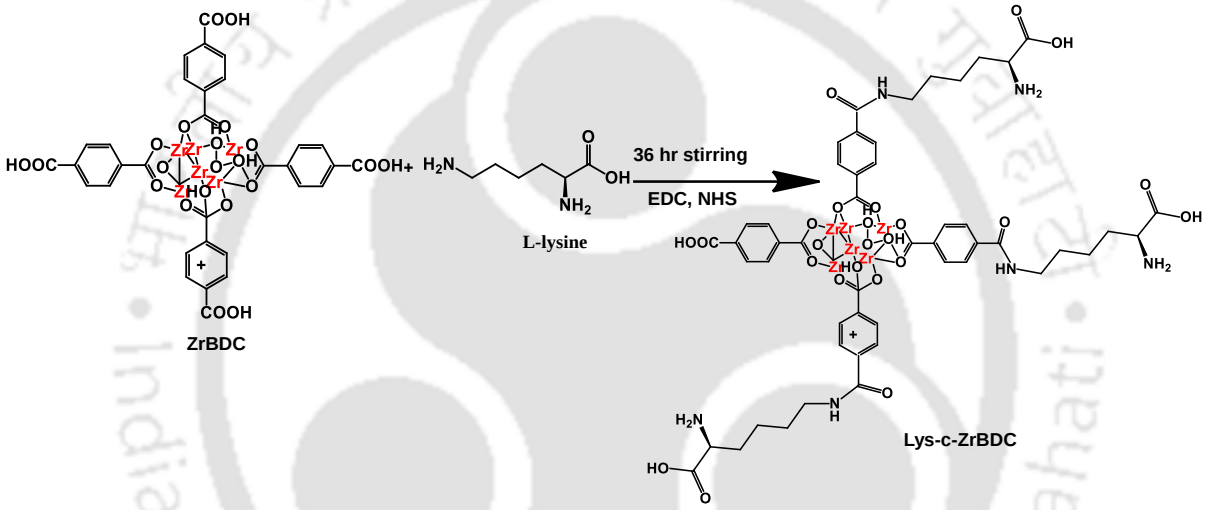

Scheme 7.1. Conjugation of Lys amino acid with Zr BDC nanoparticles in the presence of EDC and NHS.

7.2.2. Synthesis of Zr BDC and Lys-c-Zr BDC nanofillers embedded CS MMMs

The solution-casting technique was used to fabricate all of the MMMs. First, a homogeneous solution was produced by dissolving 1-wt % of CS flakes in a 1 vol% AA solution for 12 h at room temperature. In order to achieve uniform dispersion of MOF into a neat CS solution, a specific amount (3, 7 and 10 wt%) of Lys-c-Zr BDC in water was sonicated and added to the CS solution followed by 24 h stirring. Then they were subjected to ultrasonic treatment for an additional 2 h to remove air bubbles. The mixed solutions were then casted onto polyethersulfone (PES) support that had been adhered to glass plates, dried in a laminar

hood chamber for 24 h and then dried in a hot air oven at 110 °C to remove any remaining solvent. In this work, Lys-c-Zr BDC/CS with different loadings of Lys-c-Zr BDC as 3, 7 and 10 wt% were prepared using equation 7.1. The fabricated MMMs were designated as Lys-c-Zr BDC/CS (X), where X = 3, 7 and 10, referring to the weight percentage (wt %) of Lys-c-Zr BDC.

The Lys-c-Zr BDC loading is found using the following formula:

$$\text{MOF loading (wt\%)} = \frac{m_{\text{lys-c-Zr BDC}}}{m_{\text{lys-c-Zr BDC}} + m_{CS}} \times 100\% \quad (7.1)$$

Where $m_{\text{lys-c-Zr BDC}}$ is the mass of Lys-c-Zr BDC nanoparticles and m_{CS} is the mass of chitosan.

To show the effects of Lys conjugation on Zr BDC NPs for CO_2 separation we have also synthesized MMMs with only Zr BDC incorporation into CS matrix utilizing the same experimental conditions. The fabricated membranes were designated as Zr BDC/CS (3), Zr BDC/CS (7) and Zr BDC/CS (10) for 3, 7, 10 wt% Zr BDC loading respectively.

7.3. RESULTS AND DISCUSSIONS

7.3.1. Characterization of Zr BDC and Lys-c-Zr BDC MOF nanoparticles

7.3.1.1. Morphological and Elemental Analysis

The as-synthesized Zr BDC and Lys-c-Zr BDC NPs were characterized utilizing various analytical and spectroscopic techniques to validate its successful formation. Figure 7.1 shows the SEM images, TEM images and SAED pattern of the parent Zr BDC and Lys-c-Zr BDC MOF nanoparticles. As shown in the FESEM and FETEM images in Figure 7.1a-d, the synthesized NPs have a size of 80-120 nm and attained spherical morphology due to the usage of HCl acid as a modulator.[4] It was also found that the conjugation of Lys has not affected the

geometry of the Zr BDC NPs. The increase in amorphous nature upon conjugation with Lys is supported by SAED patterns as shown in Figure 7.1e,f.

Energy Dispersive X-Ray Spectroscopy (EDX) is a non-destructive analysis used to recognize the elemental composition of the synthesized NPs. It is obvious from the Figure 7.1g and h that Zr BDC contains C, O and Zr as the basic elements and after conjugation with Lys, it contains C, O, Zr and N atoms confirming the successful conjugation of Lys with Zr BDC nanoparticle.[5] The degree of conjugation was evaluated from the EDX data utilizing the normalization method. In 1 mole of both Zr BDC and lys-c-Zr BDC, the atomic content of Zr will be same so we have considered as standard to quantify the N content. The percentage increase of N was evaluated for the degree of conjugation using the following formula;

$$\text{Degree of modification (\%)} = 100 - \left[\left\{ \frac{\left(\frac{At\%_{N}}{At\%_{Zr}}\right)_{ZrBDC}}{\left(\frac{At\%_{N}}{At\%_{Zr}}\right)_{Lys\text{-}c\text{-}ZrBDC}} \right\} \times 100 \right] \quad (7.2)$$

Where, the At% is the atomic percentage of the respective elements.

The degree of conjugation of Lys onto Zr BDC was evaluated from the EDX using the Equation 7.2 and was found to be 72%. This confirms the successful covalent bond formation between the Lys and Zr BDC.

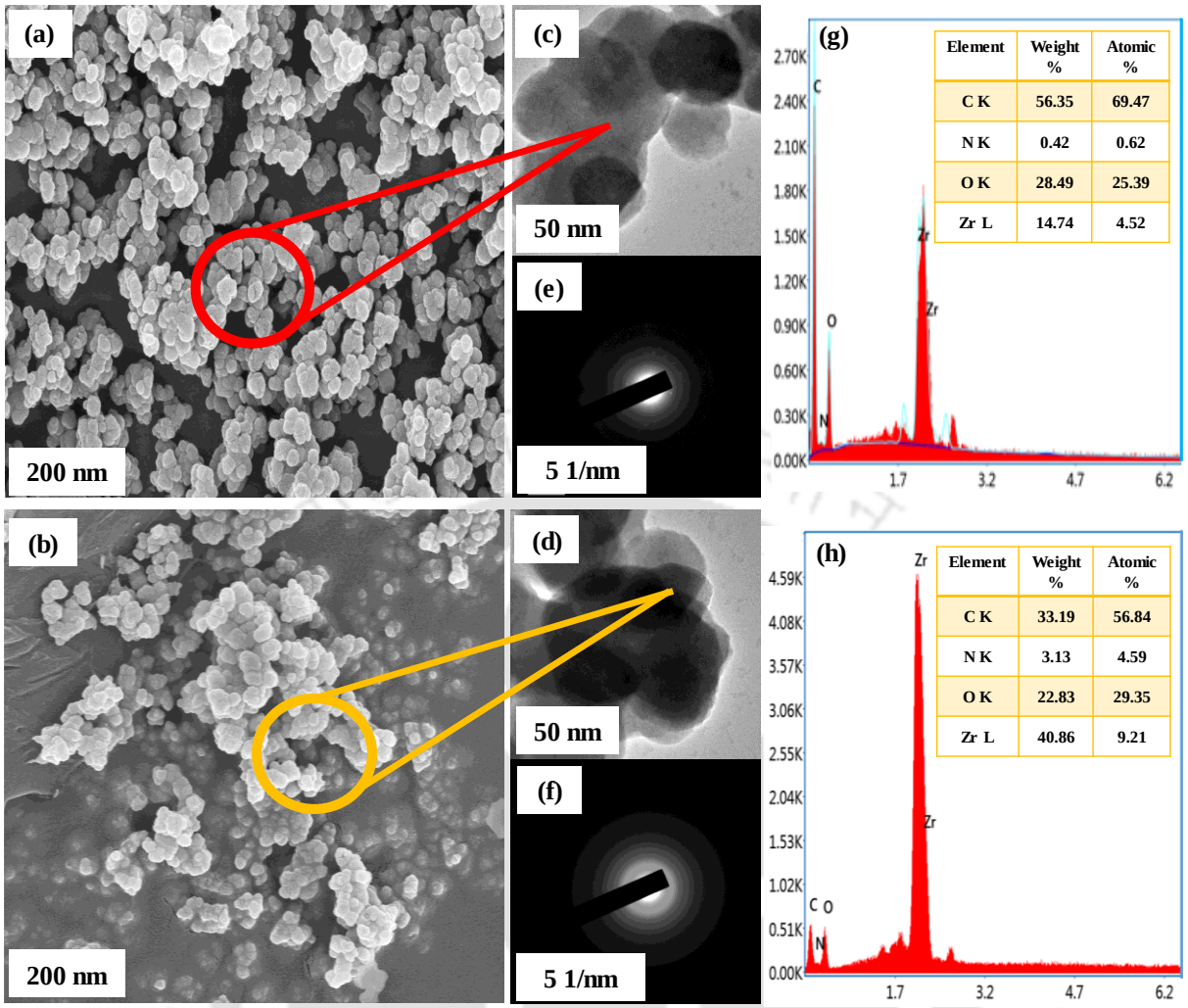

Figure 7.1. (a, b) SEM images, (c,d) TEM images, (e,f) SAED patterns and (g,h) EDX spectra of Zr BDC and Lys-c-Zr BDC NPs, respectively.

7.3.1.2. Structural Analysis

The crystalline structure of Zr BDC and modified Zr BDC NPs were analyzed through XRD and shown in Figure 7.2a. The existence of major planes (111), (002) and (006) at 2θ values of 7.35°, 8.52° and 25.94°, resembles the diffraction pattern of Zr BDC.[6] In addition, it is evident from the XRD patterns that the Zr BDC after decorating with Lys, exhibits no discernible changes. This finding implies that the surface-decorated Lys modulators had no negative effects on the inherent crystalline structure of the Zr BDC nanoparticles confirming the integrity of the Zr BDC skeleton.[7]

The chemical structure of Lys, Zr BDC and lys-c-Zr BDC was investigated using FTIR spectroscopy as shown in Figure 7.2b. The band at 1584 cm^{-1} and 1394 cm^{-1} can be assigned to the asymmetrical stretching and symmetrical stretching of C-O and C=C from carboxylates. The peak at a wavenumber of 745 cm^{-1} is for the aromatic organic compound and 547 cm^{-1} belongs to the Zr-O-C bond vibration.[8-9] The increase in the intensity of existing peaks and formation of new peaks observed at a wavenumber of 1652 cm^{-1} corresponds to the N-H bending confirming the conjugation of Lys with Zr BDC. The degree of modification via conjugation of Lys onto Zr BDC was determined from the FTIR spectra. Upon conjugation, the intensity of the C=O (amide) stretching at 1650 cm^{-1} intensifies due to the amide bond formation between dangling –COOH of Zr BDC and side chain $–NH_2$ of Lys. In particular, bands at around 2926 cm^{-1} region is attributed to the aliphatic C-H stretching of the amino acid arising due to the conjugation with lysine with UiO-66. This change is measured with respect to –CH (benzene ring) stretching peak at 745 cm^{-1} as a standard to correct for differences in sample concentration. From the FTIR spectra of Zr BDC and Lys-c-Zr BDC in Figures 7.2b, the absorbance (A) was recorded at wavenumber 1650 cm^{-1} and 745 cm^{-1} by the following formula;[10]

$$\text{Absorbance}\,(A) = 2 - \log\,(\%\ \text{Transmittance}) \tag{7.3}$$

$$\text{Degree of modification (\%)} = 100 - \left[\left\{\frac{\left(A_{1650}/A_{745}\right)_{ZrBDC}}{\left(A_{1650}/A_{745}\right)_{Lys\text{-}c\text{-}ZrBDC}}\right\}\times 100\right] \tag{7.4}$$

Where A_{1650} and A_{745} are the absorbance at 1650 cm^{-1} and 745 cm^{-1} respectively.

On substituting all the values in the Eqn 7.4, the extend of conjugation was found to be ~66 %, suggesting a successful interaction between the Lys and the Zr BDC nanoparticles.

Table 7.1: Values of transmittance and absorbance for Zr BDC and Lys-c-Zr BDC at different

wavenumbers of 1650 and 750 cm^{-1}.

	Transmittance (%)	Absorbance (%)
A_{1650} for ZrBDC	97	0.013228
A_{745} for Zr BDC	79	0.102373
A_{1650} for Lys-c-Zr BDC	93	0.031517
A_{745} for Zr BDC	83	0.080922

7.3.1.3. Thermal Stability Analysis

The thermal stability of Zr BDC and Lys-c-Zr BDC NPs was investigated using thermogravimetric analysis (TGA) from ambient temperature to 800 °C, as shown in Figure 7.2c. The curve exhibited three different stages of weight loss. The initial weight loss was observed at around 110 °C due to the evaporation of moisture from the pores of Zr-MOF. At 110 to 470 °C, a minimal weight loss of ~11% was observed indicating the thermal stability of the material. Finally, post 470 °C to 590 °C there was a sudden drop in weight% due to the degradation of the backbone structure of the organic ligand.[11,8] It can be observed upon Lys conjugation, the modified MOF displayed similar TGA plot with better thermal stability. To prove the enhanced thermal stability, we have evaluated the derivative thermogravimetric (DTG) curves from the dynamic TGA plots of Zr BDC and Lys-c-Zr BDC. As can be seen from the Figure 7.2d, at ~77 °C the first degradation peak appears which corresponds to the initiation of water loss. The more thermal degradation for Zr BDC indicates its more water loss. The second degradation peak at ~560 °C is the initiation of the breakdown of the organic moiety. For Lys-c-Zr BDC, the peak is less intense compared to that of Zr BDC confirming its high stability induced by the conjugation of two molecules.

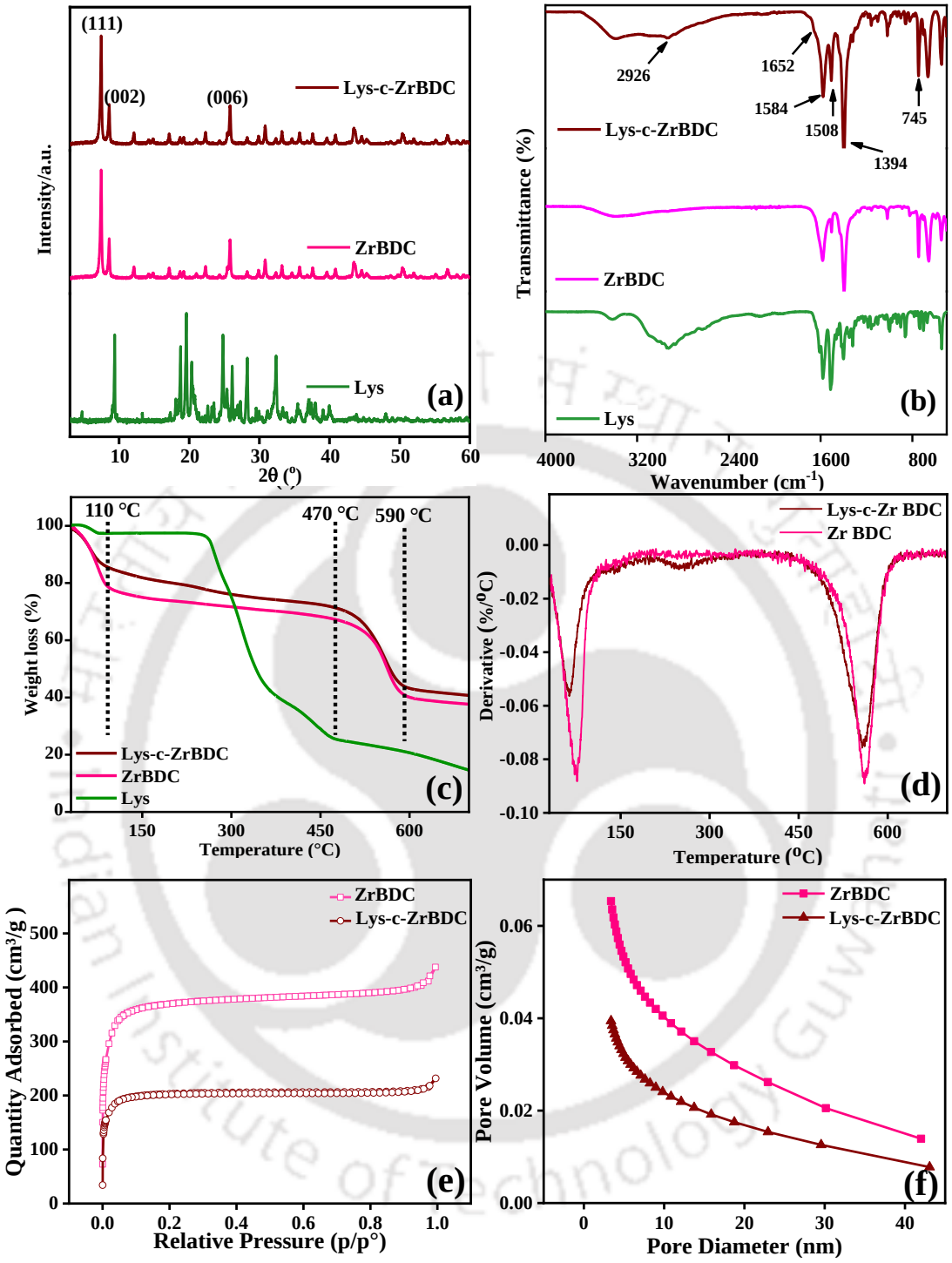

Figure 7.2. (a) XRD spectra, (b) FTIR spectra, (c) TGA profiles, and (d) DTG profiles of Lys, Zr BDC and Lys-c-Zr BDC nanoparticles; (e), (f) N_2 adsorption-desorption isotherms of Zr BDC and Lys-c-Zr BDC nanoparticles.

7.3.1.4. Surface Area Analysis

The surface area and porosity of the nanoparticles were analyzed by N_2 sorption

Brunauer-Emmet-Teller (BET) and the result is presented in Figure 7.2e and f and tabulated in Table 7.2. Zr BDC NPs exhibited an exceptionally high surface area of 1134 m^2/g and type I isotherms, indicating a microporous structure. After conjugation, the lys-c-Zr BDC NPs exhibited a reduced surface area indicating the binding of non-porous amino acid, Lys, onto the surface of Zr BDC NPs. The pore size distribution analysis showed that after post synthesis modification (PSM) of Zr BDC, the effective pore volume decreased while the pore size decreased slightly. Thus, the modification of the MOF does not alter the pore structure of Zr BDC NPs. Similar results were reported in the other literature.[7,12–14]

Table 7.2: BET and Langmuir surface area and pore volume of Zr BDC and Lys-c-Zr BDC

	Zr BDC	**Lys-c-Zr BDC**
BET surface area (m^2 g^{-1})	1134.7	619.2
Langmuir surface area (m^2 g^{-1})	1664.1	905.8
Pore volume (cm^2 g^{-1})	0.668	0.272
Pore diameter (nm)	2.356	2.322

7.3.2. Characterization of Lys-c-Zr BDC nanofillers embedded CS MMMs (Lys-c-Zr BDC/CS)

7.3.2.1. Morphological and Elemental Analysis

FESEM analysis was used to study the surface morphology and thickness of fabricated Lys-c-Zr BDC/CS membranes and presented in Figure 7.3. The top surface images of the different membranes (3 wt%, 7 wt% and 10 wt% of Lys-c-Zr BDC) obtained from FESEM, as shown in Figure 7.3a,c,e clearly depicted the agglomeration of nanoparticles at higher nanofiller loading. All the samples showed a void-free and dense structure, suggesting the

compatibility of the interface between the Lys-c-Zr BDC and CS membrane.[15]

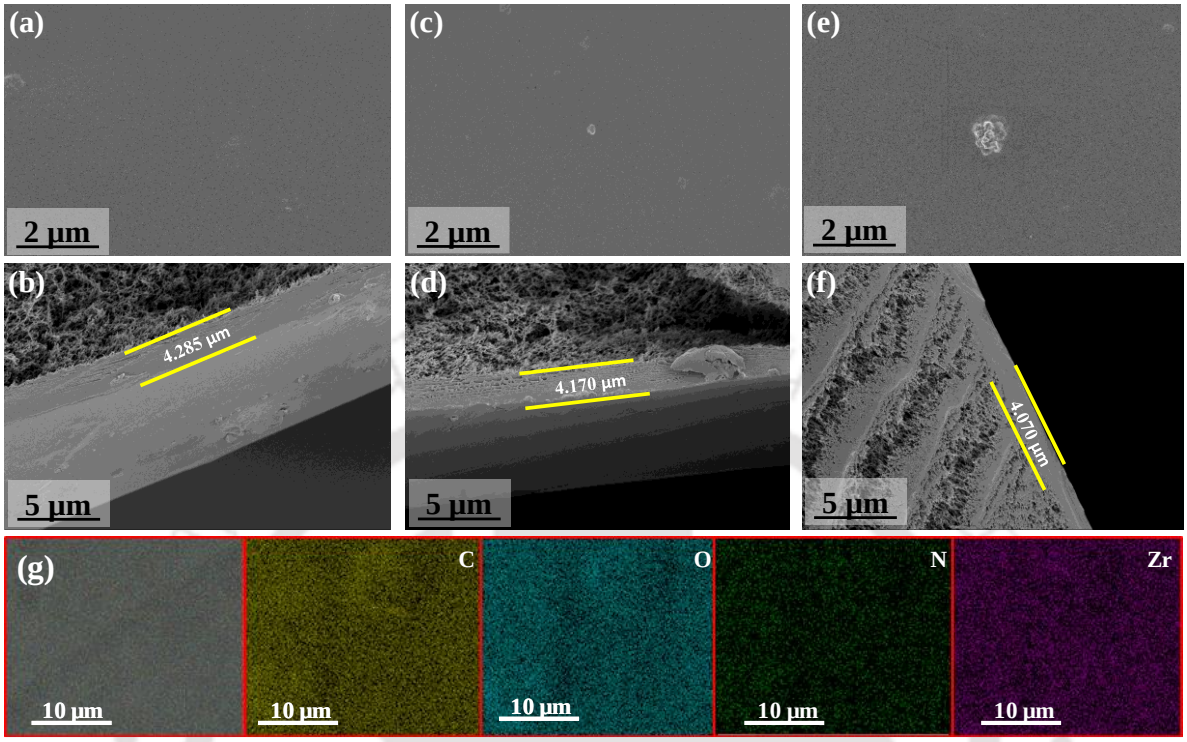

Figure 7.3. FESEM images of (a,c,e) top surfaces and (b,d,f) cross-section of Lys-c-Zr BDC/CS (3), Lys-c-Zr BDC/CS (7), Lys-c-Zr BDC /CS (10), respectively, (g) EDX mapping of Lys-c-Zr BDC/CS (7) MMM showing the presence of C, O, N, Zr elements, respectively.

The cross-section images shown in Figure 7.3b,d,f clearly showed the formation of a defect-free selective layer on the support with an approximate thickness of 4 (± 0.5) µm. The uniform distribution of all the elements was confirmed form the EDX mapping analysis of lys-c-Zr BDC/CS (7) MMM. Figure 7.3g shows the presence of all elements with carbon (yellow), oxygen (cyan), nitrogen (green) and Zr (purple), respectively. As observed the presence of Zr throughout the surface of the membrane confirms the uniform distribution of the Lys-c-Zr BDC filler into CS matrix.

7.3.2.2. Surface Roughness Analysis

Atomic force microscopy (AFM) was performed to investigate the dimensional

morphology of the top surface of the composite membranes. The AFM technique produces two- and three-dimensional (2D and 3D) images of materials by randomly counting the diameter and height of particles, which present valuable information about the surface morphology and topology of the top surfaces of the membranes.[16]

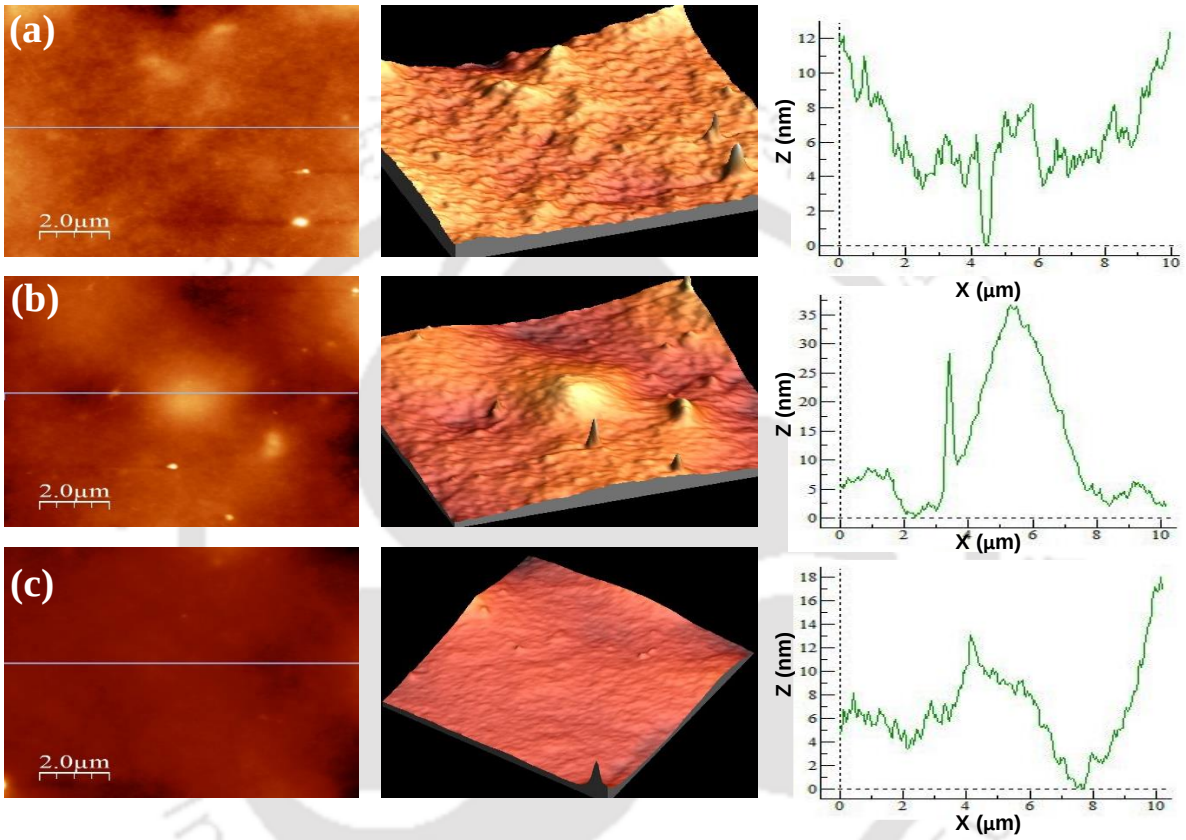

Figure 7.4. AFM images of (a,b,c) top surfaces of Lys-c-Zr BDC/CS (3), Lys-c-Zr BDC/CS (7) and Lys-c-Zr BDC/CS (10), respectively.

The obtained results, as shown in Figure 7.4 demonstrated that with increasing the MOF loading from 3 to 7 wt%, the surface roughness increases and then decreases on further increment to 10 wt%. This reduction in the roughness at 10 wt % MOF loading is due to the aggregation of the nanoparticles at specific regions of the CS membrane causing non-uniformity in the Lys-c-Zr BDC/CS (10) MMM. SEM and AFM results show co-relevance with each other and reveal that the loading densities of MOF nanoparticles greatly influence the surface morphologies and microstructures of the fabricated membranes.

7.3.2.3. Structural Analysis

The FTIR analysis was done to analyze the chemical interaction between the CS and Lys-c-Zr BDC nanoparticles in the fabricated membranes. Figure 7.5a showed the characteristics absorbance band of C=O stretching vibration of the amide group at 1651 cm^{-1}. The absorbance band at 1553 cm^{-1} and 653 cm^{-1} corresponds to the Zr-O vibration of Zr-O-C.[17] The band observed at 2863 cm^{-1} corresponds to the asymmetric stretching of CH_3 and CH_2 in the chitosan membrane. Furthermore, the peak between 3200-3500 cm^{-1} is of the hydroxyl (-OH) and ($-NH_2$) group in the CS membrane.[18]

The XRD analysis was performed to show any crystalline structure change of the nanocomposite membrane due to the incorporation of Lys-c-Zr BDC on the structure of the fabricated membrane. Figure 7.5b shows a strong and a wide distinctive peaks at 2θ values of 9.25º and 19.75º due to coexistence of the CS crystalline phase and other non-crystalline phases.[19,20] The peak intensity rapidly decreases as the loading of Lys-c-Zr BDC increases from 3 wt% to 7 wt%. This created more transport networks due to the decrease in the polymer crystalline phase, which is expected to enhance its CO_2 permeance.

7.3.2.4. Surface Hydrophilicity Analysis

The surface hydrophilicity of the composite membrane was analyzed by contact angle measurement. Due to the hydrophilic amine ($-NH_2$) group in the chitosan structure, the pure chitosan membrane exhibits hydrophilicity with a contact angle of 40°. However, excessive hydrophilicity of the CS membrane compromises its fragility in CO_2 separation application by causing excessive water uptake, producing a lot of swelling and lowering the mechanical strength. As the loading of Lys-c-Zr BDC increases and reaches an optimum concentration of 7 wt %, the contact angle value increases to 65° thereby improving the wettability condition of

the composite membrane due to the presence of the Zr BDC nanoparticle, depicted in Figure 7.5c. It is important to anticipate the balance between the hydrophobicity/hydrophilicity of the framework surface to achieve energy-efficient CO_2 separation.[21] This result is in a good agreement with the contact angle outcomes.

7.3.2.5. Thermal Stability Analysis

TGA was done to investigate the thermal stability of the MMMs. As depicted in Figure 7.5d, the weight loss was primarily observed at around 110 °C due to the loss of unbound moisture content. The second weight loss was observed at around 210 °C due to the decomposition of the polymer unit. It can be observed that the pristine chitosan membrane shows more weight loss as compared to the Lys-c-Zr BDC loaded CS membranes. With the increase in the concentration of Lys-c-Zr BDC from 3 wt% to 7 wt%, the rate of weight loss decreased confirming the enhanced thermal stability upon formation of MMMs. Beyond 7 wt% incorporation, the weight loss increased due to the presence of agglomerated nanoparticles. Finally, the major weight loss occurred at around 300 °C-400 °C due to pyrolysis of organic moieties, as confirmed by the other literature.[22] The TGA results demonstrated that the incorporation of Lys-c-Zr BDC to the fabricated membrane enhanced its thermal stability much required for the CO_2 separation and allowed it to endure temperatures up to 210 °C.

TGA isotherm at 95 °C, 115 °C and 145 °C was used to determine the thermal stability of the fabricated and optimized Lys-c-Zr BDC/CS (7) flat sheet mixed matrix membrane as shown in Figure 7.5e. The composite MMM was tested for maximum 145 °C to show its stability for practical conditions, as in general the temperature of flue gas is not more than 120 °C. A minimal weight loss was observed during the 45 min linear isotherm at 95, 115 and 145 °C thus confirming its high thermal stability without any cross linking within the membrane.

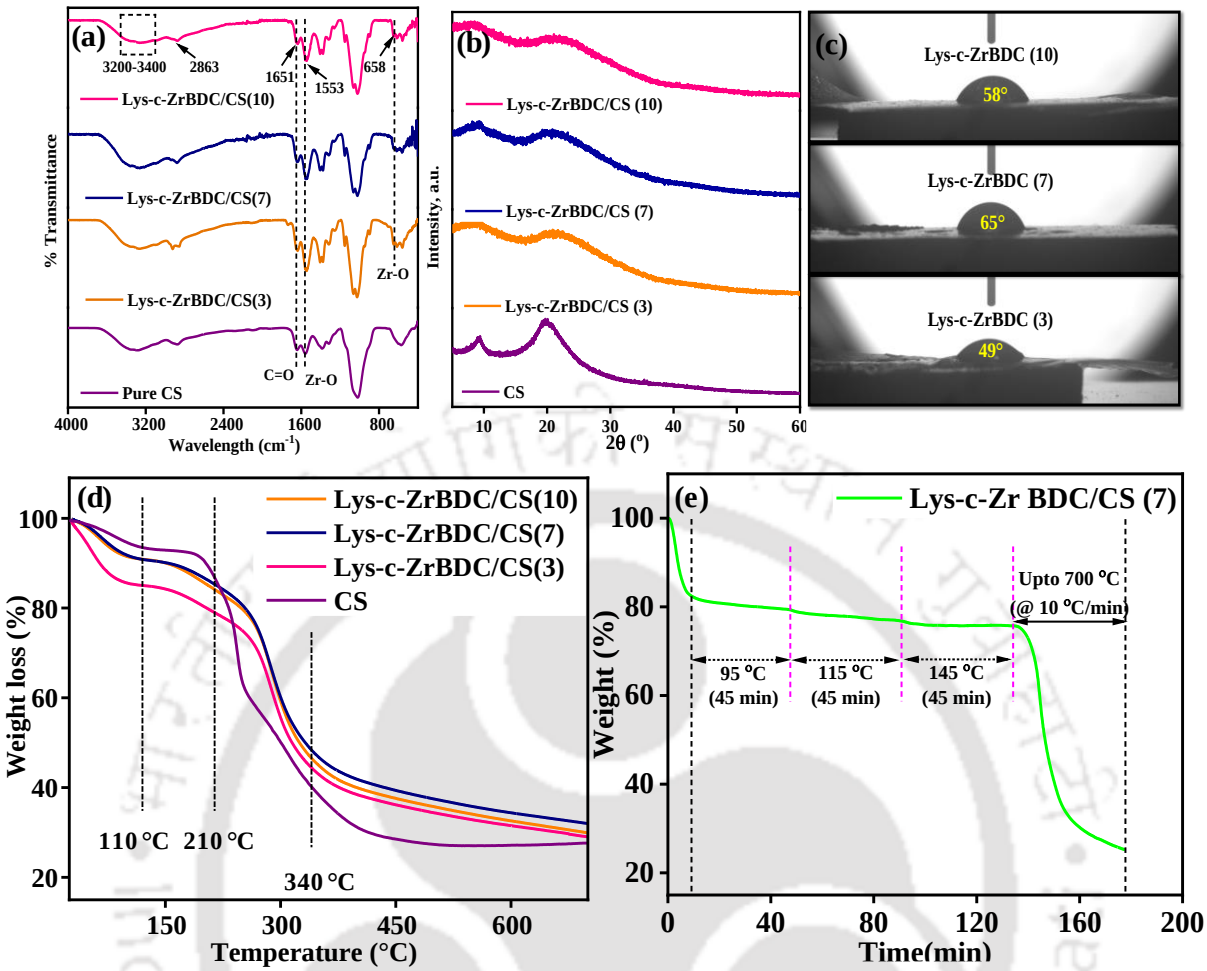

Figure 7.5. (a) FTIR spectra, (b) XRD spectra, (c) Contact angle, (d) Dynamic TGA study of all the fabricated and (e) TGA isotherm for Lys-c-Zr BDC/CS (7) membrane at 95 °C, 115 °C and 145 °C.

7.3.2.6. Characterization of Zr BDC embedded CS MMM

The uniform distribution of all the elements was confirmed form the EDX mapping analysis of pristine CS membrane, Zr BDC/CS (7) MMM. Figure 7.6a and b shows the presence of all elements with carbon (yellow), oxygen (cyan), nitrogen (green) and Zr (purple), respectively. As observed the presence of Zr throughout the surface of the membrane confirms the uniform distribution of the Zr BDC filler into CS matrix. The cross sectional and top surface FESEM images of the Zr BDC/CS (7), fabricated under similar conditions, are shown in Figure 7.6c and d to compare the thickness and uniformity of the formed MMM with composite of CS and

Zr BDC nanofillers.

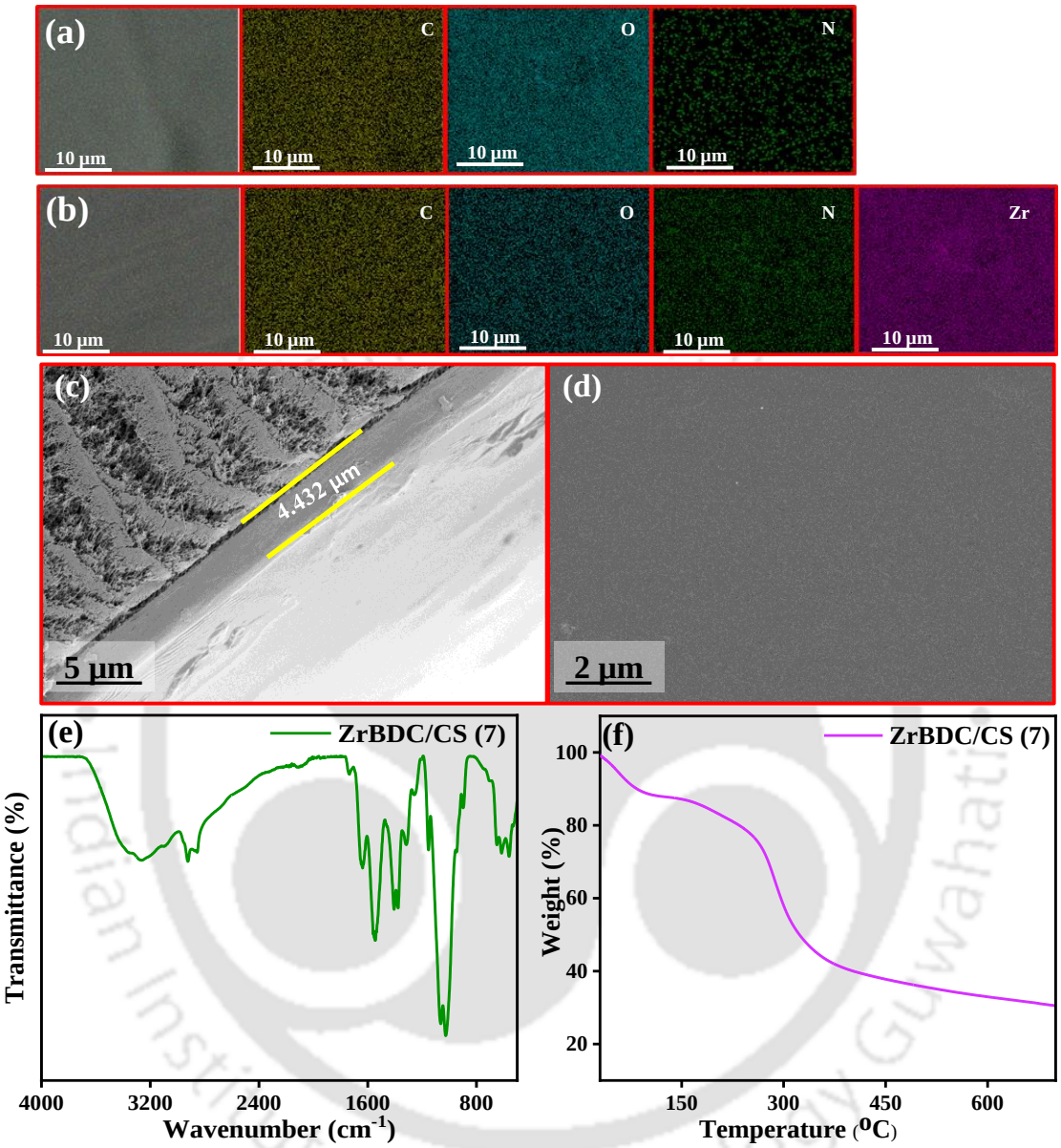

Figure 7.6. EDX mapping of (a) pristine CS membrane and (b) Zr BDC/CS (7) MMM showing the presence of the respective constituent elements, (c) cross-section FESEM image, (d) Top surface FESEM image, (e) FTIR spectra and (f) Dynamic TGA profile of optimized Zr BDC/CS (7) MMM.

FTIR spectra was obtained for the Zr BDC/CS (7) membrane, shown in Figure 7.6e, confirming the presence of similar chemical interactions and successful embedment of the Zr BDC nanoparticles onto the CS membrane. Similar to Lys-c-Zr BDC, TGA plot obtained for

the Zr BDC/CS (7) membrane is shown in Figure 7.6f, but the extend of weight loss was at the intermediate of the pristine CS and Lys-c-Zr BDC/CS membranes. This observation suggests the importance of Lys conjugation for the increment in the thermal stability of the MMMs for CO_2 separation applications.

7.4. CO_2/N_2 gas separation study

Flue gas mixture (20% CO_2 and 80% N_2) is separated using a gas permeation setup design, explained in Section 2.4 and illustrated in Scheme 2.2, at different operating conditions such as filler loading for Zr BDC/CS and Lys-c-Zr BDC/CS; the temperature under dry and humid conditions, pressure, sweep/feed humidity flow and selective layer thickness for optimized Lys-c-ZrBDC/CS (7) MMM etc.

7.4.1. Effects of Zr BDC and Lys-c-Zr BDC nanofillers loading (wt%) on CO_2 separation performance of MMMs

Gas permeation measurements investigated the CO_2 separation (GS) properties of the fabricated thin film Zr BDC /CS and lys-c-Zr BDC /CS mixed matrix flat sheet composite membranes. CO_2 and N_2 permeance, flux and CO_2/N_2 selectivity were tested across the fabricated membranes at 0.221 MPa feed pressure and 85 °C module temperature and with a sweep/feed moisture flow ratio of 1.67. CO_2 separation performance of the pristine CS membrane were taken from chapter 3. The gas permeance and CO_2/N_2 selectivity were significantly influenced by the presence of Zr BDC and lys-c-Zr BDC in the CS matrix, as shown in Figure 7.7. For the Zr BDC/CS MMM as shown in Figure 7.7a, b, c, the CO_2 separation performance improved with an increase in the loading of Lys-c-Zr BDC up to 7 wt%. However, a notable decline in performance was observed when the filler loading was further increased to 10 wt%.

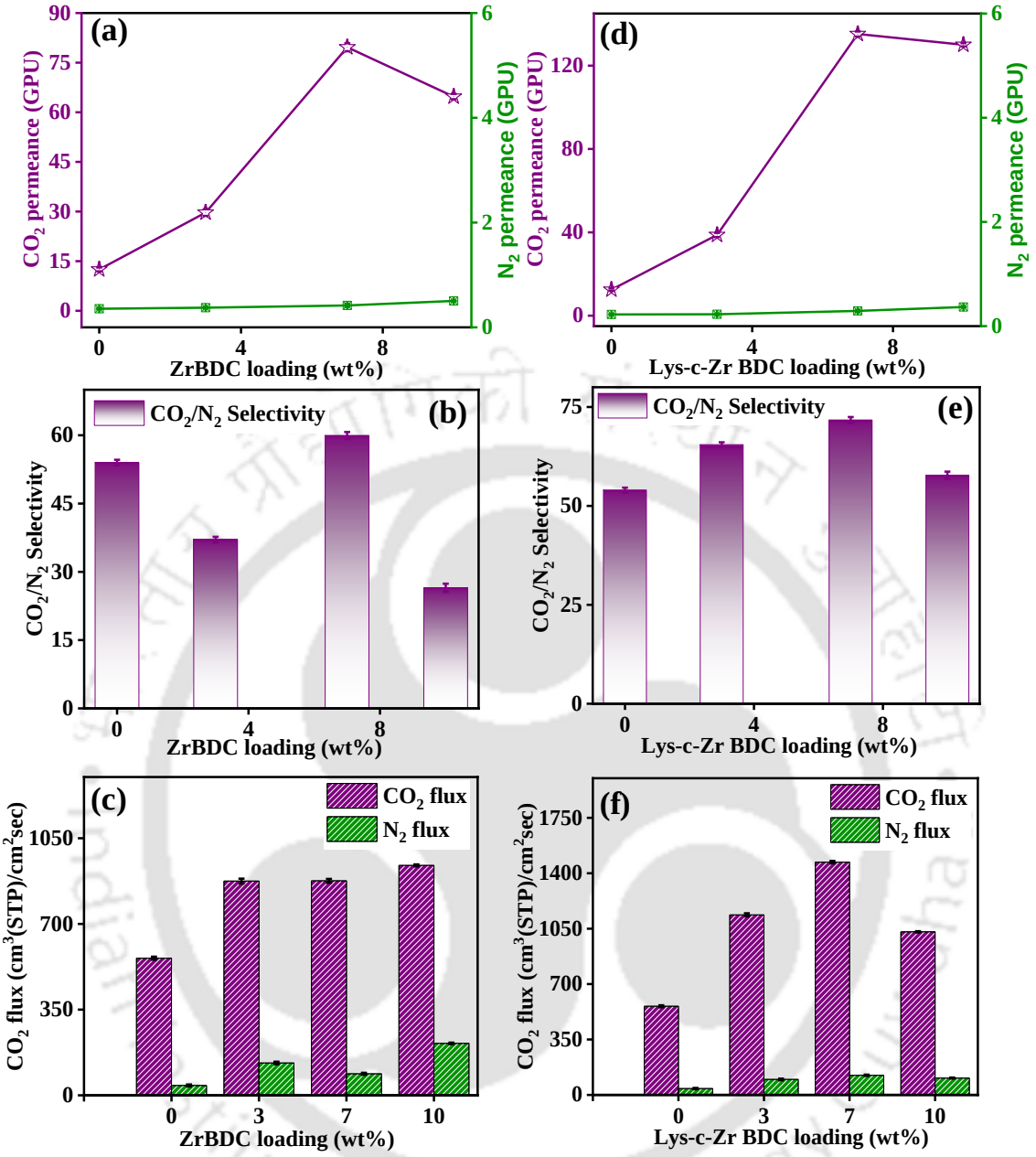

Figure 7.7. Effects of Zr BDC and Lys-c-Zr BDC loading (wt%) on (a,d) CO_2, N_2 permeance, (b,e) CO_2/N_2 selectivity, (c,f) CO_2, N_2 flux respectively.

Similarly, for the Lys-c-Zr BDC/CS MMM depicted in Figure 7.7d, e, f, a loading of 7 wt% of Lys-c-Zr BDC led to a remarkable 981% increase in CO_2 permeance and a 32% increase in selectivity, when compared to neat CS while N_2 permeance remained relatively unchanged, the obtained GC data is presented in Figure A1 and the calculations are described in Appendix A1. However, when the filler loading was increased beyond 7%, there was a

modest reduction in CO_2 permeance (from 135.2 GPU to 130.2 GPU), accompanied by a significant increase in N_2 permeance (from 2.3 GPU to 4.1 GPU) was observed. As a result, there was a substantial loss in CO_2/N_2 selectivity.

The reactive gas molecules, such as CO_2, reversibly react with the carrier sites, such as $-NH_2$ functional groups, to generate carbamate ion (HCO^{3-}) via the zwitter ion mechanism and facilitate the CO_2 transport across the membrane (from feed to permeate side) through the dissolution process. As a result, the facilitated transport MMM demonstrated strong CO_2 selectivity over N_2, whereas N_2, as an inert gas molecule, cannot react with the carrier sites.[24] The primary function of conjugation of Lys amino acid onto Zr BDC MOF surface was to offer more fixed carrier sites with its $-NH_2$ groups,[3] as well as providing physical and chemical micro-environment for CO_2 and N_2 gas transport across the MOF's channels and polymer networks. This is consistent with obtained results too, which showed that at 0% MOF loading (pristine CS), selectivity and permeance are quite lower (Table 7.3) than the results obtained by our research at 7 wt% nanofillers loading. In other words, by increasing the lys-c-Zr BDC content in the CS matrix, more fixed carrier sites were provided for better CO_2 facilitation and additional transport channels for N_2 and CO_2 gas molecules were established within the MOF network.[23] With the increase in the Zr BDC and lys-c-Zr BDC content in the CS matrix from 3 wt% to 7 wt%, there was increment in both CO_2 permeance and CO_2/N_2 selectivity for either case. Upon further increase in the nanofiller content (10 wt%), there was decrement in the CO_2 performance for both Zr BDC/CS and Lys-c-Zr BDC/CS. Thus, 7 wt% was found to be the optimum concentration of filler into the CS matrix for the formation of composite MMMs. Comparing the CO_2 permeance and selectivity results for pristine CS, Zr BDC/CS and Lys-c-Zr BDC/CS (Figure 7.7 and Table 7.3), under similar operating conditions, it was found that the Lys conjugation has advance effect on the CO_2 separation performance. Thereby, all the

advance parameter studies for the CO_2 separation performance were carried out using the Lys-c-Zr BDC/CS (7) MMM.

Table 7.3. Comparison of CO_2 separation performances of optimized bare CS, Zr BDC/CS(7) and Lys-c-Zr BDC/CS(7) MMMs.

Polymer	Filler (wt%)	Operating conditions	CO_2 permeance (GPU)	CO_2/N_2 selectivity	References
CS	-	85 °C, 0.221 MPa	15	48	This work
CS	Zr BDC (7)	85 °C, 0.221 MPa	79	60	This Work
CS	Lys-c-Zr BDC (7)	85 °C, 0.221 MPa	135	71	This Work

7.4.2. Effects of temperature on CO_2 separation performance of optimized Lys-c-Zr BDC/CS(7) MMM

Despite the fact that average temperature of the flue gas after a flue gas desulfurization (FGD) is 57 °C,[25] however, a rise in the operating temperature is observed due to the requirement of mild compression of the feed gas in the range of 0.15-0.4 MPa for most separation processes for post-combustion carbon capture. Studies showed that if the flue gas is compressed to 1.5 atm, the temperature rises from 57 to around 85 °C.[26] Figure 7.8a,b,c demonstrates the effect of temperature change at a feed pressure of 0.221 MPa under dry conditions (No moisture supply in feed and sweep gas streams) on the CO_2, N_2 permeance, CO_2/N_2 selectivity and CO_2, N_2 flux for the optimized Lys-c-Zr BDC/CS (7) MMM. For dry conditions, all the three parameters, CO_2 permeance, selectivity and flux, increased from 20.9 GPU to 34.6 GPU, 12 to 29.4 and 332 $\times 10^{-6}$ cm^3 (STP)/cm^2sec to 552$\times 10^{-6}$ cm^3 (STP)/cm^2sec,

respectively, as the feed temperature increased until 85 °C. The obtained results showed 13%, 145% and 66.26% enhancement in CO_2 permeance, CO_2/N_2 selectivity and CO_2 flux, respectively. Then a sharp fall in the membrane performance was observed on a further rise in the temperature from 85 °C to 105 °C. The trend followed by separation performance of the Lys-c-Zr BDC/CS (7) MMM can be attributed to the following reasons; (1) from zwitterion mechanism it can be understood that the CO_2 molecules are reacting reversibly with amines, present on the Lys-c-Zr BDC surface and polymer matrix. The temperature increment increased the reaction rate between CO_2 and amines and contributed to the performance enhancement. (2) With rise in temperature, the kinetic energy of gas molecules increased and consequently the diffusivity of the gas molecules through the Lys-c-Zr BDC pores and polymer matrix increased and resulted in enhancement in the CO_2 separation performance until 85 °C.

For the swollen Lys-c-Zr BDC/CS (7) membrane, as can be seen in Figure 7.8d,e,f, the CO_2 permeance increased by ~5.2 folds, CO_2/N_2 selectivity increased by ~1.7 folds and CO_2 flux increased by ~1.9 folds when the temperature was raised from ambient temperature until 85 °C. This enhancement in the performance of the swollen membranes can be explained as follows. Firstly, according to the zwitterion mechanisms, in dry conditions, 1 mole of CO_2 requires 2 moles of amines to react reversibly, whereas in the presence of water it requires only 1 mol of amines to take away 1 mole of CO_2 molecule form the mixture gas.[24,27] The presence of water and the rise in temperature greatly contributed to the enhancement of membrane separation. Secondly, the movement of polymer chains has been accelerated, which might enhance the diffusion of gases through the membrane.[28] However, as the temperature rises from 85 °C to 105 °C, the CO_2/N_2 selectivity decrease for Lys-c-Zr BDC/CS (7) MMM due to the drying of the membrane matrix.

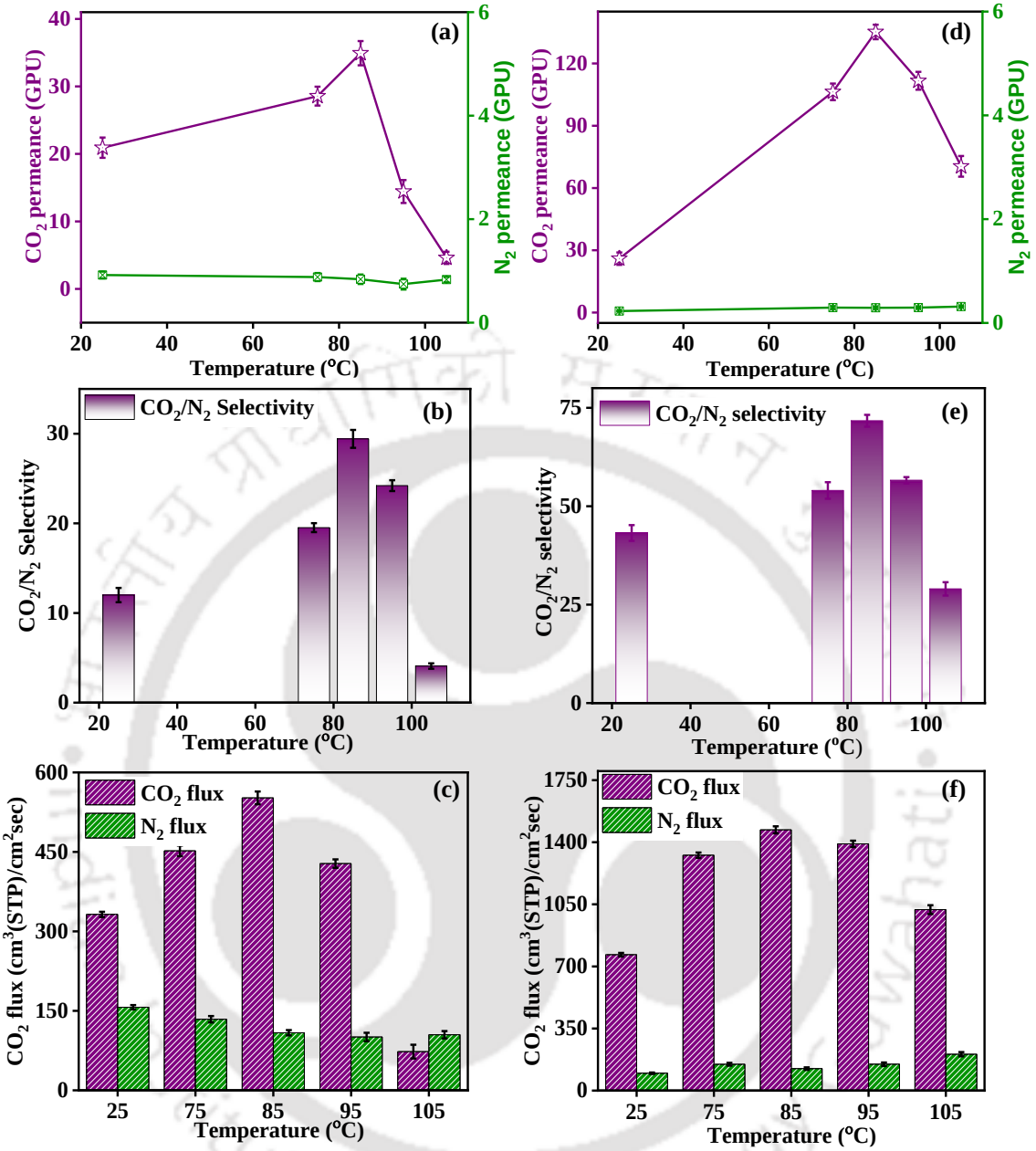

Figure 7.8. Effects of operating temperature on (a,d) CO_2, N_2 permeance, (b,e) CO_2/N_2 selectivity and (c,f) CO_2, N_2 flux under dry conditions and humid conditions, respectively, on Lys-c-Zr BDC/CS (7) MMM.

Along with CO_2 permeance, the increase in temperature has greater impact on the N_2 permeance as well. In fact, as the temperature rises and the polymer chain movement increases, larger gas molecules like N_2 have a greater chance of passing through the membrane more quickly, which results in the declination in CO_2/N_2 selectivity.[29] Since N_2 permeate through

the membrane via dominant diffusivity, their rate of diffusion was higher at high temperatures than CO_2, thus shifting the selectivity of CO_2 over N_2 to the higher temperature range.

7.4.3. Effect of feed pressure CO_2 separation performance of optimized Lys-c-Zr BDC/CS(7) MMM

Permeance tests at various feed pressures of 2.2, 3.2, 4.2 and 5.2 bar have been carried out to learn more about the effect of feed pressure on the CO_2 separation performance of membranes and displayed in Figure 7.9a,b,c. The graph illustrates the enhancement of the CO_2 permeance with the drop in the selectivity as feed pressure increased from 2.2 bar to 4.2 bar. The observed results due to the pressure enhancement on polymeric MMM can be attributed to the following reasons;[30,31] (1) decline in permeance followed by a reduction in polymer free volume; (2) an increase in driving force; and (3) plasticization effect brought on by increased gas concentration in the polymer matrix. On further rise in the pressure from 4.2 to 5.2 bar, a drastic decline in the permeance and selectivity was observed. As the literature suggests, the compactness effect of CS chains and amine carrier saturation led to a decrement in CO_2 separation performances.[32]

7.4.4. Effect Sweep/feed humidity CO_2 separation performance of optimized Lys-c-Zr BDC/CS(7) MMM

The facilitation of CO_2 molecule transport through membranes containing reactive CO_2 carriers (amines) depends critically on the presence of moisture. A number of variables, including fuel type (particularly moisture content), combustion parameters and exhaust temperature, have an impact on the water content of flue gas.[33] In this study, moisture was fed into the feed and sweep gases in controlled amount before entering the permeation cell. Using a Lys-c-Zr BDC/CS (7) MMM with an approximate selective layer thickness of 4 μm on the

porous PES support, the effect of moisture content on the membrane separation performance at 85 °C were examined. At sweep/feed moisture ratios of 0, 0.33, 1, 1.67, 2.33 and 3, the separation performances were observed with the feed gas (composed of 20% CO_2 and 80% N_2) fed to the membrane module.

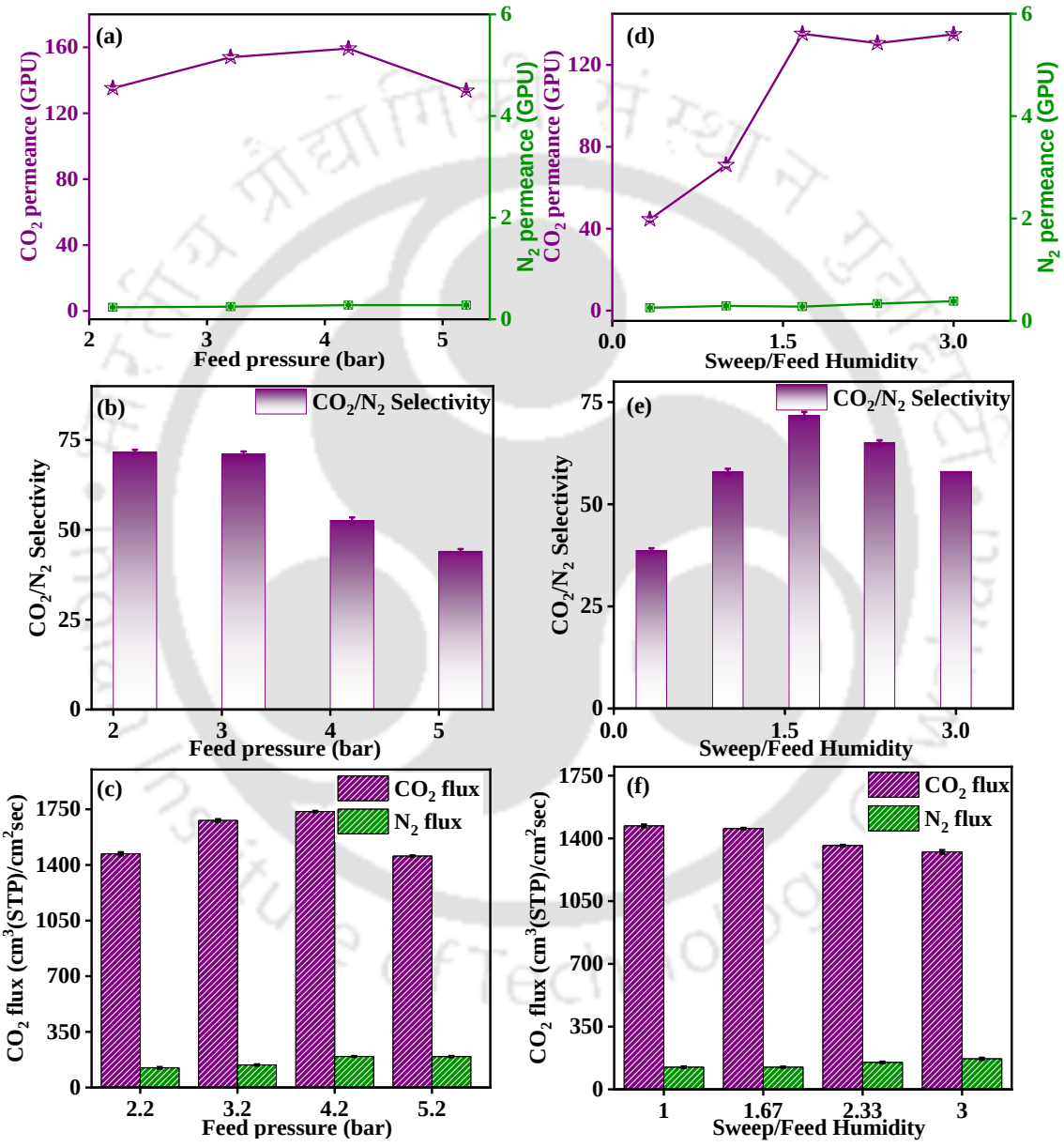

Figure 7.9. Effects of pressure and sweep/feed moisture flow on (a,d) CO_2, N_2 permeance, (b,e) CO_2/N_2 selectivity and (c,f) CO_2 and N_2 flux, respectively, under humid conditions on Lys-c-Zr BDC/CS (7) membrane.

As shown in Figure 7.8a,b,c, the dry membrane has 34.9 GPU permeance, 29.4 CO_2/N_2 selectivity and 332 $\times 10^{-6}$ cm^3 (STP)/cm^2sec flux. These values gradually increased when humidified gases were supplied to the module and sweep/feed moisture content increased from 0 to 1.67. At 1.67 sweep/feed ratio as shown in Figure 7.9d,e,f, the fabricated membrane obtained optimum values of 135.2 GPU, 71.7 CO_2/N_2 selectivity and 1455 $\times 10^{-6}$ cm^3 (STP)/cm^2sec flux. The reaction rates of CO_2 with amine carriers increases with the moisture content and higher moisture content on the permeate side increases water retention inside the membrane, thereby increasing the mobility of both mobile and fixed carriers of Zr BDC filler and CS matrix. Additionally, higher moisture content on the sweep side dilutes the permeated CO_2 concentration through the membrane in the sweep side, thus increasing the driving force. According to Quinn et al.,[34] the moisture content in the feed and sweep side increases CO_2 permeability. On further increase in the moisture content beyond 1.67, a minor loss in the CO_2 permeance and flux but a major loss in the CO_2/N_2 selectivity were observed due to the swelling of the CS matrix.

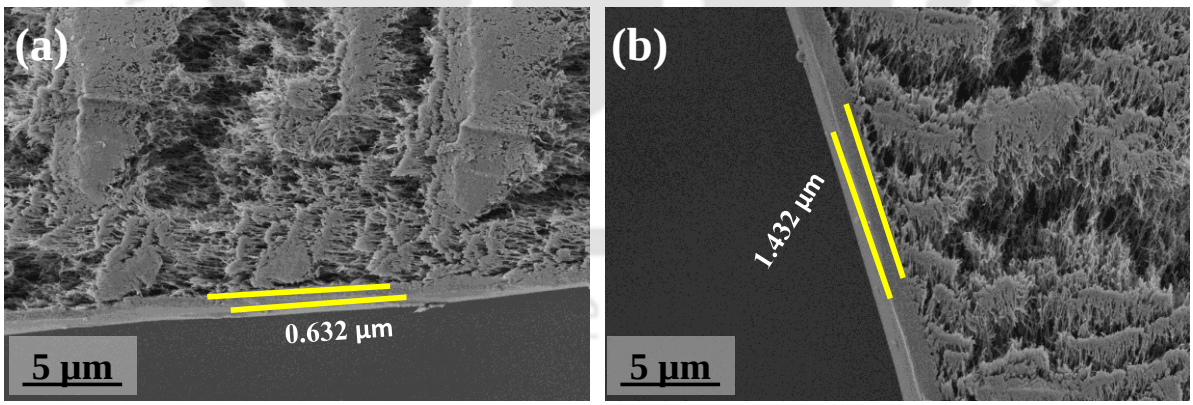

Figure 7.10. FESEM images of cross section Lys-c-Zr BDC/CS (7) with different selective layer thickness.

7.4.5. Effect of selective layer thickness CO_2 separation performance of optimized Lys-c-Zr BDC/CS(7) MMM

The thickness of the selective layer in a membrane plays a crucial role in determining its CO_2 permeance and selectivity of CO_2 over N_2. For the optimized Lys-c-ZrBDC/CS (7) MMM, we have synthesized it with three different selective layer thicknesses: ~0.5 μm, 1-1.5 μm and 4-4.5 μm as shown in Figure 7.3d and Figure 7.10. The selective layer is responsible for allowing certain gases to pass through while blocking others based on their size, solubility and diffusivity and reversible reactivity with amine carriers. As shown in Table 7.4 CO_2 permeance has increased from 135 GPU to 247 GPU but the CO_2/N_2 selectivity is significantly decreased from 71 to 43 when selective layer thickness decreased form ~4.5 μm to ~0.5 μm. As expected, the thinner the selective layer, the higher the CO_2 permeance when all other parameters are kept constant. A thinner selective layer offers less resistance to gas diffusion, allowing gas molecules to pass through more easily. A higher selectivity indicates better separation performance. The thickness of the selective layer can also influence the selectivity of CO_2 over N_2. Thicker selective layers hinder the diffusion of larger molecules like N_2, while still allowing smaller CO_2 molecules to pass through more easily. As a result, the membrane achieves a higher selectivity for CO_2 over N_2. However, there is a limit to this effect and at some point, further increasing the thickness showed diminishing returns and led to reduced selectivity due to increased resistance for all gases.

Table 7.4 Comparison of the performance of the optimized Lys-c-ZrBDC/CS (7) MMM with different selective layer thickness.

	Lys-c-ZrBDC/CS (7)	
Selective layer Thickness (μm)	**CO_2 Permeance (GPU)**	S_{CO_2/N_2}
0.5-0.6	247	43
1-1.5	169	58
4-4.5	135	71

7.4.6. Comparative study of the obtained results with the reported literature

Compared to neat CS and other reported literature, as shown in Table 7.5, the CO_2 separation data showed improvement in the separation performance of Zr BDC/CS (7) and Lys-c-Zr BDC/CS (7) MMM at optimum temperature of 85 °C. Its potential for use in gas purification is indicated by presenting the data on the Robeson upper bound curve Figure 7.11. From the curve, it is observed that, at room temperature and under humid conditions, the CO_2 separation performance of the Lys-c-Zr BDC/CS (7) membrane is comparable with that of the reported literature. However, with rise in temperature, due to the reversible zwitter ion reaction of CO_2 molecules with carrier amine, the CO_2 permeance and CO_2/N_2 selectivity increases, consequently surpassing the Robeson's upper bound curve. These results show the potential of post-synthetic modification on a Zr BDC NPs structure for use in an MMM, where one can finely tune the interaction between permeability and selectivity.

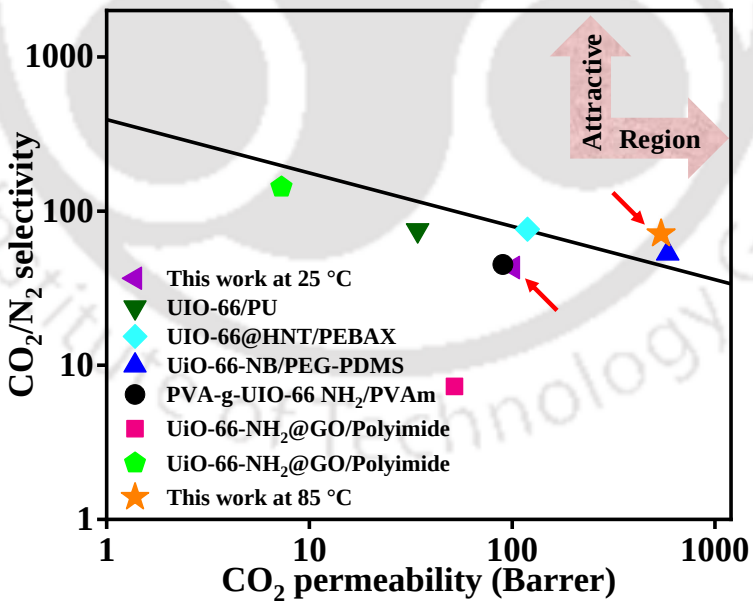

Figure 7.11. Robeson upper bound curve: Comparison of the CO_2 separation performance of the optimized Lys-c-Zr BDC/CS (7) MMM with the reported literature.

Table 7.5. A comparative account of the CO_2 separation performance of the optimized Lys-c-ZrBDC/CS (7) MMM with available literature.

Polymer	Filler	Operating conditions	CO_2 permeability (Barrer)	CO_2/N_2 selectivity	References
PEBAX	UIO-66@HNT	25 °C, 0.5 MPa	119	76.26	[35]
Polyurethane	UIO-66	25 °C, 0.4 MPa	34.2	75.2	[36]
PEG/PPG–PDMS	UiO-66-NB	30°C, 0.1 MPa	585	53	[37]
PVAm	PVA-g-UIO-66 NH_2	25°C	~90	45	[38]
Polyimide	UiO-66-NH_2@GO	25°C, 0.3 MPa	7.28	52	[39]
CS	**Lys-c-Zr BDC**	**25°C, 0.221 MPa**	**101**	**43**	**This Work**
CS	**Lys-c-Zr BDC**	**85°C, 0.221 MPa**	**541.92**	**71.18**	**This Work**

7.5. Conclusions

The intrinsic structural amphipathicity of CS polymer offered strong compatibility to the Zr-BDC nanoparticles and thus functioned as a viable polymer matrix for high-performing MMMs. Zr-BDC NPs were successfully conjugated with the CO_2-philic Lys amino acid via the amide bond formation among the dangling –COOH of the MOF and side chain –NH_2 of Lys. The solution casting method resulted in the formation of 4 (±0.5) μm thick, dense,

amorphous and thermally stable selective layers for the CO_2 separation purpose. Relative to the neat polymer, the 7 wt% loaded Zr BDC and Lys-c-Zr BDC was found to be the optimum loading amount for considerable improvement in CO_2 permeance and CO_2/N_2 selectivity. The fabricated Lys-c-Zr BDC/CS (7) membrane showed CO_2 permeance of 34.6 GPU, CO_2/N_2 selectivity of 29.4 in dry conditions and CO_2 permeance of 135 GPU, CO_2/N_2 selectivity of 71.5 in humid conditions at 85 °C and 0.221 feed pressure. From Robeson's curve, it is observed that, at room temperature and under humid conditions, the CO_2 separation performance of the Lys-c-Zr BDC/CS (7) membrane is comparable with the reported literature. However, as the temperature rises, due to the facilitated transport of CO_2 molecules, the CO_2 permeance and CO_2/N_2 selectivity increase, consequently surpassing the Robeson's upper bound curve. Hence, it is advisable to use the fabricated membranes at a higher temperature. The obtained results show that amine conjugation with MOF nanoparticles approach is very promising for CO_2 separation from flue gas. We consider that the current findings will pave the way for a new technique for MMM interface assessment in high-performance gas separation applications.

7.6. References

(1) Gelles, T.; Lawson, S.; Rownaghi, A. A.; Rezaei, F. Recent Advances in Development of Amine Functionalized Adsorbents for CO_2 Capture; *Springer US*, **2020**; Vol. 26. https://doi.org/10.1007/s10450-019-00151-0.

(2) Liu, L.; Qiao, Z.; Cui, X.; Pang, C.; Liang, H.; Xie, P.; Luo, X.; Huang, Z.; Zhang, Y.; Zhao, Z. Amino Acid Imprinted UiO-66s for Highly Recognized Adsorption of Small Angiotensin-Converting-Enzyme-Inhibitory Peptides. *ACS Appl. Mater. Interfaces* **2019**, *11* (26), 23039–23049. https://doi.org/10.1021/acsami.9b07453.

(3) Wang, S.; Luo, H.; Li, X.; Shi, L.; Cheng, B.; Zhuang, X.; Li, Z. Amino Acid-

Functionalized Metal Organic Framework with Excellent Proton Conductivity for Proton Exchange Membranes. *Int. J. Hydrogen Energy* **2021**, *46* (1), 1163–1173. https://doi.org/10.1016/j.ijhydene.2020.09.235.

(4) Huang, A.; Wan, L.; Caro, J. Microwave-Assisted Synthesis of Well-Shaped UiO-66-NH_2 with High CO_2 Adsorption Capacity. *Mater. Res. Bull.* **2018**, *98* (December 2016), 308–313. https://doi.org/10.1016/j.materresbull.2017.10.038.

(5) Nasrabadi, M.; Ghasemzadeh, M. A.; Monfared, M. R. Z. The Preparation and Characterization of UiO-66 Metal-Organic Frameworks for the Delivery of the Drug Ciprofloxacin and an Evaluation of Their Antibacterial Activities. *New J. Chem.* **2019**, *43* (40), 16033–16040. https://doi.org/10.1039/c9nj03216a.

(6) Abdelhamid, H. N. UiO-66 as a Catalyst for Hydrogen Production: Via the Hydrolysis of Sodium Borohydride. *Dalt. Trans.* **2020**, *49* (31), 10851–10857. https://doi.org/10.1039/d0dt01688h.

(7) Ghosh, P.; Colón, Y. J.; Snurr, R. Q. Water Adsorption in UiO-66: The Importance of Defects. *Chem. Commun.* **2014**, *50* (77), 11329–11331. https://doi.org/10.1039/c4cc04945d.

(8) Kandiah, M.; Nilsen, M. H.; Usseglio, S.; Jakobsen, S.; Olsbye, U.; Tilset, M.; Larabi, C.; Quadrelli, E. A.; Bonino, F.; Lillerud, K. P. Synthesis and Stability of Tagged UiO-66 Zr-MOFs. *Chem. Mater.* **2010**, *22* (24), 6632–6640. https://doi.org/10.1021/cm102601v.

(9) Chakarova, K.; Strauss, I.; Mihaylov, M.; Drenchev, N.; Hadjiivanov, K. Evolution of Acid and Basic Sites in UiO-66 and UiO-66-NH_2 Metal-Organic Frameworks: FTIR Study by Probe Molecules. *Microporous Mesoporous Mater.* **2019**, *281*, 110–122.

https://doi.org/10.1016/j.micromeso.2019.03.006.

(10) Horo, H.; Bhattacharyya, S.; Mandal, B.; Kundu, L. M. Synthesis of Functionalized Silk-Coated Chitosan-Gold Nanoparticles and Microparticles for Target-Directed Delivery of Antitumor Agents. *Carbohydr. Polym.* **2021**, *258*, 117659. https://doi.org/10.1016/j.carbpol.2021.117659.

(11) Piscopo, C. G.; Polyzoidis, A.; Schwarzer, M.; Loebbecke, S. Stability of UiO-66 under Acidic Treatment: Opportunities and Limitations for Post-Synthetic Modifications. *Microporous Mesoporous Mater.* **2015**, *208*, 30–35. https://doi.org/10.1016/j.micromeso.2015.01.032.

(12) Cao, Y.; Zhao, Y.; Lv, Z.; Song, F.; Zhong, Q. Preparation and Enhanced CO_2 Adsorption Capacity of UiO-66/Graphene Oxide Composites. *J. Ind. Eng. Chem.* **2015**, *27*, 102–107. https://doi.org/10.1016/j.jiec.2014.12.021.

(13) Qian, Q.; Wu, A. X.; Chi, W. S.; Asinger, P. A.; Lin, S.; Hypsher, A.; Smith, Z. P. Mixed-Matrix Membranes Formed from Imide-Functionalized UiO-66-NH_2 for Improved Interfacial Compatibility. *ACS Appl. Mater. Interfaces* **2019**, *11* (34), 31257–31269. https://doi.org/10.1021/acsami.9b07500.

(14) Venna, S. R.; Lartey, M.; Li, T.; Spore, A.; Kumar, S.; Nulwala, H. B.; Luebke, D. R.; Rosi, N. L.; Albenze, E. Fabrication of MMMs with Improved Gas Separation Properties Using Externally-Functionalized MOF Particles. *J. Mater. Chem. A* **2015**, *3* (9), 5014–5022. https://doi.org/10.1039/c4ta05225k.

(15) Pishnamazi, M.; Koushkbaghi, S.; Hosseini, S. S.; Darabi, M.; Yousefi, A.; Irani, M. Metal Organic Framework Nanoparticles Loaded- PVDF/Chitosan Nanofibrous Ultrafiltration Membranes for the Removal of BSA Protein and Cr(VI) Ions. *J. Mol. Liq.*

2020, *317*. https://doi.org/10.1016/j.molliq.2020.113934.

(16) Samari, M.; Zinadini, S.; Zinatizadeh, A. A.; Jafarzadeh, M.; Gholami, F. Designing of a Novel Polyethersulfone (PES) Ultrafiltration (UF) Membrane with Thermal Stability and High Fouling Resistance Using Melamine-Modified Zirconium-Based Metal-Organic Framework (UiO-66-NH_2/MOF). *Sep. Purif. Technol.* **2020**, *251* (May), 117010. https://doi.org/10.1016/j.seppur.2020.117010.

(17) Jamshidifard, S.; Koushkbaghi, S.; Hosseini, S.; Rezaei, S.; Karamipour, A.; Jafari rad, A.; Irani, M. Incorporation of UiO-66-NH_2 MOF into the PAN/Chitosan Nanofibers for Adsorption and Membrane Filtration of Pb(II), Cd(II) and Cr(VI) Ions from Aqueous Solutions. *J. Hazard. Mater.* **2019**, *368* (October 2018), 10–20. https://doi.org/10.1016/j.jhazmat.2019.01.024.

(18) Ediati, R.; Aulia, W.; Nikmatin, B. A.; Hidayat, A. R. P.; Fitriana, U. M.; Muarifah, C.; Sulistiono, D. O.; Martak, F.; Prasetyoko, D. Chitosan/UiO-66 Composites as High-Performance Adsorbents for the Removal of Methyl Orange in Aqueous Solution. *Mater. Today Chem.* **2021**, *21*, 100533. https://doi.org/10.1016/j.mtchem.2021.100533.

(19) Gupta, S.; Yogesh; Javiya, S.; Bhambi, M.; Pundir, C. S.; Singh, K.; Bhattacharya, A. Comparative Study of Performances of Lipase Immobilized Asymmetric Polysulfone and Polyether Sulfone Membranes in Olive Oil Hydrolysis. *Int. J. Biol. Macromol.* **2008**, *42* (2), 145–151. https://doi.org/10.1016/j.ijbiomac.2007.10.018.

(20) Motaghi, H.; Arabkhani, P.; Parvinnia, M.; Asfaram, A. Simultaneous Adsorption of Cobalt Ions, Azo Dye and Imidacloprid Pesticide on the Magnetic Chitosan/Activated Carbon@UiO-66 Bio-Nanocomposite: Optimization, Mechanisms, Regeneration and Application. *Sep. Purif. Technol.* **2022**, *284*, 120258.

https://doi.org/10.1016/j.seppur.2021.120258.

(21) Wang, X.; Zhou, X.; Yang, K.; Li, Q.; Wan, R.; Hu, G.; Ye, J.; Zhang, Y.; He, J.; Gu, H.; Yang, Y.; Zhu, L. Peroxidase- And UV-Triggered Oxidase Mimetic Activities of the UiO-66-NH_2/Chitosan Composite Membrane for Antibacterial Properties. *Biomater. Sci.* **2021**, *9* (7), 2647–2657. https://doi.org/10.1039/d0bm01960g.

(22) Di Noto, V.; Piga, M.; Giffin, G. A.; Vezzù, K.; Zawodzinski, T. A. Interplay between Mechanical, Electrical and Thermal Relaxations in Nanocomposite Proton Conducting Membranes Based on Nafion and a [$(ZrO_2)(Ta_2O_5)_{0.119}$] Core-Shell Nanofiller. *J. Am. Chem. Soc.* **2012**, *134* (46), 19099–19107. https://doi.org/10.1021/ja3071336.

(23) Prasad, B.; Mandal, B. CO_2 Separation Performance by Chitosan/Tetraethylenepentamine/Poly(Ether Sulfone) Composite Membrane. *J. Appl. Polym. Sci.* **2017**, *134* (34), 1–9. https://doi.org/10.1002/app.45206.

(24) Vaidya, P. D.; Konduru, P.; Vaidyanathan, M.; Kenig, E. Y. Kinetics of Carbon Dioxide Removal by Aqueous Alkaline Amino Acid Salts. *Ind. Eng. Chem. Res.* **2010**, *49* (21), 11067–11072. https://doi.org/10.1021/ie100224f.

(25) Pang, R.; Yang, Y.; Han, Y.; Chen, K. K.; Ho, W. S. W. Bicontinuous Substrates with Reduced Pore Restriction for CO_2-Selective Composite Membranes. *J. Memb. Sci.* **2022**, *654*, 120547. https://doi.org/10.1016/j.memsci.2022.120547.

(26) Han, Y.; Ho, W. S. W. Recent Advances in Polymeric Facilitated Transport Membranes for Carbon Dioxide Separation and Hydrogen Purification. *J. Polym. Sci.* **2020**, *58* (18), 2435–2449. https://doi.org/10.1002/pol.20200187.

(27) Danckwerts, P. V. The Reaction of CO_2 with Ethanolamines. *Chem. Eng. Sci.* **1979**, *34*

(4), 443–446. https://doi.org/10.1016/0009-2509(79)85087-3.

(28) Prasad, B.; Mandal, B. Moisture Responsive and CO_2 Selective Biopolymer Membrane Containing Silk Fibroin as a Green Carrier for Facilitated Transport of CO_2. *J. Memb. Sci.* **2018**, *550*, 416–426. https://doi.org/10.1016/j.memsci.2017.12.061.

(29) Borgohain, R.; Prasad, B.; Mandal, B. Synthesis and Characterization of Water-Soluble Chitosan Membrane Blended with a Mobile Carrier for CO_2 Separation. *Sep. Purif. Technol.* **2019**, *222*, 177–187. https://doi.org/10.1016/j.seppur.2019.04.038.

(30) Prasad, B.; Thakur, R. M.; Mandal, B.; Su, B. Enhanced CO_2 Separation Membrane Prepared from Waste By-Product of Silk Fibroin. *J. Memb. Sci.* **2019**, *587*, 117170. https://doi.org/10.1016/j.memsci.2019.117170.

(31) Mondal, A.; Barooah, M.; Mandal, B. Effect of Single and Blended Amine Carriers on CO_2 Separation from CO_2/N_2 Mixtures Using Crosslinked Thin-Film Poly(Vinyl Alcohol) Composite Membrane. *Int. J. Greenh. Gas Control* **2015**, *39*, 27–38. https://doi.org/10.1016/j.ijggc.2015.05.002.

(32) Han, Y.; Ho, W. S. W. Mitigated Carrier Saturation of Facilitated Transport Membranes for Decarbonizing Dilute CO_2 Sources: An Experimental and Techno-Economic Study. *J. Membr. Sci. Lett.* **2022**, *2* (1), 100014. https://doi.org/10.1016/j.memlet.2022.100014.

(33) Huang, J.; Zou, J.; Ho, W. S. W. Carbon Dioxide Capture Using a CO_2-Selective Facilitated Transport Membrane. *Ind. Eng. Chem. Res.* **2008**, *47* (4), 1261–1267. https://doi.org/10.1021/ie070794r.

(34) Sathre, R.; Breunig, H.; Greenblatt, J.; Larsen, P.; Masanet, E.; McKone, T.; Quinn, N.; Scown, C. Spatially-Explicit Water Balance Implications of Carbon Capture and

Sequestration. *Environ. Model. Softw.* **2016**, *75*, 153–162. https://doi.org/10.1016/j.envsoft.2015.10.011.

(35) Guo, F.; Li, B.; Ding, R.; Li, D.; Jiang, X.; He, G.; Xiao, W. A Novel Composite Material Uio-66@hnt/Pebax Mixed Matrix Membranes for Enhanced CO_2/N_2 Separation. *Membranes (Basel).* **2021**, *11* (9). https://doi.org/10.3390/membranes11090693.

(36) Rodrigues, M. A.; Ribeiro, J. de S.; Costa, E. de S.; de Miranda, J. L.; Ferraz, H. C. Nanostructured Membranes Containing UiO-66 (Zr) and MIL-101 (Cr) for O_2/N_2 and CO_2/N_2 Separation. *Sep. Purif. Technol.* **2018**, *192*, 491–500. https://doi.org/10.1016/j.seppur.2017.10.024.

(37) Hossain, I.; Husna, A.; Chaemchuen, S.; Verpoort, F.; Kim, T. H. Cross-Linked Mixed-Matrix Membranes Using Functionalized UiO-66-NH_2 into PEG/PPG-PDMS-Based Rubbery Polymer for Efficient CO_2 Separation. *ACS Appl. Mater. Interfaces* **2020**, *12* (52), 57916–57931. https://doi.org/10.1021/acsami.0c18415.

(38) Ashtiani, S.; Khoshnamvand, M.; Regmi, C.; Friess, K. Interfacial Design of Mixed Matrix Membranes via Grafting Pva on UiO-66-NH_2 to Enhance the Gas Separation Performance. *Membranes (Basel).* **2021**, *11* (6). https://doi.org/10.3390/membranes11060419.

(39) Jia, M.; Feng, Y.; Qiu, J.; Zhang, X. F.; Yao, J. Amine-Functionalized MOFs@GO as Filler in Mixed Matrix Membrane for Selective CO_2 Separation. *Sep. Purif. Technol.* **2019**, *213*, 63–69. https://doi.org/10.1016/j.seppur.2018.12.029

CHAPTER 8

Overall Conclusion and Recommendations for Future Work

This section provides an overview of the findings and the current thesis. It also describes potential future modifications that could be made to the polymer and filler to enhance the overall performance of the CO_2 separation.

8.1. Overall Conclusions

The overall advantages of the membranes synthesised in this work compared to the already published work can be iterated with the following key points: The membranes used in this study were synthesized from Chitosan, an affordable biodegradable biopolymer. Chitosan's inherent amino and hydroxy functional groups proved effective for CO_2/N_2 separation. To preserve the membranes' biodegradability and ensure they could be easily disposed of without generating secondary pollutants, various amino acids were used for modification. Additionally, different filler materials, such as graphene oxide (GO), MIL-100(Fe), and ZrBDC MOF, were incorporated. The MIL-100(Fe) was synthesized using a green route, but the production of GO and ZrBDC was costlier due to the use of expensive $ZrCl_4$ salt and other chemicals.

- A high-performing biodegradable polymeric material, chitosan (CS), was carefully chosen as the base material for a thin film composite membrane fabrication for CO_2 separation study. The performance of CS was further enhanced by modifying it with tyrosine amino acid using a conjugation technique. Comprehensive characterization of the resulting membranes, both the modified Tyr-c-CS and the neat CS membranes, was carried out using various analytical techniques like FTIR, XRD, TGA, AFM, FESEM. This research highlights the significant impact of amino acid conjugation on the CS backbone and its role in improving CO_2 separation efficiency. The presence of amine groups in the conjugated L-tyrosine plays a

vital role in selectively attracting CO_2 molecules, while effectively excluding N_2, due to the zwitterion mechanism for carbamate formation. The synthesized conjugated membrane, with an average thickness of 4 µm, demonstrated superior CO_2 permeance of 67 GPU and CO_2/N_2 selectivity of 44. In comparison, the neat CS membrane only exhibited CO_2 permeance of 15 GPU and CO_2/N_2 selectivity of 48 under the similar operating conditions (85 °C and 32 psi absolute feed pressure). This enhanced performance of the Tyr-c-CS matrix can be attributed to the combined effect of facilitated transport and the solution-diffusion mechanism.

- Phenylalanine amino acid was used to create various polymer blends and graft copolymers, forming thin film composite membranes designed for efficient CO_2 gas transport. The incorporation of primary amine-containing Phe components in the membranes improved CO_2 transfer by introducing both mobile and stationary carriers, enhancing gas permeance through increased free volume. The membranes underwent extensive characterization using techniques like XPS, NMR, FTIR, XRD, TGA, FESEM, AFM, etc. and were compared to the pristine CS membrane. Tested under different operating conditions, the Phe-*g*-CS membrane with ~4 µm selective layer thickness showed an impressive CO_2/N_2 selectivity of 89 and CO_2 permeance of 106 GPU at optimized conditions (85 °C, 2.21 bar feed pressure, 1.21 bar sweep side pressure and 0.667 moisture flow ratio). The Phe-b-CS (20) membrane exhibited a CO_2/N_2 selectivity of 97 and CO_2 permeance of 72 GPU under the same conditions. Stability testing for 400 hours demonstrated that the Phe-g-CS membrane maintained consistent CO_2 uptake capacity, outperforming the Phe-b-CS membrane. The results surpassed Robeson's upper bound curve, affirming the membranes' suitability for commercial CO_2 separation applications.
- To further enhance the separation efficiency of CS, we synthesized Lys-c-GO@CS MMM by incorporating Lys-c-GO nanosheets into a CS matrix. Various analytical techniques, such as FTIR, TGA, XRD, SEM, TEM and AFM, were used to characterize filler and the MMM. Comparing different doping levels, we found that MMMs with 1 wt% Lys-c-GO

showed superior CO_2 separation performance compared to those with 0.5 wt% and 2 wt% Lys-c-GO. Specifically, the MMMs containing 1 wt% Lys-c-GO with ~4 μm selective layer thickness demonstrated reasonably good CO_2 permeance of 44 GPU and CO_2/N_2 selectivity of 82.5. The presence of Lys-c-GO had a positive synergistic effect on gas separation performance. The amino groups linked to the GO sheets acted as pathways, promoting high CO_2 selectivity. Furthermore, the selective barrier formed by the amine, hydroxyl and carboxy groups of the GO nanosheets on the MMM surface contributed to increased selectivity in the membrane. In summary, the introduction of Lys-c-GO nanosheets into the CS matrix significantly improved the CO_2 separation efficiency of the MMM, making it a promising approach for enhancing gas separation performance.

- MIL-100(Fe) nanoparticles with an average particle size of approximately 100 nm were synthesized under HF-free conditions at ambient temperatures. These nanoparticles were then integrated into a biodegradable CS matrix to create mixed matrix membranes (MMMs) for CO_2 separation applications. The presence of the μ3-oxo-trimer of the MIL-100(Fe) nanoparticles facilitated the diffusion mechanism, while the amine groups of the CS polymer aided in capturing CO_2 molecules during the separation process. To optimize the MMM's performance, the maximum limit of filler incorporation into the CS matrix was assessed. Subsequently, the optimized MMM underwent testing under adverse conditions to evaluate its endurance and effectiveness. Remarkably, the CS MMM with 15 wt% loading of MIL-100(Fe) with ~4 μm selective layer thickness exhibited a CO_2 permeance of 59 GPU and a CO_2/N_2 selectivity of 65, demonstrating its potential as a promising membrane for efficient CO_2 separation over N_2.
- Zr BDC and lysine-conjugated Zr BDC MOF nanoparticles were used as fillers and incorporated into a CS matrix to create a mixed matrix membrane (MMM). The successful conjugation of lysine with Zr-BDC NPs was achieved by forming an amide bond between the dangling –COOH of the MOF and the side chain $–NH_2$ of lysine, which was crucial for CO_2

adsorption. Various analytical and spectroscopic techniques such as TEM, SEM, FTIR, XRD, TGA, EDX and AFM were employed to characterize the as-synthesized materials and MMMs. The characterization confirmed the successful conjugation of lysine with the MOF NPs, which greatly enhances CO_2 adsorption capabilities. The solution casting method yielded thin, dense, amorphous and thermally stable selective layers, specifically designed for CO_2 separation purposes. Among the various loadings tested, the MMM with 7 wt% of Zr BDC and lys-c-Zr BDC was identified as the optimum loading amount, significantly improving CO_2 permeance and CO_2/N_2 selectivity compared to the neat polymer. The resulting lys-c-Zr BDC/CS (7) with ~4 μm selective layer thickness MMM exhibited CO_2 permeance of 34.6 GPU and CO_2/N_2 selectivity of 29.4 under dry conditions, while under humid conditions at 85 °C and 0.221 feed pressure, it showed CO_2 permeance of 135 GPU and CO_2/N_2 selectivity of 71.5. In conclusion, the incorporation of lysine-conjugated Zr BDC MOF nanoparticles into the CS matrix resulted in an optimized mixed matrix membrane with excellent CO_2 separation performance, making it a promising candidate for practical applications.

Table 8.1. A comparative account on the CO_2 separation performance by the membranes with ~4 μm selective layer thickness conducted under this research study at 85 °C and absolute feed/sweep pressure = 2.21/1.21 bar having feed/sweep water flow rate of 0.03/0.05 mL/min.

Membrane composition	**Membrane code**	**CO_2 permeance (GPU)**	**CO_2/N_2 selectivity**
Neat CS	CS	15	48
Tyrosine-conjugated-CS	Tyr-c-CS	44	67
Phenyalanine-blended-CS	Phe-b-CS	72	97
Phenylalanine-grafted-CS	Phe-g-CS	106	89

1 wt% Lysine-conjugated-Graphene Oxide/CS	Lys-c-GO@CS (1)	44	82
15 wt% MIL-100(Fe)/CS	CSM-15	59	65
7 wt% Lysine-conjugated-Zr BDC/CS	Lys-c-ZrBDC/CS (7)	135	71

The thesis focused on the membrane-based separation of CO_2 from the simulated flue gas and the various strategies to be employed to enhance the overall performance. All study mainly aimed for the modification of chitosan membranes to enhance the CO_2 separation efficiency via facilitated transport mechanism. Two general approaches were taken for this purpose. The first approach involved using non-toxic, biodegradable and cost-effective amino acids (Tyrosine, Phenylalanine and Lysine) as carriers owing to the presence of the amine functional groups. The second approach involved incorporating filler materials (GO, MIL-100(Fe) and ZrBDC (UIO-66)) into the CS polymer due to their high surface area and adsorption activity.

Tyrosine was employed through conjugation and Phenylalanine was used both through conjugation and blending with the CS polymer. The addition of these amino acids increased the carrier content, facilitating CO_2 transportation, resulting in promising performance as compared to the bare CS membrane. Phenylalanine, being more soluble, was considered over the tyrosine for the blending and grafting process. Also, the absence of the phenolic -OH in phenylalanine resulted in more basicity in the composite membranes thereby increasing the interaction of the acidic CO_2 with the membrane polymer. As a result, we observed better CO_2 separation performance for phenylalanine modified CS membranes, shown in Table 8.1.

Although modification of the polymer backbone yielded better separation results, but a promising membrane was yet to be achieved. Thus, to further modify the CS membranes,

another strategy of mixed matrix membrane was opted for. To align with the current trend of the mixed matrix membranes for CO_2 separation applications, various filler materials such as graphene oxide, MIL-100(Fe) MOF and Zr BDC (UIO-66) MOFs were synthesized. As surface area plays a crucial role in the gas separation performance, the 2-dimensional (2D) graphene oxide was explored as filler material. Lysine amino acid was utilized to modify the surface of the 2D GO, enhancing its affinity for CO_2 separation with incorporation of amine functional groups.

This strategy even though yielded high selectivity, the permeance was yet much low. Therefore, the research focused on the utilization of 3-dimensional (3D) MOF materials due to high surface area and high pore volumes. The MIL-100(Fe) MOF as filler resulted in a higher permeance than the Lys-c-GO@CS (1) (Table 8.1) with selectivity being the challenge. The Zr BDC, owing to the presence of both tetrahedral and octahedral voids, when utilized as filler yielded higher permeance compared to the MIL-100(Fe). The lysine amino acid was thereby utilized to modify the 3D Zr BDC MOF to induce amine functionality into the moiety. This strategy resulted in enhanced CO_2 separation performance with much higher permeance and improved selectivity.

Among the library of prepared composite membranes, the Lys-c-Zr BDC MOF as a filler material demonstrated the best permeance and carrier stability, while the Phe blended and grafted CS membrane exhibited superior selectivity and permeance, respectively. Thus, an optimal balance between permeance and selectivity was achieved along with long-term stability test of the membranes. The Phe-g-CS membrane displayed the best stability and consistent CO_2 separation efficiency over 400 hours due to its non-leaching behavior. The incorporation of the Zr BDC nanoparticles into the nanocomposite membrane helped prevent support pore blocking during gas permeation tests. Furthermore, exploring the surface-

modified lysine conjugated Zr BDC MOF showed encouraging performance in gas permeation tests, owing to enhanced carriers and the active surface area of MOF nanoparticles.

Further I would like to add, in this research, all the flat sheet dense facilitated transport membranes were synthesized with an effective surface area of approximately 7.5 cm^2 using chitosan (CS) biopolymer for CO_2/N_2 separation studies. However, the scalability and commercialization of MMMs have been a sluggish process because they require much larger surface areas than those prepared for lab-scale experiments, which can be achieved by using asymmetric hollow fibre membranes. The primary challenge in synthesizing a defect-free MMM with a significantly larger surface area is the production and availability of porous filler materials, other than zeolite, in sufficient quantities, with the desired properties, at affordable and economically feasible prices. Additionally, the defect-free infusion of fillers into the active layer of the MMM presents further challenges to an already complicated process.

Overall, these studies introduce an innovative approach to utilize biopolymers for CO_2 separation, contributing to waste-to-wealth conversion and having a positive impact on energy and the environment.

8.2. Future Recommendations

Chitosan-based membranes and mixed matrix membranes have garnered a lot of interest for CO_2 separation because to their high CO_2 affinity, low cost, wide availability, film-forming capacity, biodegradability, mechanical and thermal durability, among other properties.

To enhance the CO_2 performance of chitosan membrane in future, the following recommendations might be considered:

1. The current work focuses on experimental studies only. To validate the separation performance, ASPEN custom modeler can be used. This will also provide more insights in

the reaction mechanism which will in turn help to understand the shortcomings in the current method.

2. In this study, simulated flue gas mixture with a composition of 20% CO_2 and 80% N_2 was used. However, it's important to note that the composition of CO_2 in real-world flue gas varies from 10-14% along with the presence of SO_x, NO_x, O_2 and water vapor. Future experiments could use feed gas with more realistic CO_2 composition for testing.
3. It is recommended to explore the incorporation of a gutter layer between the selective layer and the support in order to better understand its effects.
4. The conversion of the separated CO_2 from the flue gas to various useful compounds is also a great challenge. To incorporate the two techniques, separation and reduction of CO_2, in single-step process is worth effective.
5. In order to make informed decisions regarding the future implementation of these membranes, it is highly recommended to conduct a comprehensive economic assessment. This assessment will play a pivotal role in determining the suitability and practical applications of the prepared membranes across various industries and CO_2 capture processes.
6. Life cycle analysis (LCA) for quantifying the overall environmental benefits of synthesized, emerging CO_2-selective CS-based membranes.

Appendix 1

A.1. Gas Transport Parameters Calculation and Gas Chromatography Data:

Gas transport parameters (CO_2 and N_2 fluxes, CO_2 and N_2 permeability, CO_2/N_2 selectivity) calculation (The calculation procedure adapted here was originally taken from PhD thesis of Arijit Mondal, reference given at the end of the Appendix**)**

η_R (mol/min) = retentate molar flow rate = PV/RT

Where,

P (atmospheric pressure at which the retentate gas is emitting) = 1 atm.

V (volumetric flow rate of mixed gas at retentate side) = 55 cc/min = 55 $\times 10^{-6}$ m^3/min.T (room temperature at °K) = 298.15 °K.

R (universal gas constant) = 8.205746 × 10^{-5} m^3 atm /°K mol.

$$\boldsymbol{\eta_R}\ \textbf{mol/min} = \frac{1 \text{ X } 55 \text{ X } 10^{-6}}{8.205746 \text{ X } 10^{-5} \text{ X } 298.15} = 2.24 \text{ X } 10^{-3} \text{mole/min}$$

η_{Ar} (mol/min) = argon (carrier gas) molar flow rate = PV/RT

Where,

P (atmospheric pressure at which the carrier gas is emitting) = 1 atm

V (volumetric flow rate of carrier gas at permeate side) = 50 cc/min = 50 × 10^{-6} m^3/min.T (room temperature at °K) = 298.15 °K.

R (universal gas constant) = 8.205746 × 10^{-5} m^3 atm /°K mol.

$$\boldsymbol{\eta_{Ar}}\ \textbf{mol/min} = \frac{1 \text{ X } 50 \text{ X } 10^{-6}}{8.205746 \text{ X } 10^{-5} \text{ X } 298.15} = 2.04 \text{ X } 10^{-3} \text{mole/min}$$

η_P (mol/min) = permeate molar flow rate =

$$[CO_2 \text{mole fraction X } \frac{CO_2\ (P)_{G.C.}}{CO_2\ (P)_{F.C.}} + (N_2 \text{mole fraction X } \frac{N_2\ (P)_{G.C.}}{N_2\ (P)_{F.C.}})]$$

$$X \frac{\text{Ar molar flow rate(mol/min)}}{[1 - (CO_2 \text{mole fraction X } \frac{CO_2\ (P)_{G.C.}}{CO_2\ (P)_{F.C.}}) + (N_2 \text{mole fraction X } \frac{N_2\ (P)_{G.C.}}{N_2\ (P)_{F.C.}})]}$$

Where,

$CO_2\ (P)_{G.C.}$. = CO_2 mole fraction at permeate side from G.C. analysis (**Figure A2.1**)

$CO_2(F)_{G.C.}$ = CO_2 mole fraction at feed side from G.C. analysis (**Figure A2.1**)

$N_2(P)_{G.C.}$. = N_2 mole fraction at permeate side from G.C. analysis (**Figure A2.1**)

$N_2(F)_{G.C.}$ = N_2 mole fraction at feed side from G.C. analysis (**Figure A2.1**)

CO_2 mole fraction = 0.192

N_2 mole fraction = 0.808

Ar molar flow rate = 2.04×10^{-3} mol /min.

η_P (mol/min) = permeate molar flow rate = 4.17×10^{-5} mol/min.

pco_2 (R,psi) = CO_2 partial pressure at retentate side =

$$[BP_{F(psig)} + P_{ambient\ (kPa)} \text{ X } \frac{14.7}{101.325}] \text{ X}$$

$$\frac{[\eta_R - 0.5 \text{ X } \eta_R]\ (\text{mol/min}) \text{ X } [CO_2 \text{mole fraction X } [0.5 + 0.5 \text{ X } \frac{CO_2\ (R)_{G.C.}}{CO_2\ (F)_{G.C.}}]}{[\eta_R - 0.5 \text{ X } \eta_R]\ (\text{mol/min}) + \frac{[(0.5 \text{ X } H_2O_F) + (0.5 \text{ X } H_2O_{distribution} \text{X } (H_2O_F + H_2O_S))](\text{ml/min})}{18\ (\text{ml/mol})}}$$

Where,

BP_F =Back pressure (psig) at feed side of the membrane = 14.7 psig.

$P_{ambient}$ = Ambient pressure (kPa) =101.6 kPa

$CO_2\ (R)_{G.C.}$ = CO_2 mole fraction at retentate side from G.C. analysis (**Figure A2.1**)

$CO_2\ (F)_{G.C.}$= CO_2 mole fraction at feed side from G.C. analysis (**Figure A2.1**)

H_2O_F = Feed side water flow rate (ml/min) = 0.03 ml /min

H_2O_S = Sweep side water flow rate (ml/min) = 0.05 ml/min

H_2O distribution = Total water distribution =

$$\frac{\text{Retentate side water knockout volume}}{\text{Retentate side water knockout volume+ Sweep side water knockout volume}} = 0.64$$

$\eta_R = 2.24 \times 10^{-3}$ mole /min

$\eta_P = 4.17 \times 10^{-5}$ mol/min

CO_2 mole fraction = 0.19

p_{CO_2} (R,psi) = CO_2 partial pressure at retentate side = 2.85 psi

p_{CO_2} (P, psi) = CO_2 partial pressure at permeate side =

$$[BP_{S(psig)} + P_{ambient\ (kPa)}\ X\ \frac{14.7}{101.325}]\ X$$

$$\frac{[\eta_{Ar}\text{-}0.5\ X\ \eta_p]\ (mol/min)\ X\ [CO_2 \text{mole fraction}\ X\ 0.5\ X \frac{CO_2\ (P)_{G.C.}}{CO_2\ (F)_{G.C.}}]}{[\eta_{Ar}\text{- }0.5\ X\ \eta_P]\ (mol/min) + \frac{[(0.5\ X\ H_2O_F) + (0.5\ X(1\text{- }H_2O_{distribution})X\ (H_2O_F + H_2O_S))](ml/min)}{18\ (ml/mol)}}$$

BP_S = Back pressure at Sweep side of the membrane module = 4 psig.

Pambient = Ambient pressure (kPa) =101.6 k Pa

$CO_2\ (P)_{G.C.}$ = CO_2 mole fraction at permeate side from G.C. analysis (**Figure A2.1**)

$CO_2\ (R)_{G.C.}$ = CO_2 mole fraction at feed side from G.C. analysis (**Figure A2.1**)

H_2O_F = Feed side water flow rate (ml/min) = 0.03 ml /min

H_2O_S = Sweep side water flow rate (ml/min) = 0.05 ml/min

$H_2O_{distribution}$ = Total water distribution = 0.64

$\eta_{Ar} = 2.04 \times 10^{-3}$ mole /min

$\eta_P = 4.17 \times 10^{-5}$ mol/min

CO_2 mole fraction = 0.192

p_{CO_2} (P,psi) = CO_2 partial pressure at permeate side = 0.08 psi

p_{N_2} (R,psi) = N_2 partial pressure at retentate side =

$$\frac{[BP_{F(psig)} + P_{ambient\ (kPa)}\ X\ \frac{14.7}{101.325}]\ X\ [\eta_r - 0.5\ X\ \eta_p]\ (mol/min)\ X\ N_2 mole\ fraction\ X\ [0.5 + 0.5\ X \frac{N_2\ (R)_{G.C.}}{N_2\ (F)_{G.C.}}]}{[\eta_R - 0.5\ X\ \eta_p]\ (mol/min) + \frac{[(0.5\ X\ H_2O_F) + (0.5\ X\ H_2O_{distribution} X\ (H_2O_F + H_2O_S))](ml/min)}{18\ (ml/mol)}}$$

Where,

BP_F = Back pressure (psig) at feed side of the membrane module = 14.7 psig

$P_{ambient}$ = Ambient pressure (kPa) =101.6kPa

$N_2(R)_{G.C.}$= N_2 mole fraction at retentate side from G.C. analysis (**Figure A2.1**)

$N_2(F)_{G.C.}$= N_2 mole fraction at feed side from G.C. analysis (**Figure A2.1**)

H_2O_F = Feed side water flow rate (ml/min) = 0.03 ml/min

H_2O_S = Sweep side water flow rate (ml/min) = 0.05 ml/min

$H_2O_{distribution}$= Total water distribution = 0.375

Molecular weight of water = 18 g/mol = 18 ml/min (if density of water is 1)

η_{Ar} = 2.04 × 10^{-3} mole /min

η_P = 4.17 × 10^{-5} mol/min

N_2 mole fraction = 0.808

$\boldsymbol{p_{N_2}}$ (R,psi) = $\boldsymbol{N_2}$ partial pressure at retentate side = 13.25 psi

$\boldsymbol{p_{N_2}}$ (P,psi) = $\boldsymbol{N_2}$ partial pressure at permeate side =

$$\frac{[BP_{S(psig)} + P_{ambient\ (kPa)}\ X\ \frac{14.7}{101.325}]}{[\eta_{Ar}+0.5\ X\ \eta_p]\ (mol/min)\ X\ N_2 mole\ fraction\ X\ 0.5\ X\ \frac{N_2\ (P)_{G.C.}}{N_2\ (F)_{G.C.}}}{[\eta_{Ar}+0.5\ X\ \eta_P]\ (mol/min) + \frac{[(0.5\ X\ H_2O_S)+(0.5\ X(1-\ H_2O_{distribution})X\ (H_2O_F+H_2O_S))](ml/min)}{18\ (ml/mol)}}$$

Where,

BP_S = Back pressure (psig) at sweep side of the membrane module = 4 psig

$P_{ambient}$ = Ambient pressure (kPa) =101.6kPa

$N_2(P)_{G.C.}$ = N_2 mole fraction at permeate side from G.C. analysis (**Figure A2.1**)

$N_2(F)_{G.C.}$ = N_2 mole fraction at feed side from G.C. analysis (**Figure A2.1**)

H_2O_F = Feed side water flow rate (ml/min) = 0.03 ml/min

H_2O_S = Sweep side water flow rate (ml/min) = 0.05 ml/min

$H_2O_{distribution}$ = Total water distribution = 0.64

η_{Ar} = 2.04 × 10^{-3} mol /min

η_P = 4.17 × 10^{-5} mol/min

N_2 mole fraction = 0.808

p_{N_2} (P,psi)= **N_2 partial pressure at permeate side = 0.0062 psi**

Volumetric flow rates calculations:

V_{CO_2}(cm^3/sec) = permeate side volumetric flow rate of CO_2 at STP =

$$\frac{\eta_{Ar} \text{ X } CO_2\ (P)_{G.C.} \text{ X } CO_2 \text{mole fraction X } 8.314 \text{ X } 273.15 \text{ X } 1000000}{CO_2\ (F)_{G.C.} \text{ X } 101325 \text{ X } 60 \text{ X } [1-(CO_2 \text{mole fraction X } \frac{CO_2\ (P)_{G.C.}}{CO_2\ (F)_{G.C.}})- (N_2 \text{mole fraction X } \frac{N_2\ (R)_{G.C.}}{N_2\ (F)_{G.C.}})}$$

V_{CO_2}(cm^3/sec) = permeate volumetric gas flow rate of CO_2 = 1.445×10^{-02} cm^3/sec

$V_{N_2}(cm^3/sec)$ = permeate volumetric gas flow rate of N_2=

$$\frac{\eta_{Ar} \text{ X } N_2\ (P)_{G.C.} \text{ X } N_2 \text{mole fraction X } 8.314 \text{ X } 273.15 \text{ X } 1000000}{N_2\ (F)_{G.C.} \text{ X } 101325 \text{ X } 60 \text{ X } [1-(CO_2 \text{mole fraction X } \frac{CO_2\ (P)_{G.C.}}{CO_2\ (F)_{G.C.}})- (N_2 \text{mole fraction X } \frac{N_2\ (R)_{G.C.}}{N_2\ (F)_{G.C.}})}$$

V_{N_2} (cm^3sec) = permeate volumetric gas flow rate of N_2= 1.12×10^{-03} cm^3/sec

CO_2 Flux (10^{-6} cm^3(STP)/cm^2sec), CO_2 Permeability (Barrer), CO_2 Permeance (GPU) and CO_2/NO_2 Selectivity calculations:

$(\Delta p)_{CO_2}$ at psi = partial pressure difference at psi = p_{CO_2} (R, psi) - p_{CO_2} (P, psi)

$(\Delta p)_{CO_2}$ at psi = 3.2 psi

$(\Delta p)_{CO_2}$ at cmHg = partial pressure difference at cmHg = $\frac{(\Delta P)_{CO_2} \text{at psi}}{14.7}$ X 76

$(\Delta p)_{CO_2}$ = 14.32 cm Hg

$$CO_2 \text{ Flux} = \frac{V_{CO_2} cm^3/sec}{\text{area of membrane } (cm^2)}$$

Where,

V_{CO_2} (cm^3/sec) = 1.44 × $\mathbf{10^{-02}}$ (cm^3/sec) Area of membrane = 7.5 cm^2

CO_2 flux = 1627 × 10^{-6} cm^3 (STP)/cm^2s

CO_2 Permeability= $\frac{V_{CO_2} cm^3/sec \text{ X thickness (cm)}}{\text{area of membrane } (cm^2) \text{ X } (\Delta P)CO_2 \text{ at cm Hg}}$

Where,

V_{CO_2} (cm^3/sec) **= 9.66 × 10^{-3}** cm^3/sec

Area of membrane = 7.5 cm^2

Thickness = 0.0004 cm = 4 μm

$(\Delta p)_{CO_2}$ at cm Hg = 14.32 cm Hg

CO_2 Permeability = ~538 × 10^{-10} cm^3 (STP) cm/cm^2s cmHg = 538 Barrer

CO_2Permeance= $\frac{CO_2 \text{Permeability}}{\text{Thickness}} = \frac{538 \text{ (Barrer)}}{4}$ =~134.56 GPU

1 GPU = 10^{-6} cm^3 (STP)/cm^2s cm.Hg

$\frac{CO_2}{N_2}$ Selectivity= $\frac{\frac{CO_2 (P)_{G.C.}}{N_2 (P)_{G.C.}}}{\frac{CO_2 (R)_{G.C.}}{N_2 (R)_{G.C.}}}$ =70.45

N_2 Flux (10^{-6} cm^3 (STP)/cm^2sec), N_2 Permeability (Barrer) and N_2 Permeance (GPU):

$(\Delta p)_{N_2}$ (psi) = partial pressure difference at psi = p_{N_2} (R, psi) - p_{N_2} (P, psi)

$(\Delta p)_{N_2}$ = Partial pressure difference at cm Hg = $(\Delta p)_{N_2}$ / 14.7) x 76

$(\Delta p)_{N_2}$ = 68.47 cm Hg

N_2Flux = $\frac{V_{N_2} cm^3/sec}{\text{area of membrane } (cm^2)}$

V_{N_2}(cm^3/ sec) = 1.12 ×10^{-03} (cm^3/sec)

Area of membrane = 7.5 cm^2

N_2 flux = ~ 149 × 10^{-6} cm^3(STP)/cm^2s

$$N_2 \text{ Permeability} = \frac{V_{N_2} cm^3/sec \text{ X thickness (cm)}}{\text{area of membrane } (cm^2) \text{ X } (\Delta P)_{N_2} \text{at cm Hg}}$$

Where,

V_{N_2} = 1.12 × 10^{-03} (cm^3/sec)

Area of membrane = 7.5 cm^2 Thickness = 0.0004 cm = 4 μm

$(\Delta p)_{N_2}$ at cm Hg = 68.47 cm Hg

N_2 Permeability = 8.8 × 10^{-10} cm^3 (STP) cm/cm^2s cmHg = 8.8 Barrer

$$N_2 \text{Permeance} = \frac{N_2 \text{Permeability}}{\text{Thickness}} = \frac{8.8}{4} = 2.19 \text{ GPU}$$

1 GPU = 10^{-6} cm^3(STP)/cm^2s cmHg

A.2. Gas Chromatography Operating Protocol

Here, we have used Agilent 7890b for all the permeation experiments. The detail G.C.operating protocols are mentioned below:

Injector programing: Heater (ON) at 120 °C

Time (min)	**Split state**	**Split ratio**
Initial	ON	1
0.00	ON	1
1.00	ON	1

Oven programing:

Column oven (ON) and Rear oven (ON) at 100 °C

Rate (°C /min)	Temperature (°C)	Time (min)	Total time (min)
Initial	40	2.00	2.00
10	70	5.00	10.00

Total time = 10.00 min

Column pneumatics: (pressure program)

Rate (psi/min)	**Pressure (psi)**	**Time (min)**	**Total time (min)**
Initial	15	10.00	10.00

Total time = 10.00 min

Detector (TCD) programing: Heater (ON) at 95 °C Electronics (ON)

Filament temperature at 235 °C Filament temperature limit at 390 °C

TCD event table

Time (min)	**Range**	**Auto zero**	**Polarity**
Initial	0.05	YES	Negative

Gas sampling valve (GSV) programing:

Time (min)	Gas sampling valve
Initial	Fill
0.02	Inject

A.3. Detail Purity Percentage of all Calibration Gases

Name	Purity compositions
4 % CO_2 + 4 % N_2, balance Argon	CO_2 (99.999 %), N_2 (99.999 %), Ar (99.999 %), H_2O (< 2 ppm) and CO (< 0.5 ppm)
8 % CO_2 + 8 % N_2, balance Argon	CO_2 (99.999 %), N_2 (99.999 %), Ar (99.999 %), H_2O (< 2 ppm) and CO (< 0.5 ppm)
12 % CO_2 + 12 % N_2, balance Argon	CO_2 (99.999 %), N_2 (99.999), Ar (99.999 %), H_2O (< 2 ppm) and CO (< 0.5 ppm)
20 % CO_2, balance N_2	CO_2 (99.999 %), N_2 (99.999 %), H_2O (< 2 ppm) and CO (< 0.5 ppm)
40 % CO_2, balance N_2	CO_2 (99.999 %), N_2 (99.999 %), H_2O (< 2 ppm) and CO (< 0.5 ppm)
Pure CO_2	CO_2 (99.999 %)
Pure N_2	N_2 (99.999 %)
Pure H_2	H_2 (99.999 %)

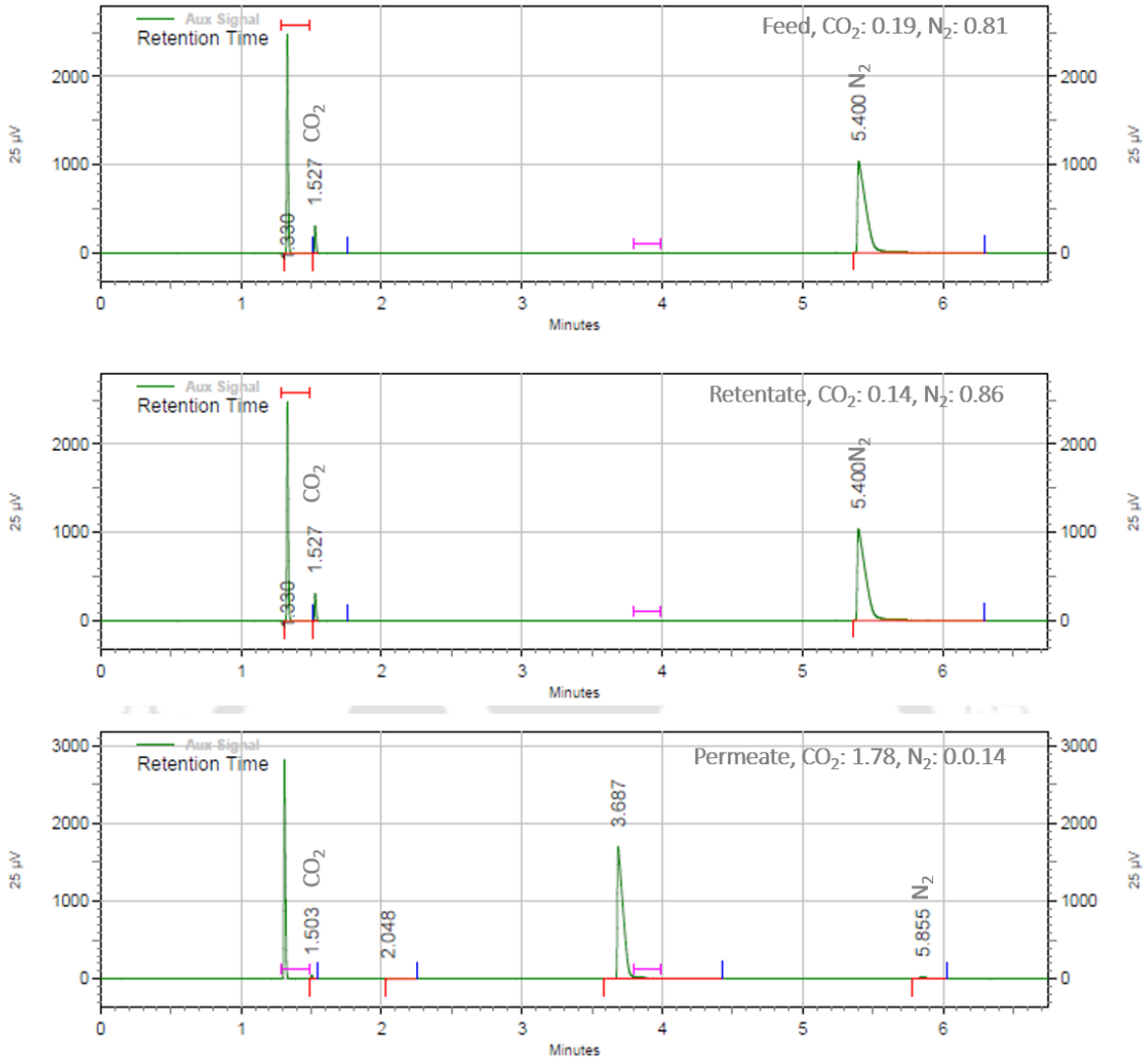

Figure A1. GC peaks of Lys-c-ZrBDC/CS MMM at 85 °C and 2.21/1.21 bar (feed/sweep) pressure having sweep/feed moisture flow ratio 1.67.

List of Publications, Conferences, And Workshops

Research Output

Publications

[1] S.K. Sharma, B.K. Sanfui, **A. Katare**, B. Mandal, "Fabrication and Performance Evaluation of Industrial Alumina Based Graded Ceramic Substrate for CO_2 Selective Amino Silicate Membrane." ACS Appl. Mater. Interfaces. 12 (2020) 40269–40284. (**ACS, Impact Factor 9.5**).

[2] **A. Katare**, S. Sharma, B. Mandal, "Effects of L-lysine-conjugated-graphene oxide as a nanofiller on the CO_2 separation performance of mixed matrix chitosan membrane." Indian Chem. Eng. 0 (2022) 1–12. (**Taylor & Francis**).

[3] **A. Katare**, R. Borgohain, B. Prasad, B. Mandal, "A Strategical Improvement in the Performance of CO_2/N_2 Gas Permeation via Conjugation of L-Tyrosine onto Chitosan Membrane." Membranes (Basel). 13 (2023) 487. (**MDPI, Impact Factor 4.2**).

[4] **A. Katare**, S. Sharma, H. Horo, S. Bhowmick, L.M. Kundu, B. Mandal, "An investigation on the effects of both amine grafting and blending with biodegradable chitosan membrane for CO_2 capture from CO_2/N_2 gas mixtures." Chem. Eng. J. 466 (2023) 143215. (**Elsevier, Impact Factor 15.1**).

[5] **A. Katare**, B. Mandal, "Green-Synthesized HF-free MIL-100(Fe) Nanoparticle-Infused Chitosan Mixed-Matrix Membranes for Enhanced CO_2 Permeance." Ind. Eng. Chem. Res. 62 (2023) 11151–11164. (**ACS, Impact Factor 4.2**).

[6] **A. Katare**, B. Mandal, "Surface Engineering of Zr BDC Nanoparticles via Conjugation with Lysine to Enhance the CO_2/N_2 Separation Performance of Chitosan Mixed Matrix Membranes under Dry and Humid Conditions." ACS Appl. Nano Mater. 6 (2023) 4821–4833. (**ACS, Impact Factor 5.9**).

[7] **A. Katare**, S. Kumar, S. Kundu, S. Sharma, L.M. Kundu, B. Mandal, "Mixed Matrix Membranes for Carbon Capture and Sequestration: Challenges and Scope." ACS Omega. 8 (2023) 17511–17522. (**ACS, Impact Factor 4.1**).

[8] **A. Katare,** S. Sikha, B. Mandal, "Synergistic Enhancement of CO_2/N_2 separation performance via Ce-MOF infused Chitosan Mixed Matrix Membrane." Environ. Sci. Pollut. Res. (2024). **(Springer, Impact Factor 5.8)**

[9] M. Barooah, S. Kundu, S. Kumar, **A. Katare,** L. Kundu, B. Mandal, "A Review on Mixed Matrix Membranes for Gas Separation: Fabrication, Application, Challenges and Opportunities." Chemosphere (2024) 141653. **(Science Direct, Impact Factor 8.8)**

[10] **A. Katare,** B. Mandal, "Chitosan/PES Mixed Matrix Composite Membranes Utilizing Amine and Non-Amine Hf-MOFs for Enhanced CO_2 Separation." **(Revision Received in J. Environ. Chem. Eng., Impact Factor 7.7)**

Conferences

[1] A. Katare, B. Mandal, "Amine doped UIO-66 nanocomposite as a high-performance filler for CO_2/N_2 gas separation." ICANN 2021, Indian Institute of Technology Guwahati, Guwahati, India. **(Oral Presentation)**

[2] A. Katare, B. Mandal, "CO_2/N_2 gas permeation study of green synthesized Fe-MOF embedded Mixed Matrix Membrane." ChemCon 2022, Harcourt Butler Technical University, Kanpur, India. **(Oral Presentation)**

[3] A. Katare, S. Kumar, S. Kundu, S. Sharma, L.M. Kundu, B. Mandal, "Mixed Matrix Membranes for Carbon Capture and Sequestration: Challenges and Scope." CUCHEAA 2022, Calcutta University, Kolkata, India. **(Oral Presentation)**

[4] A. Katare, B. Mandal, "Role of amine decorated Zr-MOF nanoparticles as a nanofiller/carrier with excellent CO_2 permeability into Chitosan mixed matrix membrane." CHEMTSF 2022, Indian Institute of Technology Roorkee, Roorkee, India. **(Oral Presentation)**

[5] A. Katare, S. Sharma, B. Mandal, "Effects of amine-conjugated-graphene oxide filler on CO_2/N_2 gas permeation through chitosan membrane." ACMS 2022, Heritage Institute of Technology, Kolkata, India. **(Oral Presentation)**

[6] A. Katare, B. Mandal, "Comparative study of effects of amine-conjugated-chitosan and amine-blended-chitosan on CO_2/N_2 Gas permeation." R&IC 2022, Indian Institute of Technology Guwahati, Guwahati, India. **(Poster Presentation)**

[7] A. Katare, B. Mandal, "Improving CO_2/N_2 gas Separation efficiency: Crafting of UIO-66 MOF with amino acid for advanced Chitosan Mixed Matrix Membrane." ICPHD 2023, Indian Institute of Technology Guwahati, Guwahati, India. **(Poster Presentation)**

[8] A. Katare, S. Sikha, B. Mandal, "Synergistic Enhancement of CO_2/N_2 separation performance via Ce-MOF infused Chitosan Mixed Matrix Membrane." CHEMCON 2023,

Heritage Institute of Technology, Kolkata, India. **(Poster Presentation)**

Awards

[1] Received **Ambuja's Young Research Award** in CHEMCON-2019 jointly organized by IIChE and IIT Delhi.

[2] Received **Best Poster Presentation Award** in ICPHD-2023 organized Jointly by jointly organized by the Department of Chemical Engineering, IIT Guwahati and IIT Guwahati Society of Petroleum Engineers (SPE) Student Chapter

Workshop

[1] Attended workshop on "Applied Statistical Modelling and data Analytics for Petroleum Engineering and Related Applications" *(2022)* organized by Indian Institute of Technology Guwahati, India.

Front Pages of

Papers Published in

Various Reputed

Journals

membranes

MDPI

Article

A Strategical Improvement in the Performance of CO_2/N_2 Gas Permeation via Conjugation of L-Tyrosine onto Chitosan Membrane

Aviti Katare [1], Rajashree Borgohain [1], Babul Prasad [2,*] and Bishnupada Mandal [1,*]

[1] Department of Chemical Engineering, Indian Institute of Technology Guwahati, Guwahati 781039, Assam, India
[2] William G. Lowrie Department of Chemical and Biomolecular Engineering, The Ohio State University, Columbus, OH 43210-1350, USA
* Correspondence: prasad.136@osu.edu (B.P.); bpmandal@iitg.ac.in (B.M.)

Abstract: Rubbery polymeric membranes, containing amine carriers, have received much attention in CO_2 separation because of their easy fabrication, low cost, and excellent separation performance. The present study focuses on the versatile aspects of covalent conjugation of L-tyrosine (Tyr) onto the high molecular weight chitosan (CS) accomplished by using carbodiimide as a coupling agent for CO_2/N_2 separation. The fabricated membrane was subjected to FTIR, XRD, TGA, AFM, FESEM, and moisture retention tests to examine the thermal and physicochemical properties. The defect-free dense layer of tyrosine-conjugated-chitosan, with active layer thickness within the range of ~600 nm, was cast and employed for mixed gas (CO_2/N_2) separation study in the temperature range of 25−115 °C in both dry and swollen conditions and compared to that of a neat CS membrane. An enhancement in the thermal stability and amorphousness was displayed by TGA and XRD spectra, respectively, for the prepared membranes. The fabricated membrane showed reasonably good CO_2 permeance of around 103 GPU and CO_2/N_2 selectivity of 32 by maintaining a sweep/feed moisture flow rate of 0.05/0.03 mL/min, respectively, an operating temperature of 85 °C, and a feed pressure of 32 psi. The composite membrane demonstrated high permeance because of the chemical grafting compared to the bare chitosan. Additionally, the excellent moisture retention capacity of the fabricated membrane accelerates high CO_2 uptake by amine carriers, owing to the reversible zwitterion reaction. All the features make this membrane a potential membrane material for CO_2 capture.

Keywords: CO_2/N_2 separation; chitosan; L-tyrosine; grafting; biopolymer; amino acid

Citation: Katare, A.; Borgohain, R.; Prasad, B.; Mandal, B. A Strategical Improvement in the Performance of CO_2/N_2 Gas Permeation via Conjugation of L-Tyrosine onto Chitosan Membrane. *Membranes* **2023**, *13*, 487. https://doi.org/10.3390/membranes13050487

Academic Editors: Johannes Carolus (John) Jansen and Eric Favre

Received: 20 February 2023
Revised: 26 April 2023
Accepted: 27 April 2023
Published: 29 April 2023

1. Introduction

The fossil fuel combustion method remains the biggest energy source for the planet's needs [1]. The sharp increase in energy demand in the previous years is responsible for almost 33 Gt CO_2 emissions in 2019, of which almost 30% comes from coal-fired energy generation plants [2]. In the pre-industrialized era, plants were the natural reservoir of carbon. They utilized CO_2 via a process called photosynthesis. However, the transition of society from the preindustrial to the industrial stage, as well as deforestation and a rapid rise in energy demand due to population growth, have greatly increased the CO_2 concentration levels [3,4]. Therefore, various technologies have been developed, investigated, and patented over the past few decades, comprising adsorption, absorption, cryogenic fractionation, and membrane technology for CO_2 capture [5,6]. Membrane technology has gained interest as the preferred alternative to CO_2 capture over more sophisticated absorption technology due to its operational simplicity, product consistency with high selectivity and CO_2 loading, energy efficiency, its economical properties, and easy handling [7].

Although many materials have been used to prepare gas separation membranes, polymers have emerged as the primary market due to their simplicity of fabrication,

Chemical Engineering Journal 466 (2023) 143215

Contents lists available at ScienceDirect

Chemical Engineering Journal

journal homepage: www.elsevier.com/locate/cej

An investigation on the effects of both amine grafting and blending with biodegradable chitosan membrane for CO_2 capture from CO_2/N_2 gas mixtures

Aviti Katare [a], Swapnil Sharma [a], Himali Horo [b], Sourav Bhowmick [c], Lal Mohan Kundu [c], Bishnupada Mandal [a,*]

[a] Department of Chemical Engineering, Indian Institute of Technology Guwahati, Guwahati, Assam 781039, India
[b] Department of Chemical Engineering, Thapar Institute of Engineering and Technology, Patiala, Punjab 147004, India
[c] Department of Chemistry, Indian Institute of Technology Guwahati, Guwahati, Assam 781039, India

ARTICLE INFO

Keywords:
Chitosan membrane
CO_2 capture
Amine grafting
Amine blending
Gas separation

ABSTRACT

The fusion of amine carriers into rubbery or glassy polymeric membranes is always preferred over neat polymeric membranes due to their enhanced CO_2/light gas separation performances. However, few studies compare the effects of two approaches: amine blending and grafting with polymer matrix, and their contribution to gas separation (GS) performance. In this study, a facilitated transport-cum-solution diffusion-based chitosan/2-Amino-3-phenylpropanoic acid, also called phenylalanine, grafted and blended membranes were prepared via the solution casting method for gas separation (GS) application. The fabricated membranes were systematically investigated to characterize their chemical, mechanical and thermal stabilities using various characterization techniques. The GS tests with 20% CO_2 and 80 % N_2 mixed gas were conducted at 85 °C and 2.21 bar feed pressure. The results suggest that the grafting and blending of phenylalanine (Phe) with the chitosan (CS) matrix boosted the CO_2 permeance and CO_2/N_2 selectivity of the fabricated membranes, respectively, when compared to the bare CS membrane under similar experimental conditions. The obtained results are validated by calculating the activation energy of permeability from the Arrhenius plots for both grafted and blended membranes. The highest obtained CO_2 permeance was 106 GPU in the Phe-grafted-CS membrane, and optimal selectivity was 97 in the 20 wt% Phe-blended-CS membrane. The stability tests were also conducted for both types of membranes. The results suggest that chemical grafting showed more stable results than physical blending when the membranes were tested for a long run of almost 400 h.

1. Introduction

The implementation of the efficacious carbon capture and sequestration (CCS) technique is important to limit the emissions of greenhouse gases such as carbon dioxide (CO_2), carbon monoxide (CO), nitrous oxides (NO_x), and sulfur oxides (SO_x), etc. [1]. These emissions have been responsible for rising global temperatures and sea levels, depraving weather patterns, and ecological and habitat changes [2]. Coal and gas-fired power plants, which are required to meet the population's current and future energy demands, are substantial contributors to these emissions [3]. Studies have demonstrated that membrane separation has proven to be a cost-effective and environment-friendly technology over other traditional gas separation methods, such as amine absorption, adsorption, cryogenic condensation, and gas distillation for removing acid gases (CO_2) in post-combustion gas treatment [4–6]. Due to their simple construction, continuous operation, low CapEx, and suitable mechanical and thermal strength, membrane separation technologies are commonly employed as economically viable procedures [7,8].

Polymers are preferable to inorganic materials for the fabrication of membranes because they are more affordable, show excellent mechanical, thermal, and chemical stabilities, and have defect-free thin film-forming properties [9–11]. Despite many benefits, the existing polymeric membranes-based gas separation systems have subpar performances, such as Robeson's upper bound trade-off between selectivity and permeability and plasticization. Blending and grafting of other

* Corresponding author.
E-mail addresses: soura176122028@iitg.ac.in (S. Bhowmick), lmkundu@iitg.ac.in (L.M. Kundu), bpmandal@iitg.ac.in (B. Mandal).

https://doi.org/10.1016/j.cej.2023.143215
Received 20 December 2022; Received in revised form 16 April 2023; Accepted 24 April 2023
Available online 28 April 2023

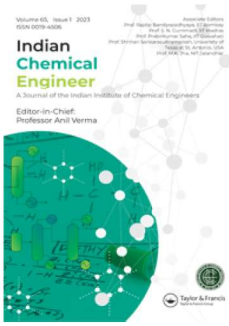

Indian Chemical Engineer

ISSN: (Print) (Online) Journal homepage: https://www.tandfonline.com/loi/tice20

Effects of L-lysine-conjugated-graphene oxide as a nanofiller on the CO_2 separation performance of mixed matrix chitosan membrane

Aviti Katare, Swapnil Sharma & Bishnupada Mandal

To cite this article: Aviti Katare, Swapnil Sharma & Bishnupada Mandal (2022): Effects of L-lysine-conjugated-graphene oxide as a nanofiller on the CO_2 separation performance of mixed matrix chitosan membrane, Indian Chemical Engineer, DOI: 10.1080/00194506.2022.2119895

To link to this article: https://doi.org/10.1080/00194506.2022.2119895

Published online: 14 Sep 2022.

I&EC research
Industrial & Engineering Chemistry Research

pubs.acs.org/IECR

Article

Green-Synthesized HF-free MIL-100(Fe) Nanoparticle-Infused Chitosan Mixed-Matrix Membranes for Enhanced CO_2 Permeance

Aviti Katare and Bishnupada Mandal*

Cite This: *Ind. Eng. Chem. Res.* 2023, 62, 11151−11164

Read Online

ACCESS | Metrics & More | Article Recommendations | Supporting Information

ABSTRACT: The green synthesis route for producing mixed-matrix membranes (MMMs) has recently received a lot of attention to capture CO_2 from the gaseous mixture. Taking this into consideration, biopolymer chitosan (CS) was selected as a matrix and MIL-100(Fe) nanoparticles (NPs) as the nanofiller, which was created using an hydrofluoric acid (HF)-free environment at ambient conditions. The advantages of the zwitterion mechanism via amine groups of CS and the high surface area and CO_2 affinity via open-metal sites of MIL-100(Fe) NPs were exploited in the study. A solution casting approach was employed to fabricate the active layer of filler-embedded CS solution with a desired thickness of ∼1 to 1.5 μm onto the poly(ether sulfone) (PES) support. The effect of MOF addition on the chemical, physical, and thermal structure of synthesized MMMs was studied by utilizing various analytical techniques and compared with the pristine CS membrane. At optimum operating conditions of 2.21 bar feed pressure and 85 °C temperature under swollen circumstances, the pure CS membrane showed CO_2/N_2 selectivity of 29 and CO_2 permeance of 24 gas permeation units (GPU). Under similar operating conditions, the optimized MMM demonstrated enhanced CO_2/N_2 selectivity and permeance of 59 and 85 GPU, respectively. Finally, when the obtained results were compared to the axis of the Robeson diagram, the performance of the polymer/MOF membranes containing 15 wt % MOF was shown to be more suitable for separating CO_2 from N_2, even at adverse conditions.

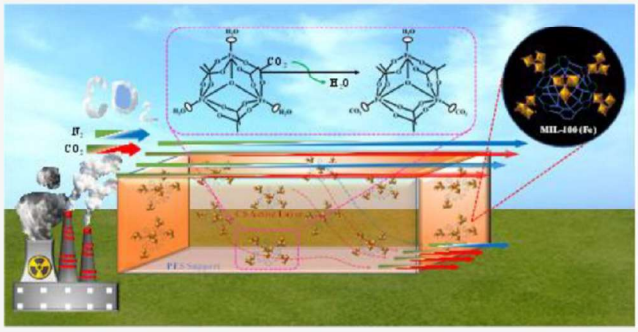

1. INTRODUCTION

Growing concerns about anthropogenic activities responsible for exaggerated greenhouse gas emissions have motivated researchers to develop advanced technologies to address these issues. The main contributors to CO_2 emissions are power stations (25%), followed by agriculture (24%), other industries (21%), and the transportation sector (14%).[1] The main goal of these sectors to mitigate the current CO_2 emission can be achieved by (i) minimizing global energy usage, (ii) substituting existing fossil-fuel-based technologies with green energy technology, and (iii) carbon capture and sequestration (CCS). CCS from flue gas is a workable and simple solution to the ongoing issue brought on by burning fossil fuels. With the development of new techniques, membrane separation has proven to be an environment-friendly technology that is anticipated to be a potential replacement of the traditional CCS methods, including solvent-based amine scrubbing, cryogenic distillation, pressure swing adsorption, etc.[2] Membrane separation using polymeric material has attracted greatly over the past few decades as it offers numerous advantages such as easy processing, better film forming property, cost-effectiveness, etc.[3,4] Various polymers have been investigated by the researchers as gas separation membranes, such as poly(methyl methacrylate),[5] polysulfone (PS),[6] Matrimid,[7] polymers of intrinsic microporosity,[8] sulfonated poly(ether ether ketone),[9] poly(vinyl alcohol),[10] and poly(ethylene oxide),[11] etc. Biobased polymers, such as cellulose acetate,[12] cellulose ester,[13] and chitosan (CS),[14,15] utilized in CO_2 separation applications, have also recently gained popularity due to their widespread availability, low cost, and biodegradability, etc. As known, the Lewis base has a strong affinity toward the acidic CO_2 molecules, thus making it a vital component in the backbone of the polymers for CO_2 separation applications. In this regard, thermally stable CS biopolymer has gained extensive attention due to the availability of amine functional groups acting as fixed CO_2 selective sites in their unit structure, making them a suitable candidate for CO_2 separation.[16]

CS-based membranes employ the facilitated transport mechanism, which involves a reversible reaction between "carrier" (such as an amine group) and CO_2 molecules.[17] CS also shows the advantage of high hydrophilicity, which results

Received: May 16, 2023
Revised: June 19, 2023
Accepted: June 23, 2023
Published: July 10, 2023

ACS APPLIED NANO MATERIALS

www.acsanm.org Article

Surface Engineering of Zr BDC Nanoparticles via Conjugation with Lysine to Enhance the CO_2/N_2 Separation Performance of Chitosan Mixed Matrix Membranes under Dry and Humid Conditions

Aviti Katare and Bishnupada Mandal*

Cite This: *ACS Appl. Nano Mater.* 2023, 6, 4821−4833 Read Online

ACCESS | Metrics & More | Article Recommendations | Supporting Information

ABSTRACT: Mixed matrix membranes (MMMs) incorporated with rigid porous metal−organic framework (MOF) nanoparticles (NPs) are well known for their increased carbon dioxide (CO_2) separation performance. For successful separation of CO_2 from the flue gas, CO_2-philic zirconium-based MOF NPs (Zr BDC or UIO-66) were synthesized and decorated with L-lysine amino acids to incorporate into a chitosan (CS) polymer matrix. The high porosity and surface area of the MOF NPs aided in the CO_2 separation permeance, while the selectivity was addressed by the amine functional groups present in L-lysine. The covalently bonded L-lysine onto Zr BDC NPs has a greater CO_2 affinity due to the dangling amine groups. Additionally, the amine conjugation strengthened the hydrogen bonds between the MOF and the CS matrix, thereby improving the dispersibility of MOF in the polymer matrix. After successful characterization studies, it was discovered that fabricated MMMs with a 7 wt % loading of lysine-conjugated Zr BDC (lys-c-Zr BDC) NPs with a 4 μm active layer thickness demonstrated better results than the pristine CS and the Zr BDC-embedded CS MMM. The composite lys-c-Zr BDC incorporated CS MMM showed a CO_2 permeance of 34.9 GPU and a steady CO_2/N_2 separation factor of 29.4 under dry conditions and a CO_2 permeance of 135.2 GPU and a steady CO_2/N_2 separation factor of 71.5 under swollen conditions at 85 °C and 0.221 MPa feed pressure. It has also been shown that, under optimum conditions, the fabricated membrane has successfully surpassed the Robeson upper bound curve, which makes it suitable for commercial applications.

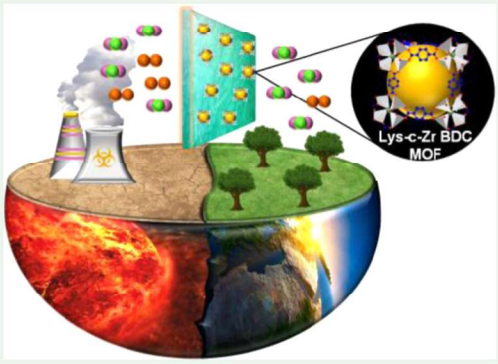

KEYWORDS: *mixed-matrix membrane, CO_2 capture, Zr BDC, UIO 66, conjugation*

1. INTRODUCTION

The amount of carbon dioxide released globally due to anthropogenic activities increased from about 20 Gt in 1990 to 31.5 Gt in 2020, causing CO_2 to reach its highest-ever average annual concentration of 412.5 ppm, as reported by NASA.[1] Approximately 65% of all anthropogenic greenhouse gas emissions now come from energy-generated power plant emissions.[2] To capture this CO_2 from flue gases in order to reverse this trend, absorption, adsorption, and membrane technologies can be used.[3] The conventional aqueous amine absorption, also referred to as amine scrubbing,[4] uses a lot of energy and has issues with corrosion and degradation despite being effective.[5] In addition, the regeneration energy for solvents is very expensive due to the strong affinity between CO_2 and amines.[6] Adsorption is still a growing technology and suffers from many disadvantages like batch operation, waste disposal, and high capital investment for CO_2 separation, etc.[7,8] Membrane technology provides a cost-saving, energy-efficient, continuous operation substitute over conventional CO_2 capture technologies in a number of crucial gas and liquid separation processes.[9−11] Currently, the majority of commercially implemented membrane technologies rely on polymeric ultrathin selective layers onto a porous support to achieve an extraordinary volumetric flux of CO_2.[12−14] However, the flexibility and solubility of the polymers ensure good processability during membrane fabrication processes, which is crucial for the development of large-area membranes devoid of significant flaws for industrial applications.

In the search for less expensive but high CO_2/N_2 separation performance polymeric membrane materials, chitosan (CS), a biodegradable polysaccharide, has shown promising results[15,16] and has been selected as a base material in the current research. But, like many other polymeric materials like PVA,[17] Pebax,[18] Matrimid,[19] PEG,[20] PVP,[21] etc., CS also suffers from the Robeson upper bound limitation". Hence, to take this drawback into consideration, incorporate a rigid porous

Received: February 5, 2023
Accepted: March 6, 2023
Published: March 15, 2023

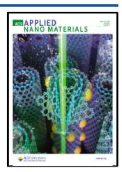

https://doi.org/10.1021/acsanm.3c00534
ACS Appl. Nano Mater. 2023, 6, 4821−4833

Environmental Science and Pollution Research
https://doi.org/10.1007/s11356-024-33061-y

SUSTAINABLE ENERGY TRANSITION: CHALLENGES AND OPPORTUNITIES

Synergistic enhancement of CO_2/N_2 separation performance via Ce-MOF-infused chitosan mixed matrix membrane

Aviti Katare[1] · **Sikha Sikha**[1] · **Bishnupada Mandal**[1]

Received: 6 January 2024 / Accepted: 20 March 2024

Abstract
Reticular chemistry, exemplified by metal–organic frameworks (MOFs), has proven invaluable in creating porous materials with finely tuned structures to address critical global energy and environmental challenges. In this context, the need for efficient carbon dioxide (CO_2) capture and utilization has taken center stage. One promising approach involves the integration of MOFs into polymer matrix to develop mixed matrix membranes (MMMs). In this work, cerium-based MOFs (Ce-MOF) were selected due to their robust CO_2 capture capabilities, while chitosan (CS) was chosen as the polymer matrix due to its reasonably good selectivity and balanced CO_2 permeance for the development of MMMs for CO_2/N_2 (20/80 vol%) separation. A comprehensive suite of analytical techniques, including FTIR, XRD, FESEM, XPS, TGA, EDX, FETEM, and BET, was applied for precise characterization of both the MOF and MMMs. Various operational parameters, such as Ce-MOF content and temperature, were systematically explored to investigate the CO_2 capture efficiency of the synthesized MMMs. The results revealed that the optimized Ce-MOF-embedded CS MMMs consistently outperformed the bare CS membranes.

Keywords Ce-MOF · Chitosan · Mixed matrix membrane · CO_2/N_2 separation · Flue gas

Introduction

The primary source of anthropogenic carbon dioxide (CO_2) emissions is the combustion of fossil fuels, accounting for 55% of global CO_2 emissions (Paraschiv and Paraschiv 2020). The CO_2 concentration in the flue gases depends on the type of fuel used, such as coal (comprising 12–15 mol-% CO_2) and natural gas (comprising 3–4 mol-% CO_2). To address the issue of anthropogenic CO_2 emissions and move toward sustainable lifestyle, it is crucial to develop technologies with carbon–neutral or even carbon-negative attributes, which hinge on the principles of carbon capture, utilization, and sequestration (CCUS) (Karnauskas et al. 2020). Among these alternatives, the capture of CO_2 from post-combustion process before its release into the atmosphere emerges as an effective strategy to curtail emissions. Within the realm of numerous CO_2 capture techniques (absorption, adsorption, membrane separation, cryogenic separation, hydrate technology, and microbial technology), post-combustion processes centered on absorption technology stands out as one of the most mature approaches (Katare et al. 2023b). Nevertheless, the widespread implementation of this process encounters a significant obstacle in the form of the substantial energy penalty associated with solvent regeneration during CO_2 absorption–desorption. Polymer-based membranes, within the domain of membrane technology, offer an energy-efficient solution for CO_2/N_2 separation due to their notable CO_2 loading capacity, compact spatial requirements, eco-friendliness, minimal energy penalties, and cost-effectiveness (Lin and Freeman 2004).

Recent scientific studies have highlighted a fundamental challenge in the widespread use of polymeric membranes that rely solely on a solution-diffusion process (Ansaloni et al. 2017). This challenge relates to the natural trade-off between two key properties of polymeric membranes: their ability to let gases pass through (permeability) and their ability to separate one gas from another (selectivity). This trade-off was first quantified by Robeson in 1991 (Zhu et al. 2019), who established upper limits using a mathematical analysis of the selectivity versus permeability (on log plot) for various gas pairs, including O_2/N_2, H_2/N_2, He/N_2,

Responsible Editor: Angeles Blanco

✉ Bishnupada Mandal
bpmandal@iitg.ac.in

[1] Department of Chemical Engineering, Indian Institute of Technology Guwahati, Guwahati 781039, Assam, India

Published online: 02 April 2024

ACS OMEGA

http://pubs.acs.org/journal/acsodf

Review

Mixed Matrix Membranes for Carbon Capture and Sequestration: Challenges and Scope

Aviti Katare, Shubham Kumar, Sukanya Kundu, Swapnil Sharma, Lal Mohan Kundu, and Bishnupada Mandal*

Cite This: *ACS Omega* 2023, 8, 17511−17522

Read Online

ACCESS | Metrics & More | Article Recommendations

ABSTRACT: Carbon dioxide (CO_2) is a major greenhouse gas responsible for the increase in global temperature, making carbon capture and sequestration (CCS) crucial for controlling global warming. Traditional CCS methods such as absorption, adsorption, and cryogenic distillation are energy-intensive and expensive. In recent years, researchers have focused on CCS using membranes, specifically solution-diffusion, glassy, and polymeric membranes, due to their favorable properties for CCS applications. However, existing polymeric membranes have limitations in terms of permeability and selectivity trade-off, despite efforts to modify their structure. Mixed matrix membranes (MMMs) offer advantages in terms of energy usage, cost, and operation for CCS, as they can overcome the limitations of polymeric membranes by incorporating inorganic fillers, such as graphene oxide, zeolite, silica, carbon nanotubes, and metal−organic frameworks. MMMs have shown superior gas separation performance compared to polymeric membranes. However, challenges with MMMs include interfacial defects between the polymeric and inorganic phases, as well as agglomeration with increasing filler content, which can decrease selectivity. Additionally, there is a need for renewable and naturally occurring polymeric materials for the industrial-scale production of MMMs for CCS applications, which poses fabrication and reproducibility challenges. Therefore, this research focuses on different methodologies for carbon capture and sequestration techniques, discusses their merits and demerits, and elaborates on the most efficient method. Factors to consider in developing MMMs for gas separation, such as matrix and filler properties, and their synergistic effect are also explained in this Review.

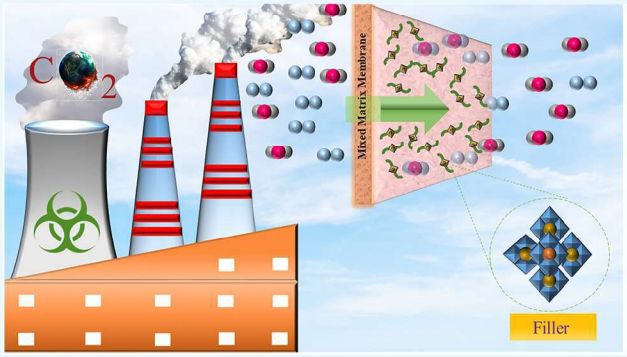

1. INTRODUCTION

Gases such as nitrous oxide (N_2O), methane (CH_4), and carbon dioxide (CO_2) are called greenhouse gases (GHGs) because these gases trap infrared radiation and radiate it back to the atmosphere, which leads to an increase in global temperature. Owing to rapid population growth and a sharp rise in energy demand, the GHG concentration in the atmosphere has amplified rapidly.[1,2] The global mean surface temperature (GMST) was 1.0 °C higher compared to that in the preindustrial era (1850−1900) in 2017 due to the increased GHG concentration.[3] The Intergovernmental Panel on Climate Change (IPCC) has reported that GMST will rise to 2.0 °C above that of the preindustrial era by 2035.[4] This rise in the GMST has severely affected our ecosystems, such as the melting of ice, floods in low-level countries, and wildfires. To stabilize the rise of the GMST under 1.5 °C, CO_2 capture, utilization, and sequestration (CCUS) are crucial processes that can be applied on an industrial scale.

To capture the CO_2 gas generated from large point sources, there are mainly four approaches available: precombustion capture, postcombustion capture, chemical-looping combustion, and oxycombustion. Oxycombustion and precombustion capture cannot be retrofitted into the existing power plants, so these two can be utilized for future power plants.[5] Postcombustion technologies include the capture of CO_2 from the exhaust gas of a fossil-fuel-fired power plant.[6] This can be considered a preferable option, as this technology can be installed as an add-on in existing power plants, which use air for fuel combustion. There are several postcombustion CO_2 capture technologies available, which include membrane separation, adsorption, absorption, and cryogenic separation.[7] Absorption is the most effective technology widely used to remove CO_2 from synthesis and natural gas.[5] The disadvan-

Received: March 12, 2023
Accepted: April 20, 2023
Published: May 15, 2023

https://doi.org/10.1021/acsomega.3c01666
ACS Omega 2023, 8, 17511−17522

ACS APPLIED MATERIALS & INTERFACES

www.acsami.org

Research Article

Fabrication and Performance Evaluation of Industrial Alumina Based Graded Ceramic Substrate for CO_2 Selective Amino Silicate Membrane

Savan Kumar Sharma, Barun K. Sanfui,* Aviti Katare, and Bishnupada Mandal*

Cite This: *ACS Appl. Mater. Interfaces* 2020, 12, 40269–40284

Read Online

ACCESS | Metrics & More | Article Recommendations

ABSTRACT: The present study mainly focuses on the careful design of an amino-silicate membrane integrated on an asymmetric graded membrane substrate, comprised of a cost-effective macroporous industrial alumina based ceramic support with a systematic graded assemblage of sol–gel derived γ-alumina intermediate and silica-CTAB sublayer-based multilayered interface, specifically dedicated for the separation of CO_2 gas from the binary gas mixture (CO_2/N_2) under nearly identical flue gas atmospheric conditions. The tailor-made industrial α-alumina-based porous ceramic support has been characterized in terms of apparent porosity, bulk density, flexural strength, microstructural feature, pore size, and its distribution to demonstrate its application feasibility toward the evolution of the subsequent membrane structure. The near surface morphology of the subsequent intermediate and submembrane layer has been carefully controlled via precisely scheming the colloidal chemistry and consequently implementing it during the deposition process of the respective γ-alumina and silica-CTAB precursor sols, whereas the potentiality of the quarantined amine groups in the final amino-silicate membrane has been methodically optimized by the appropriate heat treatment process. Finally, the real-time applicability of the hybrid amino-silicate membrane has been evaluated in terms of systematic analysis of the binary gas (CO_2/N_2) separation performance under variable operating conditions. The investigated ceramic membrane exhibited optimum CO_2 permeance of 46.44 GPU with a CO_2/N_2 selectivity of 12.5 at 80 °C under a trans-membrane pressure drop of 0.8 bar having a feed and sweep side water flow rate of 0.03 mL/min, which shows its performance reliability at nearly identical flue gas operating conditions.

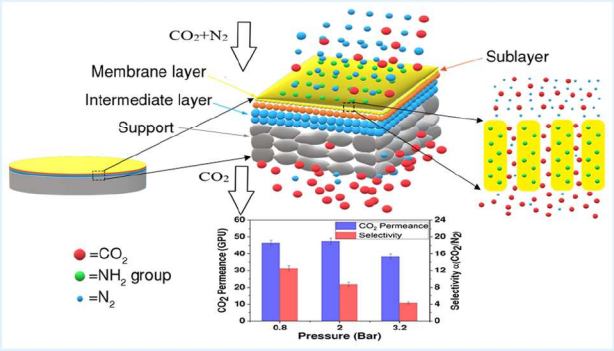

KEYWORDS: *ceramic membrane, industrial alumina, γ-alumina, graded multilayer support, amorphous silica, carbon dioxide separation, sol–gel*

1. INTRODUCTION

The present scenario of increasing global industrialization and urbanization has led to a sharp rise in uncertainty of the global climate change by increasing emission of anthropogenic greenhouse gases, which in turn propelled serious environmental concerns such as global warming, increased frequency, and the duration of the El Niño event and coastal erosion.[1,2] Among all of the greenhouse gases, CO_2 has a major contribution toward the greenhouse effect due to its gratuitously increasing concentration since 1958, which is evidenced to be 408 ppm as of 2018.[3] This is also recorded as the highest accretion rate of CO_2 emission in past decades, which made the mitigation of "CO_2 separation technology" a major scientific concern to fight global climate change. The three well-established CO_2 capturing strategies are optimistically considered in this regard: precombustion, postcombustion, and oxy fuel combustion.[4,5] Notably, these exceedingly mature technologies mainly associate with the phenomena of physical and chemical absorption, adsorption, cryogenic distillation, and membrane separation. Among them, membrane technology has acquired an immense techno-economic feasibility for the selective removal of CO_2 due to its energy-efficiency, easy handling, low cost, and operation satiability with corrosion free nature.[6]

Moreover, in considering membrane technology, the preliminary concern has been devoted toward the careful identification of the chemical composition and physical characteristics of the respective CO_2 gas emission sources.[7]

Received: May 19, 2020
Accepted: August 11, 2020
Published: August 11, 2020

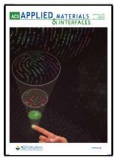

https://dx.doi.org/10.1021/acsami.0c09188
ACS Appl. Mater. Interfaces 2020, 12, 40269–40284

Chemosphere 354 (2024) 141653

Contents lists available at ScienceDirect

Chemosphere

journal homepage: www.elsevier.com/locate/chemosphere

New generation mixed matrix membrane for CO_2 separation: Transition from binary to quaternary mixed matrix membrane

Mridusmita Barooah [a], Sukanya Kundu [a], Shubham Kumar [a], Aviti Katare [a], Rajashree Borgohain [a], Ramagopal V.S. Uppaluri [a], Lal Mohan Kundu [b], Bishnupada Mandal [a,*]

[a] Department of Chemical Engineering, Indian Institute of Technology Guwahati, Guwahati, 781039, Assam, India
[b] Department of Chemistry, Indian Institute of Technology Guwahati, Guwahati, 781039, Assam, India

HIGHLIGHTS

- Comprehensive review of the advanced MMMs wrapping various facets of membranes.
- Filler modification to improve the gas separation performance.
- Ternary/quaternary MMMs to overcome the lacunae of binary MMM.
- Defect-free biopolymeric MMMs are an option for large-scale applications.
- MMM with MOFs, and MXenes enhanced the CO_2 separation performance.

GRAPHICAL ABSTRACT

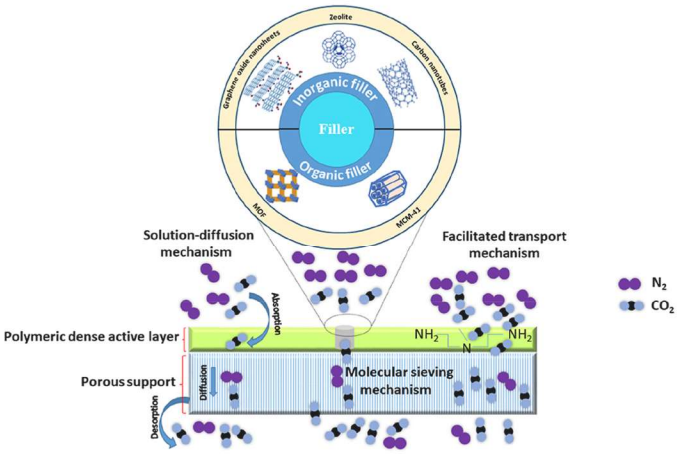

ARTICLE INFO

Handling editor:

Keywords:
Fillers
Permeability
Flue gas
Composite membranes
CO_2 capture

ABSTRACT

Contemporary advances in material development associated with membrane gas separation refer to the cost-effective fabrication of high-performance, defect-free mixed matrix membranes (MMMs). For clean energy production, natural gas purification, and CO_2 capture from flue gas systems, constituting a functional integration of polymer matrix and inorganic filler materials find huge applications. The broad domain of research and development of MMMs focused on the selection of appropriate materials, inexpensive membrane fabrication, and comparative study with other gas separation membranes for real-world applications. This study addressed a comprehensive review of the advanced MMMs wrapping various facets of membrane material selection; polymer and filler particle morphology and compatibility between the phases and the relevance of several fillers in the assembly of MMMs are analyzed. Further, the research on binary MMMs, their problems, and solutions to

* Corresponding author.
E-mail addresses: barooahmri20@gmail.com (M. Barooah), sukanyakundu26@gmail.com (S. Kundu), shubhamkumar@iitg.ac.in (S. Kumar), avitikatare.iitg@gmail.com (A. Katare), borgohainrajashree@gmail.com (R. Borgohain), ramgopalu@iitg.ac.in (R.V.S. Uppaluri), lmkundu@iitg.ac.in (L.M. Kundu), bpmandal@iitg.ac.in (B. Mandal).

https://doi.org/10.1016/j.chemosphere.2024.141653
Received 31 December 2023; Received in revised form 1 March 2024; Accepted 4 March 2024
Available online 12 March 2024